LEHIGH UNIVERSITY

THE CHANNELING OF 35, 100, AND 250 GEV/C MIXED BEAM OF PIONS, KAONS, AND PROTONS IN A 2 CM THICK GERMANIUM SINGLE CRYSTAL

by

Muhammad Abul Hasan

and

Alvin S. Kanofsky

Based on a dissertation by M. A. Hasan
Presented to the Graduate Committee
of Lehigh University
in Candidacy for the Degree of
Doctor of Philosophy
in
Physics

Lehigh University

1980

LEH-HEP 80-9-1

Supported in Part by D.O.E. under
Contract DE-AS02-76ER02894

Approved and recommended for acceptance as a dissertation in partial fulfillment of the requirements for the degree of Doctor of Philosophy.

AUGUST 28, 1980
(Date)

Professor in Charge

Accepted AUGUST 28, 1980
(Date)

Special committee directing
the doctoral work of
Muhammad Abul Hasan

Chairman

ACKNOWLEDGEMENTS

The author gratefully acknowledges the constant help, guidance, and encouragement of his thesis advisor, Professor Alvin Kanofsky, in all stages of this work. He is indebted to all the members of the Lehigh-Fermilab-Albany-Dubna-UCLA collaboration, without whose efforts this experiment would not have been possible. The author wishes to thank Dr. Richard Carrigan of Fermilab for providing pertinent information in the initial stages of the data analysis.

He is grateful to his Ph.D. committee members for patiently reviewing this dissertation. He is thankful to his fellow graduate students Dick Allen, Donna Gockley, and Arun Chatterjee for their help. He acknowledges the efforts of Mr. Joe Krosetz for drafting some of the figures and of Ms. Jeanne Loosbrock for typing this dissertation.

He is most grateful to his former school teacher, Mr. Eta Elahi, for creating in him such lasting interest in Physics and to his parents for encouraging and sustaining the interest.

TABLE OF CONTENTS

LIST OF FIGURES

LIST OF TABLES

ABSTRACT

In an analysis of high energy particle channeling data, the <110> axial and (111) planar channeling distribution widths were found to scale as $1/\sqrt{E}$ (Lindhard Theory) for 35, 100, and 250 GeV/c beam particles incident on a 2 cm thick hyperpure Germanium single crystal. The width of the blocking dip around the <110> axis direction also scaled as $1/\sqrt{E}$ (Lindhard Theory).

The radial component of the transverse motion of the <110> axially channeled particles was explained by the diffusion equation. The azimuthal component of the transverse motion exhibited complete statistical equilibrium for channeled and quasi-channeled particles, leading to the doughnut effect in the quasi-channeling incident angle region.

The inward shift of the transverse energy for 250 GeV/c momentum at 3.5 ψ_1 (where ψ_1 is the Lindhard critical angle) suggested that "cooling" may be observed for an $\sim$3 TeV/c beam along the <110> axis direction in a 2 cm thick Germanium crystal.

The density effect and the restricted energy loss of the delta rays were important corrections in the calculations of the mean stopping power for random orientation of the crystal.

The stopping power corresponding to the intercept on the low energy side of the energy loss distribution of the well channeled particles were compared with Esbensen and Golovchenko's calculation.

The mean energy loss of the channeled particles as a function of their incident angle followed the functional form predicted by Lindhard.

The negative particles behaved quite differently from the positive particles. The 35 GeV/c negative particles showed a broad dip ($\sim 3\psi_1$) around the <110> axis position for low energy loss particles. The particles going along the <110> axis direction exhibited higher than average energy loss. There was statistical equilibrium in the azimuthal component of the transverse motion for zero to $2\psi_1$ incident angles. The negative particles showed greater radial scattering for particles incident at small angles to the <110> axis direction compared to positive particles.

CHAPTER 1

INTRODUCTION

When a beam of positively charged particles is incident on a crystal at small angles to a major crystal axis or planar direction, the motion of the particles is influenced to a great extent by the regular arrangement of the atoms along these axes or planar directions.* The particles experience a set of correlated, gentle collisions with a large number of atoms, forming a row ("string") or a plane in the crystal; i.e., the atoms in the "string" or plane act collectively to deflect the particles. These collisions tend to steer the particles away from the high density regions of rows and planes of atoms. The motion of the particles, therefore, is restricted to the open channels in between the strings and planes of atoms in the crystal. This phenomenon is known as CHANNELING. It is illustrated in Fig. 1.1.

*The quantum interference effects are very small for heavy relativistic particles and they are neglected in the discussion here.

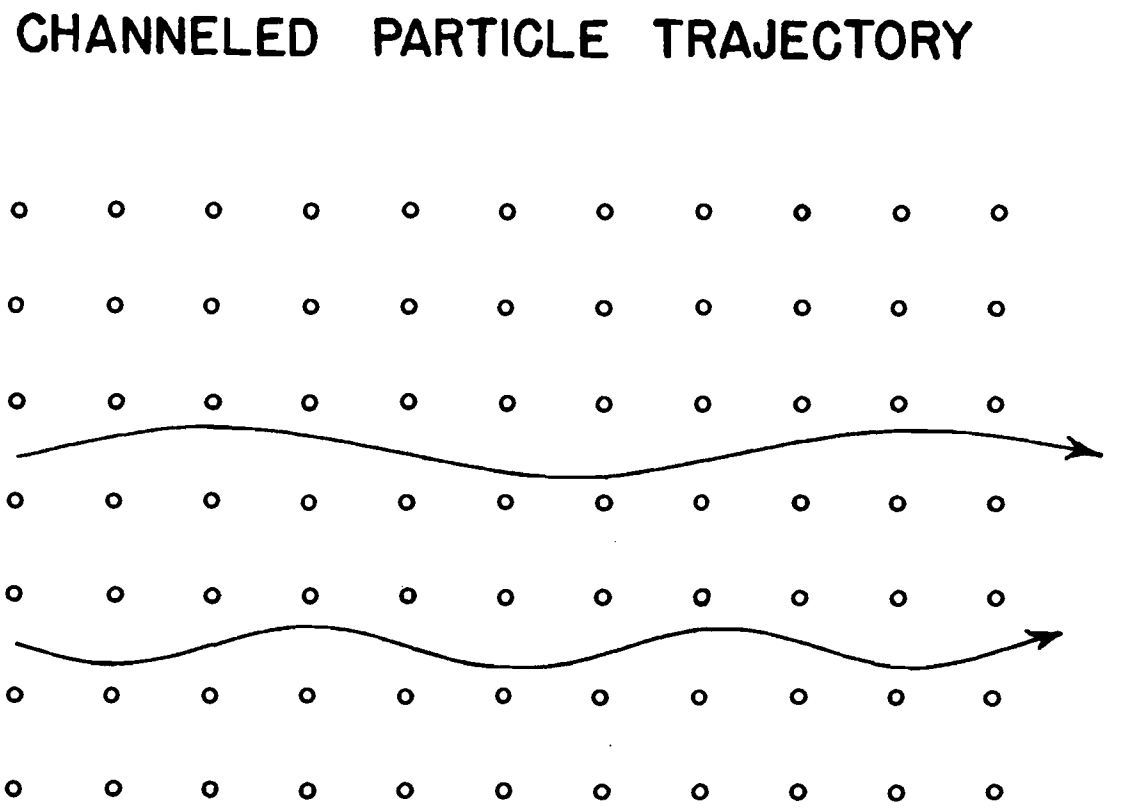

Fig. 1.1 The open circles represent atoms in a simple cubic crystal. The solid lines are exaggerated trajectories of the channeled particles between rows of atoms.

Since the channeled particles stay away from the high density regions of rows and planes of atoms, they show a decrease in all the physical phenomena that involve small impact parameter collisions with the atoms in the crystal, e.g., large angle Rutherford scattering with the nucleus, inner shell excitation and ionization of the atoms leading to x-ray production, dE/dx loss, multiple scattering, nuclear reaction, etc.

The correlation between the geometrical and physical aspects of the interaction of particles with the crystal which give rise to channeling and other related effects have generated a great deal of interest because of their many interesting applications to high energy physics, nuclear physics, and solid state physics. Some of these applications are outlined in the next section.

1.1 APPLICATIONS

Collimated Beams:

The decrease of multiple scattering for channeled particles gives rise to an enhancement in the intensity of the transmitted beam along the crystal axis direction. The narrow exit angle distribution of the channeled particles at high energy may be used to get well collimated beams of particles for experiments requiring such good collimation.

Blocking:

The blocking effect (to be explained in detail in later chapters) has already been used at MeV energies to measure lifetimes of short lived nuclei in the range of 10^{-18} to 10^{-14} seconds. This range is inaccessible to other techniques of measuring lifetimes. It has been proposed that such techniques could also be applied to the measurement of elementary particle lifetimes, e.g., the lifetime of the eta particle.

Form Factors:

Channeled particles are ideal for studying the interaction of beam particles with electrons, as in the measurements of the form factor of the beam particles, such as pions, kaons, sigmas, etc. This is because there is a large reduction of the nuclear interaction background for channeled particles.

Nuclear Interactions:

Nuclear interactions may be studied more efficiently by tilting the crystal axis, with respect to the beam direction, slightly beyond the Lindhard critical angle of channeling (defined in Sec. 2.1). At this orientation of the crystal, there is a large increase in the cross-section for small impact parameter collisions, including nuclear interactions.

Synchrotron Radiation:

The channeled particles are a good source of intense synchrotron radiation. These radiations are produced coherently, at the turning points, close to the large electric field large acceleration regions near the plane of atoms, as the charged particles oscillate between them, in their motion through the crystal. The frequency of the radiation emitted by the channeled particles is proportional to $\gamma^{3/2}$ ($\gamma = E/M_o c^2$) of the particle [Pa78]. Therefore, a knowledge of the energy and/or momentum of the incident particles and the frequency of the emitted radiation may be used to identify the beam particles. The possibility of obtaining stimulated emission from channeled electrons has also been suggested [Te77].

Acceleration:

It has been proposed [Ka77] that the channeled particles could be accelerated by shining LASERS at a properly oriented, suitably masked crystal, transparent to the Laser beam. The principle is similar to the linear accelerators using RF power in between drift tubes.

Focusing or "Cooling":

The focusing or "cooling" (reduction in transverse energy of the particles and resultant reduction in exit

angles) of the channeled particles has been proposed by many authors [Li65,Ka76,Ku76]. The results of this experiment suggest that the cooling of the channeled particles could be observed for beam momentum greater than 3 TeV/c (cf. Sec. 7.3). Such a focusing of the beam is very useful at high energy.

Bending:

The bending or sharp deflection of the channeled particles has been reported [E179] recently for a bent silicon crystal. This raises the interesting possibility of replacing magnets with crystals in order to steer external high energy beam particles from accelerators. The bending power of the crystal electro-static field appears to be much stronger (greater than 100,000 gauss) than the conventional magnets.

Short Lifetime Particle Interactions:

With the discovery of new, short lived particles like mesons, the interest in the interaction of such particles with nuclei has led to the suggestion of using targeting to study these interactions [Ca75]. The short lived particles could be produced by the interaction of the beam with the nucleus at the lattice site and emitted in the forward direction along a major crystal axis direction. These particles would be blocked from going along the axis direction because of

the intervening nuclei. This would greatly increase the interaction probability of the particles with the nuclei.

Fast Triggers:

The use of the channeling phenomena as a fast trigger in various configurations for high energy experiments has also been proposed [Ka78]. In all these cases the directional nature of the channeling of particles in a crystal has been exploited.

Solid State Studies:

In solid state physics the channeling phenomenon has been used at low energies to, among other things,

a) determine structure of the crystal.
b) implant ions in semi-conductors to different depths along channeling axes directions.
c) locate dopants and impurity atoms in interstitial positions.
d) study disorder and imperfections of crystal lattice.
e) study surface and epitaxial layers on crystals.
f) study radiation damage in a crystal.

1.2 BRIEF HISTORY OF CHANNELING AT GEV ENERGIES

The channeling of particles through a crystal was first suggested in 1912 [St12]. The experimental discovery showing anomalously long range of particles in crystalline solids was made in 1960 [Da60], and its

relation to crystal orientation was pointed out two years later [Ro62] and beautifully demonstrated by computer calculations [Ro63]. The initial stages of the development of channeling theory are outlined in the beginning of chapter 2.

One of the first channeling experiments done with the energy of the beam particles in the GeV-region was performed at Brookhaven National Laboratory (BNL) in the summer of 1974 by a Lehigh-Bell Labs-BNL group. The dechanneling of the negative pions of 4 GeV/c momentum was observed along <110> axis direction in a 1.0 cm thick Germanium Single Crystal [A176].

Experiments were also performed at the CERN accelerator facility by an AARHUS-CERN group and their results were first published in April 1975 [Fic75]. The channeling of 1.1 GeV/c protons and pions were reported in 1 mm thick Germanium Single Crystal. Axial channeling along the <110> axis direction and planar channeling along the (110) and (111) planes were observed in the exit, projected angle scatter diagram.

The AARHUS-CERN group, in collaboration with STRASBOURG, obtained the first data on ionization energy loss of channeled pions and protons in the GeV-region [Fic76]. The energy loss for 1.35 GeV/c well channeled pions and protons, along the <110> axis direction in 0.67 mm

Germanium crystal, was found to be 1/3 of the mean energy loss for random orientation of the crystal.

Further results of the channeling of protons, pions and deutrons of 1.15 and 1.35 GeV/c momenta were reported by AARHUS-CERN-STRASBOURG collaboration in February 1977 [Es77]. The negative particle dechanneling dip with a small peak near the centre of the channel was observed. The energy loss data of the negative particles was also presented.

In a series of papers published in 1978, the AARHUS-CERN-STRASBOURG group presented results for beam particles up to a momentum of 15 GeV/c. They presented a comprehensive study of the energy loss of positive and negative, 2 to 15 GeV/c pions, kaons, and protons in thin Germanium and Silicon crystals for channeled and random orientation [Es78a]. They reported the channeling results of 15 GeV/c negative pions [Es78b]. They also presented the nuclear interaction results of channeled and random beam at 15 GeV/c momentum [An78].

The next large increase in the beam momentum value was in the FERMILAB channeling experiment. This experiment was performed in the Spring of 1977, and it was a LEHIGH-ALBANY-FERMILAB-DUBNA-UCLA collaboration. The channeling of 35, 100, and 250 GeV/c mixed beam of pions, kaons, and protons along <110> axis in a 2 cm

thick Germanium Single Crystal was observed. This dissertation is a presentation of the results of the FERMILAB channeling experiment.

1.3 MOTIVATIONS

The experiment on channeling at FERMILAB with the beam momentum of hundreds of GeV/c was proposed because of the intrinsic physics interest and the convenience of carrying it out. The apparatus used a major part of the Kaon Form Factor Experiment which had been taking data previously in the M1 beam line of the Meson Laboratory. The use of the Kaon Form Factor experiment apparatus saved a lot of preparation time and expense.

Some of the physics reasons for doing the channeling experiment with such high energy beams of partices are listed below.

a) Channeling effects were seen in the 1 to 15 GeV/c momentum region by the AARHUS-CERN-STRASBOURG group at CERN (cf. Sec. 1.2). This experiment at FERMILAB would be a logical extension of the beam momentum to higher values.

b) The present theory of channeling, proposed by Lindhard [Li65], is based on classical impulse collision approximation with the continuum potential due to the strings or planes of atoms (cf. Sections 2.1 and 2.2). The calculations become more exact at higher

beam momentum values. This experiment would therefore be a good test of Lindhard's theory of channeling.

c) The dechanneling of the channeled particles is due to the multiple scattering, which scales as 1/E (cf. Chapter 8). The Lindhard critical angle ψ_1 (defined in Sec. 2.1)is a measure of the extent of the channeling region,and this scales as $1/\sqrt{E}$ (cf. Sec. 2.1). Therefore,the region of influence of dechanneling would shrink faster than that of channeling, and the channeling effect would become more prominent at higher beam energies.

d) The dechanneling length (the thickness of the crystal in which half of the channeled particles are scattered out of the channeling region) is longer at higher beam momentum values. Therefore thicker crystals could be used without any appreciable loss of channeled particles. It then would be possible, using a thick crystal at high energies, to observe statistical equilibrium in the transverse momentum of the channeled and quasi-channeled particles, in the same way that it is observed at MeV energies, using very thin crystals.

e) The focusing or "cooling" of the transverse energy of the beam particles at high energy has been suggested by some authors [Li65,Ka76,Ku76]. This hypothesis could be checked out in the FERMILAB experiment.

f) Negative particles heavier than the electron, e.g. pions, kaons, and anti-protons, were available at the FERMILAB facility. Therefore, the channeling or dechanneling effects of the negative particles could be studied with negligible interference from quantum effects.

CHAPTER 2

THEORY

The channeling of particles between atomic rows and planes was first suggested by Stark [Stal2] in 1912. But the idea was not taken up seriously because it was thought, at that time, that the thermal vibration of the lattice atoms would destroy any such effect in a finite thickness of the crystal.

It was not until fifty years later, in 1960, that the channeling effect was discovered, when it was observed that there was anomalously long range for ions incident on a crystal [Da60]. The correlation between the anomalously long range and the crystal orientation was suggested by Robinson in 1962 [Ro62]. This was beautifully demonstrated a year later, by computer calculations of Robinson and Oen [Ro63]. Thereafter the interest in the channeling phenomenon grew very rapidly.

A comprehensive theory for the channeling phenomenon was presented by Lindhard [Li65] in 1965. In this theory the incident ion was considered as a classical particle which was channeled when it entered the crystal at a small angle to a major crystal axis or planar direction (the details will be presented in later

sections). This classical particle approximation would be more exact for higher incident particle energies because the wavelength of the particle would become much smaller compared to the lattice spacing in the crystal and this would greatly reduce the quantum interference effects. Therefore the results of this experiment on channeling at high energy was considered to be suitable for checking the validity of the Lindhard theory.

In the following sections, Lindhard's theory for axial and planar channeling is described. The blocking effect, a result of the rule of reversibility, is presented. Other effects such as azimuthal and radial diffusions are also described. The theory of energy loss is presented along with the results in Chapter 9.

2.1 AXIAL CHANNELING

Positively charged energetic particles, incident on a single crystal at a small angle to a major crystal axis direction will be channeled if the following conditions are satisfied.

1. The particles undergo small angle elastic scattering with the nucleus. Large angle scattering and inelastic scattering with the nuclei are not allowed, because any such interactions will involve close collisions with the nuclei and the directional effect due to the crystal structure will be lost.

2. The channeled particles interact with a large number of atoms in the row along the crystal axis in each collision. This leads to a collective, correlated steering of the particles away from the rows of atoms. The energy loss due to excitation and ionization of the electrons is neglected. This is the source of multiple scattering, dechanneling, and energy loss in the crystal and will be discussed in later sections. In other words, the longitudinal motion parallel to the string is constant and the transverse energy is conserved.

3. The wavelength of the channeled particles is small compared to the lattice spacing so that there are no appreciable quantum interference effects and the particle may be considered as a classical particle. This condition is usually satisfied by fast moving, heavy particles.

4. The crystal lattice is almost perfect with a small number of impurities, defects, and dislocations. The thermal vibrations of the lattice atoms are not considered in the first approximation. These may be introduced later as perturbations.

The first two conditions mentioned above lead naturally to the concept of a string of atoms. A continuum potential due to a string is found by calculating the average of the potentials due to each atom on the string as indicated below

$$U(r) = \frac{1}{d} \int_{-\infty}^{+\infty} V(\sqrt{r^2+z^2})\,dz \qquad 2.1$$

where $V(\sqrt{r^2+z^2})$ is the ion-atom potential, d is the distance between two atoms on the string, $r^2 = x^2+y^2$, z is the coordinate along the string direction and x and y are the transverse coordinates.

The potential $V(\sqrt{r^2+z^2})$ is of the Thomas-Fermi type and has the form

$$V(R) = \frac{Z_1 Z_2 e^2}{R}\,\phi(R/a) \qquad 2.2$$

where Z_1 and Z_2 are the atomic numbers of the incident ions and the target atoms, respectively, a is the screening length equal to $a = 0.8853a_o(Z_1^{2/3} + Z_2^{2/3})^{-\frac{1}{2}}$ and $\phi(R/a)$ is the screening function.

An exact analytical form for $\phi(R/a)$ does not exist. However, approximate analytical expressions for the screening function have been suggested by various authors. Moliere's expression for the screening function is used extensively and has the form

$$\phi(R/a) = 0.1 \exp(-6.0R/a) + 0.55 \exp(-1.2R/a) + 0.35 \exp(-0.3R/a) \quad 2.3$$

A simpler expression has been suggested by Lindhard, who writes

$$\phi(R/a) = 1-[1+(Ca/R)^2]^{-\frac{1}{2}} \quad 2.4$$

where $C = \sqrt{3}$. From eqs. 2.2 and 2.4 one obtains the following screened coulomb potential

$$V(R) = \frac{Z_1Z_2e^2}{R}[1-\{1+(\frac{Ca}{R})^2\}^{-\frac{1}{2}}] \quad 2.5$$

The continuum potential is obtained by substituting eq. 2.5 in eq. 2.1 and integrating, i.e.,

$$U(R) = \frac{Z_1Z_2e^2}{R} \ell n[1 + (\frac{Ca}{R})^2] \quad 2.6$$

(where now R is the distance to the atomic string) which has been called the standard potential by Lindhard. This potential reduces to an even simpler form

for Ca > R, i.e.,

$$U(R) \simeq \frac{2Z_1Z_2e^2}{d} \ln\left(\frac{Ca}{R}\right) \qquad 2.7$$

A plot of the continuum potential for two strings of atoms is shown in Fig. 2.1(b). The contributions due to the next nearest neighbours and other strings are small and are therefore neglected. A constant potential is subtracted from U(R) so that the minimum value of U(R) is zero.

Since the channeled particle interacts with a large number of atoms in the string, in each "collision" with the string, a condition for the continuum potential approximation and hence channeling is that the collision length, L_c, must be greater than the distance, d, between the atoms on the string. The collision time Δt is of the order of $\frac{r_{min}(1)}{v\sin\psi}$, where v is the velocity of the particle, ψ is the angle that the particle makes with the string direction at the center of the channel, $r_{min}(1)$ is the minimum distance of approach to the string as a function of 1, and 1 is the impact parameter to the string in the transverse plane. Some of these quantities are indicated in Fig. 2.1(a). The velocity component parallel to the string is $v.\cos(\psi)$ and therefore for small angle, ψ,

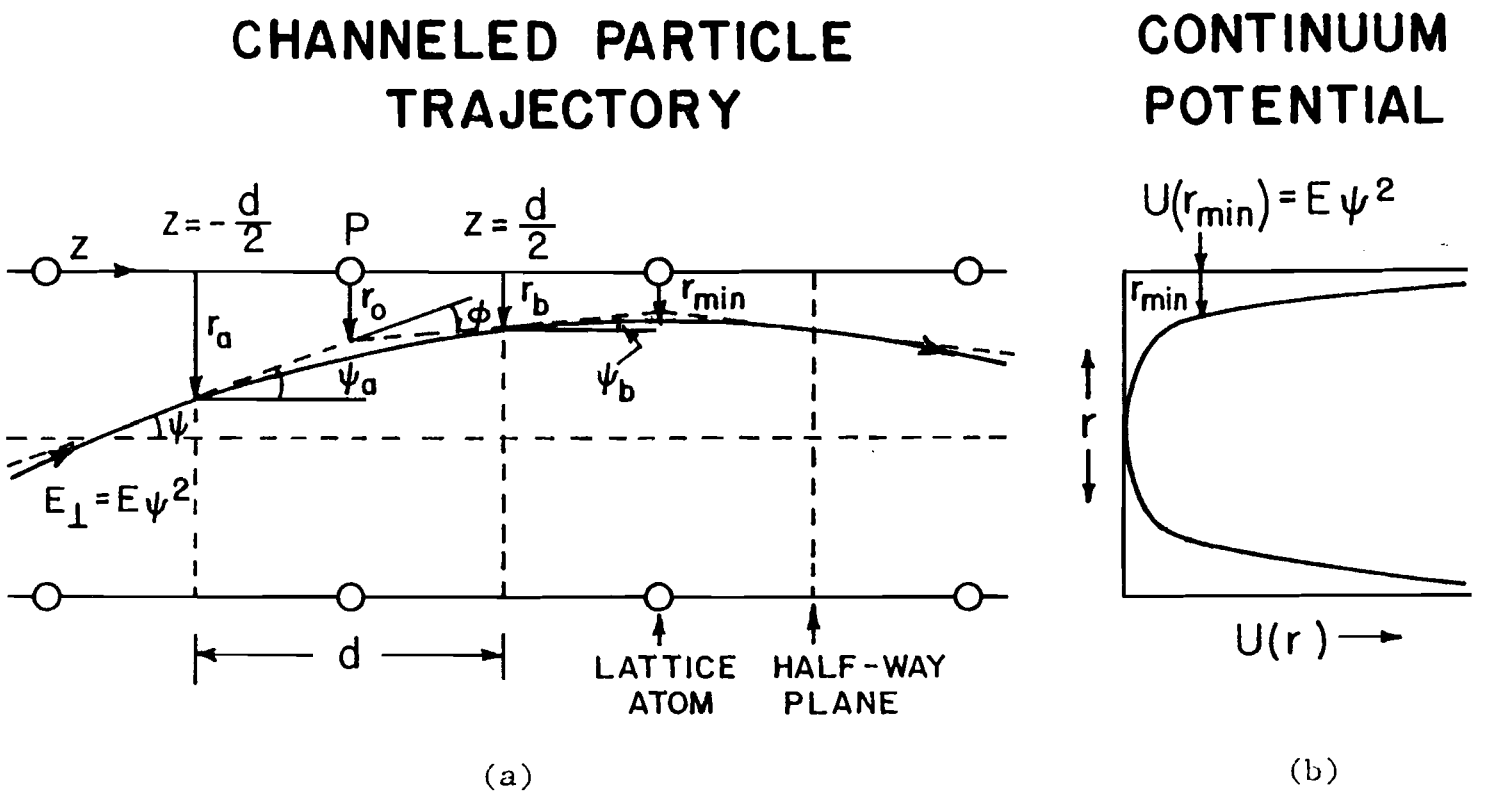

Fig. 2.1 (a) An exaggerated view of the deflection of the channeled particle by the string of atoms. (b) The continuum potential due to the string of atoms. The minimum potential is taken as zero.

$$\Delta t \cdot v \cdot \cos(\psi) \simeq \frac{r_{min}(l)}{\psi} > d \qquad 2.8$$

The closest distance of approach $r_{min}(l)$ is minimum for $l=0$ and for this case the condition in eq. 2.8 becomes

$$r_{min} > \psi d \qquad 2.9$$

The minimum distance of approach is obtained by considering the conservation of transverse energy. From Figs. 2.1(a) and (b)

$$U(r_{min}) = E_{\perp} = E \cdot \psi^2 \qquad 2.10$$

As the energy is increased for fixed value of ψ the r_{min} value will tend to zero, and, therefore, at high energy, where $C \cdot a > r$, the continuum potential will have the form indicated in eq. 2.7. From eqs. 2.10 and 2.7 one obtains

$$r_{min} = C \cdot a \cdot \exp\left(-\frac{dE\psi^2}{2Z_1 Z_2 e^2}\right) \qquad 2.11$$

Thus the condition of eq. 2.9 becomes

$$\frac{Ca}{\psi d} \exp\left(-\frac{d \cdot E \cdot \psi^2}{2Z_1 Z_2 e^2}\right) > 1 \qquad 2.12$$

For ψ increasing from zero, the above inequality is violated first when ψ^2 becomes large compared to $\frac{2Z_1 Z_2 e^2}{dE}$ in the exponent. Thus for the continuum potential to be valid and the channeling condition to be

satisfied at high energy, one must have

$$\psi \leq \psi_1 = \left(\frac{2Z_1Z_2e^2}{dE}\right)^{\frac{1}{2}} \qquad 2.13$$

provided $\frac{Ca}{\psi_1 d}$ is larger than unity, i.e., approximately

$$E > E' = 2Z_1Z_2e^2 \frac{d}{a^2} \qquad 2.14$$

In this experiment, the lowest energy of the beam particles was 35×10^3 MeV and for the <110> axis in Germanium crystal E' = 0.187 MeV. Therefore, the inequality in eq. 2.14 is more than satisfied and the condition in eq. 2.13 determines the maximum angle for channeling. In other words, the angle ψ_1 is the maximum angle with respect to the axis direction for which the particle remains channeled. The angle ψ_1 is very important for the channeling phenomenon and it is called the Lindhard critical angle for axial channeling.

The condition for the validity of the continuum potential may also be obtained by comparing the motion of the channeled particle in the continuum potential case with the perfect lattice case. The solid line in Fig.2.1(a) shows the motion for the continuum potential case where the particle is steered continuously as it passes close by the string. The dashed line is the trajectory for the perfect lattice case where the particle undergoes a sudden change in direction at the

closest approach to the atom under the impulse collision approximation. Angular momentum is zero for this trajectory. The positions of the particle in the two cases are the same at the half-way plane between the atoms, but differ most at the closest point of approach to the atom. The angles and the distances shown in Fig. 2.1(a) are related as follows

$$\phi = \psi_a - \psi_b \qquad 2.15$$

and

$$r_o = \frac{r_a + r_b}{2} - \phi\frac{d}{4} \qquad 2.16$$

The scattering angle, ϕ, in the motion between the two half-way planes is the same for both the trajectories. The change of momentum perpendicular to the axis direction between z = -d/2 and z = -d/2 is:

$$\Delta p = \int_{-\frac{d}{2}}^{+\frac{d}{2}} - U'(r)\ \frac{dz}{v} \qquad 2.17$$

where U'(r) is the first derivative of the potential with respect to r. The scattering angle is:

$$\phi = \frac{\Delta p}{p} = \frac{1}{2E}\int_{-\frac{d}{2}}^{+\frac{d}{2}} U'(r)\ dz \qquad 2.18$$

The change in r between z = -d/2 and z = +d/2 is small and therefore U'(r) may be assumed constant and equal to $U'(r_o)$. Then eq. 2.18 becomes

$$\phi = - \frac{dU'(r)}{2E} \qquad 2.19$$

The trajectory for the continuun potential changes very slowly and therefore the distance of the trajectory from atom P may be approximated by $r = \frac{r_a+r_b}{2}$. Substituting this and eq. 2.19 in eq. 2.16 one obtains

$$r = r_o - \frac{d^2U'(r_o)}{8E} \qquad 2.20$$

Differentiation of eq. 2.20 yields

$$dr = dr_o[1 - \frac{d^2U''(r_o)}{8E}] \qquad 2.21$$

where now $U''(r)$ is the second derivative of the potential with respect to r. When r_o is large, the two differentials dr and dr_o are approximately equal. They remain approximately equal as r_o is decreased until the term in the bracket of eq. 2.21 becomes zero. Thereafter r increases rapidly as r_o goes to zero. Therefore, the condition for the continuum potential to be valid is

$$E > \frac{d^2}{8} U''(r_{min}) \qquad 2.22$$

This condition is equivalent to the condition in eq. 2.13 as one can see by differentiating eq. 2.7 and substituting it in eq. 2.22.

A critical distance of approach to the string, r_c, is obtained by substituting ψ_1 in eq. 2.10, i.e.,

$$U(r_c) = E\ \psi_1^2 \qquad 2.23$$

and solving for r_c with the value of $U(r_c)$ substituted from eq. 2.6. For the Germanium crystal used in this experiment one obtains:

$$r_c = \frac{Ca}{\sqrt{C-1}} = 0.18556\ \text{Å} \qquad 2.24$$

The effect of crystal temperature and consequent lattice atom vibrations is to further smear out the continuum potential. If the root mean square (rms) displacement transverse to the string of vibrating atoms is u_1, then the modified axial channeling critical angle ψ_1' is obtained by substituting $r_c' = \sqrt{r_c^2+u_1^2}$ for r_c in the eq. 2.23.

The rms displacement u_1 for the Germanium crystal at 128°K (the temperature at which the crystal was maintained in this experiment) has been estimated from the Debye approximation [Ge74] to be 0.06158 Å. This value of u_1 may be neglected when added in quadrature to r_c. Therefore the crystal temperature had very little effect on the critical angle of channeling in this experiment and will be disregarded in all the calculations.

The Germanium Single Crystal was hyperpure with no dislocation density and mosaic spread. The bending of the crystal due to crystal mount was very small. Therefore, the contribution of these to the critical angle was also negligible.

2.2 PLANAR CHANNELING

A situation similar to axial channeling arises when positively charged particles are incident on a plane of atoms at a small angle to the plane as shown in Fig. 2.2.

One can define a continuum potential for the plane of atoms similar to the continuum potential due to the string of atoms (cf Eq. 2.6), i.e.,

$$Y(y) = N \cdot d_p \cdot \int_o^\infty 2\pi\, r\, V(\sqrt{y^2+r^2})\,dt \qquad 2.25$$

where $r^2 = x^2 + z^2$, y is the perpendicular distance from the plane of atoms, N is the number of atoms in the crystal per unit volume, d_p is the separation between planes, r is the radial distance in the x-z plane and $V(\sqrt{y^2+r^2})$ is the ion atom potential. Substituting the Lindhard ion-atom potential from Eq. 2.5 in Eq. 2.25 and integrating one gets:

$$Y(y) = 2\pi Z_1 Z_2 e^2 N d_p \left[(y^2+C^2a^2)^{\frac{1}{2}} - y\right] \qquad 2.26$$

Following an argument similar to that used in deriving the condition of Eq. 2.13 in axial channeling, one obtains the following condition for planar channeling:

$$\psi \leq \psi_a = \left(\frac{4\pi Z_1 Z_2 e^2 N d_p a}{pv}\right)^{\frac{1}{2}} \qquad 2.27$$

where ψ_a is the Lindhard's critical angle for planar channeling.

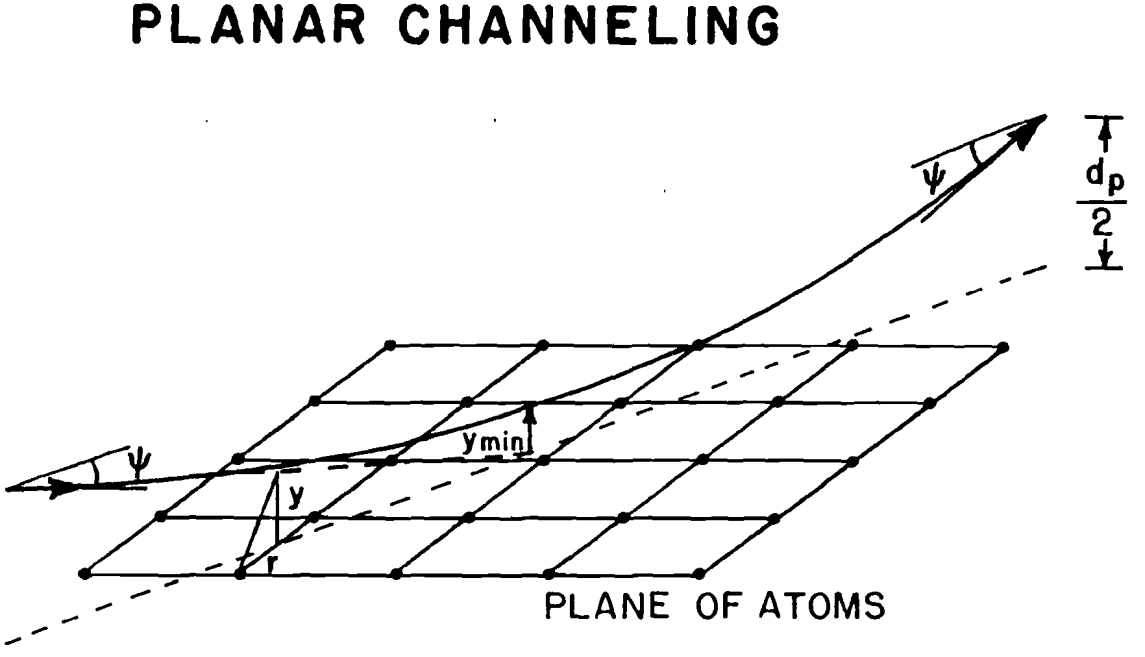

Fig. 2.2 An exaggerated view of the deflection of the channeled particle by the plane of atoms.

The critical distance of approach, y_c, is obtained by considering the conservation of transverse energy, i.e.,

$$Y(y_c) = E\,\psi_a^2 \qquad 2.28$$

On substituting $Y(y_c)$ and ψ_a from Eqs. 2.26 and 2.27, respectively, in Eq. 2.28, one gets the value of y_c, i.e., $y_c = a = 0.141$ Å.

The rms displacement for the thermal vibrations of the atoms in the plane, $u_1 = 0.0616$ Å will produce less than 10% change in the critical distance, y_c, and its effect may be neglected.

2.3 BLOCKING

Positively charged particles originating from lattice sites or regions close to it in a crystal are prevented from emerging along any major crystal axis direction because of the intervening rows of atoms. This is known as the blocking effect.

The minimum angle of emergence to the string of atoms, ψ_{min}, and the angular distribution of the particles may be obtained from the conservation of transverse energy. Let a positively charged particle emerge from the lattice atom site P at an angle ϕ to the string of atoms as shown in Fig. 2.3. The transverse energy at the half-way plane is $E_\perp = E\phi^2 + U(\phi\frac{d}{2})$. The conser-

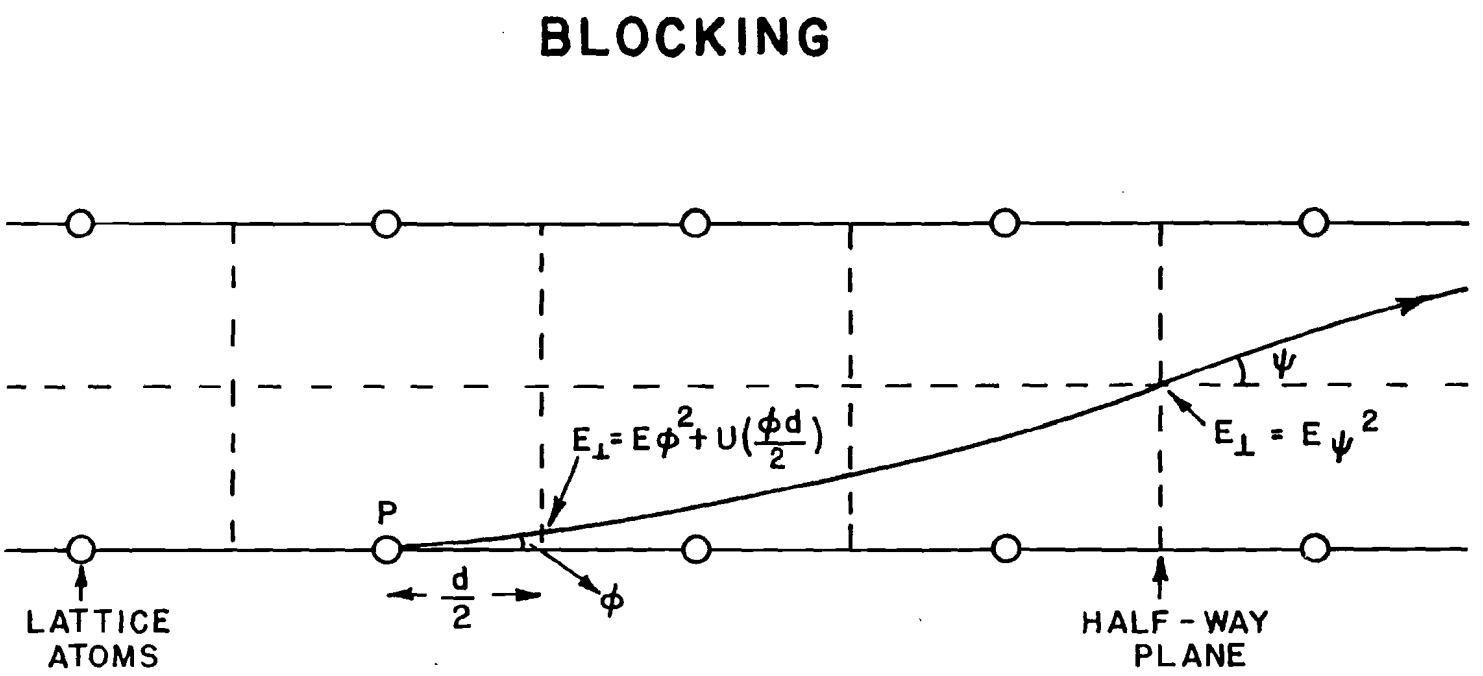

Fig. 2.3 Trajectory of a particle emitted from one of the atoms in the string of atoms. An exaggerated view.

vation of transverse energy implies that this should be equal to the transverse energy $E_{\perp} = E\psi^2$ mid-way between the two rows of atoms, i.e.,

$$E\psi^2 = E\phi^2 + U(\phi\tfrac{d}{2}) \qquad 2.29$$

The condition for ψ to be minimum is obtained by substituting the Standard Potential from Eq. 2.6 in Eq. 2.29 and differentiating it with respect to ϕ. The result is:

$$\phi^2 = -\frac{2C^2a^2}{d^2} + \frac{4C^4a^4}{d^4} + \frac{2\psi_1^2C^2a_2}{d^2} \qquad 2.30$$

In the high energy limit, where $\psi_1 < \frac{a}{d}$, the minimum angle is obtained by substituting Eq. 2.30 in Eq. 2.29 and simplifying, i.e.,

$$\psi_{min} \simeq \psi_1 \left[\ell n \frac{2^{3/2}e^{\frac{1}{2}}Ca}{\psi_1 d} \right]^{\frac{1}{2}} \qquad 2.31$$

The expression in the bracket ranges from 2.5 at 35 GeV/c to 3.0 at 250 GeV/c momentum. Comparing Eqs. 2.13 and 2.31 one can see that the critical angle ψ_1 plays an important role in the axial channeling as well as the blocking effect. It defines a maximum angle for channeling and a minimum angle for blocking. It therefore appears that these two effects are complementary.

The simplest experimental situation where particles

may originate at the lattice site is found in crystals with radioactive atoms at the lattice positions. The alpha particles emitted from the radioactive atoms are blocked from coming out along the directions of rows of atoms and a blocking pattern is observed.

Since the crystal was cooled to near liquid nitrogen temperature, the effect of the lattice vibrations on the blocking distribution in this experiment was small and could be neglected.

2.4 AZIMUTHAL DIFFUSION

Theoretical predictions have been made for the azimuthal angle distribution with respect to the crystal axis direction by solving the Boltzmann transport equation for channeled particles [Go76].

The crystal is assumed to consist of randomly distributed parallel strings of atoms (Random String Approximation). A narrow beam of positively charged particles (with an intially well defined direction) incident at small angle to any major crystal axis direction, will undergo elastic scattering with the string, conserving transverse momentum, but changing its azimuthal direction at each collision with the string. The time evolution of the azimuthal angle distribution $A(\phi,t)$ is given by the Boltzmann Transport Equation, i.e.,

$$\frac{\partial}{\partial t} A(\phi,t) = \int_{-\infty}^{+\infty} d\phi' P(\phi') \left[A(\phi-\phi',t) - A(\phi,t)\right] \qquad 2.32$$

where ϕ is the azimuthal angle, t is the time and $P(\phi')$ is the transition rate obtained from the scattering potential.

The transport equation 2.32 has been solved for a continuum potential of the form:

$$U(r) = \frac{Z_1 Z_2 e^2}{d} \frac{\pi a}{2r} \qquad 2.33$$

where Z_1, Z_2, d and a are quantities already defined in the previous sections. The transition probability is obtained as

$$P(\phi) = N d v_\perp a \frac{Z_1 Z_2 e^2}{d} \frac{\pi}{8} \frac{1}{E_\perp \sin^2(\frac{\phi}{2})} \qquad 2.34$$

and the distribution function is

$$A(\phi,T) = \frac{1}{2\pi} \frac{\sinh(T)}{\cosh(T)-\cos(\phi)} \qquad 2.35$$

where T is a dimensionless parameter which is a measure of the thickness of the crystal, i.e.,

$$T = \frac{N d v_\perp Z_1 Z_2 e^2}{E_\perp d} \frac{\pi^2}{2} \text{ at} \qquad 2.36$$

Here t is the thickness of the crystal, $v_\perp$ is the perpendicular component of the velocity and the other terms have the same meaning as in the previous sections.

For thick crystals with large T values the distribution function, $A(\phi,T)$, will be constant for all values of ϕ. This will mean a statistical equilibrium in the exit, azimuthal angle distribution of the transverse momentum of the particles.

The attainment of the statistical equilibrium in the aximuthal angle distribution, as the beam particles pass through the crystal, is illustrated in Figs. 2.4(a) and (b). The dotted area in the incident angle plane in Fig. 2.4(a) represents particles with well defined transverse momentum with respect to the crystal axis direction, which is at the origin. The exit angle plane in Fig. 2.4(b) shows the beam, spread out uniformly in the aximuthal angle. There is also a broadening along the radial direction and this will be discussed in the next section. The formation of the ring distribution in the exit angle plane is known as the "doughnut" effect.

2.5 RADIAL DISTRIBUTION

The channeling and the blocking critical angles were calculated on the assumption of conservation of transverse energy of the beam particles. The azimuthal angle distribution was also obtained by assuming the conservation of the magnitude of the transverse energy. In each of these cases the effect of thermal

DONUT EFFECT

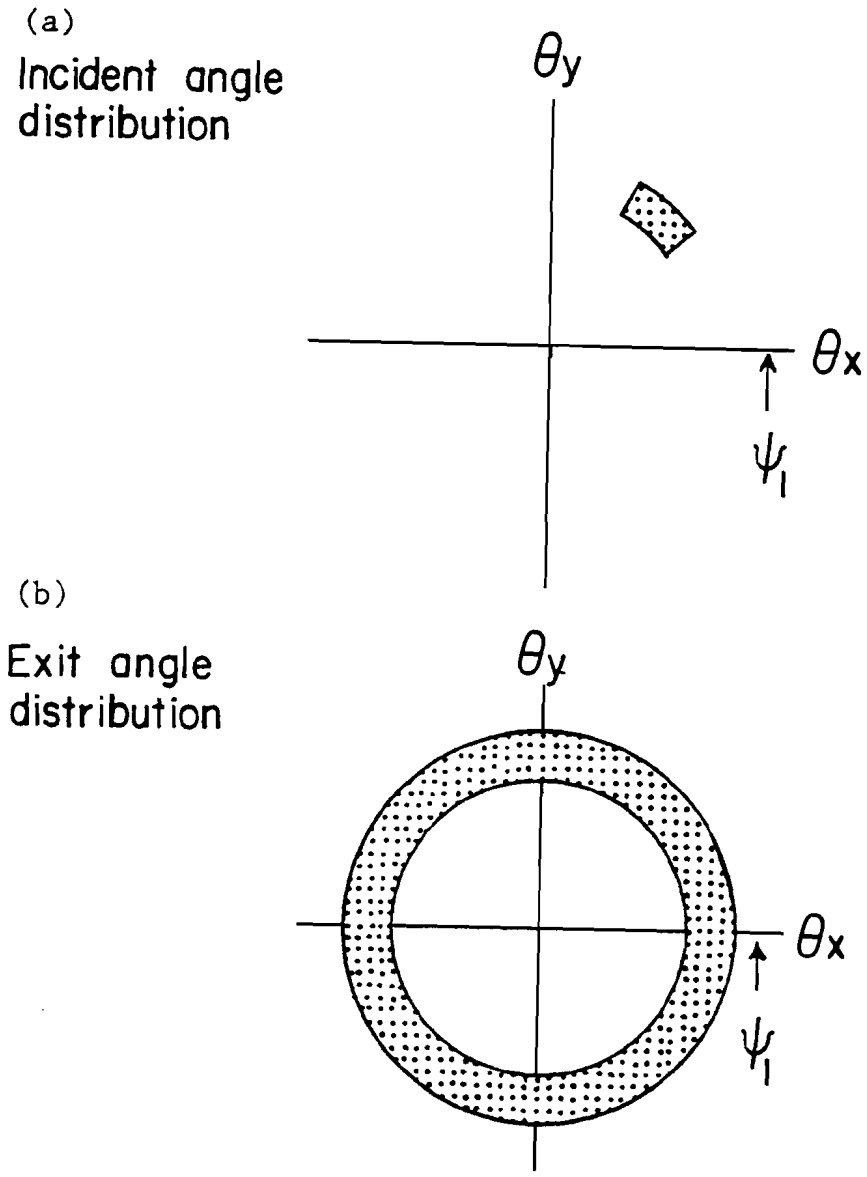

$(\theta x, \theta y) = (0,0)$ = Channeling axis direction

Fig. 2.4 (a) Dotted area represents selection on incident angle indicating well defined transverse momentum. (b) Exit angle distribution shows equilibrium in azimuthal scattering angle.

vibration of the lattice atoms and the defects and impurities in the crystal were introduced as small perturbations. In this section, these effects, which produce local force fluctuations and nonconservation of the transverse energy, will be considered in greater detail.

The change in the transverse energy with penetration depth in the crystal is obtained by differentiating the transverse energy in Eq. 2.10 with respect to z and taking the mean value, i.e.,

$$\left\langle \frac{dE_\perp}{dz} \right\rangle = E \left\langle \frac{d\psi^2}{dz} \right\rangle + \left\langle \psi^2 \frac{dE}{dz} \right\rangle \qquad 2.37$$

The first term on the right is the multiple scattering term and it is responsible for the increase of the transverse energy and the spreading of the beam distribution. The second term is the damping factor and under some special condition ($M_1\psi_1^2 > 2m$, [Li65]) may actually produce a net decrease in the transverse energy and therefore cooling of the beam transverse energy. Under the conditions of this experiment, the damping effect on the channeled particles was very small in comparison to the multiple scattering spread of the beam and will therefore be neglected in further discussions.

Since the local force fluctuation due to the thermal vibrations of the atoms in the string are statisti-

cal in nature, the differential probability function $g(\vec{P}_\perp,z)dp_{\perp,x}dp_{\perp,y}$ is governed by a diffusion equation of the form [Li65]:

$$\frac{\partial}{\partial z} g(\vec{P}_\perp,z) = \mathrm{div}_{\vec{P}_\perp} D(\vec{P}_\perp)\mathrm{grad}_{\vec{P}_\perp} g(\vec{P}_\perp,z) \qquad 2.38$$

where $D(\vec{P}_\perp)$ is the diffusion function. Lindhard [Li65] obtained the following relationship between the diffusion function and the change in the mean transverse energy for axial symmetry:

$$2D(P_\perp) + P_\perp \frac{\partial}{\partial P_\perp} D(P_\perp) = M_1 \frac{\delta}{\delta z} \langle E \rangle \qquad 2.39$$

He also calculated from the diffusion equation 2.38 the diffusion function in terms of the mean square fluctuation of the transverse momentum, i.e.,

$$\frac{D(P_\perp)}{M_1} = \frac{1}{2M_1} \delta\langle (P_\perp - \langle P_\perp \rangle)^2 \rangle \qquad 2.40$$

Substituting $P_\perp \simeq p\psi$ for small ψ (ψ is the angle that the beam particle makes with the string direction at regions of minimum potential energy, as opposed to ϕ, the instantaneous angle of the beam particle with respect to the axis direction as shown in Fig. 2.1) in Eq. 2.40, one obtains the diffusion constant as a function of ψ as

$$D(\psi) = M_1 E \frac{\delta}{\delta z} \langle (\psi - \langle \psi \rangle)^2 \rangle \qquad 2.41$$

Thus the change in the mean square spread of the angle

of the beam particles is a measure of the diffusion function $D(\psi)$. From Eqs. 2.10, 2.39 and 2.41 one obtains

$$2\frac{\delta}{\delta z}\langle(\psi-\langle\psi\rangle)^2\rangle+\psi\frac{\partial}{\partial\psi}\frac{\delta}{\delta z}\langle(\psi-\langle\psi\rangle)^2\rangle=\frac{\delta}{\delta z}\langle\psi^2\rangle \qquad 2.42$$

The experimental confirmation of this equation would imply the validity of the diffusion picture of the beam spreading around the channeling axis region.

CHAPTER 3

EXPERIMENT

The channeling experiment was performed in April-May of 1977 in the M1 beam line of the Meson Laboratory at the Fermi National Accelerator Laboratory (Fermilab).

The main ring accelerator at the laboratory accelerated protons to 400 GeV maximum energy, and the protons were allowed to strike a Beryllium target producing a large variety of secondary particles with a wide range of energy. Most of the short lived particles decay in less than 10^{-8} seconds. Mesons with lifetimes of the order of 10^{-8} seconds, and stable particles such as leptons and nucleons, survive long enough (for mesons, this is due to the time dilation factor, E/m) to be focused and guided by the dipole and quadrupole magnets to the Meson Laboratory building half a mile away from the target point. There are several beam lines provided for simultaneous running of many experiments.

The channeling experiment was set up in the M1 beam line. The data were taken for positive and negative beam polarity at three different beam momenta, viz: 35, 100, and 250 GeV/c. The momentum spread,

$\Delta p/p$, was less than 5%. The beam composition for the above mentioned momenta and polarity configurations are listed in Table 3.1 [Ba78].

In the following sections, the experimental setup will be described in detail. These include descriptions of the M1 beam line layout, crystal, and the experimental apparatus. This will be followed by explanations of the event trigger logic, the data acquisition system and the tedious process of searching for the crystal axis.

3.1 BEAM LINE LAYOUT

The experimental layout in the M1 beam line is shown in Fig. 3.1 (the dimension transverse to the beam is shown in an expanded scale).

The Germanium Single Crystal was mounted in the goniometer and placed one meter downstream of the second Drift Chamber Module, DC2. The first Drift Chamber Module, DC1, was 31 meters upstream and the third, DC3, was 17 meters downstream of the crystal position. The Cerenkov counter C_K was upstream of DC1 and was used to discriminate between pions, kaons, and protons during parts of the experimental run. The Vacuum Pipes VP1 and VP2 were placed in between the drift chamber modules to reduce multiple coulomb scattering in air. They covered 91% of the space between the drift chambers.

Table 3.1 Beam composition for 35, 100, and 250 GeV/c momentum.

BEAM COMPOSITION

(M1 BEAM LINE, MESON LABORATORY AT FERMILAB)

	35 GeV/c	100 GeV/c	250 GeV/c
	%	%	%
π^+	88 ± 1	62 ± 1	6.7 ± 0.4
K^+	5.8 ± 0.7	5.1 ± 0.7	1.75 ± 0.05
p	6.8 ± 1.0	31 ± 1	92 ± 1
π^-	92 ± 1	93 ± 1	97 ± 1
K^-	5.4 ± 0.7	5.4 ± 0.7	2.35 ± 0.05
$\bar{p}$	2.10 ± 0.05	1.80 ± 0.05	0.175 ± 0.005

EXPERIMENTAL SETUP

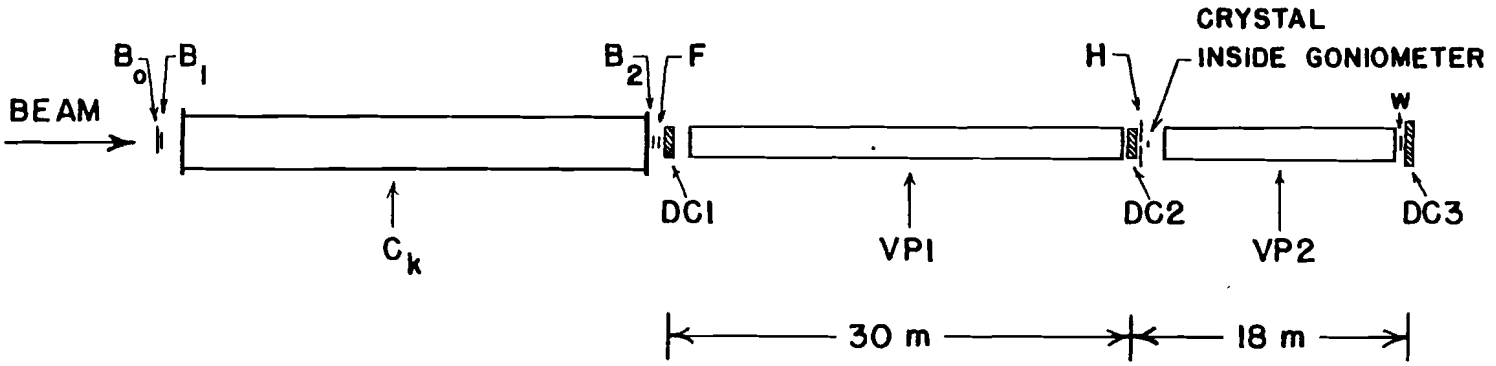

Fig. 3.1 Schematic illustration of the experimental setup. DC1-3 are drift chambers that define particle track. C_k is the Cerenkov counter that identifies the particle. The beam defining scintillation counters are B_0, B_1, B_2, F, H, and W. VP1 and VP2 are the vacuum pipes to reduce multiple scattering in air. The dimension transverse to the beam is shown in an expanded scale.

The scintillation counter H had a 6 mm diameter hole that was centred on the crystal and partially covered it. It was placed between the second drift chamber and the crystal and was used to select particles that went through the crystal. The other scintillation counters B_o, B_1, B_2, F, and W were used to define the beam particles. The dimensions of the scintillation counters are listed below:

Scintillation Counter	Width (cms)	Height (cms)	Thickness (cms)
B_o	10.16	10.16	0.635
B_1	7.62	7.62	0.635
B_2	7.62	7.62	0.635
F	5.08		
H	15.25	20.32	0.635
W	6.35 (diameter)		0.320

3.2 GONIOMETER

The crystal was mounted in the goniometer and cooled to liquid nitrogen temperature with the help of a movable cold-finger. The cold-finger consisted of a bent Copper rod. One end of the rod came out of the goniometer through a vacuum tight seal and was immersed in the liquid nitrogen contained in a dewar flask. A flexible braided ground wire connected the other end of the copper rod to the crystal frame. A

thermocouple was attached to the crystal end of the rod to monitor the temperature of the crystal.

The goniometer chamber was evacuated initially by a roughing pump to 1 Torr and then by a diffusion pump to $(3.0\pm0.2)\times10^{-6}$ Torr. This pressure was maintained for all the experimental runs.

The goniometer crystal mount was remotely controlled and had azimuthal and polar degrees of freedom with respect to the beam direction (details are presented in the axis search section). It could be rotated independently in either direction in steps of 20 microradians. This step size, which is comparable to the Half Width at Half the Maximum height (HWHM) of the Axial Channeling distribution at 250 GeV/c, was sufficient to align the crystal roughly along the beam direction. Accurate alignment was not necessary because the complete trajectory of the beam particle accepted in each event was recorded.

3.3 DRIFT CHAMBER MODULES

It has been found that for some gas mixtures the electron cluster, produced by the passage of an ionizing particle (which produces electrons and positive atomic ions along its path length), drifts with a uniform saturated velocity in an electric field larger than a threshold value [Br74]. The drift chamber

utilizes this uniform velocity of the electron cluster to calculate the position of the point, where the ionizing particle passed through the gas mixture, from the drift time of the electrons to a signal wire. The detailed construction of the drift chambers will be presented in this section, and the mechanism of position calculation will be described in chapter 4.

The three high precision drift chamber modules were used to measure the position of each particle 31 and 1 meter upstream and 17 meters downstream of the crystal position. These drift chamber modules were originally built at the Joint Institute for Nuclear Research in Dubna, USSR [Fil78]. They were further modified at Fermilab. The two upstream modules, DC1 and DC2, were of the same size, i.e., 12.5 x 12.5 cms^2 and the third downstream module was twice the size of the first and the second, i.e., 25 x 25 cms^2. Each module contained four X and four Y planes as shown in the schematic diagram in Fig. 3.2(a). The signal wires are vertical in the X planes and horizontal in the Y planes. The eight planes were in the same gas enclosure. Fig. 3.2(b) shows a set of two drift planes. Each plane consisted of signal wires separated by a distance of 42 mm. In between the signal wires were the potential wires which divided the region between the signal wires into two drift cells.

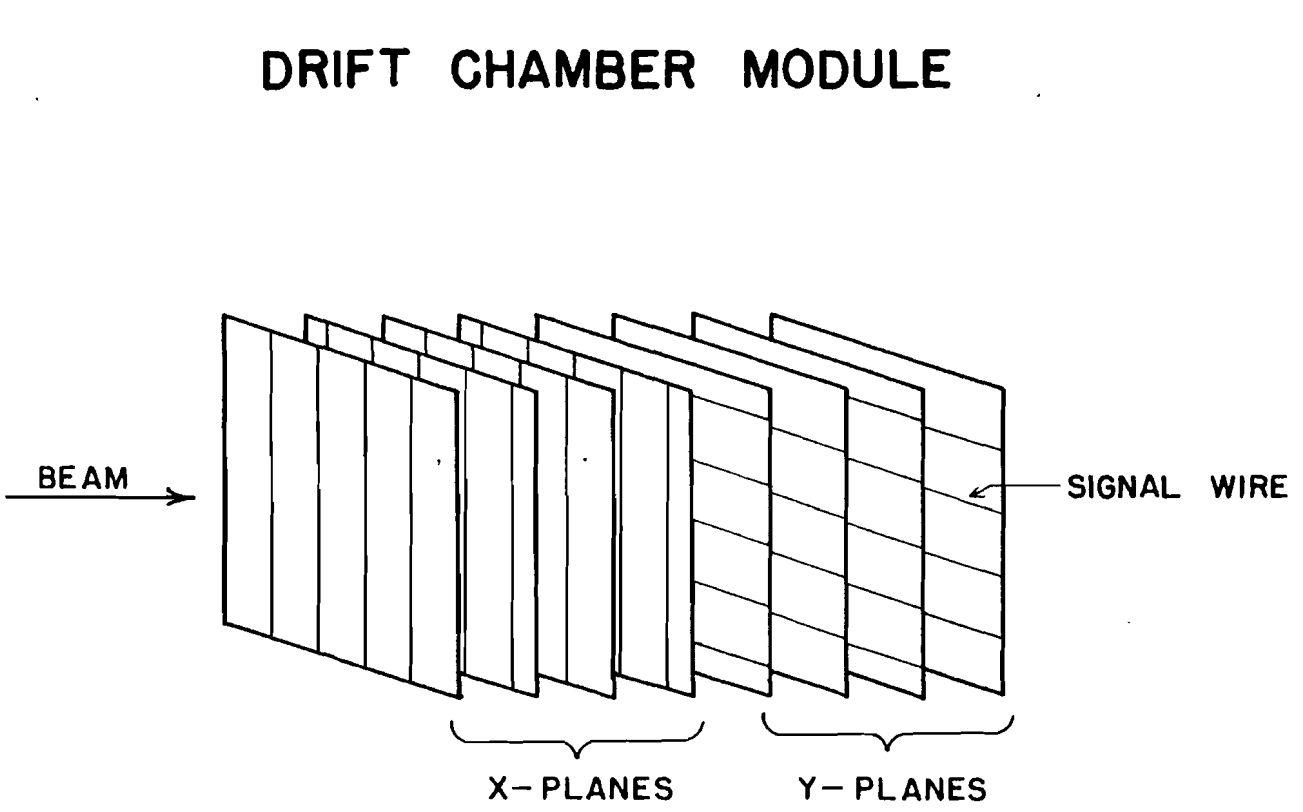

Fig. 3.2 (a) The schematic diagram of the four X and four Y planes in a drift chamber module. The signal wires are shifted by half the distance between them in alternate planes.

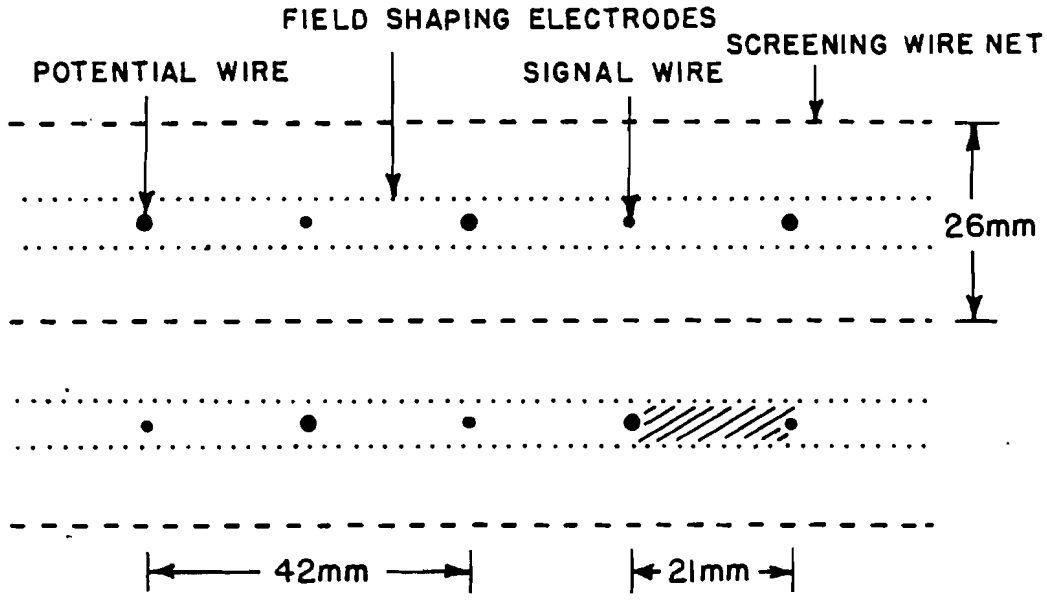

Fig. 3.2 (b) Two planes of a drift chamber module showing relative positions of the various wires. The size of the potential wires and the signal wires are exaggerated. The shaded area represents a drift cell.

The field shaping electrodes were put on either side of the plane containing the signal and potential wires. These were used to produce uniform electric fields in the drift region in each drift cell. The separation between the signal wire plane and the electrode plane was 3 mm and the electrodes were 2 mm apart. The signal wires in the adjacent drift planes were shifted by 21 mm to resolve left-right ambiguity. This ambiguity was there because each signal wire served two drift cells, one on its left side and the other on its right. With a single drift plane it would be impossible to say which side of the signal wire the charged particle went through.

The following gas mixture was used in the drift chambers:

GAS MIXTURE

Argon.....67.2%

Isobutane.....(30.3±0.5)%

Methylal.....(2.50±0.10)%

These gases were stored in separate tanks. They were mixed and allowed to flow through the drift chamber modules at atmospheric pressure.

For this gas mixture the drift velocity saturated at above 800 V/cm [Br74]. A uniform field of 1500 V/cm was maintained in the drift region by applying + 1750

volts to the signal wire and -3500 to 0 volts on the potential wires and field shaping electrodes with a resistance divider as shown in Fig. 3.2(c). This produced a fairly uniform drift velocity in a large region of the drift space. Further details about the drift chambers will be discussed in the track reconstruction section.

3.4 GERMANIUM SINGLE CRYSTAL

The Germanium Single Crystal was 20x10x8.5 mm^3 in dimension. It was fabricated at ORTEC by a technique originally developed by Czochralski [Hu77]. This technique was used to grow dislocation free hyperpure Germanium Single Crystals with no mosaic spread. The crystal was doped with $1x10^{10}$ n-type Phosphorus per cm^3.

It was aligned lengthwise along <110> crystal axis direction by an optical reflection technique [Mo], cut with a wire saw using Silicon Carbide slurry and etched by Hydrofluoric acid. The uncertainty in the alignment of the crystal face, cut perpendicular to <110> axis, was less than 2 degrees.

The crystal was used as a transverse field intrinsic solid state detector capable of measuring energy deposited in the crystal by a penetrating charged particle. A Boron implanted p contact and a 0.5 mm

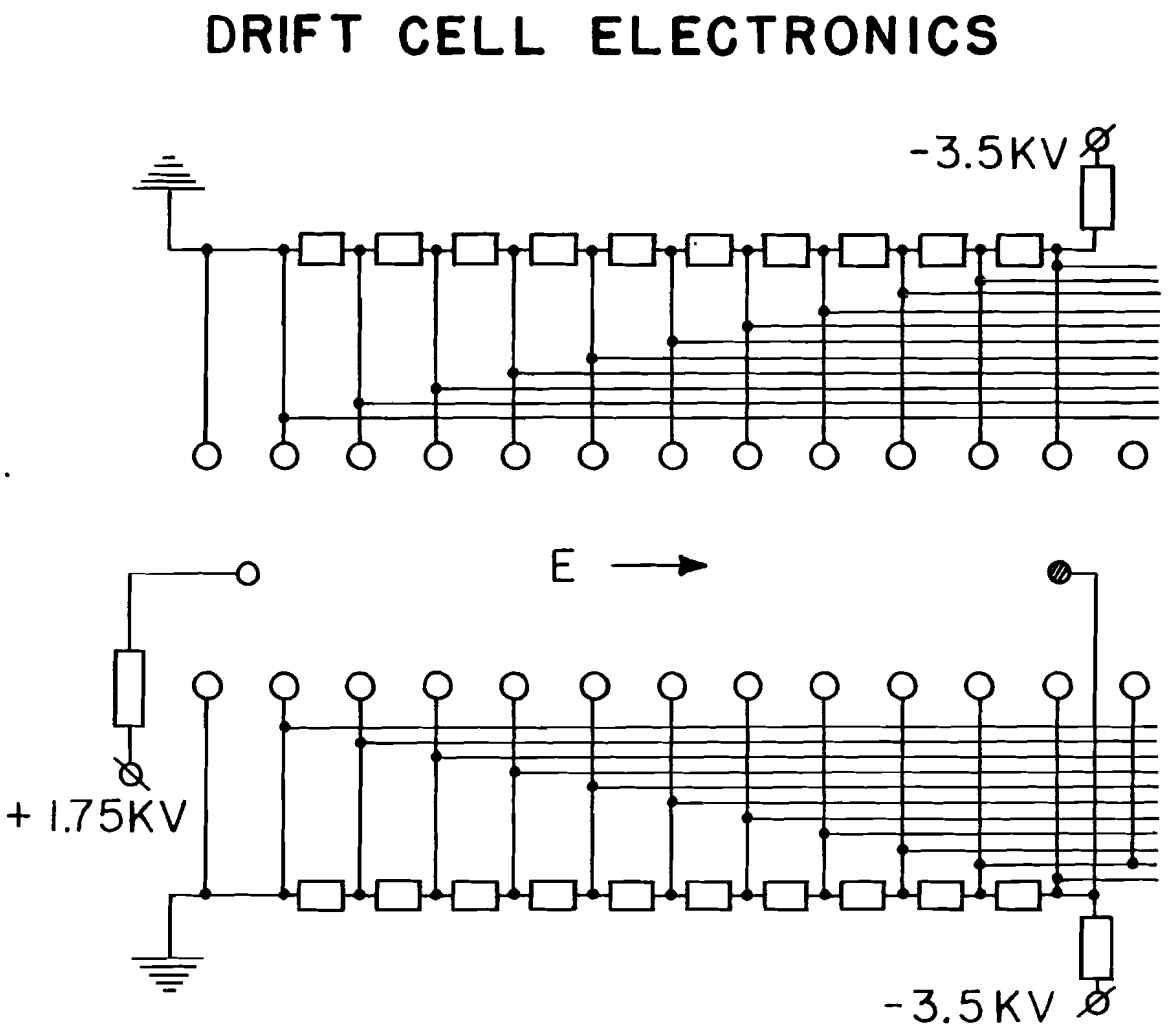

Fig. 3.2 (c) Schematic diagram of the electronics for a single drift cell. The rectangular blocks are resistors used as potential divider.

thick Lithium diffused Indium foil n contact were used to apply the bias voltage across the 8.5 mm thick side of the crystal.

The crystal was maintained at about 128 K (50 K above the liquid nitrogen temperature) as measured by a thermocouple. The low temperature was necessary for its operation as an intrinsic detector.

A 500 volt reverse bias was sufficient to deplete the entire crystal volume. The signal from the crystal was fed into a conventional Nuclear Linear Electronics Amplifier system. These signals were proportional to the energy deposited by the charged particles passing through it.

The crystal detector system was calibrated using a Na^{22} gamma ray source. The resolution was found to be 10 keV (rms).

3.5 EVENT TRIGGER LOGIC AND DATA ACQUISITION ELECTRONICS

A block diagram of the event trigger logic and data acquisition electronics is shown in Fig. 3.3.

Beam particles were identified by a coincidence of B_1, B_2, F, and W with H (the scintillation counter with a hole) in anti-coincidence. C_k was used in coincidence for some runs to identify pions. Signals from B_2' were discriminated in pulse height such that the

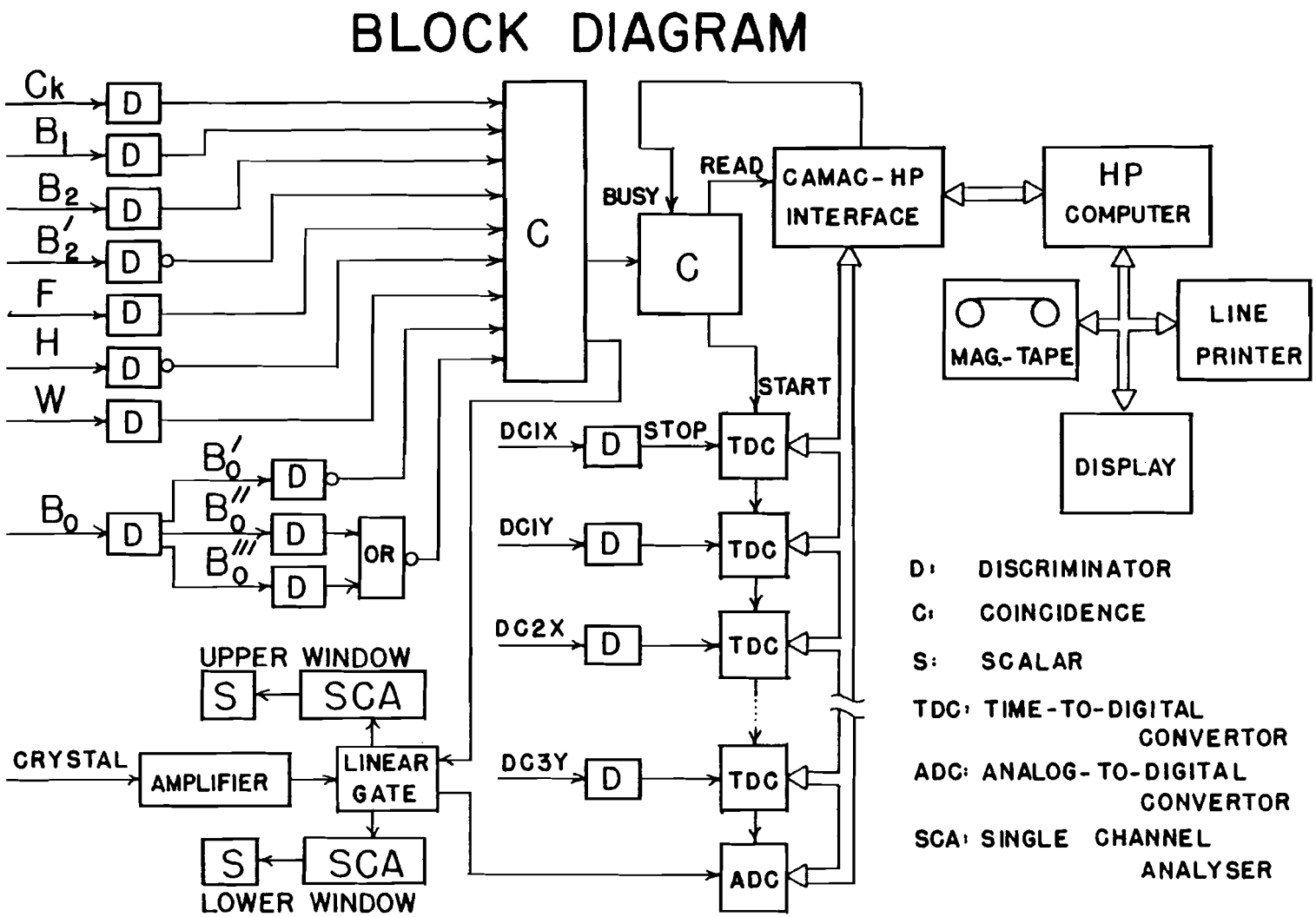

Fig. 3.3 The block diagram for the event trigger logic and data acquisition electronics.

large pulse heights due to two particles passing through the scintillation counter at the same time produced a veto signal. This eliminated particles coming at the same time (i.e., in the same R.F. bucket).

By introducing proper delays in B_o', B_o'' , and B_o''', all the particles arriving within the time interval of 500 nano-seconds before and 80 nano-seconds after the trigger pulse, were vetoed. The final event trigger logic was

$$C_k \; B_1 \; B_2 \; \overline{B_2'} \; F \; \overline{H} \; W \; B_o' \; \overline{(B_o'' / B_o''')}$$

The event trigger pulse was used to gate the amplified signal from the crystal to the Analog-to-Digital Converter (ADC) and to the two Single Channel Analysers (SCA's). The two SCA's defined an upper and a lower window in the total pulse height spectrum. The events falling in either of the two windows were counted and displayed on their respective scalars. The criteria for selecting the range of the upper and the lower windows, and the way the ratio of the counts in these windows was used to search and locate the crystal axis will be discussed in the crystal axis search section.

The trigger pulse was also used to start the counting in all the Time-to-Digital Convertors (TDC's). The 48 active signal wires in the three drift chamber modules were each connected to a TDC through a discrimi-

nator. A signal, produced by the passage of a charged beam particle close to any of these wires, stopped the counting in the corresponding TDC. The other TDC's, corresponding to wires without particles passing by, would count to an overflow number.

The trigger pulse also initiated the transfer of data from the TDC's and ADC to the HP2100 computer through the interface and cleared all the TDC's and ADC for the next event. A small sample of the stored data in the computer could be analyzed on-line and displayed on the visual display for continuously monitoring the beam profiles, and, more importantly, the crystal alignment.

The alignment of the crystal was monitored by looking at the exit angle distribution of the particles with selection on small scattering angle and low energy loss. These selections should preferentially pick out channeled particles and a peak in the exit angle distribution should then be observed. (See Fig. 3.8.) The presence of this channeling peak at the same position would then indicate the proper alignment of the crystal.

3.6 INITIAL SETUP

The experimental equipment was moved into the M1 beam line on April 14, 1977. The crystal was mounted

in the goniometer and a rough alignment was done by surveyors using optical reflection from the flat ends of the crystal. The 20 mm side was along the beam direction.

The goniometer ports were closed and the chamber was evacuated by a roughing pump to 1 Torr. The diffusion pump was then turned on, and it reduced the pressure to $(3.0\pm0.2)\times10^{-6}$ Torr. When the pressure had stabilized, the crystal was cooled by filling up the dewar flask with liquid nitrogen. The thermocouple, attached to the crystal end of the cold finger, was monitored to see the gradual decrease and eventual stabilization of the crystal temperature, and thereafter it was used as a check for the constancy of the crystal temperature. Since the liquid nitrogen dewar flask was physically connected to the goniometer, the periodic filling of the dewar caused a change in the position of the crystal. This showed up as a shift in the crystal axis position from run to run, and was compensated for in the data analysis.

A reverse bias of 500 volts was applied to the crystal. The crystal, the amplifier system, and the ADC, used as a dE/dx loss detector, was calibrated with Na^{22} gamma ray source. The energy of the most prominent gamma ray from Na^{22} is 1.28 MeV and this total

energy was absorbed in the crystal to generate the calibration pulse.

All the TDC's were also calibrated by sending two standard pulses with an accurately known time interval between them. The beam momentum was set to 35 GeV/c for positive particles by setting the currents in the beam quadrupole magnets to predetermined values. The beam stop was raised and adjustments were made in the focusing quadrupole magnets to make the beam as divergent as possible, at the crystal position (the rms beam spread are listed in Table 4.5 in Chapter 4). This was necessary for crystal axis alignment. The broader the beam spread, the easier it would be to bring the crystal axis position within the beam spread. Precise alignment and parallel beam were not required because, as mentioned before, the trajectory of each event particle could be obtained from the drift chamber data.

The beam intensity per pulse was $\sim$20 k/pulse and the trigger logic accepted $\sim$300 events per pulse.

3.7 CRYSTAL AXIS SEARCH

It was mentioned briefly in Section 3.7 that the two SCA's, which defined an upper window and a lower window in the pulse height spectrum from the crystal, were used at the beginning of the experiment to locate the crystal axis.

The fact that positively charged particles which are channeled along a crystal axis or planar direction have a lower dE/dx loss was used to define the range of the two windows in the pulse height spectrum. Typical pulse height spectra are shown in Fig. 3.4. These were obtained on-line for different orientations of the crystal. The curve with a greater number of events at low pulse height was called aligned and had a large fraction of particles that were channeled. The other curve was called random because it had smaller number of low pulse height events compared to the aligned crystal spectrum.

The lower and the upper windows are indicated in the Fig. 3.4. The ratio R of the counts in the lower to upper window was therefore a measure of the degree to which channeled particles were present in the beam at the exit window of the crystal.

The crystal, mounted in the goniometer, had two axes of rotation. One axis corresponded to a tilt angle θ with respect to the beam direction and the other one to a rotation angle ϕ around the tilt axis, as shown in Fig. 3.5. The crystal axis and the beam direction are also shown in the figure. The angle β between the crystal axis and the rotation axis was fixed once the crystal was mounted in the goniometer.

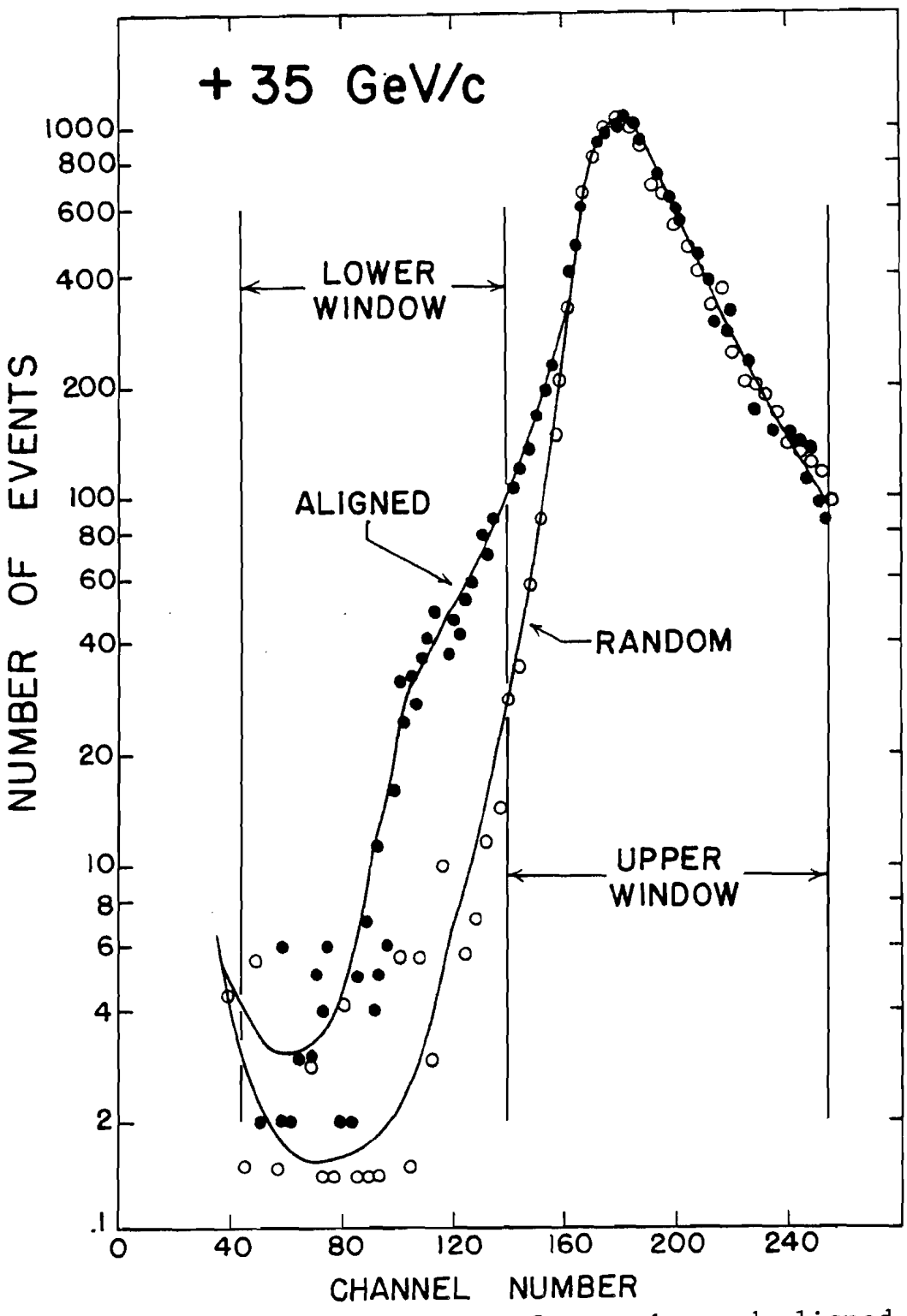

Fig. 3.4 Pulse height spectra for random and aligned orientation of the crystal. The lower and the upper windows are also shown.

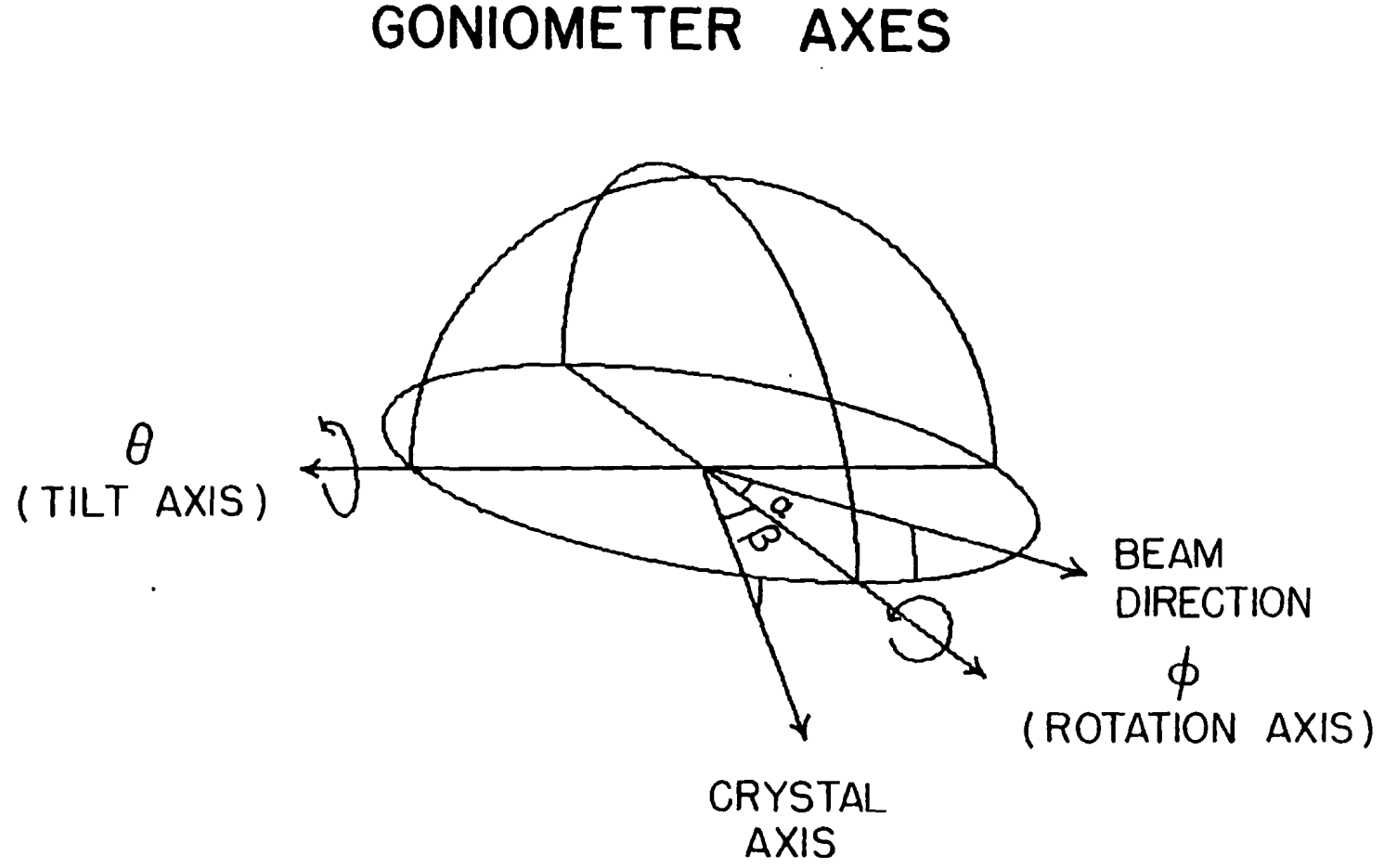

Fig. 3.5 The orientation of the rotation and the tilt axes of the goniometer with respect to the crystal axis and beam direction are shown.

The other angle α between the beam direction and the rotation axis could be changed by changing the tilt angle θ. It had a minimum value α_{min} when the tilt axis, the rotation axis and the beam direction were coplanar.

From the geometry of the figure it is clear that the crystal axis can be aligned along the beam direction by proper rotation around θ and ϕ axes if and only if β is greater than or equal to α_{min}, i.e.,

$$\beta \geq \alpha_{min} \qquad 3.2$$

This condition was fortunately found to be satisfied after the initial setup.

Fig. 3.6 shows major planes in the Germanium crystal as one looks down along <110> axis (the Germanium crystal structure and the Miller Indices representation for axes and planes are defined in Appendix C). It was apparent that the chances of scanning through a major plane was much greater than through an axis.

The crystal was scanned through ϕ for fixed values of θ and the ratio R was calculated for each setting of θ and ϕ. A plot of R versus ϕ showed two peaks. From the FWHM (full width at half the maximum height) values the peaks were identified as (110) and (111) planes. The angular separation was found to decrease

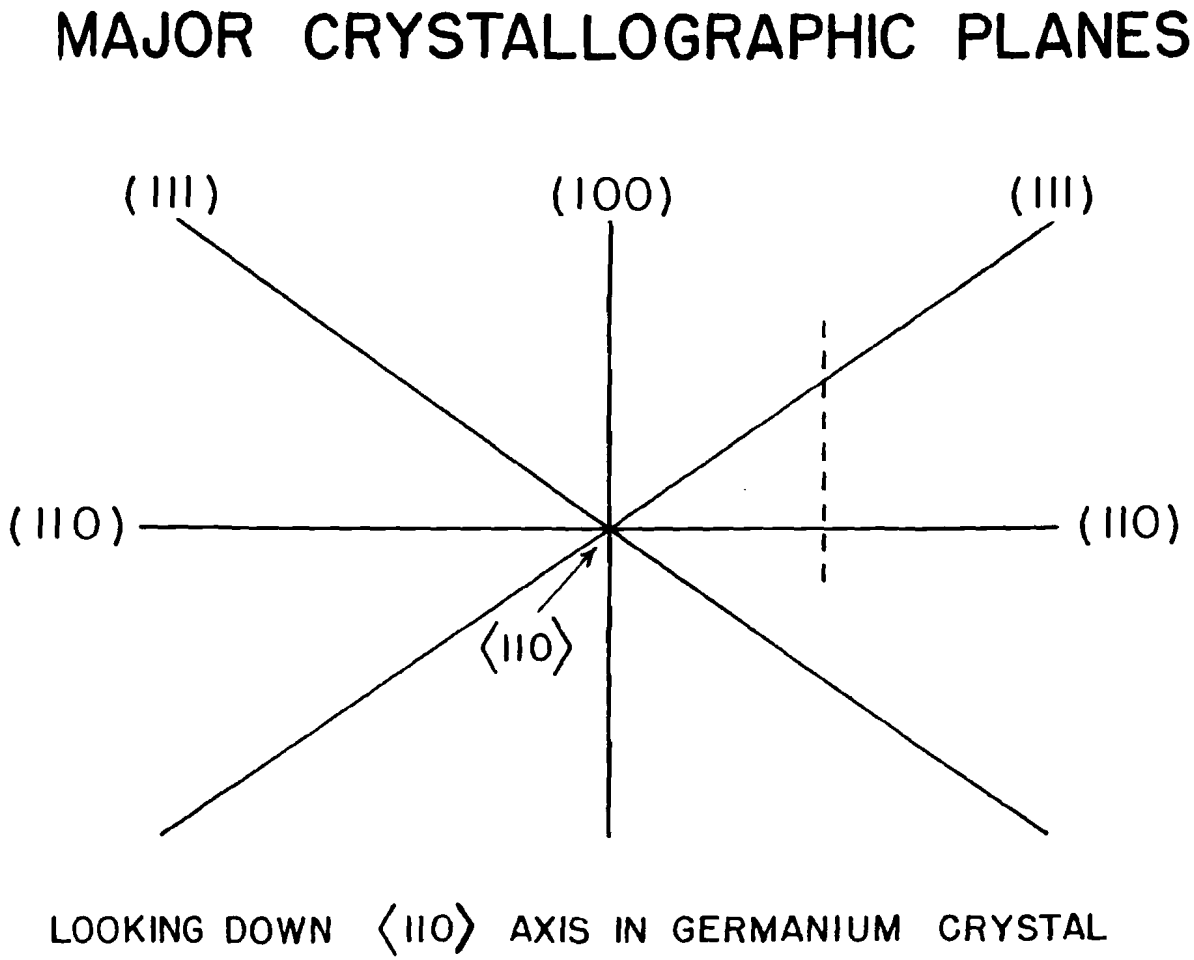

Fig. 3.6 The major low index planes parallel to <110> axis in Germanium crystal are indicated. The dashed line shows the region of initial scan.

between the (110) and (111) planar peaks. This indicated that the change in ϕ was moving the crystal axis closer to the beam direction.

The process of scanning ϕ for each θ-increment was repeated till the two planar peaks merged and the axis was aligned along the beam direction.

A check was done on the alignment by analyzing a sample of the data on the on-line computer. Scatter diagrams of projected, exit angle distributions (these angles are defined in Fig. 4.5) were displayed with selections on low pulse height and small scattering angle. These selections picked out channeled particles predominantly and an enhancement along axial and planar channeling directions was observed. A typical, computer generated, on-line scatter diagram is shown in Fig. 3.7. This is an exit projected angle plot. The angle coordinates are in micro-radians. The number in each bin represents events with the range of exit angle for that bin. The cluster of large numbers in the bins near the left end of the scatter diagram represents the axis position. This can be seen better in the three dimensional graph of the scatter diagram in Fig. 3.8 plotted off-line. The highest peak is along <110> axis direction and the smaller ridges, radiating out from the axis position, are along the (111), (110), and (111) planes.

ONLINE SCATTER PLOT

HIST(OCT) # 112

```
SCATTER PLOT: # ENTRIES=29190
  3   1   3   5   5   3   1   4   2   0   1   0   0   1   0   0   0   0
  3   6   9  12  11  12   6   5   3   5   6   2   5   2   0   0   0   0
  6  12  24  22  23  25  30  13  10   9   8  10   3   6   2   1   0   0
 26  40  55  47  32  58  57  29  23  29  30  19   9   5   1   0   0   0
 53  64  91  66  83 117  86  70  64  49  53  29  11  11   3   1   0   0
 93  84 140 133 128 195 124  88  86  93  64  43  26  17   7   0   0   0
142 169 154 170 214 207 152 133 118  90  67  61  46  19   5   2   1   1
138 228 206 224 256 158 159 132 130 125 140  90  59  19   2   3   1   2
127 175 317 584 422 215 184 177 160 160 116  93  53  25   8   2   2   1
158 203 421 1028 745 242 173 154 150 134 110  73  50  21  10   3   0   0
151 174 294 515 383 253 180 157 156 114 131  88  59  19  16   1   2   0
130 174 200 242 218 249 297 184 169 143 126 101  61  26  12   5   1   0
122 134 217 213 183 181 215 352 242 132 108  72  61  25  13   1   1   0
 76 135 225 184 181 158 159 200 352 256 141  77  69  28   9   6   0   2
 60 135 162 127 142 225 147 126 168 249 196  97  38  21   3   6   0   0
 45 129 117  97 136 200 138 117 122  97 151 125  47  13   8   3   1   1
 70  92  75  81  86 129 103  74  72  75  64  63  44  17   8   2   1   0
 47  58  48  58  50 100  89  69  58  52  45  50  27  10   5   1   0   1
 39  35  39  53  44  60  87  51  43  30  34  36  20  10   4   1   0   0
 26  23  26  36  35  44  58  34  33  37  31  19  20   5   3   2   0   1
# OVERFLOWS= 4072

RUN #   47
X ORIGIN: -200
Y ORIGIN: -500
X BIN SIZE:   50
Y BIN SIZE:   50
```

Fig.3.7 Scatter diagram obtained from online analysis by HP2100 computer. All angles are measured in microradians.

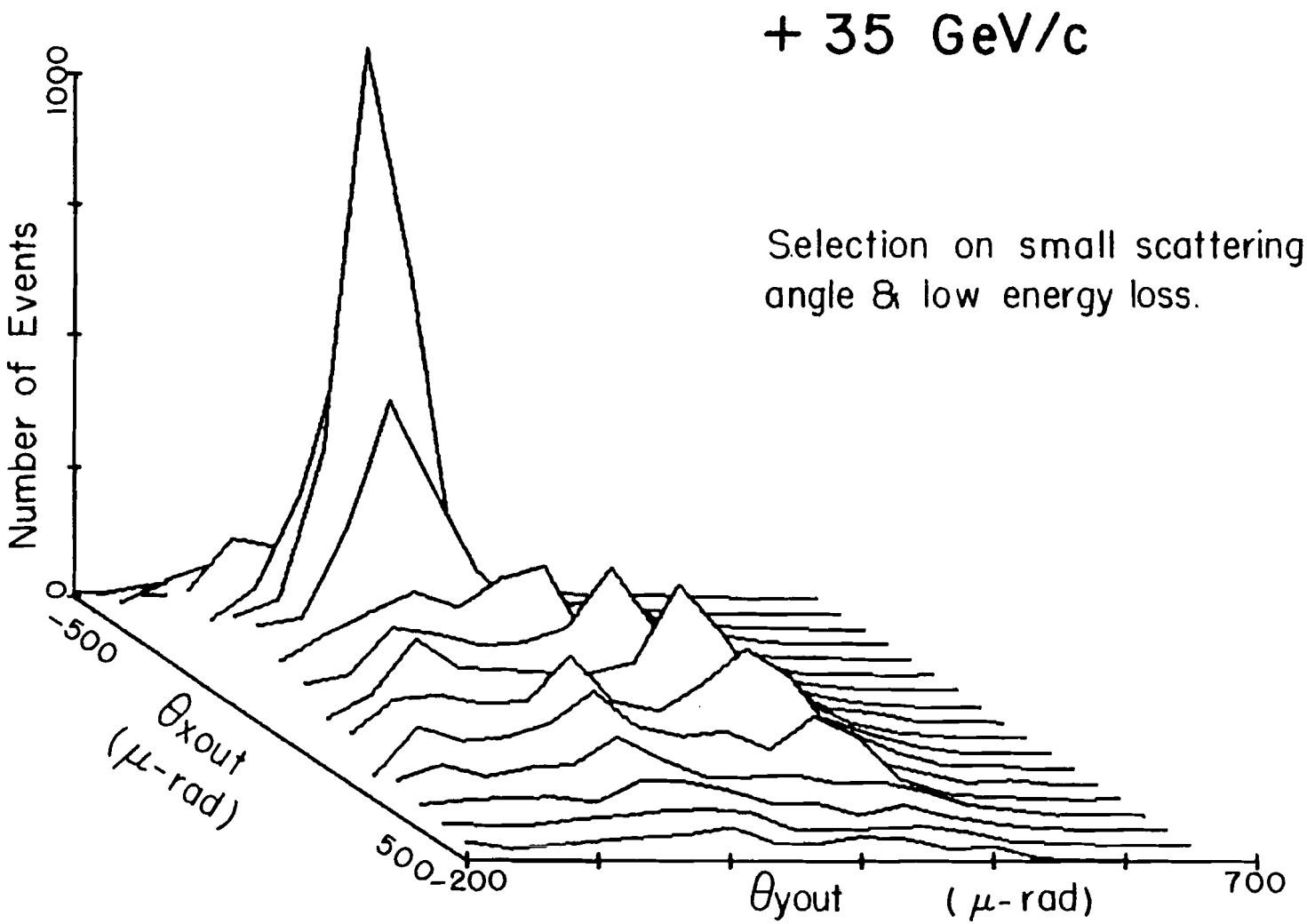

Fig. 3.8 Three dimensional display of the exit angle scatter diagram in Fig.3.7.

3.8 DATA SUMMARY

Once crystal axis alignment had been done and checked, the beam was set to the desired momentum value and polarity. The data from the 48 TDC's and the ADC were transferred to the computer after each event and recorded on tape. This process was repeated for the various configurations of the beam momentum, polarity and crystal orientation which are listed in Table 3.2.

An average of 120000 events was recorded on each tape of 2400 feet length. The recording density was 1600 bpi (bits per inch). Twenty tapes of good data were recorded in the entire experimental run.

The following items were monitored and checked periodically during the data recording period:

a) crystal temperature

b) goniometer chamber pressure

c) gas flow in drift chambers

d) beam momentum

e) crystal orientation angles θ and ϕ

The nitrogen in the dewar flask, cooling the crystal, was refilled every four hours.

Table 3.2 Summary of the data recorded on tape for off-line analysis.

DATA SUMMARY

Energy & Type of Particles	Channeling Condition	No. of Events Recorded
35 GeV/c π^+	Axial	360000
35 GeV/c π^-	Axial	360000
100 GeV/c +	Axial	120000
250 GeV/c +	Axial	420000
35 GeV/c +	Planar	150000
250 GeV/c +	Planar	360000
250 GeV/c +	Random	180000
35 GeV/c +	No Crystal	180000
250 GeV/c +	No Crystal	180000

CHAPTER 4

DATA ANALYSIS

The data from the channeling experiment were copied onto tapes at Fermilab and brought to Lehigh University for analysis. In all, there were twenty nine-track tapes containing data for all the configurations listed in Table 3.3.

Besides the tape number and the run rumber needed to identify the configuration of the experimental run, each tape contained the TDC counts for all signal wires and the ADC channel number for each event.

The first phase of the analysis was to convert the ADC channel number to the energy lost by the beam particle in the crystal and to calculate the position of each particle in the three drift chamber modules from the TDC counts. This yielded complete information about the trajectory of the particle before and after emerging from the crystal.

The conversion formula for calculating the dE/dx loss from the channel number was obtained from the calibration data using Na^{22} source. The energy loss, ΔE, in MeV was given by the following equation:

$$\Delta E = 0.01978\ N_c + 0.7582 \qquad 4.1$$

where N_c is the channel number.

The calculation of the position coordinates in the three drift chamber modules was more involved and will be described in the following sections.

4.1 DRIFT MECHANISM AND DRIFT TIME

A single drift cell with its associated electronics is shown in Fig. 4.1(a). In the experimental operations, a charged beam particle satisfying the event trigger logic produced a trigger pulse that started all the TDC's counting at time zero. After a time interval, T_o', the particle passed through the drift cell. The gas mixture in its path was ionized and the electron cluster started drifting towards the signal wire under the action of a uniform electric field of 1500 volts/cm. The drift velocity was fairly uniform throughout the drift cell (average velocity $\sim$50 microns/nano-seconds) except for regions close to the signal and potential wires. The electrons produced an electron avalanche very close to the signal wire due to the high electric field in the vicinity of the signal wire and they were then collected by it.

The drift time of the electron cluster in the drift cell was T. In a time interval T_o'' the electric pulse, produced at the signal wire, travelled through the discriminator to the TDC and stopped counting. The

(a) SINGLE DRIFT CELL

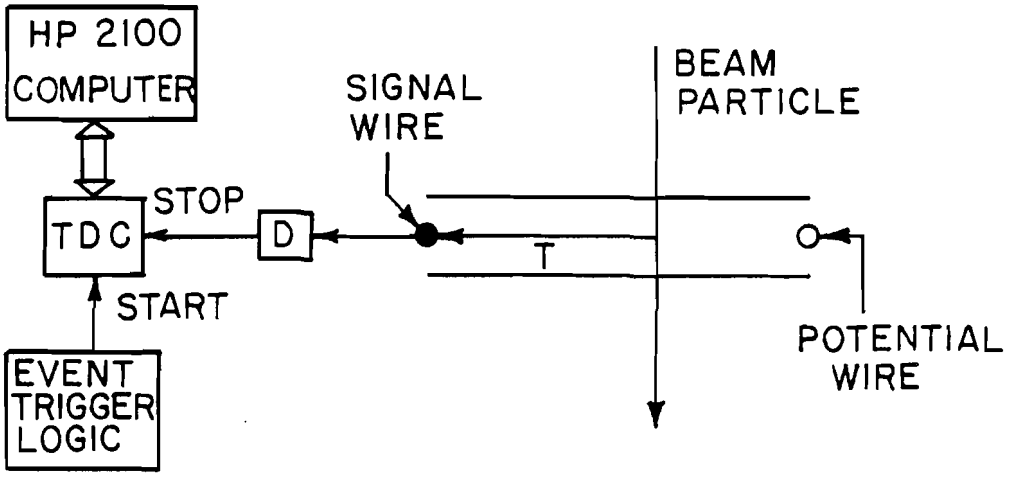

D : DISCRIMINATOR

TDC : TIME-TO-DIGITAL CONVERTOR

(b) DRIFT TIMES

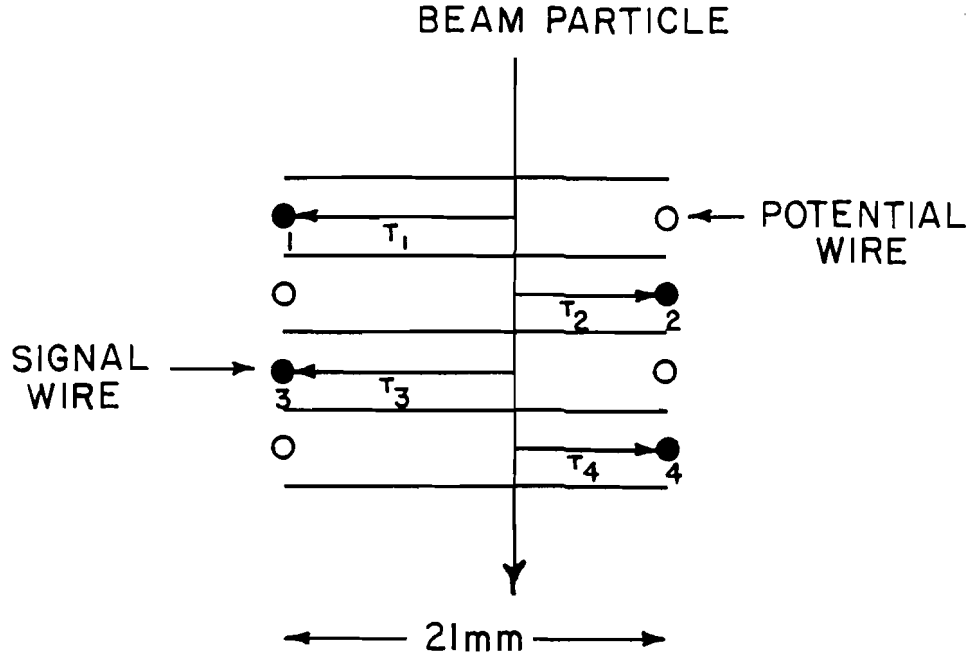

Fig. 4.1 (a) Schematic of a single drift cell and the associated electronics. (b) The drift direction and time in the four drift cells. View is looking along wire directions.

total time interval, T', counted by the TDC was thus the sum of T_o', T and T_o'', i.e.

$$T' = T_o' + T + T_o'' \qquad 4.2$$

The TDC counts were converted to time intervals in nano-seconds by multiplying them with the TDC least counts (a scale factor giving the number of nano-seconds corresponding to one count of the TDC). The least counts were obtained from a TDC calibration run and their values for each signal wire are listed in Table A.1 in Appendix A. Each signal wire was identified by a number. These numbers are indicated for signal wires in the three drift chamber modules in Fig. A.1 in Appendix A. The wires 19, 20, 21, 22, 23, 24, 38, and 39 were dead for all the runs in the experiment. The detection efficiency of the active signal wires were found to be always greater than 98%.

The value of $T_o = T_o' + T_o''$ for each signal wire was estimated by a straightforward method outlined in Appendix B.

The actual drift time, T, in the drift cell was obtained by subtracting T_o from the TDC time interval T', i.e.,

$$T = T' - T_o \qquad 4.3$$

4.2 DRIFT VELOCITY AND COORDINATE CALCULATIONS

Whenever a charged particle passed through a drift chamber module, it produced ions and electrons in four X and four Y drift cells in the path of the particle. Four of these drift cells representing either X or Y planes are shown in Fig. 4.1(b). The electrons drifted to the signal wires in the opposite directions in the alternate drift cell and the drift times T_1, T_2, T_3, and T_4 are shown in the figure.

The maximum beam divergence was 1000 micro-radians and this would produce a transverse shift of less than 80 microns between the first and the fourth drift cell. This shift was neglected.

The projected distance on the axis between the signal wires was D = (21000 ± 14) microns and the average drift velocity in the first and second drift cell was

$$\bar{v} = \frac{D}{T_1+T_2} \qquad 4.4$$

Since the distance, D, was constant, the total drift time, $T_1 + T_2$, was inversely proportional to the drift velocity and could be used as a check for the constancy of the drift velocity.

Figure 4.2 shows a typical plot of $T_1 + T_2$ versus $T_1 - T_2$. The difference, $T_1 - T_2$, covers the total distance between the two wires. The first wire was

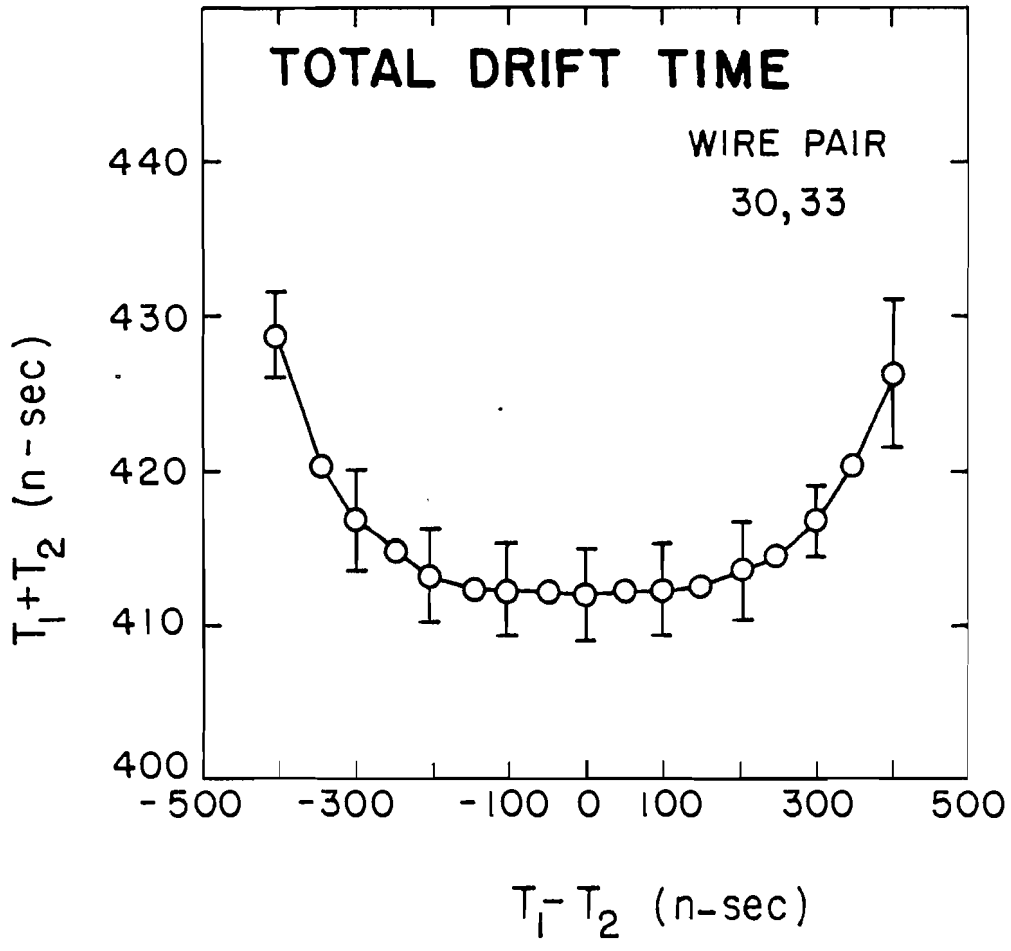

Fig. 4.2 The variation of the total drift time, T_1+T_2, with position in the drift cell indicated by T_1-T_2.

at the maximum value of $T_1 - T_2$ and the second at the minimum value of $T_1 - T_2$.

The total drift time, $T_1 + T_2$, was constant near the middle of the drift region for one half of the total drift space. It increased near the wire positions and this indicated a decrease in the drift velocity near the signal wire or the proportional wire or both, in the two drift cells. The decrease near the signal wire could not be physically justified and therefore the drift velocity was assumed to be constant in the region from the signal wire to the middle of the drift cell and decrease beyond the mid-point to the other end. This is shown in Fig. 4.3. Here the projected distance on the axis is drawn on the horizontal axis and the time is plotted on the vertical axis. X_1 and X_2 measures the distance from wires 1 and 2, respectively. The curve marked T_1 gives the dependence of the distance on the time of the electron drift in the first drift cell and the one marked T_2 is for the second.

The following relations were written for the two curves, i.e.,

Signal wire 1:

$$X_1 = v_1 T_1 \qquad T_1 < T_2 \qquad 4.5a$$

$$X_1 = v_1 T_1 - w_1 |(T_1 - T_2)^{n_1}| \qquad T_1 > T_2 \qquad 4.5b$$

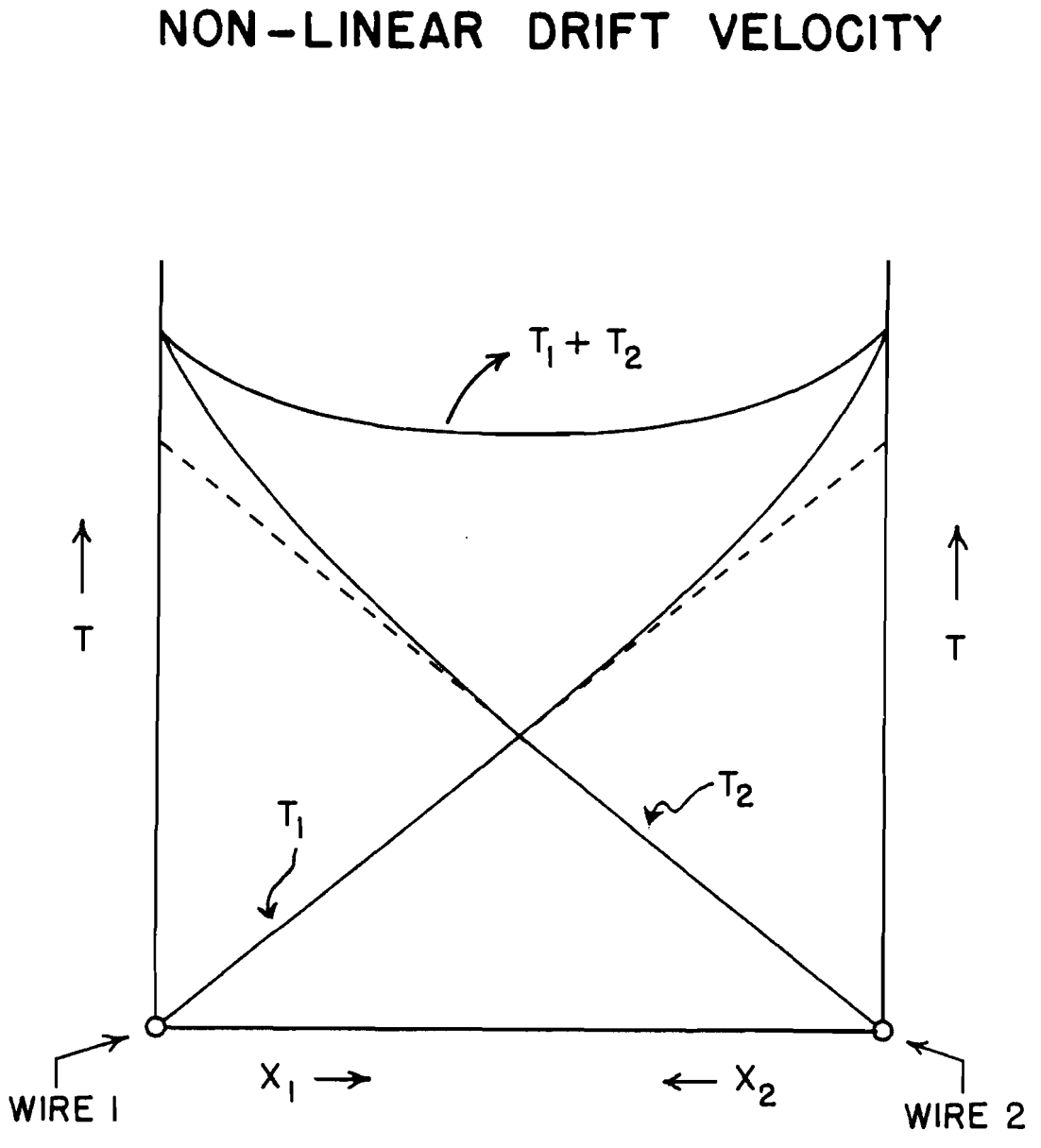

Fig. 4.3 Projected distance versus time graph showing non-linear behaviour of the drift velocity for two signal wires in adjacent drift planes. The inverse slope of the curve is the velocity.

Signal wire 2:

$$X_2 = v_2 T_2 \qquad T_1 > T_2 \qquad 4.6a$$

$$X_2 = v_2 T_2 - w_2 |(T_1 - T_2)^{n_2}| \qquad T_1 < T_2 \qquad 4.6b$$

where v_1 and v_2 are the drift velocities in the drift cells 1 and 2, respectively, w_1 and w_2 are the coefficients of the non-linear term, and n_1 and n_2 are integer exponents. Since the data available were not sufficient to calculate the drift velocities v_1 and v_2 in each drift cell, therefore an average velocity $v = (v_1 + v_2)/2$ was substituted for v_1 and v_2. Symmetry was assumed for the non-linearity, i.e., $w_1 = w_2 = w$ and $n_1 = n_2 = n$.

With these simplifying assumptions one obtains from Eqs. 4.5 and 4.6 the following relation:

$$T_1 + T_2 = \frac{X_1 + X_2}{v} + \frac{w}{v} |(T_1 - T_2)^n|$$

or

$$T_1 + T_2 = A + B|(T_1 - T_2)^n| \qquad 4.7$$

where $A = \frac{X_1 + X_2}{v}$ and $B = \frac{w}{v}$.

The average drift velocity was calculated by dividing the projected distance between the two signal wires ($X_1 + X_2$ = (21000±50) microns) on the axis by the sum of the drift time near the middle of the drift cell ($T_{mid} = (T_1 + T_2)_{\text{middle of the drift cell}}$), i.e., $v = (2100 \pm 14)/T_{mid}$.

The total drift time, T_{mid}, near the middle of the drift cell, and therefore the drift velocity, v, was different for different pairs of signal wires. This was probably due to the difference in the electric field distribution in the different cells within the same drift chamber module and also the difference in the gas mixture composition in the three modules (all the drift cells in the same module were enclosed in the same gas enclosure).

The drift velocity, v, was also found to change from run to run. This change was similar for all the wire pairs in the three modules. The change in temperature was found to be the most likely cause for this variation.

The B and n parameters in Eq. 4.7 were obtained from a curve fitting program* for all adjacent pairs of wires in the three drift chamber modules, and an average value was calculated for the X and Y coordinates in each module. The range of values for T_{mid} and v and the average values of the B and n parameters are listed in Table 4.1

---

*An interactive statistical package, ISIS, originally written in Florida State University and modified at Lehigh University, was used to fit n^{th} order polynomial to T_1+T_2 curve of Eq. 4.7.

Table 4.1 The value of the parameters used in calculating the position in drift cells of the beam particle tracks from the drift times T_1-T_2 using Eq. 4.8 for drift chambers DC1, DC 2, and DC 3.

Drift Chamber	T_{mid} (n-sec)	v (micron/n-sec)	B $(n\text{-sec})^{1-n}$	n
DC1X	404.2-409.5	51.28-51.95	5.27×10^{-10}	4
DC1Y	409.2-416.1	50.47-51.32	2.00×10^{-7}	3
DC2X	399.8-409.8	51.24-52.53	2.00×10^{-7}	3
DC2Y	405.4-415.3	50.57-51.80	2.00×10^{-7}	3
DC3X	390.7-397.0	52.90-53.75	1.80×10^{-7}	3
DC3Y	391.8-396.1	53.02-53.60	1.80×10^{-7}	3

Table 4.2 Resolutions of the X and Y coordinate measurements in the three drift chamber modules, DC1, DC2, and DC3.

Drift Chamber	Minimum (micron)	Maximum (micron)
DC1X	72.8	103.0
DC1Y	55.3	78.1
DC2X	50.1	70.8
DC2Y	53.0	74.9
DC3X	45.2	63.9
DC3Y	44.2	62.4

The position coordinate was measured from the middle of each drift cell. The formula used was obtained by subtracting X_2 from X_1 in Eqs. 4.5 and 4.6 and dividing by 2, i.e.,

$$X = \frac{X_1 - X_2}{2} = \frac{(T_1 - T_2)v}{2} \pm \frac{w}{2}\left|(T_1 - T_2)^n\right| \quad \begin{matrix} + \text{ for } T_1 < T_2 \\ - \text{ for } T_1 > T_2 \end{matrix} \qquad 4.8$$

The coordinates in the two pairs of the drift cells shown in Fig. 4.1(b) were calculated using the above formula and an average value was taken as the position coordinate along the axis in the drift chamber module. This was done for the X and Y planes in the three modules and the position coordinates (X_1, Y_1), (X_2, Y_2), and (X_3, Y_3) were obtained in the first, second, and third drift chambers.

The validity of the above non-linear formula was tested by looking at the distribution of events along X and Y axes near the wire positions where the non-linearity was maximum. Fig. 4.4 shows the distribution of events along X-axis in the third drift chamber. The positions were calculated with and without the non-linear term in Eq. 4.8. The distribution was smoother across the wire position for the case where the non-linear term was included. This was a direct indication that the above technique, used to compensate for the non-linearity of the drift velocity, was correct.

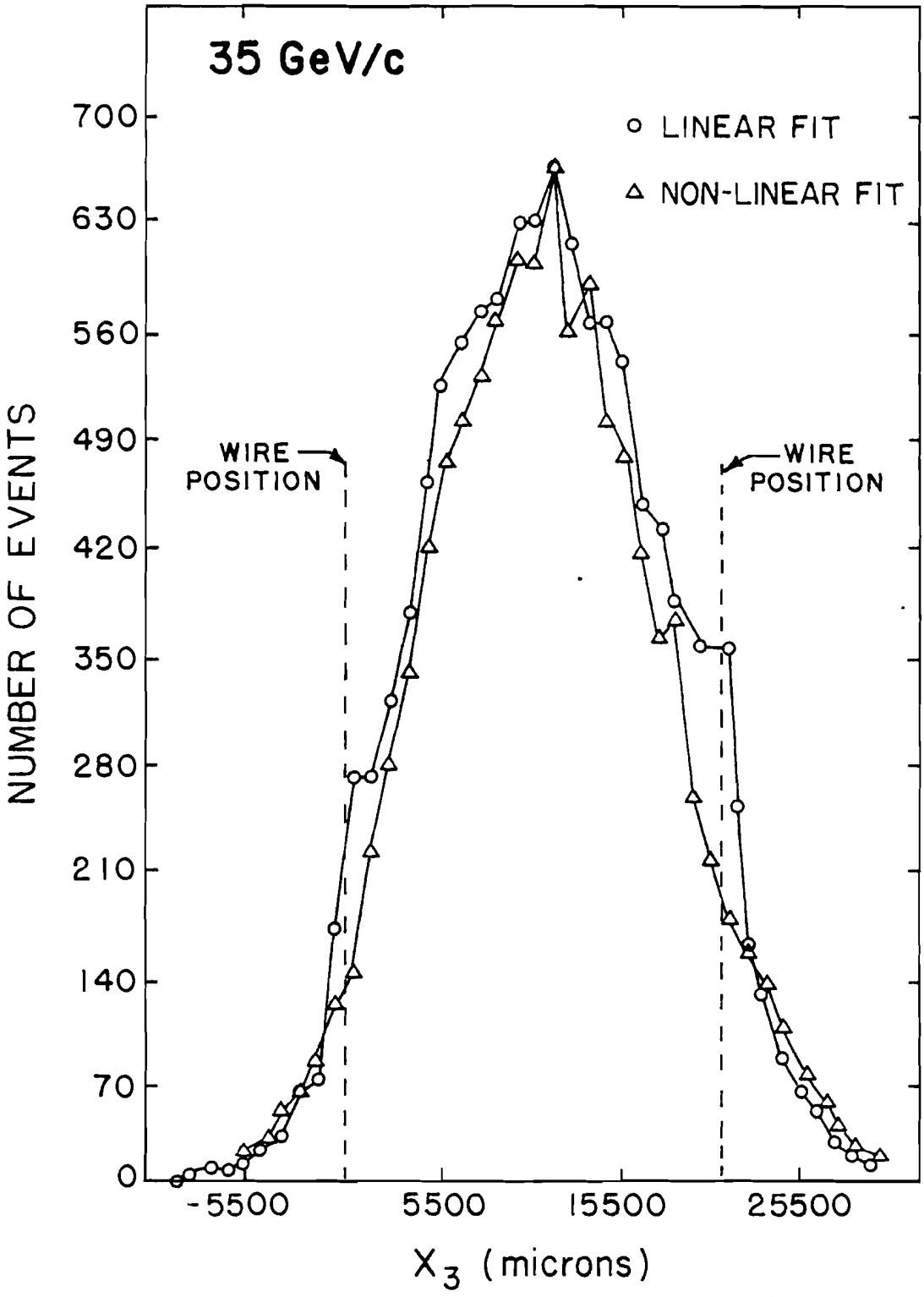

Fig. 4.4 The particle distribution in X_3 coordinate calculated by using linear (circles) and non-linear (triangles) fit to drift velocity.

4.3 RESOLUTION OF THE DRIFT CHAMBERS

A rms (root mean square) spread was observed in the total drift time, $T = T_1 + T_2$, between the two signal wires in the adjacent drift cells, as can be seen in Fig. 4.2. This was due to three factors -- the statistical nature of the electron collection at the signal wire, the spread due to diffusion of the electron cluster as it drifted to the signal wire, and the fluctuation due to electronic jitter (time variations in triggering of electronic circuits).

The position uncertainty of the signal wires was 10 microns in the drift chamber modules. Therefore the standard error in the projected distance, D = 21000 microns between the two signal wires in the adjacent drift planes, was $\sigma_D = \sqrt{10^2+10^2} = 14$ microns. This error was less than 0.1% and was insignificant when added in quadrature to the other errors.

The spread in the total drift time of σ_T led to an error in the velocity measurement of $\sigma_v = \sigma_T D/(T_1+T_2)^2$, and this in turn produced an error in the distance calculation of magnitude

$$\sigma_d = \frac{D}{2}\frac{\sigma_T}{T_1+T_2}\left\{1 + \left(\frac{T_1-T_2}{T_1+T_2}\right)^2\right\}^{\frac{1}{2}} \qquad 4.9$$

The error had a minimum value in the middle of the drift cell where $T_1 = T_2$ and was maximum near the wire positions.

The maximum and the minimum errors were calculated for all the active signal wire pairs, in widely separated runs covering the entire experimental run period. From these values an average of the standard error was found for X and Y coordinates in the three drift chamber modules. These values are listed in Table 4.2. The error was largest for the X-coordinate in DC1 because only two drift planes instead of four were active in this case.

4.4 MULTIPLE SCATTERING AND SYSTEM RESOLUTION

The variables used in studying channeling and other related effects in this experiment are shown in Fig. 4.5. These variables were calculated from the position coordinates (X_1,Y_1), (X_2,Y_2) and (X_3,Y_3) in the three drift chamber modules. The variable names in full and in abbreviated form for display in the computer plotted graphs, along with the formulas used to calculate them, are presented in Table 4.3.

The net resolution in the measurement of the channeling variables was due to the resolution in position calculation in the three drift chamber modules and the multiple scattering in the various components of the system. The multiple scattering in air was reduced to a large extent by placing vacuum pipes in between the drift chamber modules. The other sources of multiple

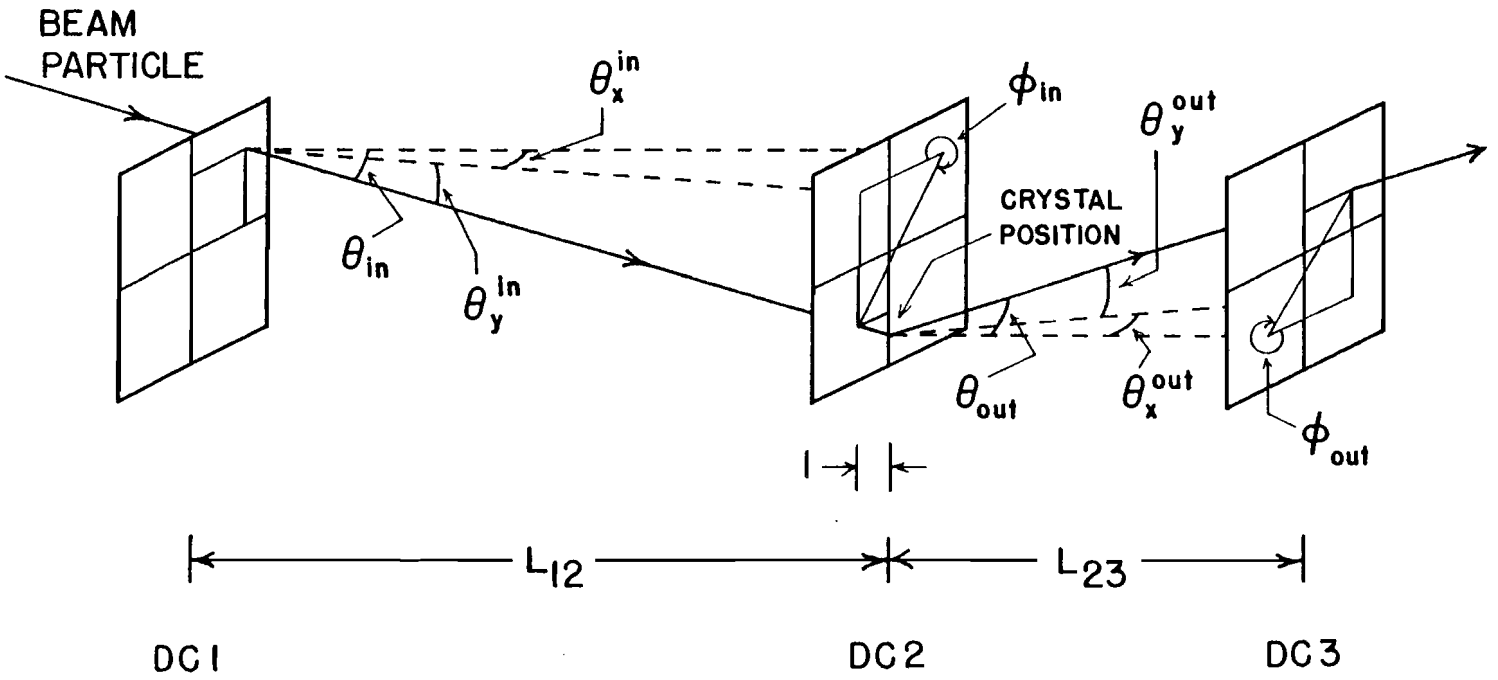

Fig. 4.5 The incident and the exit angles of a beam particle are indicated in terms of the positions in the three drift chambers.

Table 4.3 List of variables used in the data analysis, their abbreviated form appearing in the computer plotted graphs and the formulas used to calculate them.

VARIABLE NAME		
IN FULL	ABBREVIATED	FORMULA
Energy loss	PULSE HT.	ΔE
Projected Incident Angle	THETAX IN	$\theta_X^{in} = (X_2-X_1)/L_{12}$
	THETAY IN	$\theta_Y^{in} = (Y_2-Y_1)/L_{12}$
Projected Exit Angle	THTAX OUT	$\theta_X^{out} = \frac{(X_3-X_2)}{(L_{23}-\ell)} - \frac{(X_2-X_1)}{L_{12}(L_{23}-\ell)}$
	THTAY OUT	$\theta_Y^{out} = \frac{(Y_3-Y_2)}{(L_{23}-\ell)} - \frac{(Y_2-Y_1)}{L_{12}(L_{23}-\ell)}$
Projected Scattering Angle	D THETAX	$\Delta\theta_X = \theta_X^{out} - \theta_X^{in}$
	D THETAY	$\Delta\theta_Y = \theta_Y^{out} - \theta_Y^{in}$
Scattering Angle	DEL THETA	$\Delta\theta = (\Delta\theta_X^2 + \Delta\theta_Y^2)^{\frac{1}{2}}$
Incident Angle	THETA IN	$\theta_{in} = (\theta_X^{in^2} + \theta_Y^{in^2})^{\frac{1}{2}}$
Exit Angle	THETA OUT	$\theta_{out} = (\theta_X^{out^2} + \theta_Y^{out^2})^{\frac{1}{2}}$
Incident Azimuthal Angle	PHI IN	$\phi_{in} = \text{ARCTAN}(\theta_Y^{in}/\theta_X^{in})$
Exit Azimuthal Angle	PHI OUT	$\phi_{out} = \text{ARCTAN}(\theta_Y^{out}/\theta_X^{out})$
Azimuthal Scattering Angle	DELTA PHI	$\Delta\phi = \phi_{out} - \phi_{in}$
Radial Scattering Angle	D THETA	$\delta\theta = \lvert\theta_{out} - \theta_{in}\rvert$

scattering were the mylar windows on the vacuum pipes, the goniometer, the drift chamber modules and scintillation counters, etc. The rms spread in the incident, exit and the scattering angle due to the multiple scattering in the various components of the system were calculated by using the following formula [Ba78].

$$\theta^{rms}_{plane} = (1 + \varepsilon) z \frac{15 \text{ MeV/c}}{p} \sqrt{\frac{\delta x}{L_R}} \text{ (radians)} \qquad 4.10$$

where θ^{rms}_{plane} is the standard deviation of the distribution of net deflection angles projected onto any plane, p is the projectile momentum, βc is its speed, δx is the thickness of the medium, L_R is the radiation length for the medium and ε is a constant which for this calculation was taken as zero. The radiation lengths for the different materials were taken from ref. Br78.

The net resolution was computed by adding the resolution due to the drift chambers and the multiple scattering in the system in quadrature. These values along with the net system resolution, obtained experimentally at 35 and 250 GeV/c by removing the crystal and measuring the angular spreads, are listed in Table 4.4. The agreement was very good between the computed and the experimental values. The data at 100 GeV/c momentum for the system resolution were not taken.

Table 4.4 The standard error due to the drift chamber resolution, the multiple scattering in the system, and their sum in quadrature. The experimental total error at 35 and 250 GeV/c are also listed

	STANDARD ERROR (micro-radians)					
	Drift Chamber		Multp. Scat. in the System	Total (Computed)		Experimental
	min	max		min	min	
35 GeV/c						
θ_X^{in}	2.95	4.17	25.33	25.50	25.67	
θ_Y^{in}	2.55	3.61	25.33	25.45	25.58	
θ_X^{out}	3.75	5.30	33.88	34.09	34.30	
θ_Y^{out}	3.83	5.42	33.88	34.10	34.31	
$\Delta\theta_X$	5.66	7.80	45.64	45.99	46.30	46.25±0.23
$\Delta\theta_Y$	5.62	7.94	45.64	45.98	46.32	47.69±0.24
100 GeV/c						
θ_X^{in}	2.95	4.17	8.87	9.35	9.81	
θ_Y^{in}	2.55	3.61	8.87	9.23	9.58	
θ_X^{out}	3.75	5.30	11.61	12.44	12.99	
θ_Y^{out}	3.83	5.42	11.61	12.46	13.04	
$\Delta\theta_X$	5.66	7.80	15.98	16.95	17.78	
$\Delta\theta_Y$	5.62	7.94	15.98	16.94	17.85	
250 GeV/c						
θ_X^{in}	2.95	4.17	3.55	4.42	5.48	
θ_Y^{in}	2.55	3.61	3.55	4.37	5.06	
θ_X^{out}	3.75	5.30	4.75	6.05	7.11	
θ_Y^{out}	3.83	5.42	4.75	6.10	7.20	
$\Delta\theta_X$	5.66	7.80	6.39	8.54	10.09	10.00±0.05
$\Delta\theta_Y$	5.62	7.94	6.39	8.51	10.19	9.47±0.05

Lindhard's critical angles ψ_1 and ψ_a for <110> axis and (110) planes, respectively, are plotted as a function of beam momentum in Fig. 4.6. The scattering angle resolutions of the system at 35 and 250 GeV/c are also shown in the figure. The resolution of the system was 1/3 to 1/4 of ψ_1 but nearly equal to ψ_a at 250 GeV/c and about twice the value of ψ_a at 35 GeV/c. It is therefore more difficult to get accurate quantitative results for planar channeling, especially at 35 GeV/c, than for axial channeling.

The rms beam divergence in the projected incident, exit, and scattering angle plane at the three different momenta with the Germanium crystal aligned along the <110> axis are listed in Table 4.5. The beam was broad enough at 35 GeV/c momentum to show axial as well as planar channeling peaks in the projected angle plane (see Fig. 3.8). This was not the case for the 100 and 250 GeV/c data.

4.5 WANDERING OF THE CRYSTAL AXIS

The position of the crystal channeling axis <110> in the projected incident and exit angle planes were determined by looking at the beam particle distribution with selections on small dE/dx loss and small scattering angles. Channeled particles would satisfy these selection criteria with greater probability and

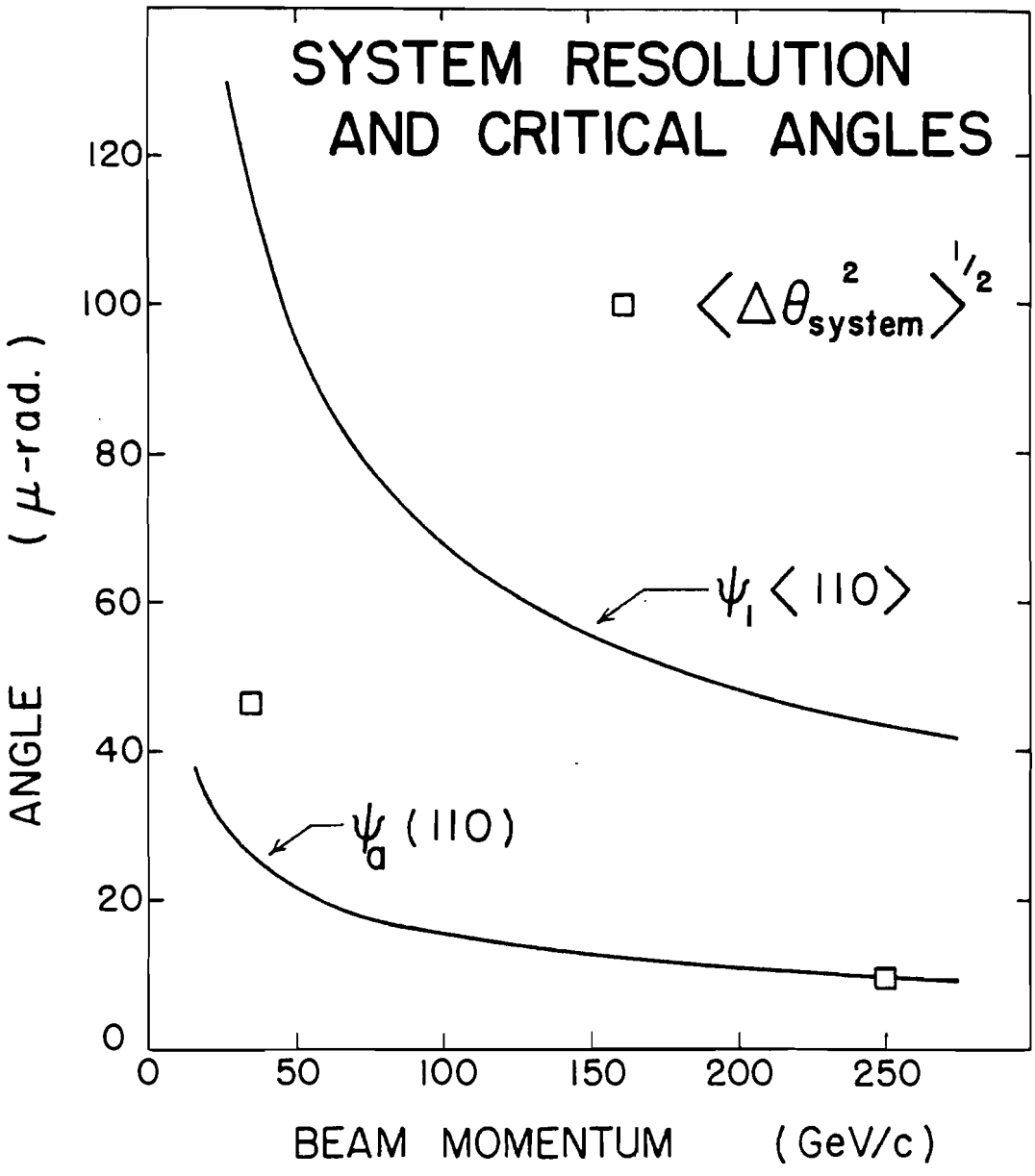

Fig. 4.6 Comparison of axial and planar critical angles ψ_1 and ψ_a, respectively, and the rms spread in the scattering angle due to multiple scattering in the system.

Table 4.5 The rms spread of the incident, exit and scattering angle of the beam particles at 35, 100 and 250 GeV/c beam momenta.

ANGLE (micro-rad.)	BEAM MOMENTUM 35 GeV/c	100 GeV/c	250 GeV/c
θ_X^{in}	58.0	65.6	125.1
θ_Y^{in}	45.8	134.0	178.6
θ_X^{out}	91.2	148.3	349.6
θ_Y^{out}	83.1	166.2	360.9
$\Delta\theta_X$	79.9	153.5	372.2
$\Delta\theta_Y$	83.5	161.7	382.4

the projected angle distributions would show enhancements along the axis direction.

The data from six runs (each run had approximately 24000 events) at 35 and 250 GeV/c and 4 runs at 100 GeV/c were analyzed. A fixed selection window of ΔE = 6.0 to 12.0 MeV on the energy loss in the crystal was applied. The selection window on the scattering angle was varied from 0 to $\frac{1}{4}\psi_1$ to 0 to $11/4\psi_1$ with an increment of $\frac{1}{4}\psi_1$ in the upper limit of the window. Channeling axial peaks were observed in the projected incident and exit angle scatter diagrams. A gaussian curve was fitted to the normalized axial peak to locate the centroid of the axial channeling distribution.* An average of the axis position value for the same run but different scattering angle selection was obtained. It was found that the axis position shifted from run to run. This is shown in Fig. 4.7.

As mentioned before in Section 3.6, this shift of the crystal axis position from run to run was attributed to the liquid nitrogen filling cycle of the crystal

---

*A curve fitting subroutine, named LSQMIN, obtained from the Lehigh Computing Center Library (No. -E20002) was used to do all the curve fittings mentioned in this dissertation. The technique is outlined in ref. Po65.

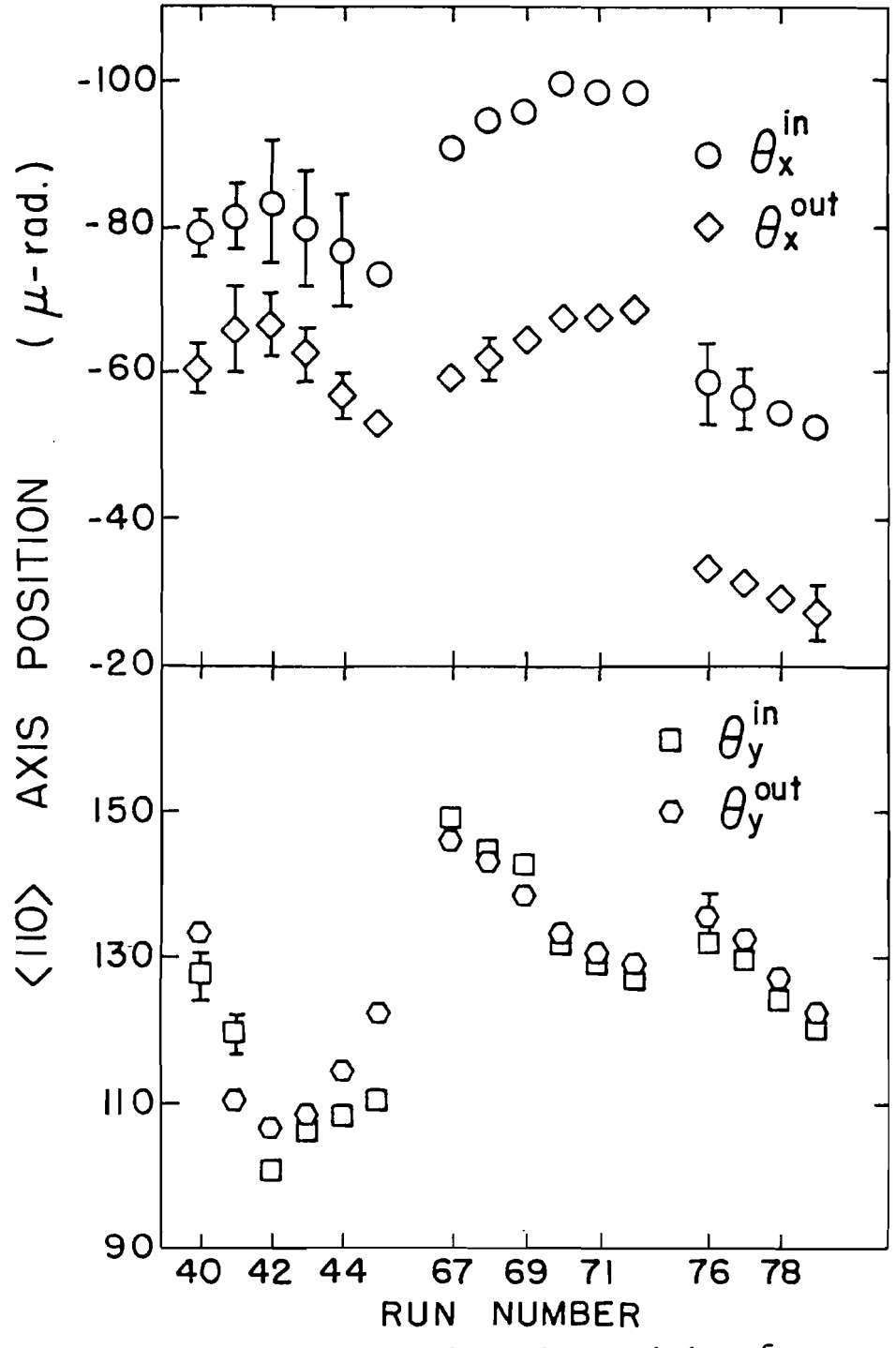

Fig. 4.7 Shift of the <110> axis position from run to run in the projected incident and exit angles.

cooling dewar flask. No direct correlation could be made between the shift in the crystal axis position and the liquid nitrogen filling cycle because no record was kept of the time of liquid nitrogen fillings.

The shift in the channeling axis position was compensated for in the analysis of the axial channeling data.

In the results presented in the following chapters, the crystal referred to is the 2 cms thick, Hyperpure Germanium Single Crystal. The"axis of the crystal" refers to the <110> axis. By "beam particles" is meant positive beam particles (unless mentioned otherwise) with the composition listed in Table 3.1. The results for positive particles are for 35, 100 and 250 GeV/c beam momenta. The negative particle results are for 35 GeV/e beam momenta only. In some cases the results for random orientation of the crystal at 250 GeV/c are also presented for comparison.

CHAPTER 5

CHANNELING

The incident particles that are channeled between atomic rows and planes in a crystal have a greater probability of emerging at small angles to the axes and planar directions than those which are not channeled. These particles are distributed in the projected angle plane with peaking along the axes and planar directions. The width of the distributions are very important characteristics and they are related to the crystal structure and the incident particle energy through the Lindhard critical angles, ψ_1 and ψ_a, for axial and planar channeling, respectively (these angles were defined in Chapter 2).

The channeled particles were identified by their reduced energy loss and scattering angle -- both consequences of the decrease in the probability of small impact parameter collisions for the channeled particles.

Figure 5.1 displays the distribution of the particles in the exit angle plane at 35 GeV/c beam momentum. The selection on the energy loss in the crystal was 6 to 12 MeV. The lower limit of 6 MeV was chosen be-

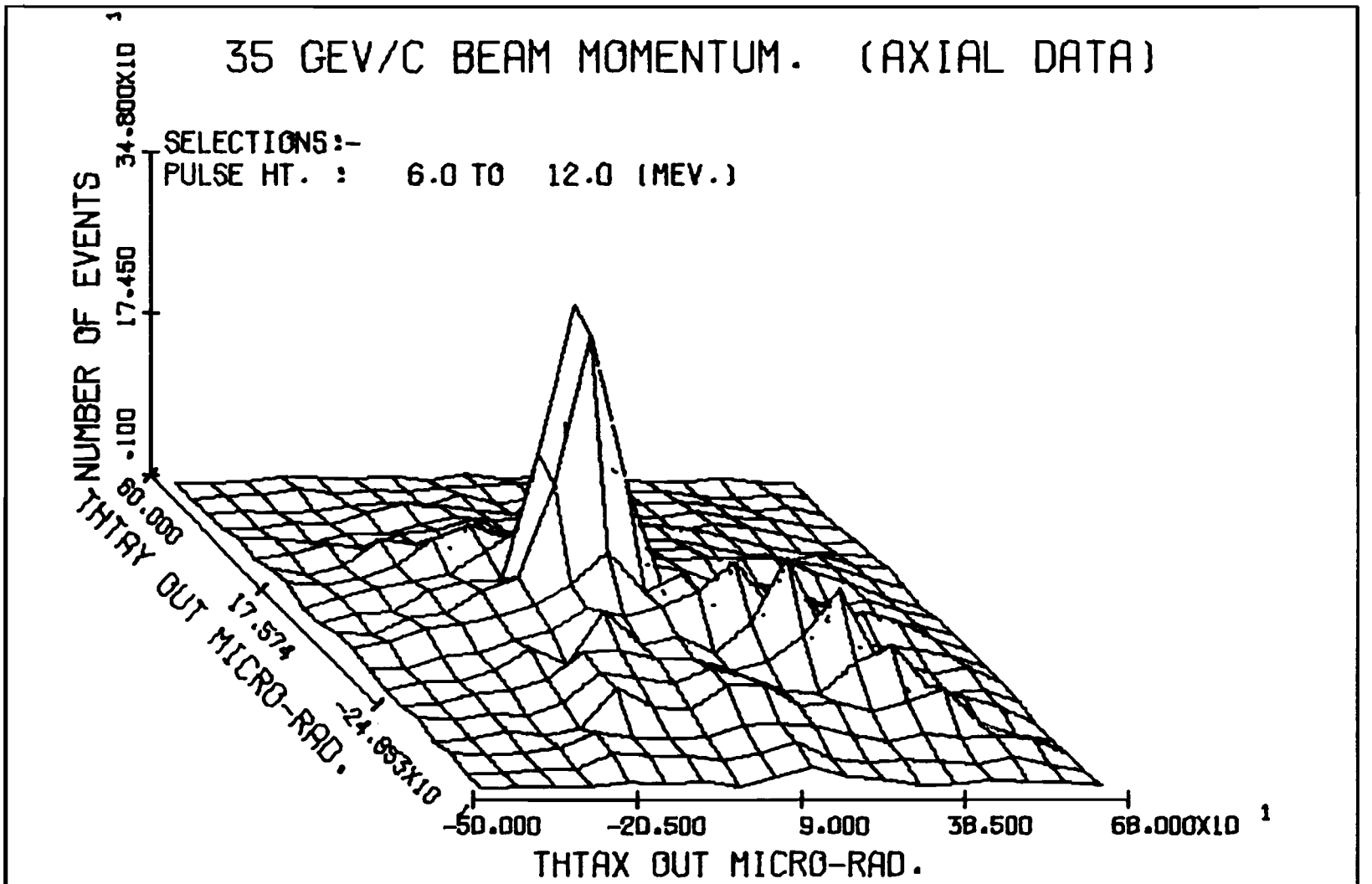

Fig. 5.1 Projected exit angle distribution showing axial and planar channeling.

cause this was the energy loss of the well channeled particles (see Sec. 9.4 in Chapter 9). The upper limit of 12 MeV was a good compromise between accepting as many channeled particles as possible and at the same time rejecting those in the random energy loss group (cf. Fig. 9.3). The highest peak in Fig. 5.1 is along the <110> axis. The prominent ridges, radiating out from the axis position, are the (111) planes (this being the plane with the widest interplanar spacing, Fig. 5.5). The beam spreads at 100 and 250 GeV/c beam momentum were not broad enough to show the axes and planes in the exit projected angle plane simultaneously (Table 4.5).

The widths of the axial and the planar channeling distributions are presented in the following sections.

5.1 AXIAL CHANNELING

The channeled particle distributions were obtained in the incident and the exit angle plane by selecting those particles that had energy loss of 6 to 12 MeV in the crystal. (The reasons for selecting this range have already been mentioned in the previous section.) The events were integrated over the azimuthal angle, ϕ, around the axis position and displayed in the radial angle, θ, to improve statistics. The axial channeling distributions were normalized with respect to the

corresponding distributions with no selection on energy loss.

It was possible to look at the channeling distribution in the exit as well as the incident angle plane because of the approximate conservation of the transverse energy for the channeled particles. In other words, the channeled particles which were incident on the crystal at a certain angle to the crystal axis had energy losses similar to the particles which emerged from the crystal at the same angle to the axis as the incident angle.

The channeled particle distributions around the <110> axis in the Germanium crystal at 250 GeV/c beam momentum are shown in Figs. 5.2(a) and (b). The <110> axis is at the origin of the θ_{in} and θ_{out} axes. A gaussian function, centered on the axis, was fitted to each of the distributions to obtain their width, (see footnote in Sec. 4.5).

Similar curve fittings were done to the axial channeling distributions at 35 and 100 GeV/c beam momenta.

The decrease of the energy loss for the channeled particles was employed in another way to obtain the width of the axial channeling distribution profile. The mean energy loss was plotted against the incident

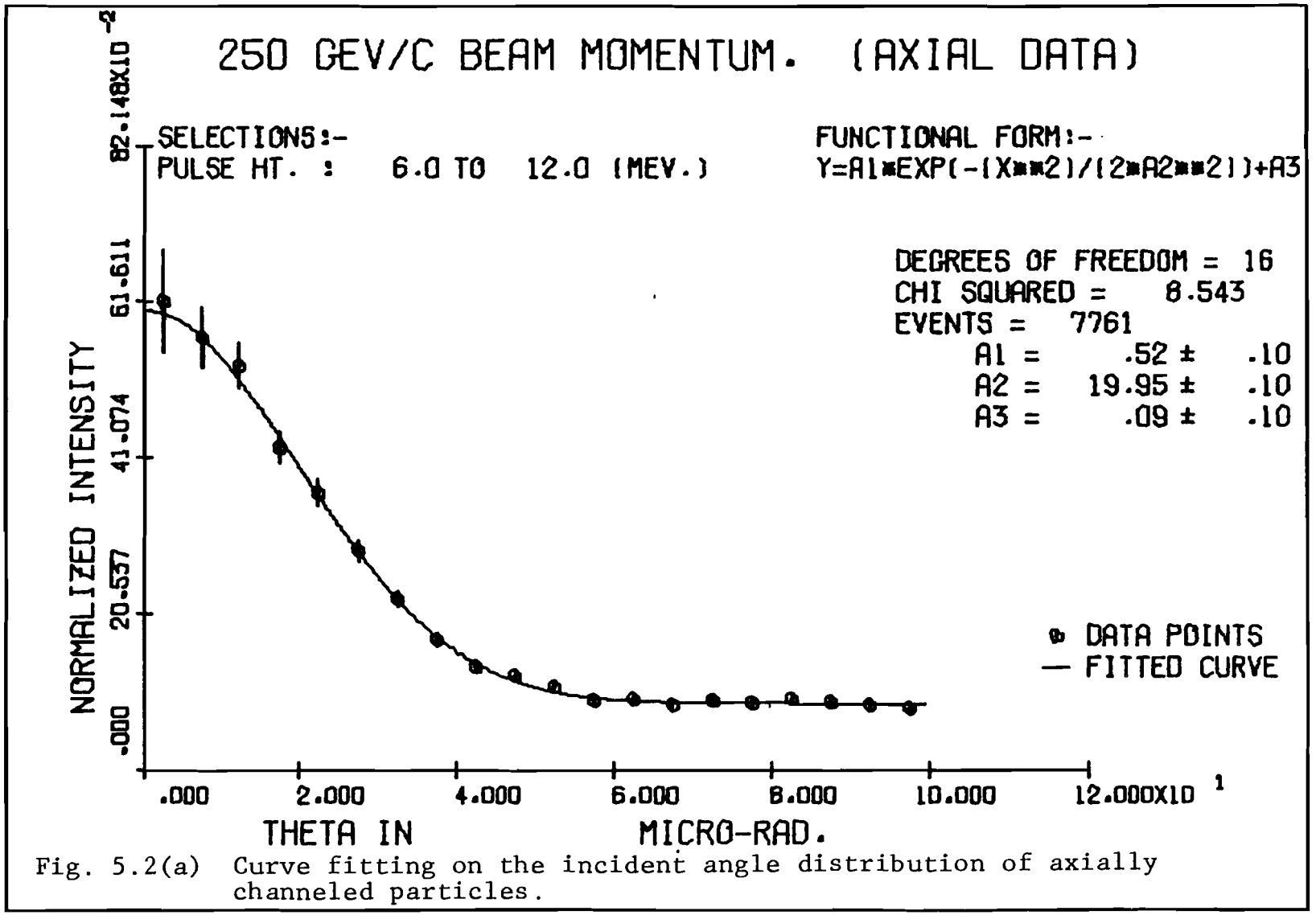

Fig. 5.2(a) Curve fitting on the incident angle distribution of axially channeled particles.

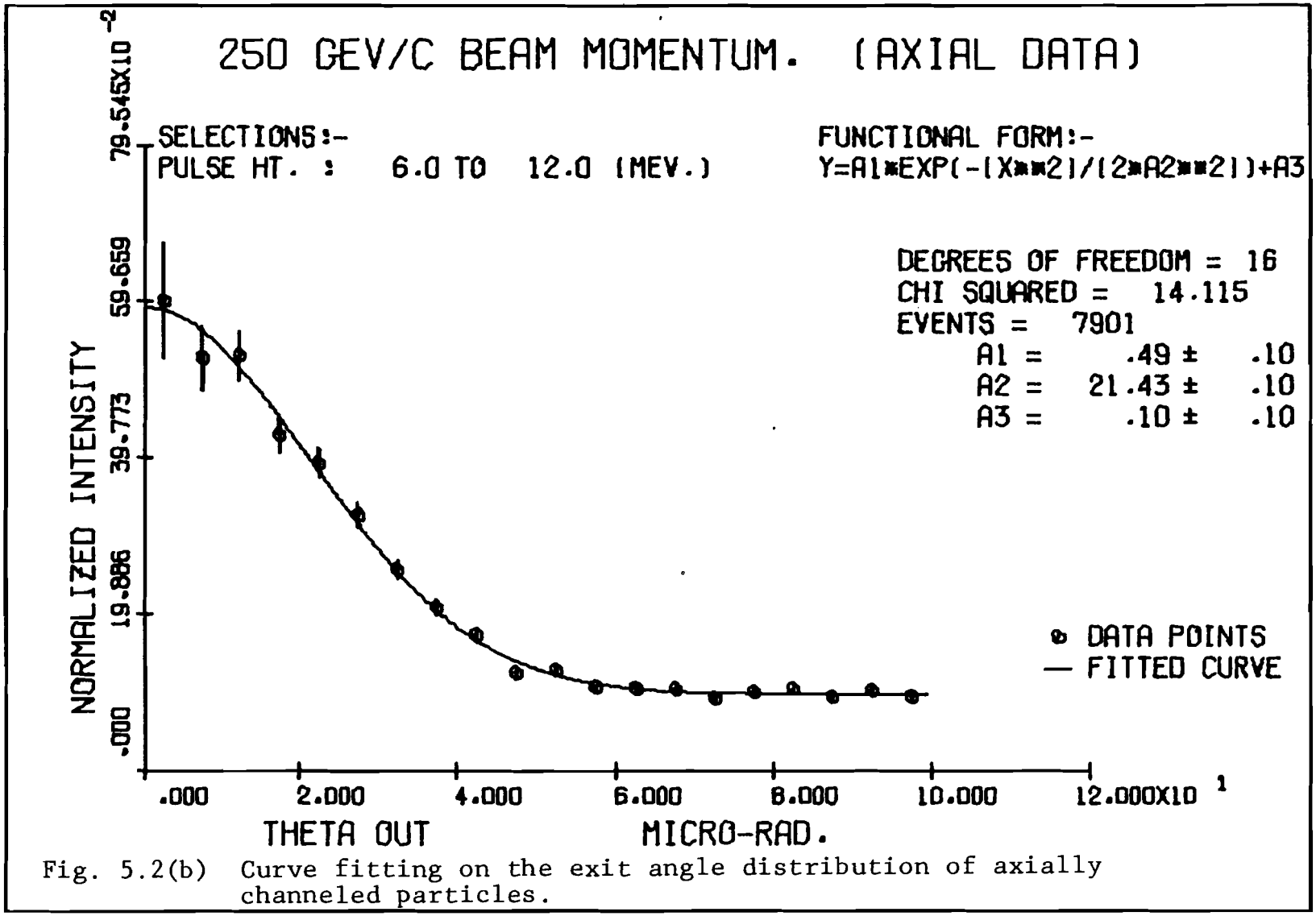

Fig. 5.2(b) Curve fitting on the exit angle distribution of axially channeled particles.

and the exit angles with respect to the <110> axis for 35, 100, and 250 GeV/c beam momenta. Figures 5.3(a) and (b) show such plots for 250 GeV/c particles. The mean energy loss was lower for smaller values of the incident and the exit angles, and increased to a constant random orientation value at around the critical angle, ψ_1<110>. Inverted gaussian profiles were fitted to the points and the widths of the profiles were extracted from the fitted curves.

The observed values of the width of the axial channeling distributions, σ_{obs}, obtained by the above two methods for 35, 100, and 250 GeV/c momenta are listed in Table 5.1. The beam spread due to the multiple scattering in the system, σ_{sys}, (cf. Table 4.4), was subtracted in quadrature from the observed width, σ_{obs}, to get the actual width of the channeling distribution, σ_{ch}, i.e.,

$$\sigma_{ch}^2 = \sigma_{obs}^2 - \sigma_{sys}^2 \qquad 5.1$$

The widths, σ_{ch}, were converted to Half Width at Half the Maximum height value (HWHM), $\psi_{\frac{1}{2}}$<110>, by multiplying them with $\sqrt{2\ln 2} = 1.177$.

The χ^2 value (a measure of the goodness of the fitted curve) was within the first standard deviation ($\sigma_{\chi^2} \simeq \sqrt{2n_D}$, where n_D is the number of degrees of

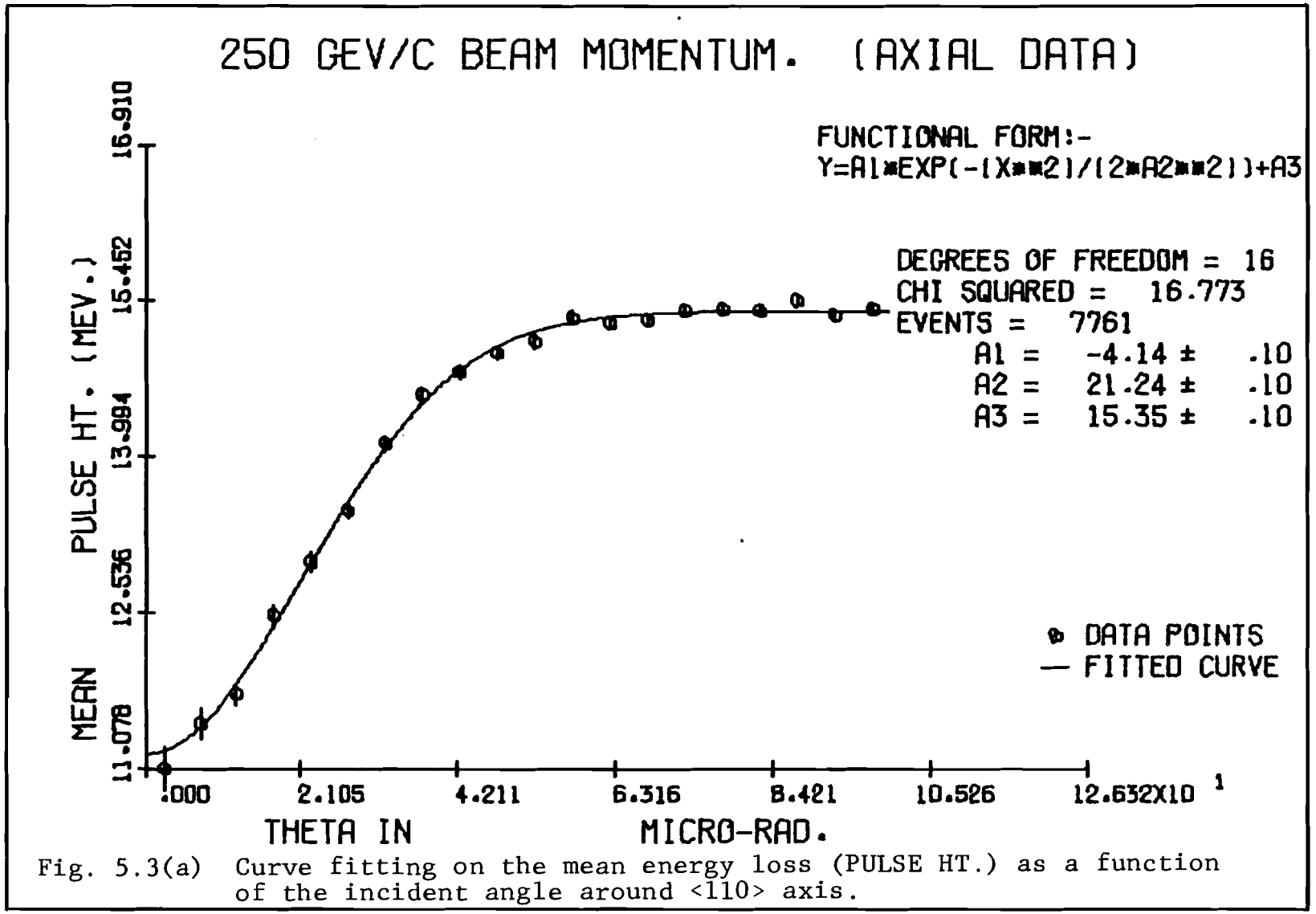

Fig. 5.3(a) Curve fitting on the mean energy loss (PULSE HT.) as a function of the incident angle around <110> axis.

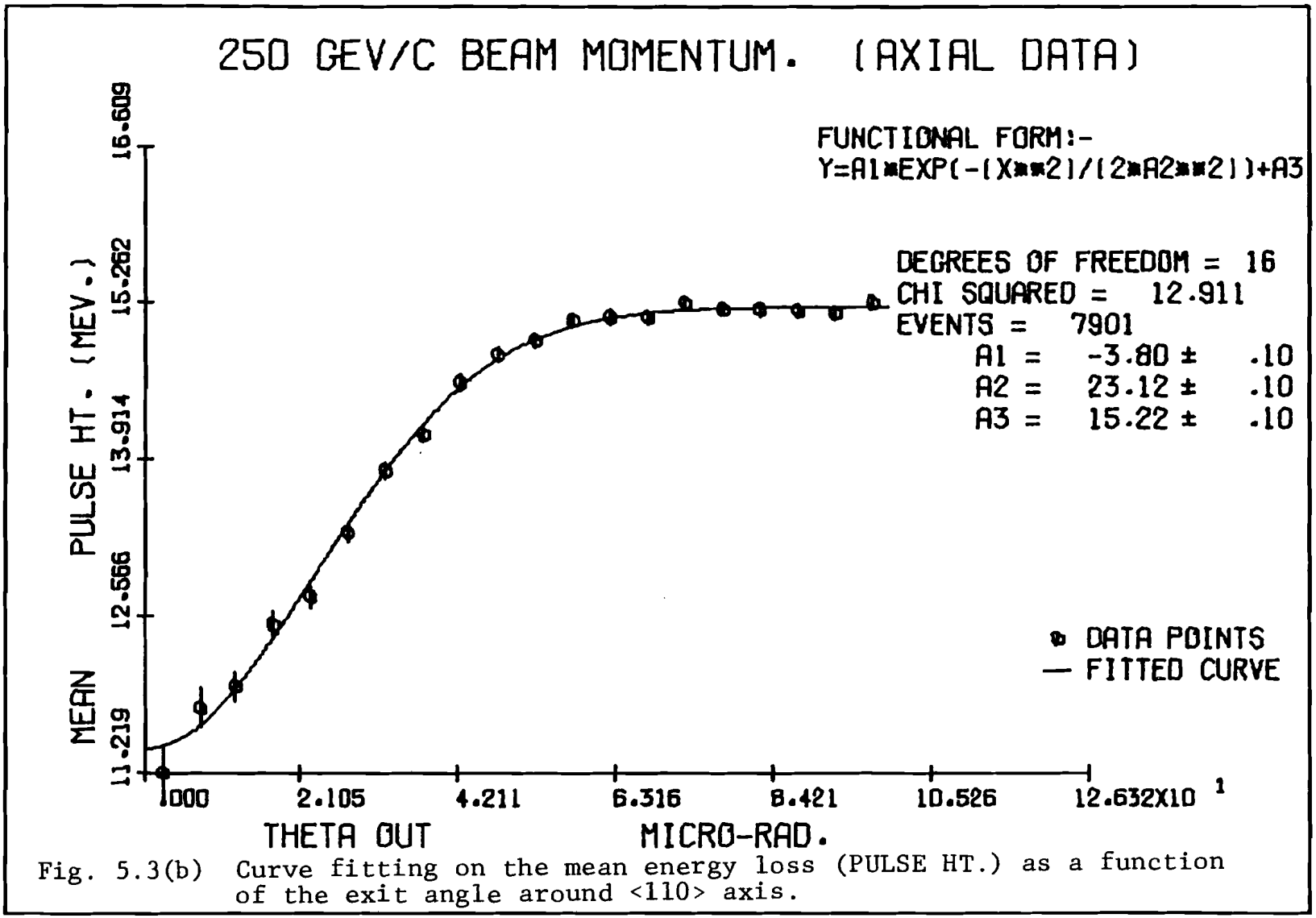

Fig. 5.3(b) Curve fitting on the mean energy loss (PULSE HT.) as a function of the exit angle around <110> axis.

Table 5.1 The HWHM for the axially channeled particle distributions in the incident and exit angle plane at 250, 100, and 35 GeV/c momenta.

Beam Momentum (GeV/c)	Variables	Selection	n_D	χ^2	σ_{obs} (micro-radians)
250	θ_{in} vs. Norm. Inten.	E:6-12 MeV	16	9	19.95±0.16
250	θ_{out} vs. Norm. Inten.	E:6-12 MeV	16	14	21.43±0.17
250	θ_{in} vs. $<\Delta E>$	None	16	17	21.24±0.17
250	θ_{out} vs. $<\Delta E>$	None	16	13	23.12±0.18
100	θ_{in} vs. Norm. Inten.	E:6-12 MeV	16	15	30.98±0.31
100	θ_{out} vs. Norm. Inten.	E:6-12 MeV	16	6	35.41±0.38
100	θ_{in} vs. $<\Delta E>$	None	16	17	32.64±0.15
100	θ_{out} vs. $<\Delta E>$	None	16	9	35.77±0.19
35	θ_{in} vs. Norm. Inten.	E:6-12 MeV	16	20	52.89±0.46
35	θ_{out} vs. Norm. Inten.	E:6-12 MeV	16	23	45.41±0.44
35	θ_{in} vs. $<\Delta E>$	None	16	24	51.23±0.18
35	θ_{out} vs. $<\Delta E>$	None	16	34	47.85±0.22

freedom) of the χ^2 distribution for 100 and 250 GeV/c data. The χ^2 value was beyond the first standard deviation interval for 35 GeV/c data and therefore the fitted curve in this case does not represent the distribution as well as for 100 and 250 GeV/c data.

The HWHM, $\psi_{\frac{1}{2}}\langle 110\rangle$, is proportional to the Lindhard critical angle, $\psi_1\langle 110\rangle$, i.e.,

$$\psi_{\frac{1}{2}}\langle 110\rangle = \propto\psi_1\langle 110\rangle \qquad 5.2$$

where $\propto$ is a constant, which incorporates the effect of temperature (shown to be negligible for this experiment; Sec. 2.1) and other imperfections and defects of the crystal. Its value is in the range of 1/2 to 1. Substituting the value of ψ_1 from Eq. 2.13 in Eq. 5.2 and using $E = \frac{1}{2}pv$ for the relativistic particles, one obtains:

$$\psi_{\frac{1}{2}}\langle 110\rangle = \frac{A}{\sqrt{pv}} \qquad 5.3$$

where $A = \propto\left[\frac{4Z_1Z_2e^2}{d}\right]^{\frac{1}{2}}$. Eq. 5.3 shows that $\psi_{\frac{1}{2}}\langle 110\rangle$ is inversely proportional to the square root of the energy of the beam particles (at relativistic energies $v \sim c$ and $E = \sqrt{p^2c^2+m^2c^4} \simeq pc$) and is independent of the masses of the beam particles. Thus the pions, kaons, and protons in the incident beam will have the same $\psi_{\frac{1}{2}}\langle 110\rangle$ value at the same beam momentum.

The $\psi_{\frac{1}{2}}$<110> value the Lindhard critical angle and their ratios, α, for 35, 100, and 250 GeV/c beam momenta are listed below:

	250 GeV/c	100 GeV/c	35 GeV/c
$\psi_{\frac{1}{2}}$<110> (micro-radians)	24.12±1.34	37.32±2.11	45.22±9.52
ψ_1<110> (micro-radians)	42.9	67.9	114.7
α	0.56±0.03	0.55±0.03	0.39±0.08

The momenta and the corresponding $\psi_{\frac{1}{2}}$<110> values for 35, 100, and 250 GeV/c data were fitted to the functional form of Eq. 5.3. The best value for the parameter was $\alpha = 0.51 \pm 0.14$.

The experimental $\psi_{\frac{1}{2}}$<110> values at 35, 100, and 250 GeV/c momenta are shown in Fig. 5.4 by open circles. The solid line in the figure is the Lindhard critical angle, ψ_1, for the <110> axis in Germanium crystal. The dashed line is the extrapolated curve obtained from $\psi_{\frac{1}{2}}$<110> value at 1.35 GeV/c momentum of the AARHUS-CERN-STRASBOURG group [Es77], using a $\frac{1}{\sqrt{pv}}$ dependence. The curve obtained from the best fit value of the parameter, α, falls almost on top of the extrapolated curve.

From the above considerations it is clear that the width of the distribution of the axially channeled

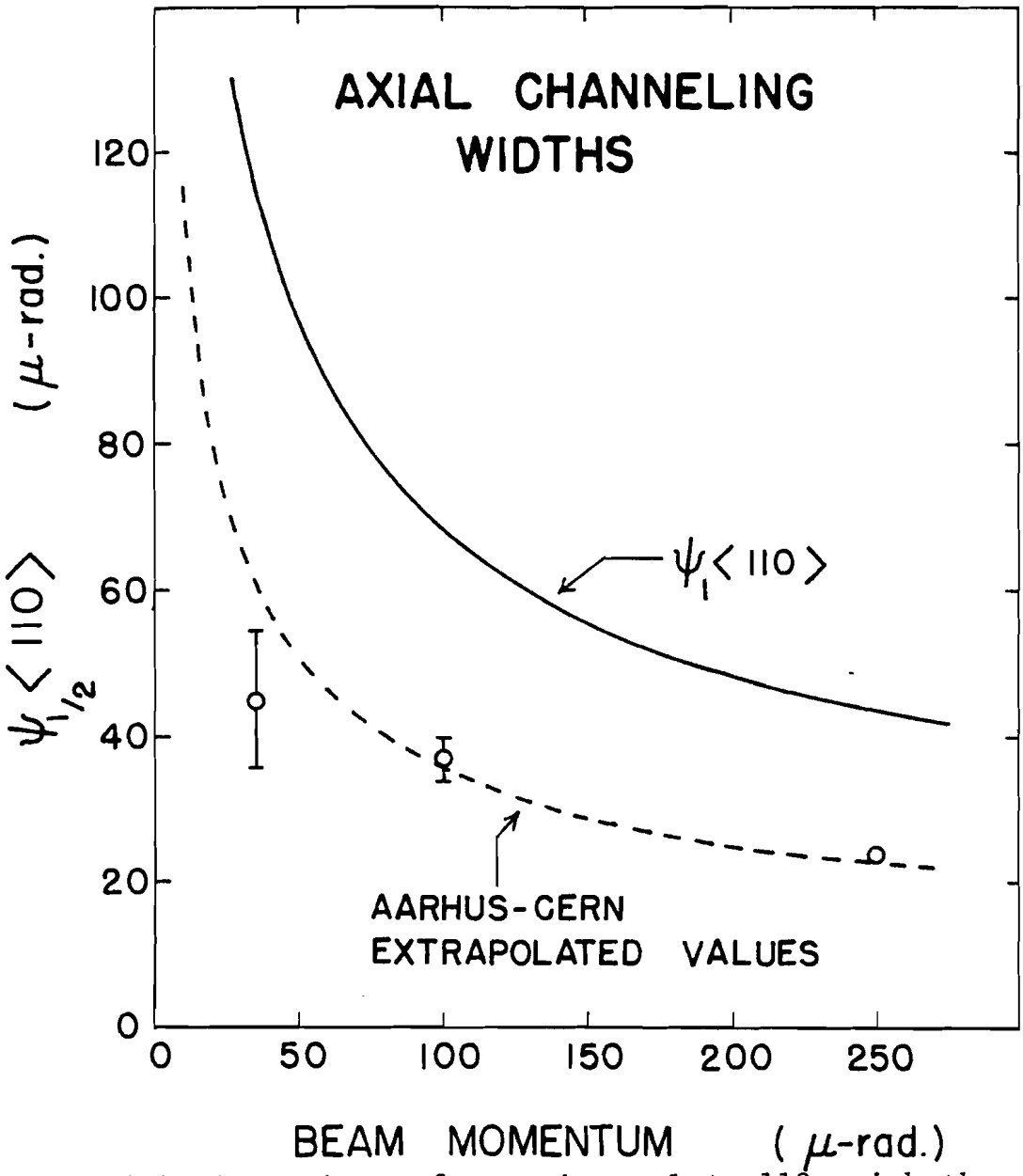

Fig. 5.4 Comparison of experimental $\psi_{\frac{1}{2}}$<110> with the extrapolated values (dashed line) obtained from the $\psi_{\frac{1}{2}}$<110> value of the AARHUS-CERN group at 1.35 GeV/c using a $1/\sqrt{pv}$ dependence. The Lindhard critical angle, ψ_1<110>, is also shown in the figure.

particles scales as $\frac{1}{\sqrt{E}}$ as predicted by Lindhard [Li65].

5.2 PLANAR CHANNELING

Some of the major low index crystallographic planes, parallel to the <110> axis in Germanium crystal, are shown in Fig. 5.5. The relative orientation of the planes is also indicated. The widest interplanar spacing is between (111) planes and therefore these planes should be most prominent among the planes indicated in the figure. The prominent planar ridges in Fig. 5.1 were hence identified as (111) planes.

A better identification of the various planes was obtained by integrating the events over the radial direction around the axis position and displaying the azimuthal angle distribution in the exit angle plane. These distributions for 35 and 100 GeV/c beam momenta are shown in Figs. 5.6 and 5.7, respectively. A selection on energy loss of 6 to 12 MeV was applied to pick out the channeled particles. The various peaks in the ϕ_{out} distribution were identified by looking at their relative intensities and positions. The relative angular spacing between the planes agrees very well with the values shown in Fig. 5.5.

It is a characteristic of the channeling distribution in the incident and exit angle plane that the planar ridges do not start at the base of the axial

MAJOR CRYSTALLOGRAPHIC PLANES

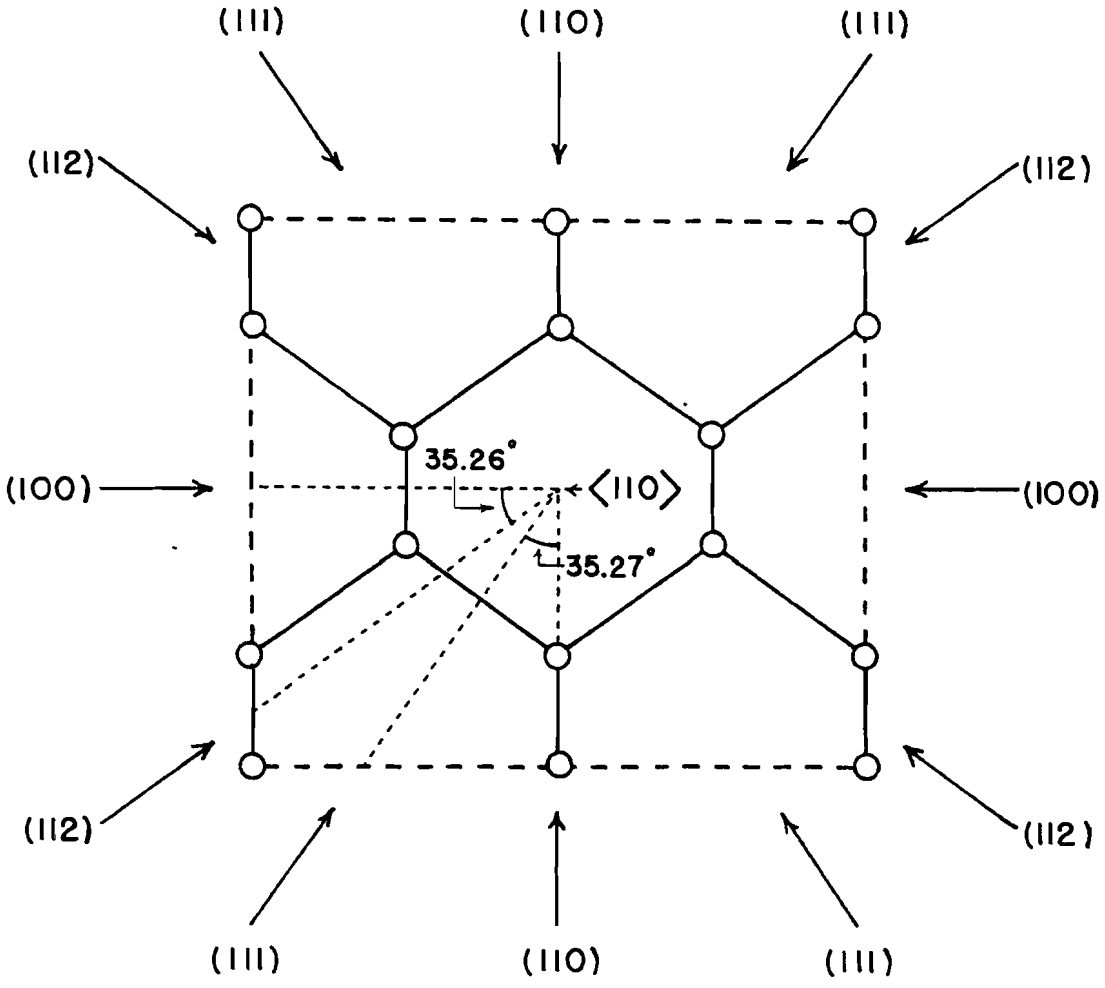

Fig. 5.5 The major crystallographic planes parallel to <110> axis in the Germanium crystal. The relative angles between the planes are also indicated.

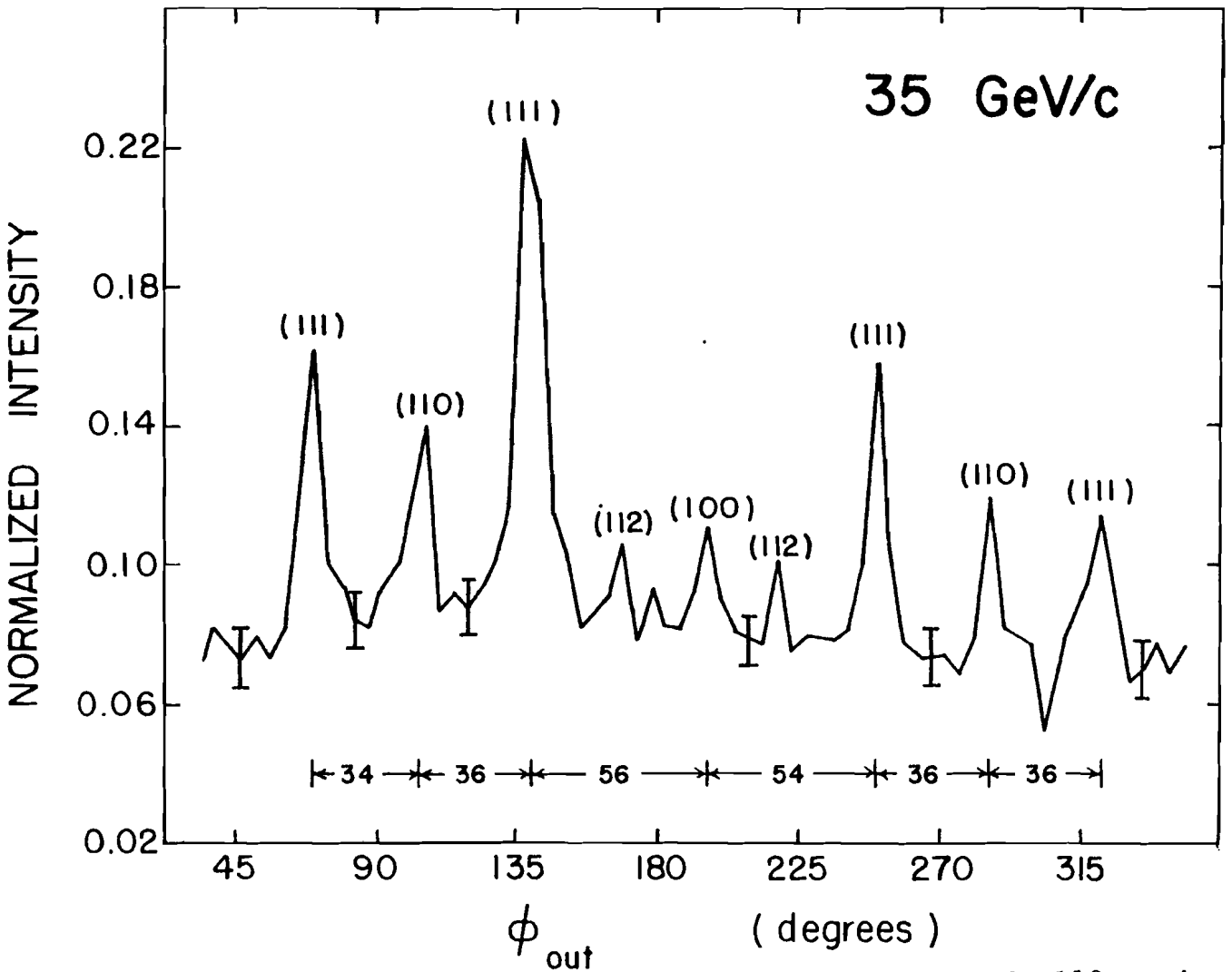

Fig. 5.6 Low index planar peaks in the ϕ_{out} distribution around <110> axis. The selection on energy loss was 6 to 12 MeV.

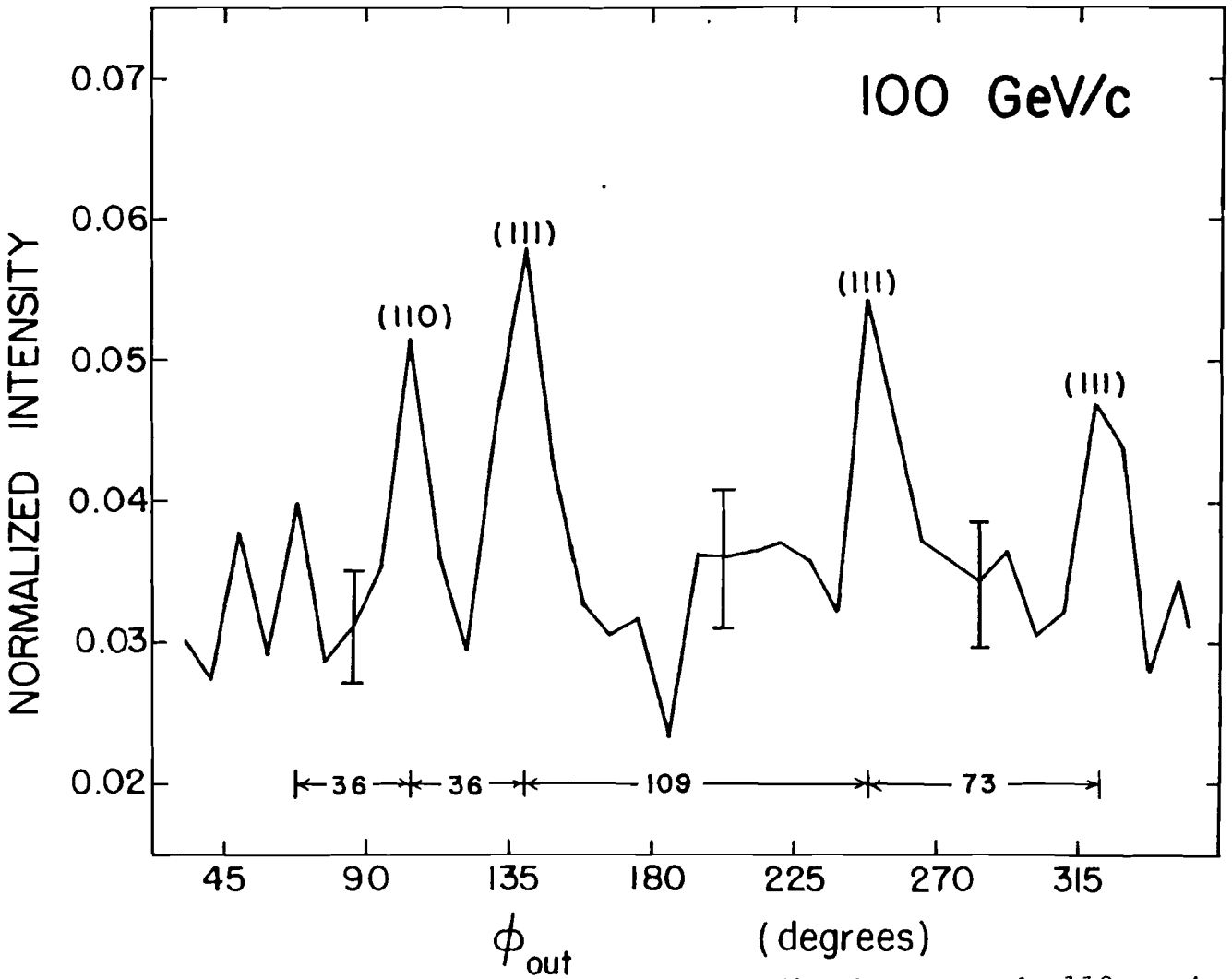

Fig. 5.7 Low index planar peaks in the ϕ_{out} distribution around <110> axis. The selection on energy loss was 6 to 12 MeV.

channeling peak. There is a gap between the base of the axial peak and the starting point of the planar ridges. This gap is wider for planes with narrower interplanar spacings. This is the reason for the absence of (100) and (112) planes in the ϕ_{out} distribution at 100 GeV/c beam momentum. The beam divergence was not wide enough to cover these planes (see Table 4.5 for beam spread). The beam divergence was even narrower at 250 GeV/c than at 100 GeV/c momentum, and therefore it was difficult to identify even the most prominent (111) planes in the ϕ_{out} distribution at 250 GeV/c beam momentum.

During the experimental running the planar channeling data were obtained by rotating the axial channeling peak out of the beam divergence and bringing the (111) plane within the beam spread. In the analysis the statistics were improved by rotating the incident and the exit angle planes such that the (111) planar ridge was parallel to the θ_x-axis, and then integrating the events along the θ_x-axis direction. The planar channeling distribution was then observed along the θ_y-axis.

A fixed selection of 6 to 12 MeV on the energy loss and a variable selection on the scattering angle was applied to pick out the channeled particles. Gaussian functions were fitted to the planar channeling

distributions and the widths, σ_{θ_y}, of the distributions were extracted from the fitted curves.

The planar channeling widths, as a function of the scattering angle selection, are plotted in Figs. 5.8(a) and (b). The widths leveled off for larger values of the scattering angle selection. The averages of the last three values for the θ_y^{in} and θ_y^{out} distributions were taken as the (111) planar channeling widths. The values obtained for 35 and 250 GeV/c data (planar channeling data were recorded for 35 and 250 GeV/c momenta only) were corrected for system resolution by subtracting the system resolutions from the planar channeling widths in quadrature as in the axial channeling case. The HWHM values, $\psi_{\frac{1}{2}}(111)$, of the planar channeling distributions were than obtained by multiplying them by $\sqrt{21n2} = 1.77$. The HWHM values are listed below:

	35 Gev/c	250 GeV/c
$\psi_{\frac{1}{2}}(111)$(micro-radians)	39.96±2.3	17.4±0.4

The Lindhard critical angle for planar channeling, $\psi_a(111)$, scales as $\frac{1}{\sqrt{pv}}$ (eq. 2.27 with E = ½pv substituted for relativistic particles). Consequently the planar channeling width (which is proportional to $\psi_a(111)$) should also scale as $\frac{1}{\sqrt{pv}}$, i.e.,

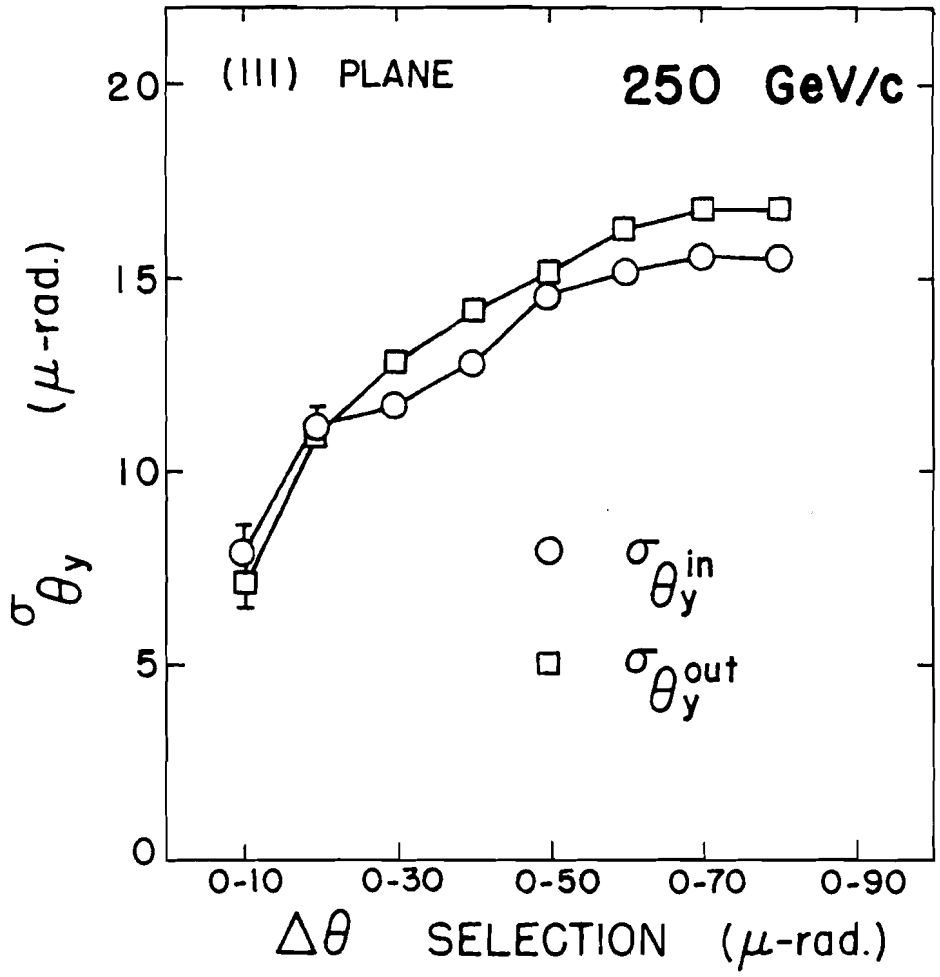

Fig. 5.8(a) The width of the (111) planar channeling distribution as a function of $\Delta\theta$ selection. The fixed selection on energy loss was 6 to 12 MeV.

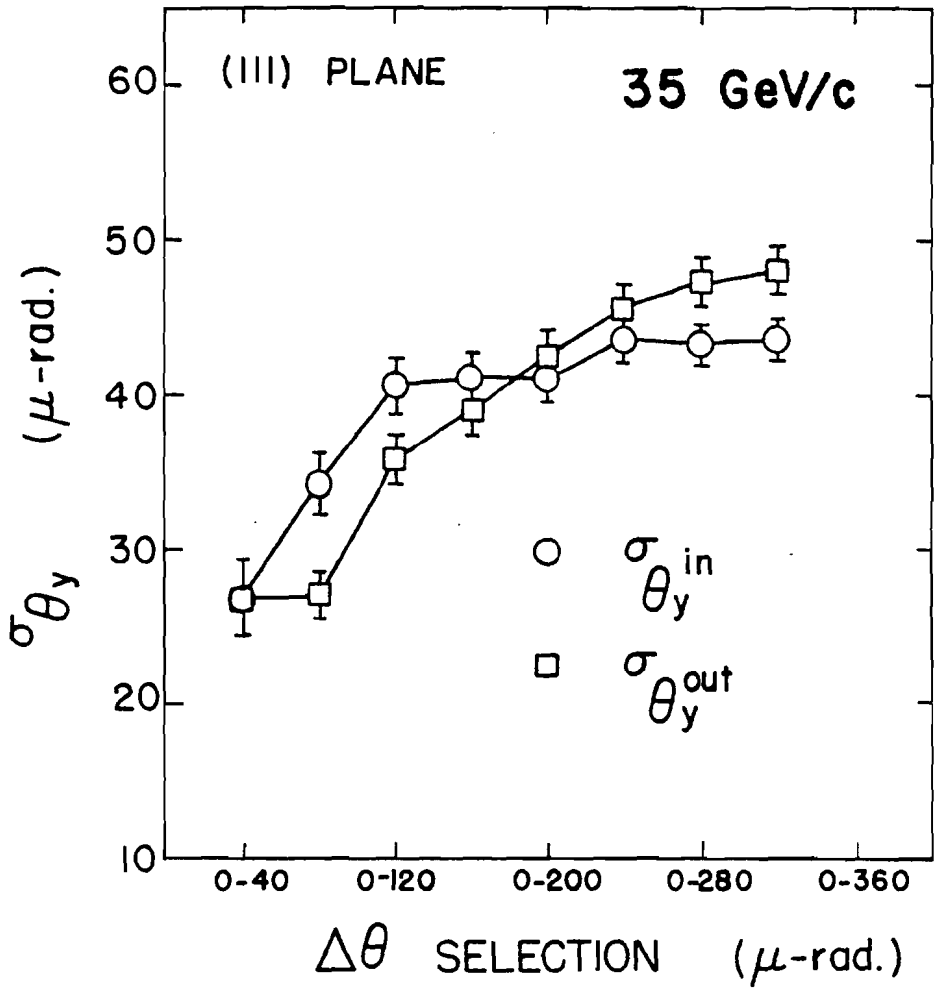

Fig. 5.8(b) The width of the (111) planar channeling distribution as a function of $\Delta\theta$ selection. The fixed selection on energy loss was 6 to 12 MeV.

$$\psi_{\frac{1}{2}}(111) = \frac{B}{\sqrt{pv}} \qquad 5.4$$

where B is a parameter to be determined from experimental results. The above functional form was fitted to the two $\psi_{\frac{1}{2}}(111)$ values at 35 and 250 GeV/c beam momenta. The best fit value of the fitting parameter was $B = 255.4 \pm 9.4\ \sqrt{GeV}$ radians. The fitted curve and the two data points are displayed in Fig. 5.9.

It is apparent from these considerations that the planar channeling widths also scale as $\frac{1}{\sqrt{E}}$ as predicted by Lindhard [Li65].

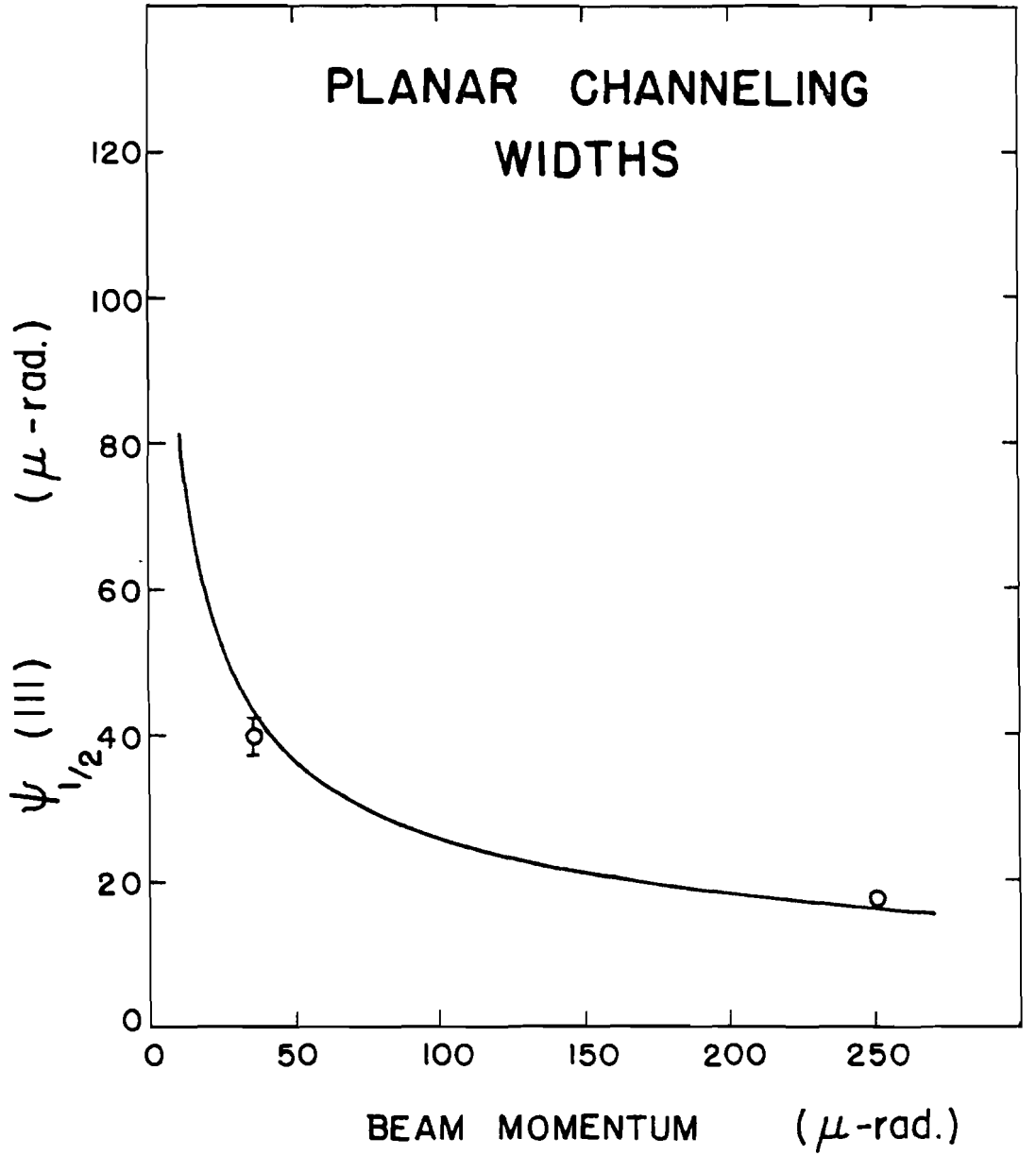

Fig. 5.9 The $\psi_1(11\bar{1})$ values (open circles) at 35 and 250 GeV/c beam momenta. The best fit curve of the form $B/\sqrt{pv}$ is drawn as a solid line.

CHAPTER 6

BLOCKING

It was mentioned in Sec. 2.3 that the ideal blocking experiment requires the particles to originate from the nuclei of the atoms in the strings in a crystal. The particles coming out from the nucleus would then be blocked from going along the string direction because of the intervening atoms (shadow effect) and a blocking dip would be observed in the exit angle plane.

This is the opposite of the channeling effect where particles, incident on a crystal at small angle to the crystal axis, have a greater probability of emerging at small angles with respect to the crystal axis direction.

A minimum exit angle, ψ_{min}<110>, with respect to the crystal axis direction was defined in Sec. 2.3. Its value was found to be 2.5 to 3.0 times the Lindhard critical angle for axial channeling, ψ_1<110>, in the 35 to 250 beam momentum range (cf. Sec. 2.3). The minimum angle was derived on the assumption of conservation of the transverse momentum. The thermal vibration of the atoms would cause the particles to be ejected from a region around the string, of radius equal

to the root mean square (rms) displacement of the atoms in the transverse plane. This would have the effect of smearing out the exit angle distribution and decreasing the angular width of the blocking dip.

The particles that were incident at a large angle to the axis would penetrate very close to the nuclei of the lattice atoms. The small impact parameter collision would lead to greater energy loss of the incident particles. The emerging particles would lose, to a large extent, their sense of initial direction and behave as if they originated from within a small distance of the lattice site. This situation would be similar to that of the particles ejected from a thermally vibrating nuclei and a blocking dip would be observed in the exit angle distribution. The width of the blocking dip would be smaller in this case than in the case of the particles originating at the stationary lattice site.

A larger than average energy loss for the particles that undergo many small impact parameter collisions, was used to identify the particles that had a greater chance of exhibiting the blocking effect. These particles would come very close to the nuclei of the atoms in the string and would be blocked from scattering out along the string direction because of the intervening atoms.

The average energy loss of the positive beam particles at 35, 100, and 250 GeV/c beam momentum values for random orientation of the 2 cm thick Germanium crystal was found to be the same and equal to 15.65 ± 0.05 MeV (see Sec. 9.2). Two ranges of energy loss, greater than the mean value, i.e., 16 to 20 MeV and 18 to 26 MeV, were used to select particles that had a greater probability of showing a blocking effect. This overlap in the two ranges of the selection window was used to improve statistics. The channeled particle contamination was less than 2.5% as observed from the ratios of the number of events in the axial channeling and random orientation distributions of the energy loss in the above mentioned ranges of the selection windows.

The exit angle distribution was integrated along the azimuthal angle direction around the <110> axis position to improve statistics. The distribution was normalized by dividing it by the similar exit angle distribution with no selection applied. Blocking dips were observed in the exit angle distribution. These blocking dips are not reflections of the axial channeling peak distributions obtained with low energy loss selection of 6 to 12 MeV because of the following reasons:

(a) A flat distribution in the exit angle is obtained

for intermediate energy loss selection.

(b) The widths of the distributions for axial channeling (cf. Sec. 5.1) and the blocking distribution (Table 6.1) obtained by the method outlined above are different.

(c) The fraction of particles in the channeling peaks are very small compared to the fraction of particles missing from the blocking dip.

A gaussian curve was fitted to the normalized exit angle distributions with the selections on energy loss indicated above. The data points and the fitted curves for the two different selections at 100 GeV/c beam momentum are shown in Figs. 6.1(a) and (b). The curve fitting was also done to the data at 35 and 250 GeV/c momenta. The half width at half maximum (HWHM) angles, $\psi_{\frac{1}{2}}'<110>$, of the blocking distributions were extracted from the fitted parameters. The $\psi_{\frac{1}{2}}'<110>$ values are listed in Table 6.1. It is seen from the table that the $\psi_{\frac{1}{2}}'<110>$ values for the two different energy loss selection ranges do not differ very much from each other at each momentum value.

The maximum difference was for 35 GeV/c data and this was because of the bad system resolution for angle measurement at this beam momentum (cf. Table 4.4).

The width of the blocking dip, $\psi_{\frac{1}{2}}'<110>$, the criti-

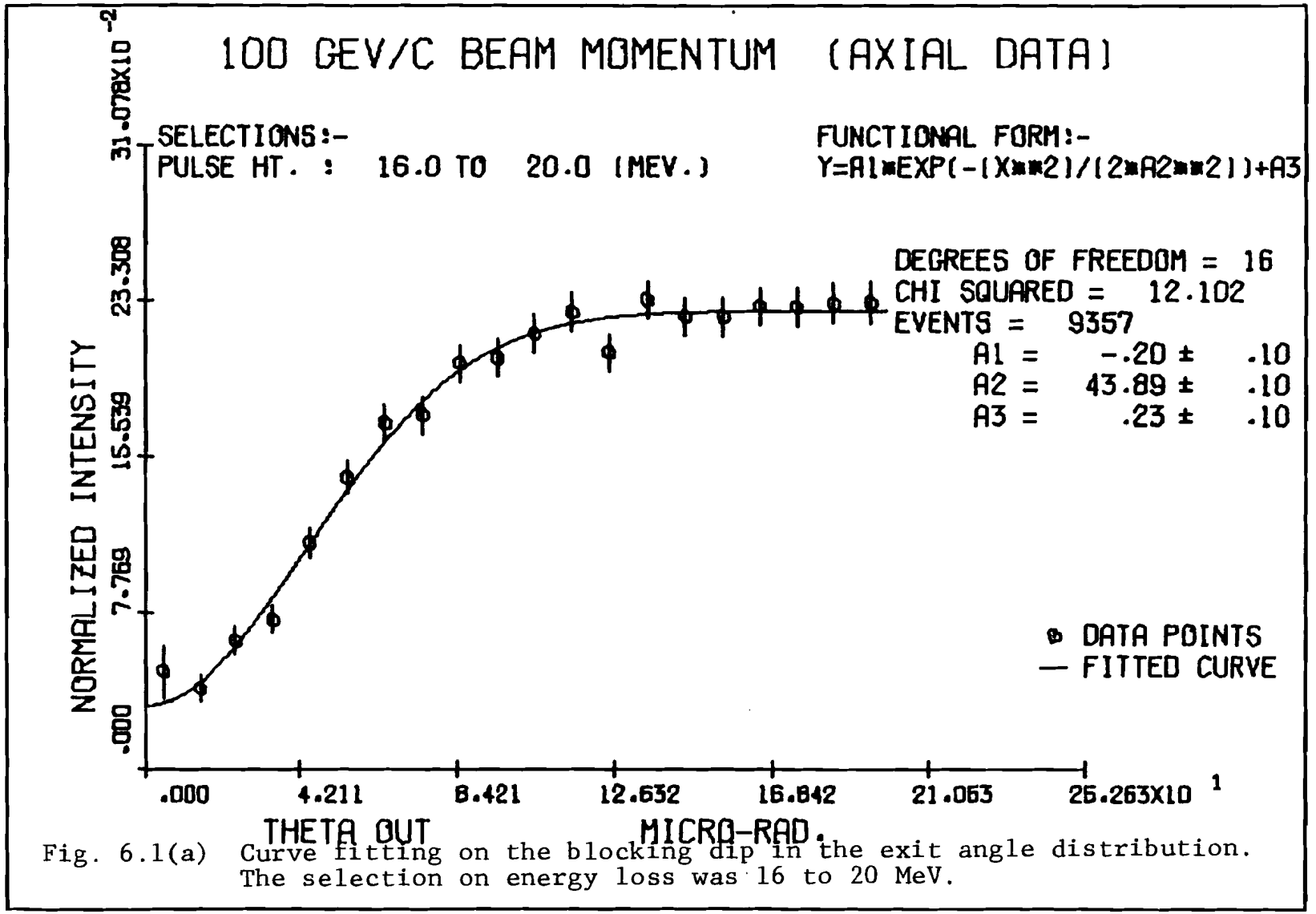

Fig. 6.1(a) Curve fitting on the blocking dip in the exit angle distribution. The selection on energy loss was 16 to 20 MeV.

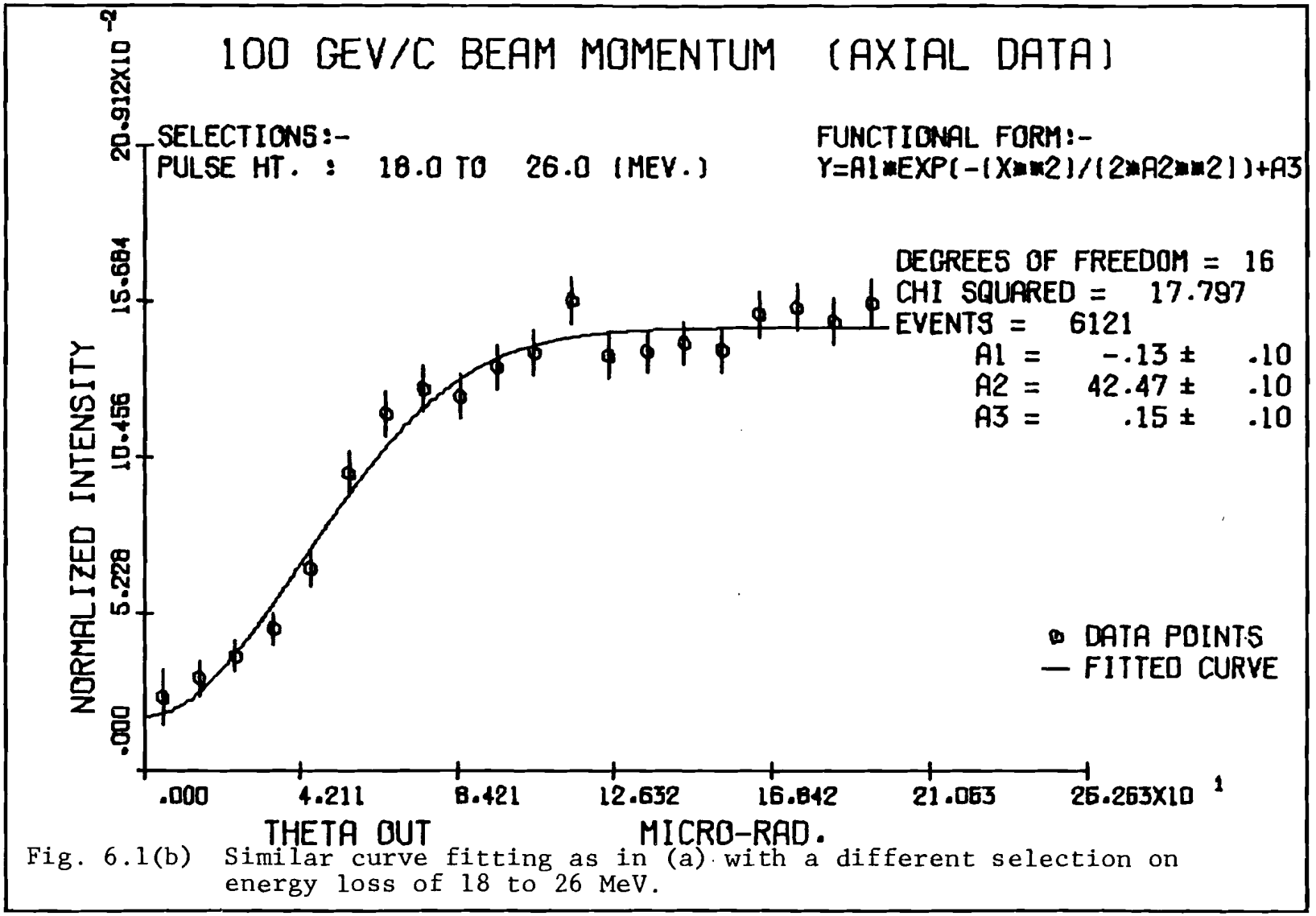

Fig. 6.1(b) Similar curve fitting as in (a) with a different selection on energy loss of 18 to 26 MeV.

Table 6.1 Blocking dip widths in the exit angle distributions.

Beam Momentum (GeV/c)	Selection on Energy Loss (MeV)	χ^2 (n_D = 21)	$\psi_{\frac{1}{2}}'$ <110> (micro-radians)
250	16 to 20	11	33.05±0.21
250	18 to 26	12	31.76±0.24
		Mean =	32.4±0.9
100	16 to 20	20	53.07±0.41
100	18 to 26	27	52.08±0.34
		Mean =	52.6±0.7
35	16 to 20	20	67.71±0.54
35	18 to 26	16	73.17±0.74
		Mean =	70.4±3.9

cal angle, ψ_1<110>, and their ratios, α', at the 35, 100, and 250 GeV/c beam momentum values are listed below:

	35 GeV/c	100 GeV/c	250 GeV/c
$\psi_{\frac{1}{2}}'$<110> (micro-radians)	70.4±3.9	52.6±0.7	32.4±0.9
ψ_1<110> (micro-radians)	114.7	67.9	42.9
α'	0.61±0.03	0.77±0.01	0.76±0.02

The α' value at 35 GeV/c is different from the value at 100 and 250 GeV/c because the exit angle measurement had a larger percentage error due to system resolution at 35 GeV/c than at 100 and 250 GeV/c momenta (see Table 4.4).

Taking into account the large error in angle measurement at 35 GeV/c momentum one can say that α' is approximately constant at the three above mentioned beam momentum values and therefore the $\psi_{\frac{1}{2}}'$<110> value is proportional to the critical angle of channeling, ψ_1<110>, and hence inversely proportional to $\sqrt{E}$.

CHAPTER 7

DIFFUSION

The word diffusion used here means the changes that take place in the transverse motion (with respect to the crystal axis direction), of a beam of particles passing through a crystal, due to processes which are statistical in nature.

The motion has two components, the radial and the azimuthal. The changes in the azimuthal distribution are due to the random reflections of the beam particles from the parallel strings of atoms. The larger the number of such collisions, the greater are the chances of producing equilibrium in the azimuthal distribution. The radial distribution changes because of the local force fluctuations due to the thermal vibrations of the atoms on the string, the periodic nature of the actual potential due to the individual atoms on the string, impurities, dislocations, defects, etc. This tends to increase the mean transverse energy of the beam as it penetrates deeper into the crystal. It also increases the mean square spread of the transverse momentum of the beam.

The radial and the azimuthal angles that are used

in describing the transverse motion of the particles are shown in Fig. 7.1.

The particles associated with a particular value of the incident radial angle, θ_{in}, are indicated by the annular ring with a small width around θ_{in}. Similarly the particles associated with a value of the exit angle, θ_{out}, are shown as θ_{out} annular ring. The difference between θ_{out} and θ_{in} is the radial scattering angle, $\delta\theta$, which may be positive as well as negative.

The mean of the incident angle, θ_{in}, or the exit angle, θ_{out}, is found by summing the product of the number of particles in the annular ring with the value of the angle for that ring and dividing the sum by the total number of events in the distribution. The mean of the square of the distribution of the incident or the exit angle is also calculated in a similar manner.

The particles falling within a small angle wedge around the azimuthal incident angle, ϕ_{in}, and exit angle, ϕ_{out}, are associated with ϕ_{in} and ϕ_{out} angles, respectively. The azimuthal scattering angle, $\Delta\phi$, is the difference between ϕ_{out} and ϕ_{in}. The mean and the mean square spread of the azimuthal angles are calculated in a manner similar to the corresponding quantities for radial angles.

The relevant formulas and equations describing

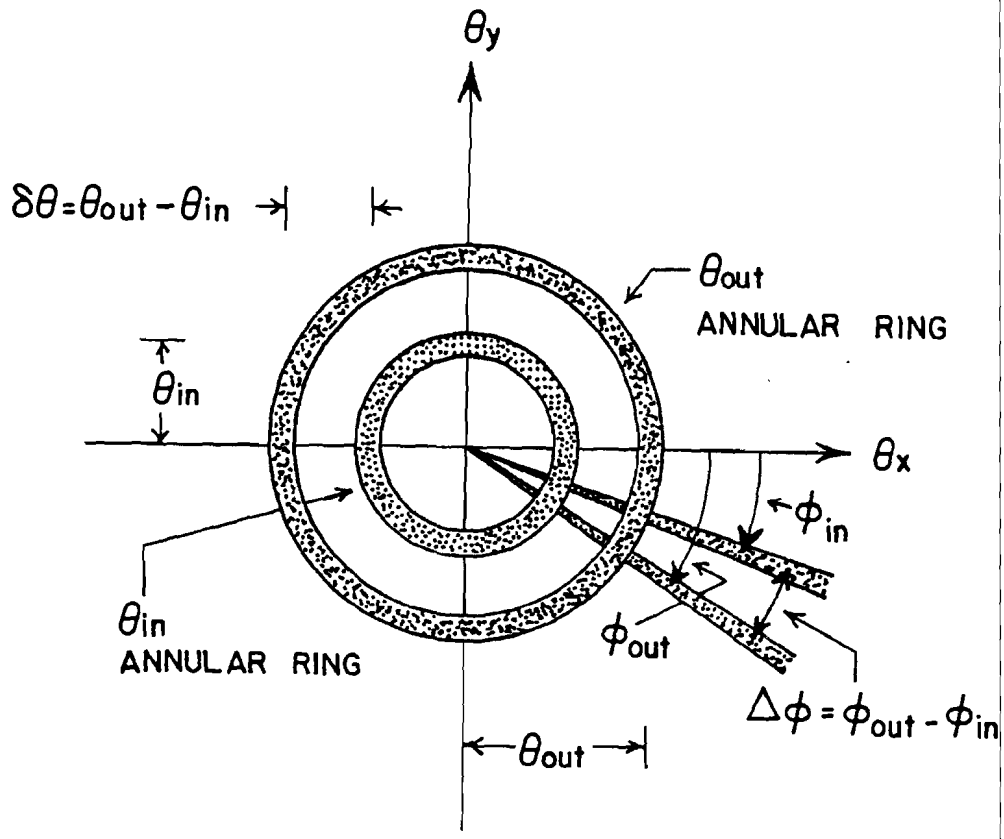

Fig. 7.1 The angle plane showing the radial and the azimuthal components of the incident and the exit angle of the beam particles. The origin is along <110> axis direction.

the azimuthal and the radial distribution of the channeled particles have been given in Secs. 2.4 and 2.5. The results of the diffusion on the transverse motion of a composite beam of positive particles passing through a 2 cm thick Germanium crystal, in the neighbourhood of <110> axis direction, for 35, 100, and 250 GeV/c beam momenta are presented in the following sections.

7.1 AN OVERVIEW

A pictorial and qualitative behaviour of the 250 GeV/c beam particles traversing the Germanium crystal, in the vicinity of the crystal axis direction, is presented in Figs. 7.2(a) to (h).

These figures represent the distribution of events in the exit angle plane. The crystal axis direction is at the origin of the coordinate system and it is indicated by a cross in the figures. The shaded area represents the selection on the incident angle of the beam. This type of selection represents a beam with a well defined initial transverse momentum and energy.

The selection in the Y-component of the projected incident angle is the same in all the eight configurations in Fig. 7.2, i.e., -20.0 to 20.0 micro-radians. The selection on the X-component is 40 micro-radians wide and its lower limit is shifted by 20 micro-radians from one configuration to the next, starting at the origin in Fig. 7.2(a).

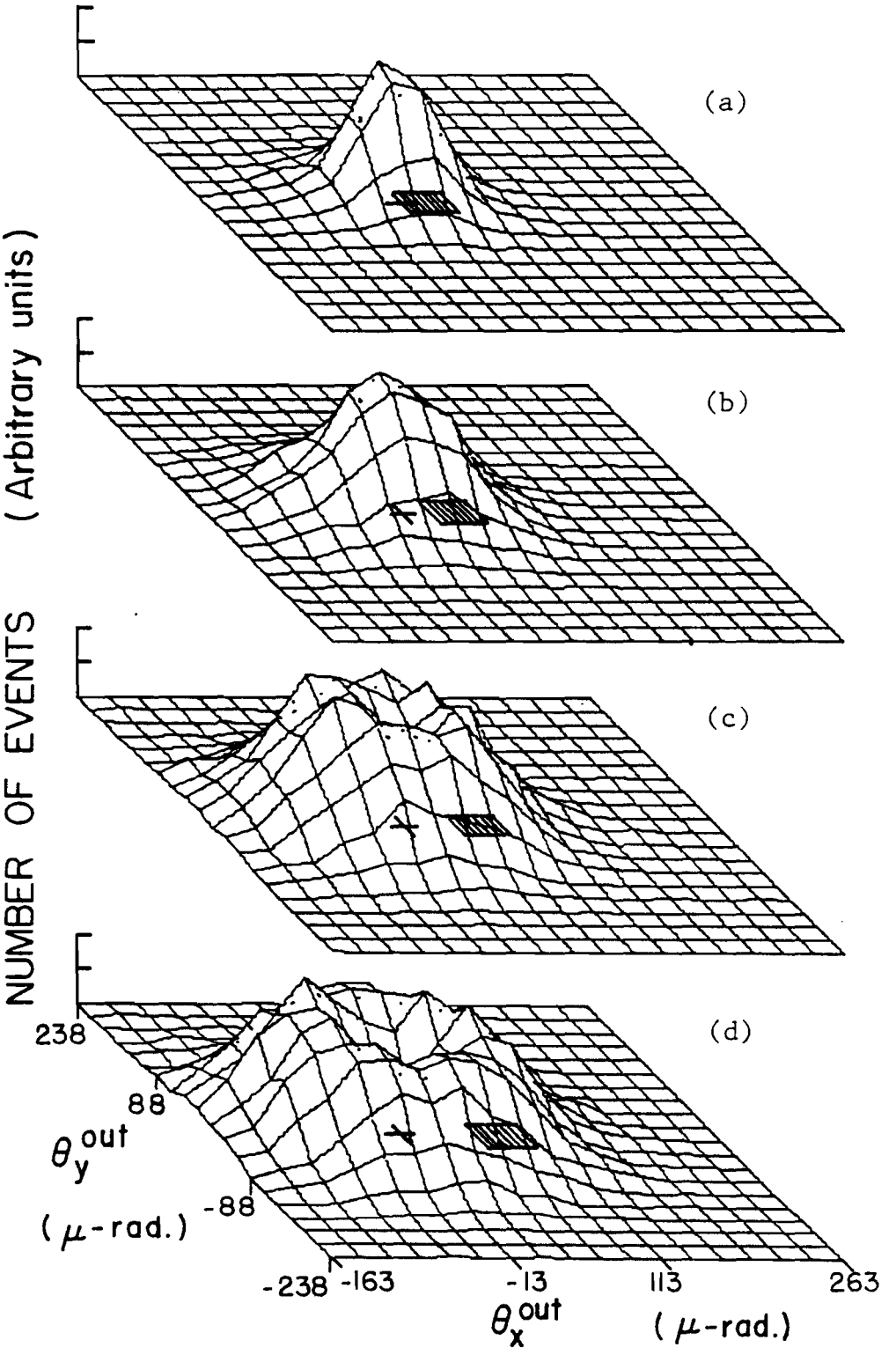

Fig. 7.2 (a) to (h) The distribution of particles in the exit angle plane. The cross indicates the <110> axis position and the shaded area represents selection in the incident angle plane.

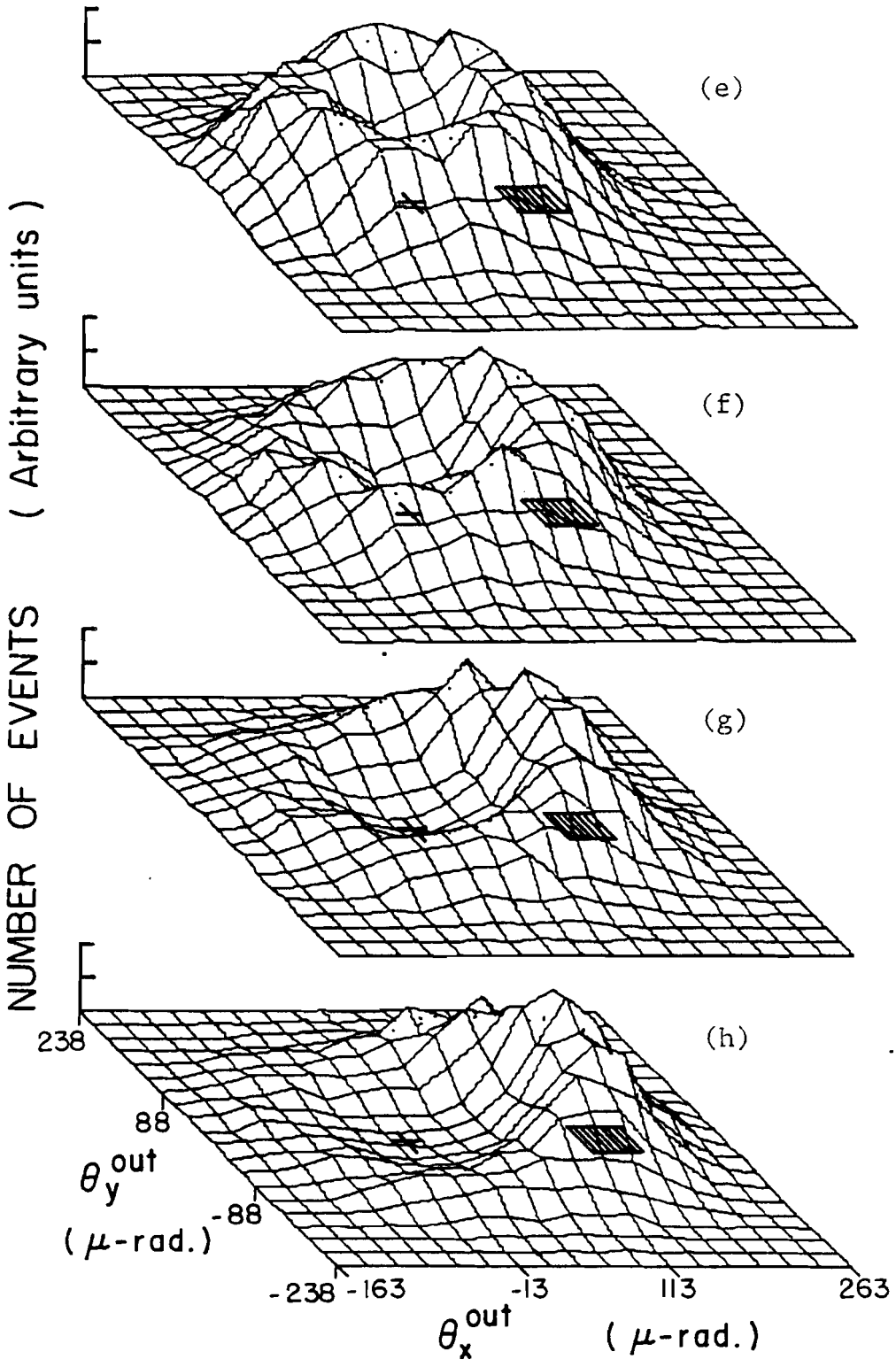

Fig. 7.2 (Continued)

The first two configurations, (a) and (b), show a filling of the region near the axis position. The beam distribution was uniform around the crystal axis even though the selection on incident angle was on one side of the axis position. Since the selection was within the critical angle for axial channeling (ψ_1<110> = 42.9 micro-radians for 250 GeV/c beam on Germanium crystal), it was expected that the large number of random elastic scatterings with parallel strings of atoms would produce statistical equilibrium in the azimuthal angle distribution around the axis position. The broader distribution in the (b) configuration indicates greater radial scattering near the critical angle of channeling.

The incident angle selections for configurations (c) and (d) were in the 0.93 ψ_1 to 2.3 ψ_1 range. This is the region where particles are quasi-channeled, i.e., the particles experience a few correlated collisions with the strings and then get dechanneled and behave as a random beam (random beam meaning a beam penetrating a crystal in random orientation, i.e., an orientation far away from any major low index crystal axes or planar directions). The first few correlated collisions with the strings, for a large number of beam particles, was enough to produce equilibrium distributions in the azimuthal angle and resulted in the dough-

nut shaped ring distributions shown in the figures. The spread of the beam in the radial direction was the same in both the configurations. The production of such a ring shaped distribution is known as the "doughnut" effect.

In Figs. 7.2(e) to (h) there was no longer a complete equilibrium in the azimuthal angle distribution around the axis position. But it is interesting to note that the string effect persists (to a lesser degree) even at incident angle equal to four times the critical angle, ψ_1. As the incident angle selection window shifted away from the axis position, fewer particles were quasi-channeled and the distribution became peaked along the beam direction. The beam spread remained constant in the radial direction for all the configurations.

These eight pictorial representations of the behaviour of the beam tend to indicate that the string of atoms, along any major crystal axis direction, has a very strong influence on the azimuthal component of the transverse motion of the beam. This influence leads to a complete equilibrium in the transverse motion for the beam particles incident in the range of zero to $2\psi_1$ with respect to the crystal axis direction. The influence of the string decreases beyond $2\psi_1$ but is still detectable at $4\psi_1$. The radial component of the trans-

verse motion of the beam, on the other hand, is affected very little by the string of atoms for incident angles greater than the critical angle ψ_1.

The "doughnut" effect (which results from the statistical equilibrium of the azimuthal component of the transverse motion) was also observed, to a lesser extent, in 100 and 35 GeV/c data. The effect was least prominent at 35 GeV/c beam momentum because the radial scattering spread of the beam at that beam momentum value was twice the critical angle, and the channeling axis region filled up even with the incident angle selection window at $2\psi_1$.

7.2 AZIMUTHAL DIFFUSION

The azimuthal distribution function, $A(\phi,T)$, for the channeled and the quasi-channeled beam particles is given by Eq. 2.35. This is a function of the azimuthal angle, ϕ, and a dimensionless parameter, T, which is a measure of the crystal thickness (Eq. 2.36). The values of the parameter, T, for particles incident at the critical angle, ψ_1<110>, on the 2 cm thick Germanium crystal for 35, 100, and 250 GeV/c data are:

($\psi = \psi_1$)	35 GeV/c	100 GeV/c	250 GeV/c
T =	1407.6	833.3	526.5

With the above values for T it can be determined that one obtains a constant value of $1/2\pi$ for the

distribution function, $A(\phi,T)$, independent of ϕ. This indicates that the beam particles attain equilibrium in the azimuthal angle distribution for the channeled and quasi-channeled particles. This is observed in the pictorial description presented in the previous section.

The range of the incident angle for which there is complete equilibrium in the azimuthal angle distribution was obtained by looking at the root mean square (rms) spread, $\langle\Delta\phi^2\rangle^{\frac{1}{2}}$, in the aximuthal scattering angle distribution. A flat distribution in the scattering angle, $\Delta\phi$, between $-\pi$ and π would give the following value for $\langle\Delta\phi^2\rangle^{\frac{1}{2}}$, i.e.,

$$\langle\Delta\phi^2\rangle^{\frac{1}{2}} = \frac{\int_{-\pi}^{\pi} \Delta\phi^2 d\Delta\phi}{\int_{-\pi}^{\pi} d\Delta\phi} = 1.813 \qquad 7.1$$

Figure 7.3 shows the rms spread of $\Delta\phi$ at the three different beam momentum values. The solid line is the expected value for the equilibrium distribution. The $\langle\Delta\phi^2\rangle^{\frac{1}{2}}$ values are plotted as a function of the ratio of the incident angle and the Lindhard critical angle, $\psi_1\langle 110\rangle$, so that the effects depending on the critical angle can be compared for 35, 100 and 250 GeV/c data.

From Fig. 7.3 it is clear that there was statistical equilibrium in the azimuthal scattering angle

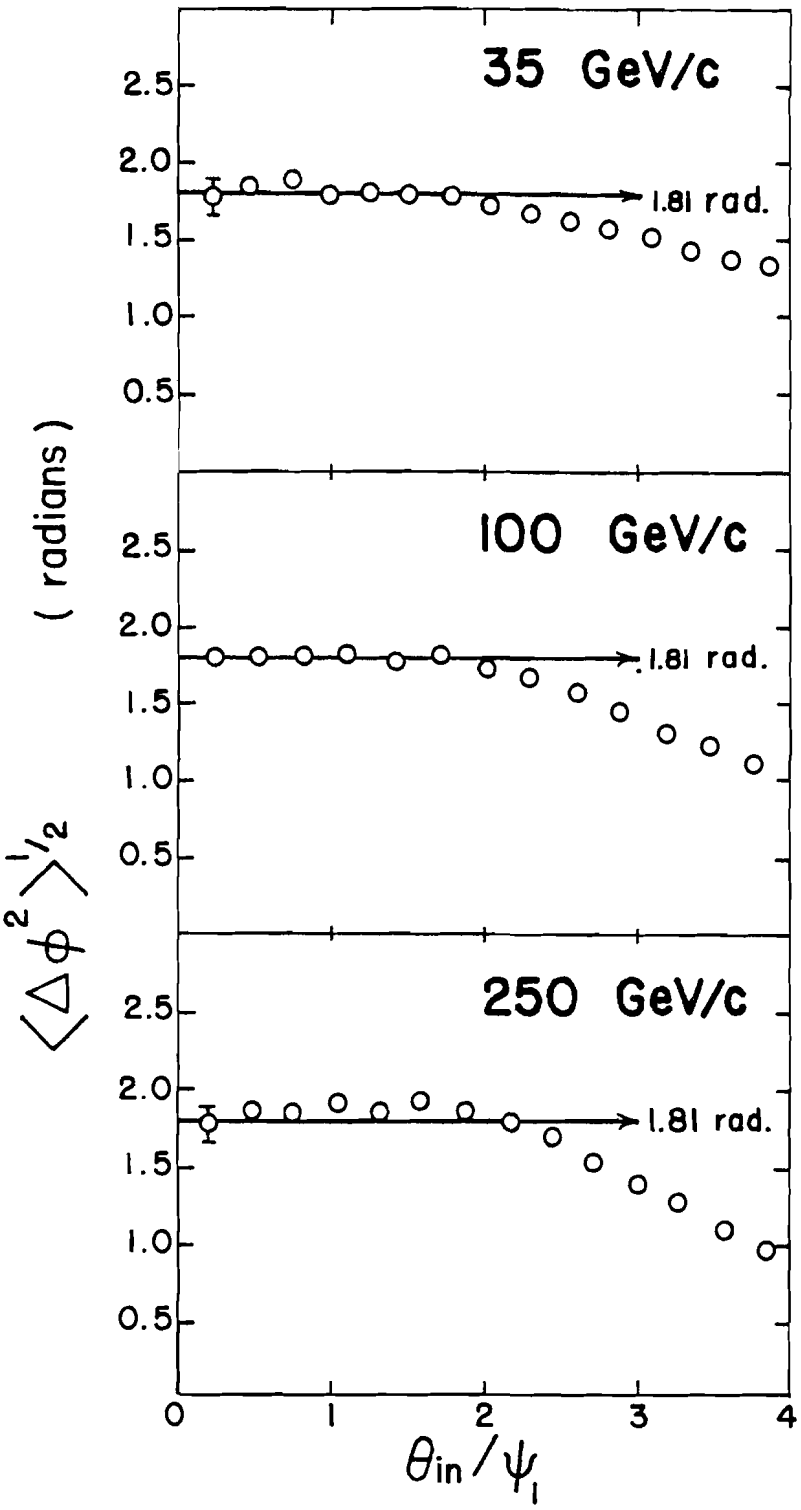

Fig. 7.3 Comparison of the rms spread of the azimuthal scattering angle distribution. The expected value of 1.81 for uniform distribution in $\Delta\phi$ is also shown.

distribution for particles incident in the range of zero to $2\psi_1$<110>, at the three different beam momentum values. Here again is an indication that the quasi-channeled particles also achieve statistical eqiulibrium in their azimuthal angle distribution.

A rough estimate of the mean free path, $\lambda_\perp$, for the channeled particles has been given by Lindhard [Li65] as:

$$\lambda_\perp = \frac{4}{\pi^2 Nda\psi_1} \left(\frac{\psi}{\psi_1}\right) \qquad 7.2$$

The mean free path is the distance in which the channeled particles, on the average, collide (point at which its momentum "reverses") with a string of atoms in the crystal. It is proportional to the incident angle, ψ, that the beam particle makes with the axis direction. The $\lambda_\perp$ value for $\psi = \psi_1$ at the three beam momenta are:

($\psi = \psi_1$)	35 GeV/c	100 GeV/c	250 GeV/c
$\lambda_\perp$ (micron)	14.2	23.9	37.8

The particles that are incident at very small angles to the crystal axis direction will have shorter mean free paths. Since a few collisions with the strings of atoms are enough to produce all possible azimuthal scattering angles between $-\pi$ and π, therefore, these particles will attain equilibrium in their transverse

motion in the first few microns of penetration in the crystal. But for angles up to and beyond the critical angle the mean free path is still much less than the 2 cm thickness of the crystal used in this experiment.

Thus the 2 cm thick Germanium crystal used in this experiment was more than adequate in all respects to produce statistical equilibrium in the transverse motion of the beam. In fact, the crystal was a little too thick for studying channeling at 35 GeV/c momentum. The random multiple scattering angle spread was 4 to 5 times larger than the critical angle, for the 2 cm thick Germanium crystal (see Chapter 8). Therefore the masking effect of the multiple scattering concealed some of the interesting effects of channeling that were seen at 250 GeV/c beam momentum.

7.3 RADIAL DIFFUSION

The theoretical description of the diffusion of transverse momentum and transverse energy, for axial symmetry, has already been given in Sec. 2.5.

Two major diffusion processes take place when a beam of particles with an initially well defined transverse momentum and energy penetrates a crystal along a major crystal axis direction. In the first process, the mean value of the transverse energy diffuses outward from the crystal axis direction. This process

is governed by the diffusion equation 2.39. Secondly, the transverse momentum itself spreads around its mean value as the beam of particles progresses through the crystal. This spread is related to the diffusion function.

7.3.1 The diffusion function (change in the transverse momentum spread

The relation between the diffusion function, $D(P_\perp)$, and the mean square spread of the transverse momentum is given by Eq. 2.40 (and Eq. 2.41 in terms of the radial angle ψ). The term $\delta<(\psi-<\psi>)^2>$ in Eq. 2.41 may be expressed as a function of the measurable angles θ_{in} and θ_{out} as follows:

$$\delta<(\psi-<\psi>)^2> \simeq <(\theta_{out}-<\theta_{out}>)^2> \qquad 7.2$$

Substituting this value in Eq. 2.41 and also replacing E by $p^2/2M_1$ one gets for the diffusion function:

$$D(\theta_{in}) \simeq \frac{p^2}{2\Delta z} <(\theta_{out}-<\theta_{out}>)^2> \qquad 7.3$$

where Δz is the thickness of the crystal. For the same beam momentum and crystal thickness, the diffusion function is proportional to the mean square spread of the exit angle of the beam particles. Since the diffusion function is independent of the masses of the incident particles, the composite nature of the beam

will not affect the diffusion function as long as the particles have the same momentum.

The mean square spread of the exit angle (and therefore the diffusion function multiplied by a constant factor, $\frac{2\Delta z}{p^2}$) are plotted in Fig. 7.4, as a function of the scaled incident angle. The diffusion function shows a prominent peak near the critical angle region in the 35 and 100 GeV/c data. The peak is smaller and broader at 250 GeV/c momentum. This indicates an increase in the radial scattering angle for the beam particles incident at angles in the neighbourhood of the critical angle. Such an increase in the radial scattering is expected because these particles spend more time in the neighbourhood of the high density regions close to the string of atoms and therefore have a greater probability of being scattered.

7.3.2 The diffusion equation (change in the mean transverse energy)

The diffusion equation (Eq. 2.39) relates the change, per unit depth of penetration in the crystal, of the mean transverse energy of axially channeled particles, to the diffusion function and its derivatives.

The difference of the mean square exit and incident angle is a measure of the change in the mean transverse energy for the channeled particles passing through

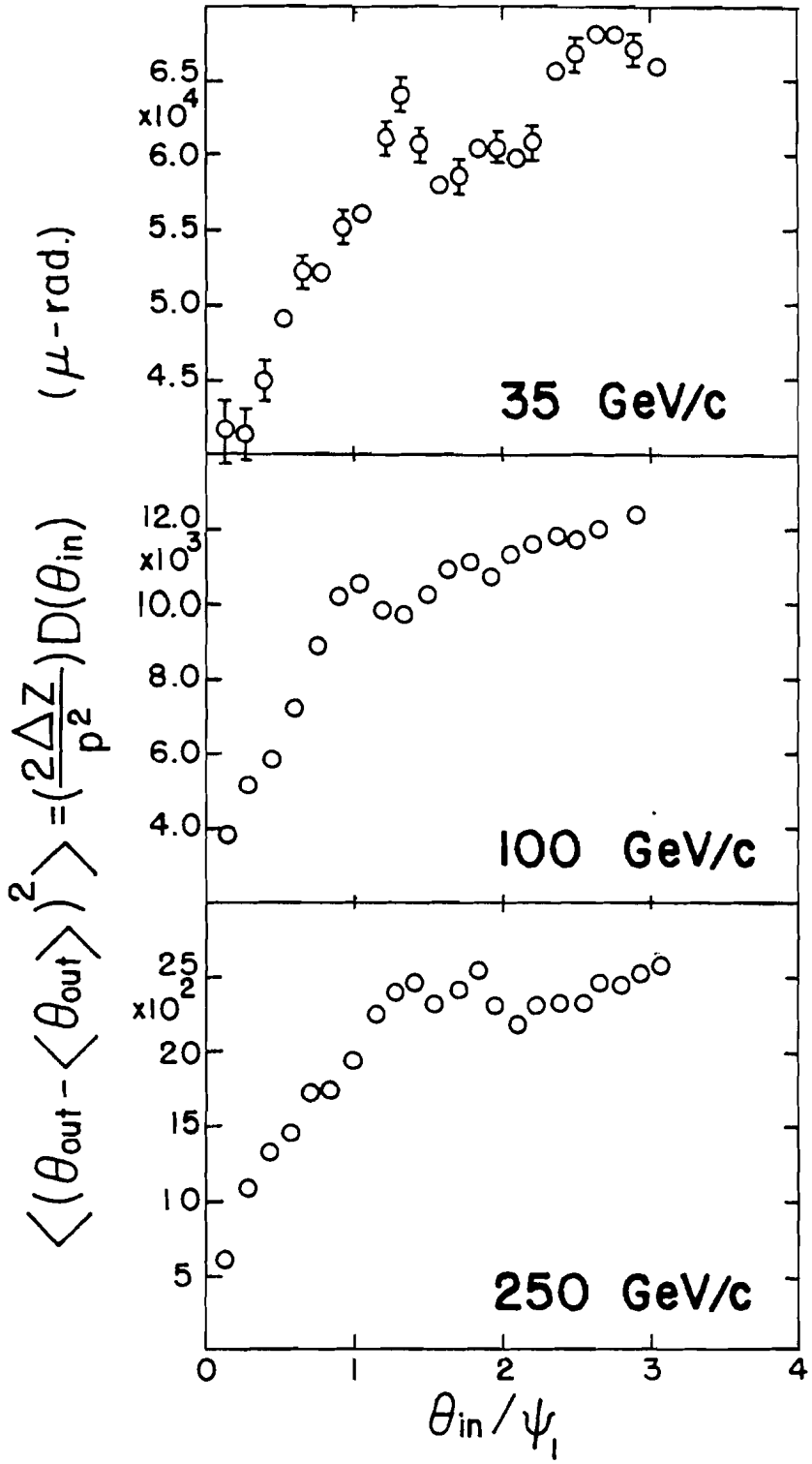

Fig. 7.4 The variation of the diffusion function (multiplied by a factor $2\Delta z/p^2$) with scaled incident angle, θ_{in}/ψ_1.

the crystal. This is plotted as open circles in Fig. 7.5 for 35, 100, and 250 GeV/c momenta. There is an increase in the mean transverse energy of the channeled particles and this increase becomes larger with the increasing angle of incidence. It reaches a maximum value beyond the critical angle and then levels off for 35 and 100 GeV/c data. The 250 GeV/c data showed a different behaviour outside the critical angle region. The change in the mean transverse energy decreased and changed sign in the neighbourhood of 3.4 ψ_1. This meant that there was a net decrease of the mean transverse energy of the beam as it passed through the crystal. In other words, there was a "cooling" of the beam transverse energy and the beam contracted in size in the projected angle space. The cooling of the beam transverse energy has been predicted for the channeled particles [Li65,Ka76,Ku76], but not for particles that are incident at angles 3 to 4 times the Lindhard critical angle, ψ_1.

This decrease in the transverse energy and therefore the net inward shift of the beam towards the channeling axis direction, is due to the feeding-in of the beam particles into the axial channeling region.

Beyond the critical angle, the random scattering in the radial direction tends to push the beam outwards

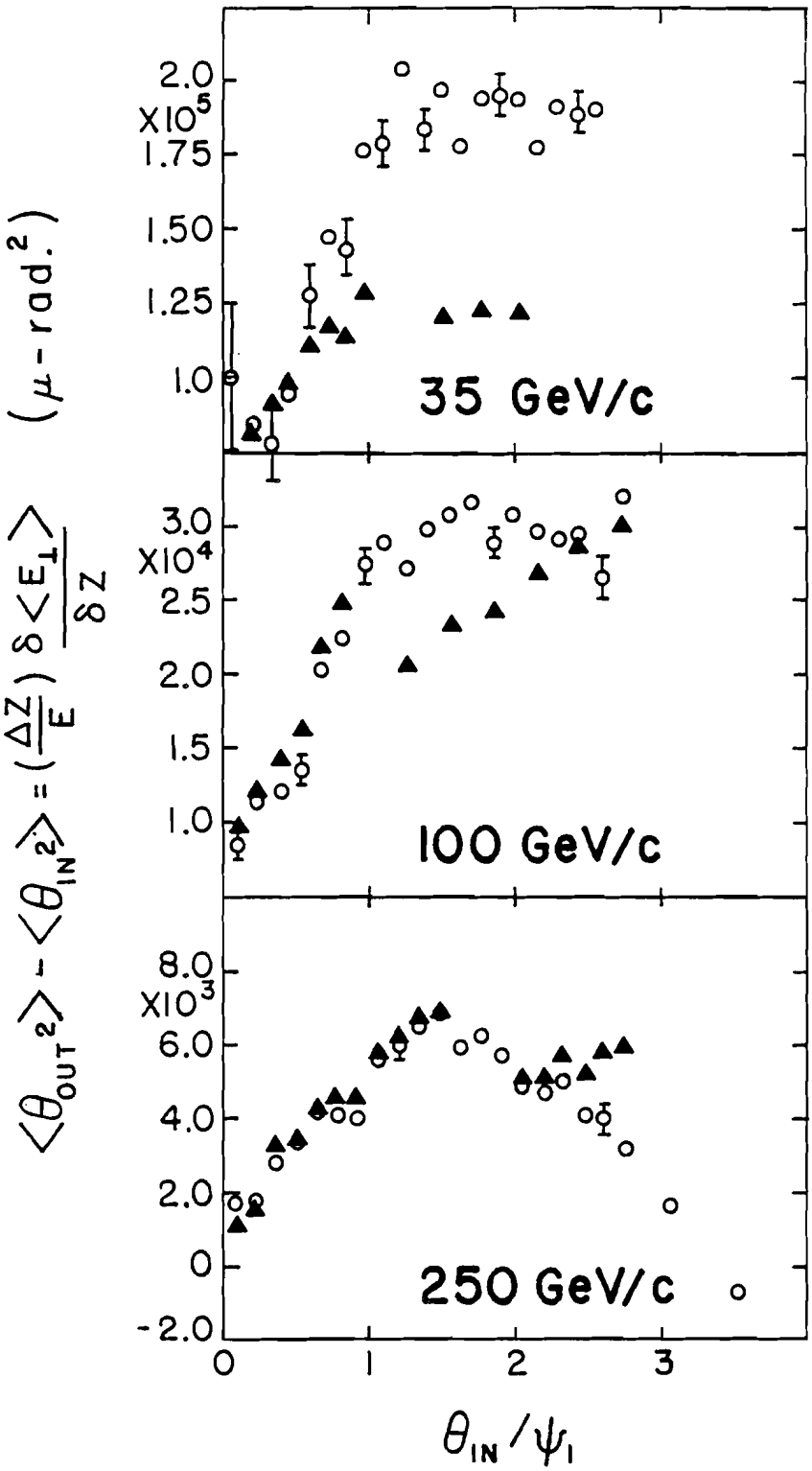

Fig. 7.5 The experimental (open circles) and the calculated (solid triangles) values of the change in the mean transverse energy.

from the channeling axis direction. The extent and region of influence of the outward push is determined by the multiple scattering spread of the beam for random orientation. There is a competing force due to the string of atoms that tends to attract the particles towards the axial channeling region in the angle space. This is the feeding-in effect and its influence extends to 2 to 3 times the critical angle.

The theoretically predicted rms multiple scattering angle spread (cf, Chapter 8) and the critical angle at the three beam momentum values are listed below:

	35 GeV/c	100 GeV/c	250 GeV/c
ψ_1<110> (micro-radians)	114.7	67.9	42.9
$<\Delta\theta^2>^{\frac{1}{2}}$ (micro-radians)	525.6	183.9	73.6

For the 250 GeV/c data it was seen that the outward push of the multiple scattering spread became small enough at twice the $<\Delta\theta^2>^{\frac{1}{2}}$ value that the feeding-in effect started to dominate. The value of $2<\Delta\theta^2>^{\frac{1}{2}}$ for 250 GeV/c data is 147.2 micro-radians, which is 3.4 ψ_1 and the change in the beam transverse energy reversed sign at exactly this value of the incident angle for 250 GeV/c data (Fig. 7.4).

Hypothesizing that the inward shift of the beam

transverse energy would occur at $2<\Delta\theta^2>^{\frac{1}{2}}$ for the 35 and 100 GeV/c data, one finds the turning point of the beam transverse energy shift as 9.2 ψ_1 and 5.4 ψ_1, respectively. The beam incident angle spread was not broad enough to get statistically significant data in these regions of incident angle space. But even if the beam spread was large enough to cover these angles, one might not see the net inward shift of the beam transverse energy because the string influence would be negligible at such large angles of incidence.

The above argument may be applied to beam momenta higher than 250 GeV/c.. Since the critical angle scales as $\frac{1}{\sqrt{E}}$ (Eq. 2.13) and the rms multiple scattering angle spread as $\frac{1}{E}$, the region of influence of the outward push ($\sim 2<\Delta\theta^2>^{\frac{1}{2}}$) will shrink faster than the region of axial channeling ($\sim\psi_1<110>$), with increasing beam momentum.

The influence of the string and therefore the feeding-in effect will become stronger with decreasing angle of incidence (θ_{in}). Assuming a constant feeding-in for all angles of incidence one can estimate the value of the beam momentum for which the change in the transverse energy reverses sign <u>within</u> the critical angle of channeling, i.e., when $2<\Delta\theta^2>^{\frac{1}{2}} = \psi_1$. The estimate for 2 cm thick Germanium crystal along <110>

channeling axis is ∿3000 GeV/c momentum. Since the feeding-in effect increases with decreasing θ_{in} value, the incident beam momentum value of 3000 GeV/c may be considered as the upper limit at which the beam transverse energy starts to shift inwards within the critical angle region. In other words, "cooling" of the beam transverse energy would take place for channeled particles with energies greater than 3000 GeV/c.

Going back to the diffusion equation 2.39 (and Eq. 2.42), one can write it in terms of the incident angle θ_{in} and the exit angle θ_{out}, for a crystal of known thickness as:

$$2\langle(\theta_{out}-\langle\theta_{out}\rangle)^2\rangle + \theta_{in}\frac{\partial}{\partial\theta_{in}}\langle(\theta_{out}-\langle\theta_{out}\rangle)^2\rangle$$

$$= \langle\theta_{out}^2\rangle - \langle\theta_{in}^2\rangle \qquad 7.4$$

The right hand side of the above equation is proportional to the change in transverse energy and its plot has already been shown as open circles in Fig. 7.5. The two expressions on the left hand side were obtained from Fig. 7.4. The slopes were obtained from an "eyeball" fit smooth curve through the data points in Fig. 7.4.

The sum of the two expressions on the left hand side of the diffusion equation are plotted as solid

triangles in Fig. 7.5. The circles and the triangles follow each other quite well for beam particles incident in the range of zero to the critical angle, ψ_1, for 35 and 100 GeV/c data and even slightly beyond the critical angle for 250 GeV/c data. For particles incident at 1.5 ψ_1 and beyond, the triangles and the circles follow different trends, being accidentally equal at certain values of the incident angles.

The above considerations indicate that the diffusion equation 7.4 predicts the behaviour of the transverse motion of the channeled particles quite accurately, but fails to predict the transverse motion of the quasi-channeled and random particles.

7.4 DECHANNELING

The changes in the mean value of the radial angle distribution, $\langle\theta_{out}-\theta_{in}\rangle$ (the angles are defined in Fig. 4.5), for the beam particles passing through the crystal, in the vicinity of the <110> axis direction, are shown in Fig. 7.6. The open circles represent the axial channeling data and the solid triangles are for random orientation (data for random orientation was recorded at 250 GeV/c beam momentum only).

In a fixed length crystal the rms multiple scattering angle spread, $\langle\Delta\theta^2\rangle^{\frac{1}{2}}$, for the random orientation of the crystal is constant at all angles of incidence.

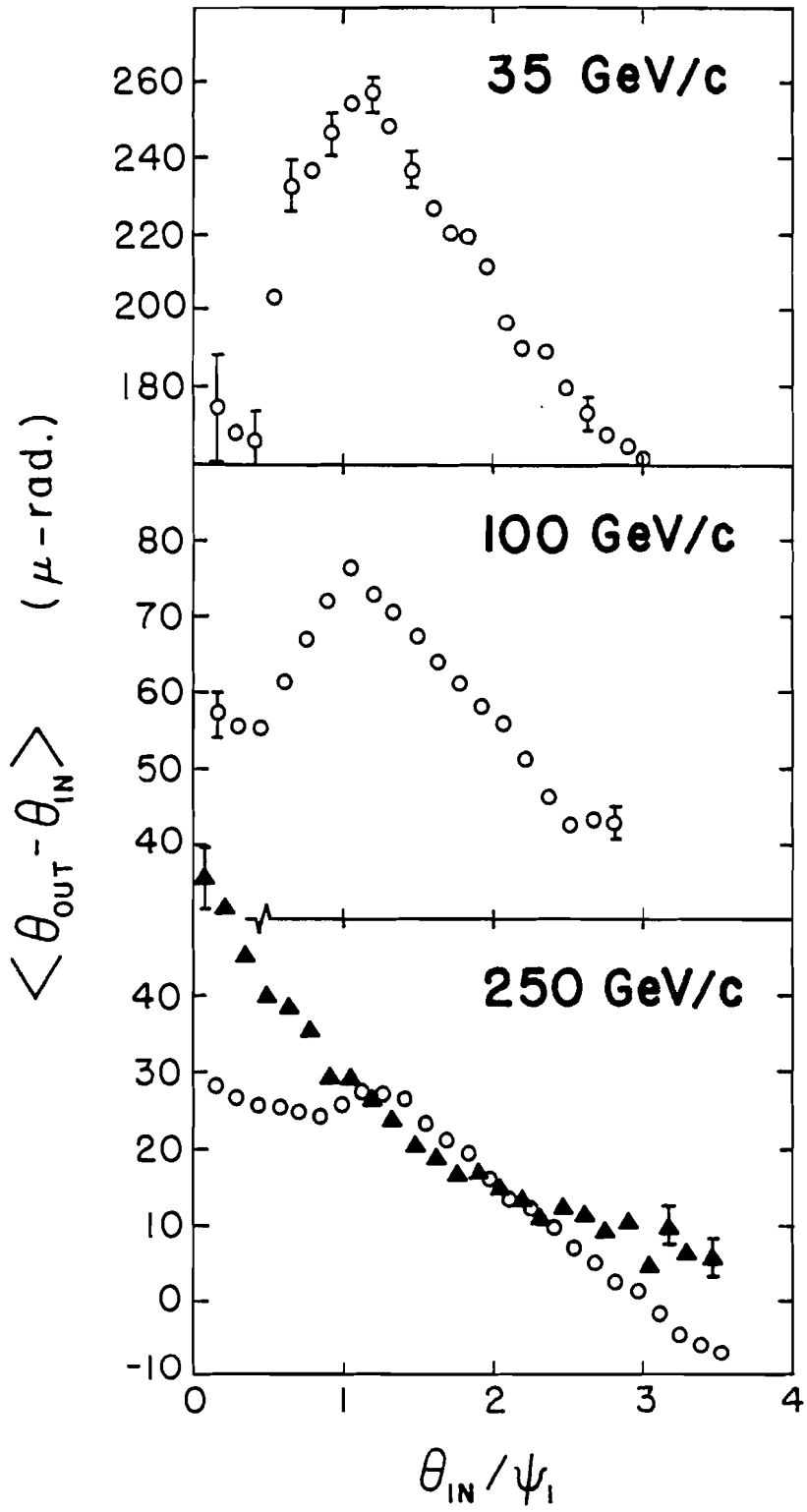

Fig. 7.6 The shift in the mean values of the radial angle distributions for channeled (open circles) and random (solid triangles) particles.

Because of this multiple scattering, the beam appears to shift outwards if one looks at the mean displacement of the radial angle distribution around any arbitrary direction as origin. This displacement is maximum for zero incident angle and is given by:

$$\langle\theta_{out}\rangle = 2\pi\int_{o}^{\infty} \theta_{out}\, f(\theta_{out})\,\theta_{out}\, d\theta_{out}$$

$$= 2\pi\int_{o}^{\infty} \frac{\theta_{out}}{\pi\langle\Delta\theta^2\rangle}\, e^{-\frac{\theta_{out}^2}{\langle\Delta\theta^2\rangle 2}}\, d\theta_{out}$$

$$= \frac{\sqrt{\pi}}{2}\langle\Delta\theta^2\rangle^{\frac{1}{2}} \qquad 7.5$$

For 250 GeV/c data the theoretically predicted value of $\langle\Delta\theta^2\rangle^{\frac{1}{2}}$ in 2 cm thick Germanium crystal in random orientation is 73.3 micro-radians (cf. Chapter 8), and therefore $\langle\theta_{out}\rangle$ = 65.0 micro-radians. This value is in agreement with the extrapolated results of the random orientation data for zero angle of incidence, as shown in Fig. 7.6. The value of the shift in the mean radial angle should decrease with increasing angle of incidence and should be practically zero beyond $3\langle\Delta\theta^2\rangle^{\frac{1}{2}}$ which is equivalent to 5.13 ψ_1 for 250 GeV/c beam momentum. Such a trend is observed in the random orientation data.

For the axial channeling data, the displacement of the radial angle distribution was close to the random orientation behaviour for incident angle beyond the

critical angle, ψ_1. Within the critical angle region the displacement increases with increasing angle of incidence and reaches a maximum value near the critical angle, for 35 and 100 GeV/c data. The shift shows a broad peak for the 250 GeV/c data.

The outward shift in the radial angle distribution for incident angle up to the critical angle, ψ_1, was a measure of the extent of dechanneling (a process in which the channeled particles are scattered out of the critical angle region around the axis position) taking place in the crystal. The dechanneling was largest in the neighbourhood of the critical angle, as one would expect, because of the increased probability of scattering with the string of atoms.

The measure of the degree of dechanneling is obtained from the dechanneling length defined below.

The number of particles, $N_{ch}(z)$, that remain channeled, i.e., have angles less than the critical angle of channeling, ψ_1, after the beam has penetrated a depth of z in the crystal, may be taken as:

$$N_{ch}(z) = N_{ch}(0)e^{-\frac{z}{\lambda(E)}} \qquad 7.6$$

where $\lambda(E)$ is the dechanneling constant and it is a function of the beam energy, the crystal material, imperfections and defects in the crystal, and the

crystal axis. Then the dechanneling length may be defined as the depth of penetration, $z_{1/2}$, in the crystal in which the number of particles within the critical angle region is reduced by one half. Therefore, the dechanneling length from Eq. 7.6 is:

$$Z_{1/2}(E) = \lambda(E)\ln(2) \qquad 7.7$$

The values of the fraction of particles, f_{ch}, that remained channeled in passing through the 2 cm thick crystal, the dechanneling constant, and the dechanneling lengths are listed below:

	35 GeV/c	100 GeV/c	250 GeV/c
$f_{ch}(E)$	0.25±0.01	0.39±0.01	0.46±0.01
$\lambda(e)$ (cm^{-1})	1.44±0.04	2.12±0.06	2.58±0.07
$Z_{\frac{1}{2}}(E)$ (cm)	1.00±0.03	1.47±0.04	1.79±0.05

From these numbers one can see that the dechanneling was maximum at 35 GeV/c and that 3/4 of the beam particles incident within the critical angle region were scattered out of the 2 cm thick crystal. The crystal length was of the order of dechanneling length at 250 GeV/c momentum.

7.5 COMPARISON WITH COMPUTER SIMULATION RESULTS

It has already been seen in Sec. 7.3.2 that the radial diffusion of the transverse motion of the beam

particles, for angles of incidence within the critical angle region, is governed by the diffusion equation. The diffusion equation does not predict correctly the transverse motion of the beam in the quasi-channeling region (cf. Fig. 7.5). In the absence of any theoretical prediction of the behaviour of the beam particles in the quasi-channeling region, the experimental results were compared with the results of computer simulation.

The computer simulation results of Edge et al. [Ed75] showed behaviour very similar to the results of this experiment. They used the impulse collision approximation to calculate the angular distribution of protons with a string of Gold atoms in <110> orientation. This approximation was first suggested by Lindhard (cf. Sec. 2.1) in his 1965 paper on the subject of channeling [Li65]. The computer simulation included the effect of thermal vibration of the atoms in the crystal but neglected the multiple scattering with the electrons. Their results were therefore accurate for incident angles in the neighbourhood of the critical angle and in the quasi-channeling region (ψ_1 to $2\psi_1$) where the nuclear scattering was dominant and the electronic scattering was small.

Two aspects of the computer simulation results are presented in Figs. 7.7(a) and (b). These simulation

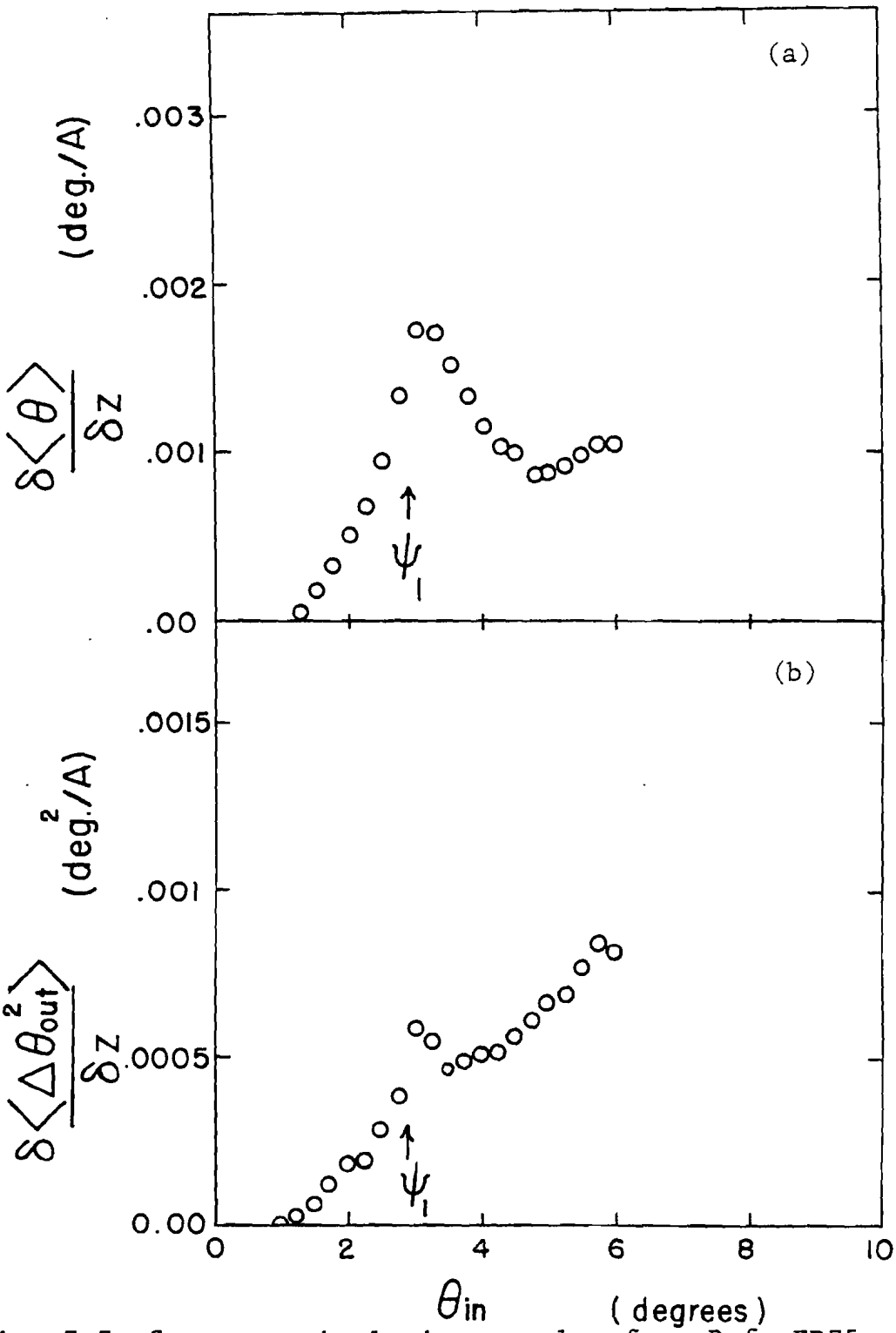

Fig. 7.7 Computer simulation results from Ref. ED75 showing the change in the (a) mean and (b) mean square spread values of the angular distribution per unit depth of penetration along <110> axis.

results were for 334 KeV protons and at this energy the Lindhard critical angle, ψ_1, is 2.78 degrees. The critical angle is also indicated in the figures.

The Fig. 7.7(b) is a plot of the change in the mean square spread of the radial angle of the beam distribution per unit depth of penetration in the crystal versus the incident angle. This is qualitatively similar to the results of this experiment in the neighbourhood of the critical angle and in the quasi-channeling region as shown in Fig. 7.4. The similarity is very striking for 35 GeV/c data. The prominent peak just beyond the critical angle, ψ_1, is present in both the cases. As it was seen in the 100 GeV/c data, the peak is not very prominent, but it is present and in the 250 GeV/c data the peak is smaller and broader.

The change in the mean value of the radial angle distribution obtained by Edge et al. [Ed75] is shown in Fig. 7.7(a). The corresponding results for this experiment are presented in Fig. 7.6. The behaviour is again qualitatively very similar in the neighbourhood of the critical angle and in the quasi-channeling region of the incident angle.

These strong similarities between the computer simulation results and the experimental data for critical angle and quasi-channeling angle regions suggest

that the theoretical model used in the simulation must be the correct model for calculation of the behaviour of the beam particles in these angular regions. This model is obviously Lindhard's model [Li65] for calculating the motion of the channeled particles. The interesting feature of this similarity is that the model works for quasi-channeled particles too. This was not pointed out in Lindhard's paper [Li65]. In fact, the continuum potential approximation due to the string of atoms was supposed to break down beyond the critical angle.

CHAPTER 8

MULTIPLE SCATTERING

A beam of particles incident on a crystal in random orientation will undergo many small scattering angle collisions with the electrons and the nuclei and a few small impact parameters, large scattering angle collisions with the nuclei only. The large number of small scattering angle collisions are mainly responsible for the spreading of the angular distribution of the beam. These are called the multiple scattering collisions and they produce a gaussian distribution for a well collimated incident beam of particles. The long tail on the gaussian distribution for a well collimated incident beam is due to the single large scattering angle events.

The gaussian part of the distribution has the form:

$$P(\Delta\theta)2\pi\Delta\theta d\Delta\theta = \frac{e^{-\frac{\Delta\theta^2}{\langle\Delta\theta^2\rangle}}}{\pi\langle\Delta\theta^2\rangle} 2\pi\Delta\phi d\Delta\theta \qquad 8.1$$

where the mean square spread of the gaussian distribution, $\langle\Delta\theta^2\rangle$, has been given by Williams [Wi29] and Bohr [Boh48] as

$$\langle\Delta\theta^2\rangle = 8\pi\left(\frac{Z_1 Z_2 e^2}{pv}\right)^2 N\Delta Z \ \ell n \left(\frac{pa\langle\Delta\theta^2\rangle^{\frac{1}{2}}}{\hbar}\right) \qquad 8.2$$

where Δz is the thickness of the target material and the other quantities have been defined in Chapter 2.

Since $\langle\Delta\theta^2\rangle$ occurs on both sides of the transcendental equation 8.2, the values of $\langle\Delta\theta^2\rangle$ were obtained by the Newton-Ralphson iteration method for a 2 cm thick Germanium crystal at 35, 100, and 250 GeV/c beam momenta. The values of $\langle\Delta\theta^2\rangle^{\frac{1}{2}}$ are listed below

	35GeV/c	100 GeV/c	250 GeV/c
$\langle\Delta\theta^2\rangle^{\frac{1}{2}}$ (micro-radians)	525.6	183.9	73.6

The $\langle\Delta\theta^2\rangle^{\frac{1}{2}}$ value for 250 GeV/c beam particles, incident on the crystal oriented in a random direction, are shown as solid triangles for different angles of incidence scaled to the critical angle value, ψ_1, in Fig. 8.1 (random orientation data were taken for 250 GeV/c beam momentum only). The theoretically calculated values of $\langle\Delta\theta^2\rangle^{\frac{1}{2}}$ obtained above are also shown in the figure. The agreement between the predicted value and the experimental data is quite good.

The open circles in Fig. 8.1 are the $\langle\Delta\theta^2\rangle^{\frac{1}{2}}$ values for particles incident at different angles to the <110> axis. The rms scattering angle, $\langle\Delta\theta^2\rangle^{\frac{1}{2}}$, was minimum

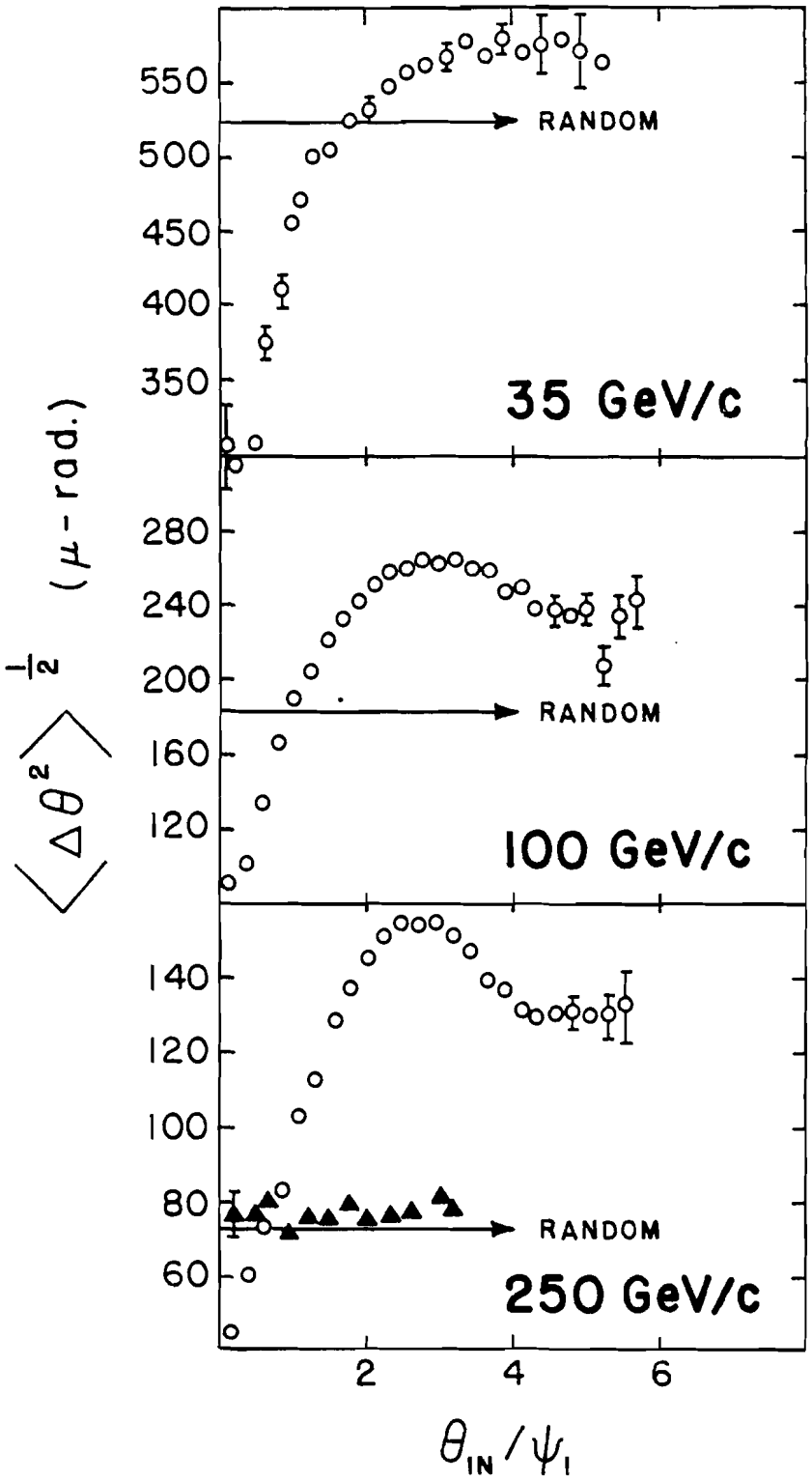

Fig. 8.1 The rms multiple scattering angle spread for <110> axial (open circles) and random (solid triangles) orientation of the crystal.

for zero angle of incidence and this value was less than the random orientation value, as one would expect, for particles going through the low density regions in the center of the channel. The minimum value of $\langle\Delta\theta^2\rangle^{\frac{1}{2}}$ at the three beam momenta, as obtained from Fig. 8.1, are listed below

	35 GeV/c	100 GeV/c	250 GeV/c
$\langle\Delta\theta^2\rangle^{\frac{1}{2}}$ (micro-radians)	290±15	90 ± 10	40 ± 5

The rms spread of the scattering angle, $\langle\Delta\theta^2\rangle^{\frac{1}{2}}$, is inversely proportional to the energy of the beam particles (cf. Eq. 8.2) for random orientation of the crystal. Assuming such a proportionality for the multiple scattering angle spread of the well channeled particles one has

$$\langle\Delta\theta^2\rangle^{\frac{1}{2}}_{min} = \frac{K}{E} \qquad 8.3$$

where the best fit value for K, with the three data points listed above, is K = 9973 GeV-rad.

The theoretically predicted multiple scattering curve for random orientation and the best fit curve of Eq. 8.3 for well channeled particles multiple scattering are shown in Fig. 8.2. The circles are the $\langle\Delta\theta^2\rangle^{\frac{1}{2}}$ values for the particles incident along <110> axis direction. This is in effect the multiple scat-

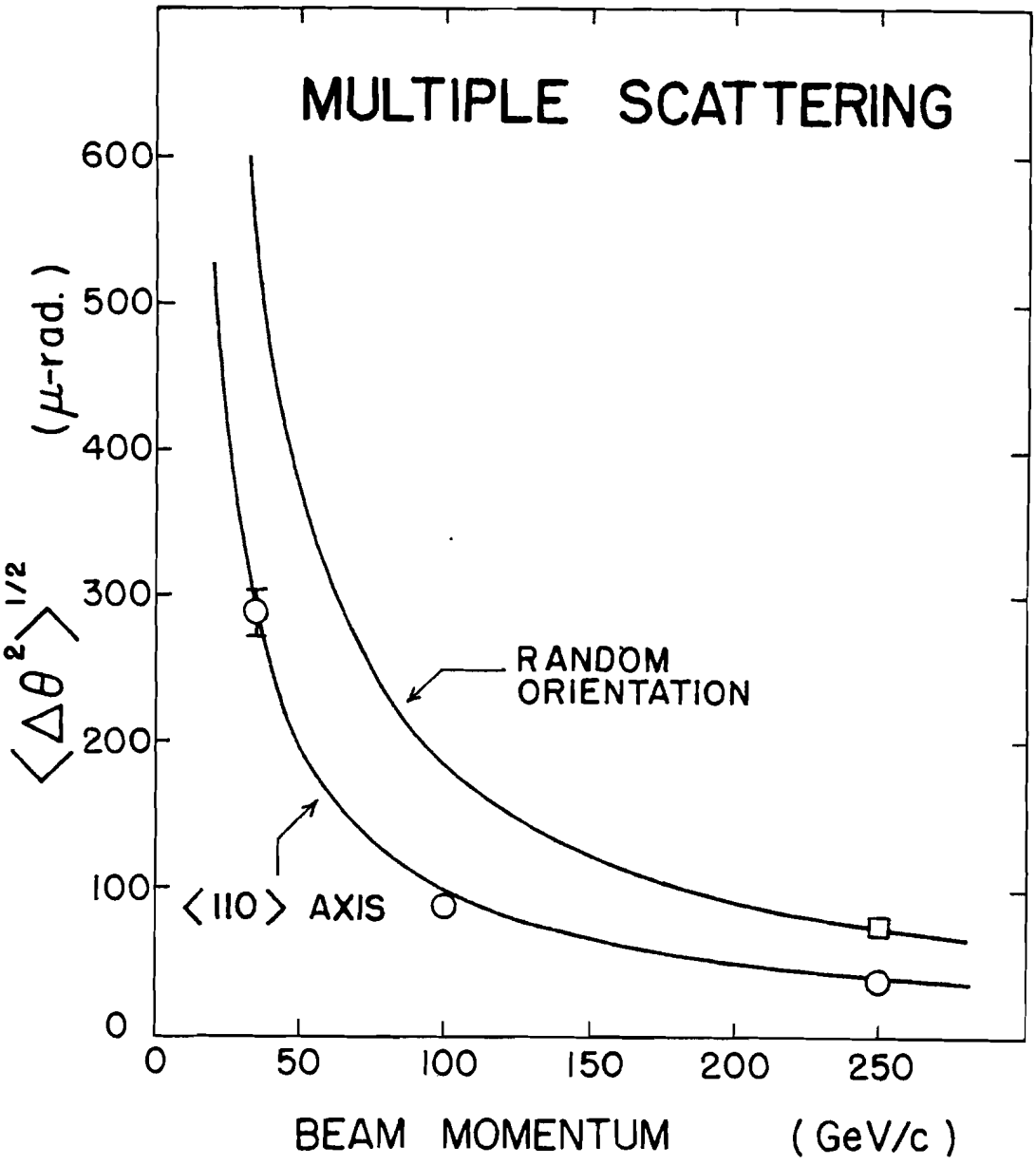

Fig. 8.2 The expected curve for rms spread of the multiple scattering angle for random orientation and the best fit curve through the experimental values (open circles) for particles incident at zero degrees to the <110> axis. The square is the experimental random orientation value at 250 GeV/c momentum.

tering within the channel. The square in Fig. 8.2 is the random orientation value at 250 GeV/c beam momentum.

The <110> axis curve and the data points represented by circles indicate that the rms multiple scattering angle spread of the best channeled particles scale as 1/E. Thus the rms multiple scattering angle spread decreased more rapidly than the extent of the axial channeling region measured by the Lindhard critical angle, ψ_1 (ψ_1 scales as $1/\sqrt{E}$). This reinforces the argument presented in Sec. 7.8. that beyond a certain value of the beam energy, the focusing effect of the string will dominate over the multiple scattering. effect within the critical angle region, and one may observe cooling in the transverse energy of the beam.

Going back to Fig. 8.1, the rms spread of the multiple scattering angle may be resolved into a radial, $\langle\Delta\theta^2\rangle_r^{\frac{1}{2}}$, and an azimuthal, $\langle\Delta\theta^2\rangle_a^{\frac{1}{2}}$, component. For small scattering angles one can write

$$\langle\Delta\theta^2\rangle \simeq \langle\Delta\theta^2\rangle_r + \langle\Delta\theta^2\rangle_a \qquad 8.4$$

At large angle of incidence there will be equal contribution from the radial and azimuthal components to the total multiple scattering spread and these would equal the random orientation value, i.e., for $\theta_{in} >> \psi_1$

	35 GeV/c	100 GeV/c	250 GeV/c
$\langle\Delta\theta^2\rangle_r^{\frac{1}{2}} = \langle\Delta\theta^2\rangle_a^{\frac{1}{2}}$ = (micro-radians)	371.7	130.0	52.0

The radial components of the multiple scattering are plotted in Fig. 8.3. The random orientation value is also shown in the figure. The $\langle\Delta\theta^2\rangle_r^{\frac{1}{2}}$ value increased with increasing angle of incidence of the beam. It reached a maximum value at the critical angle of incidence, $\psi_1\langle 110\rangle$, and then leveled off beyond $\psi_1\langle 110\rangle$, for 100 and 250 GeV/c data.

In terms of the incident angle, θ_{in}, the exit angle, θ_{out}, and the aximuthal scattering angle, $\Delta\theta$, the equation Eq. 8.4 becomes

$$\langle\Delta\theta^2\rangle \simeq \langle(\theta_{out}-\theta_{in})^2\rangle + 2\langle\theta_{in}\rangle\langle\theta_{out}\rangle(1-\langle\cos\Delta\phi\rangle) \quad 8.5$$

For an equilibrium distribution of the azimuthal scattering angle, $\Delta\phi$, the mean of the cosine term will be zero. Then Eq. 8.4 will reduce to

$$\langle\Delta\theta^2\rangle \simeq \langle(\theta_{out}-\theta_{in})^2\rangle + 2\langle\theta_{in}\rangle\langle\theta_{out}\rangle$$

$$\text{or} \quad \frac{\langle\Delta\theta^2\rangle - \langle(\theta_{out}-\theta_{in})^2\rangle}{\langle\theta_{in}\rangle\langle\theta_{out}\rangle} = \frac{\langle\Delta\theta^2\rangle_a}{\langle\theta_{in}\rangle\langle\theta_{out}\rangle} = 2.0 \quad 8.6$$

Fig. 8.4 is a plot of the left hand side of the above equation versus the scaled incident angle. The

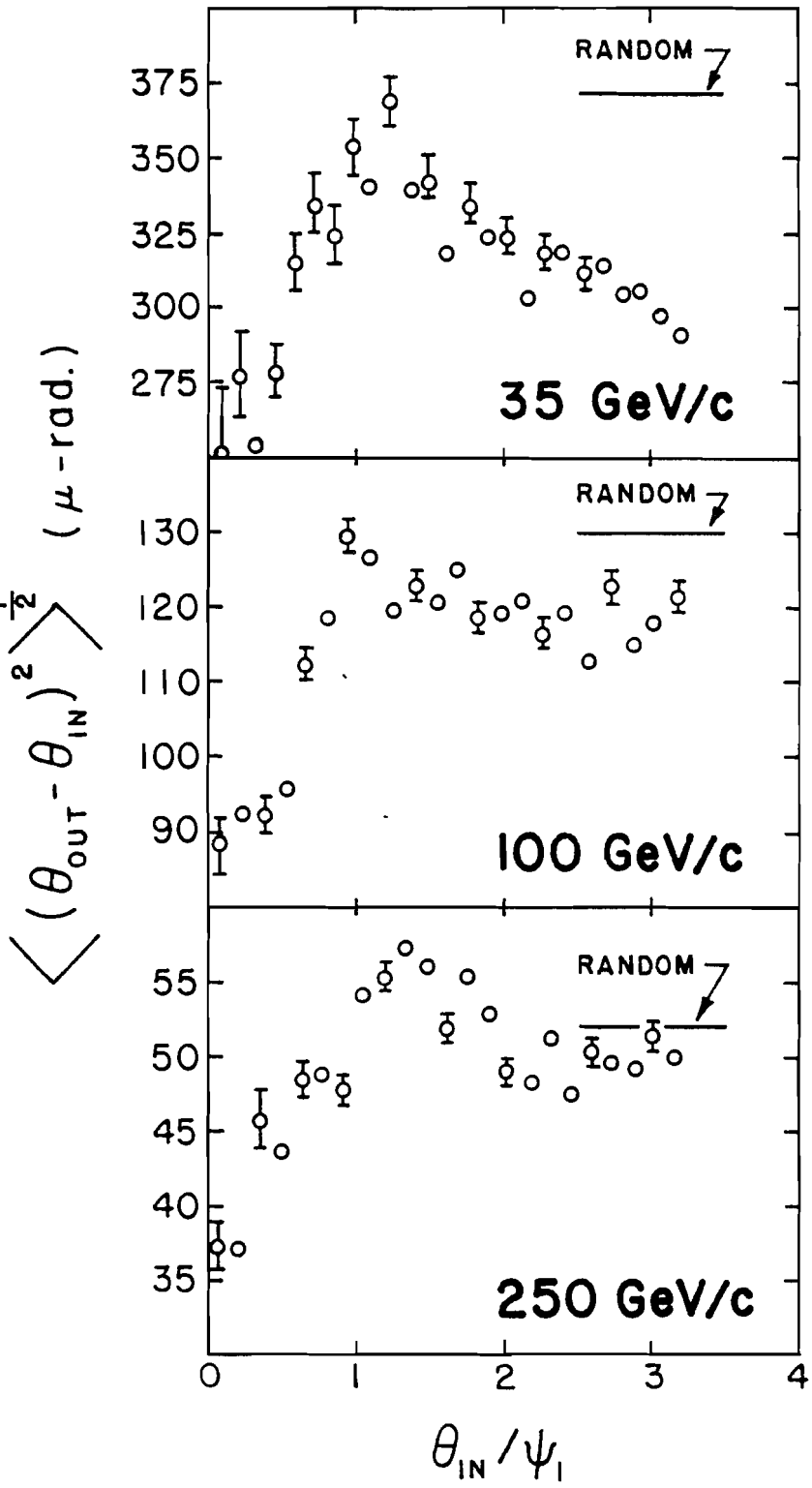

Fig. 8.3 The radial component of the rms spread of the multiple scattering angle. The expected values for random orientation of the crystal are also indicated.

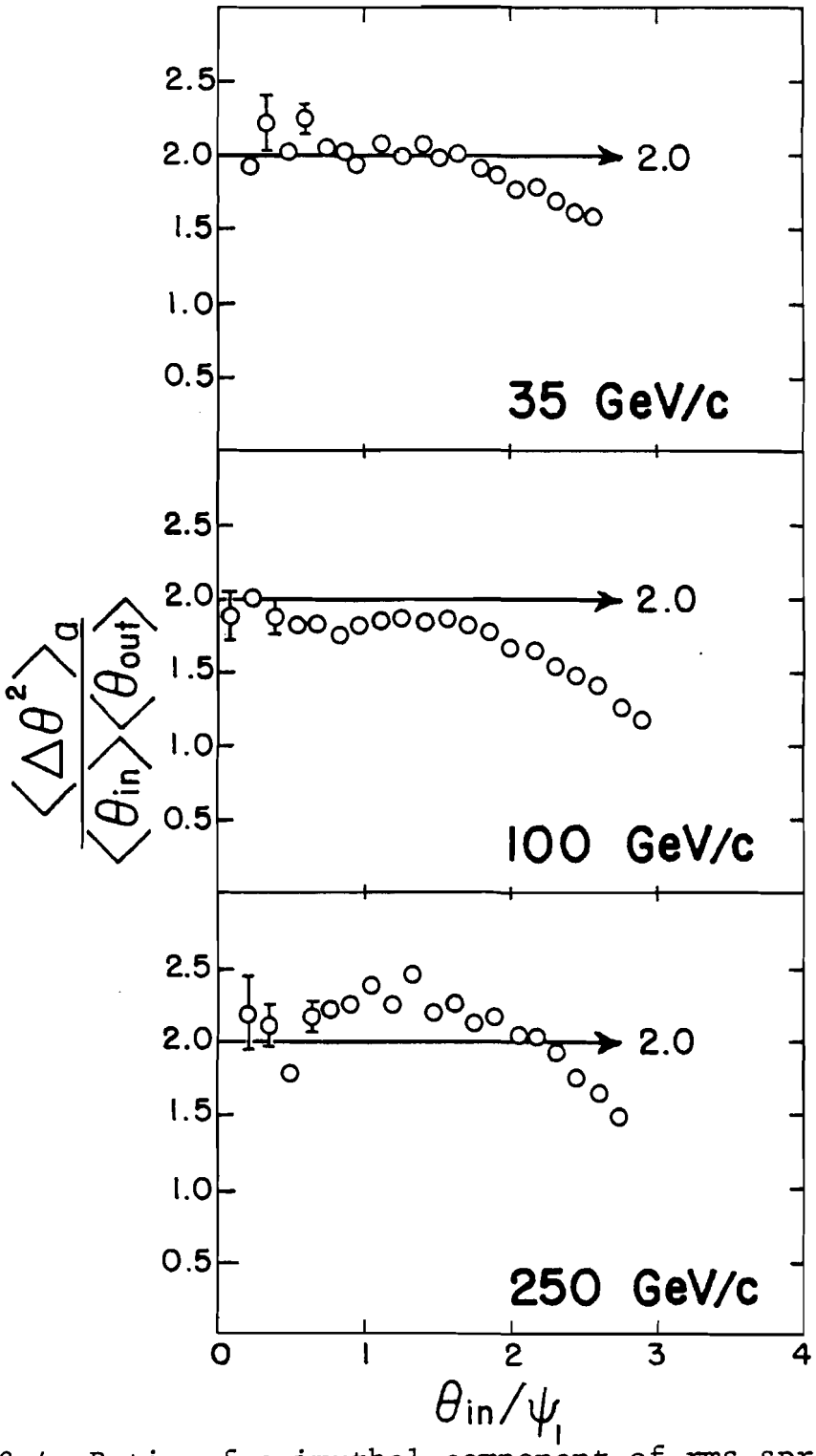

Fig. 8.4 Ratio of azimuthal component of rms spread of multiple scattering angle and the product of mean incident and exit angles. The expected value of 2.0 is also indicated.

predicted value of 2.0 for statistical eqiulibrium in the azimuthal scattering angle is also shown in the figure. The agreement with the predicted value is very good for incident angles from zero to ψ_1 in the 35 GeV/c data. The 100 and 250 GeV/c data show a constant shift below and above the 2.0 line, respectively. This was probably due to some systematic error. The important point to note is that the value remains constant for incident angles of up to $2\psi_1$ and therefore there is statistical equilibrium in the aximuthal angle distribution for this range of incident angles.

Since the azimuthal component of the multiple scattering angle in the statistical equilibrium region (incident angle in the range of zero to $2\psi_1$) is a product of the mean value of the incident angle and the exit angle (second term in Eq. 8.5), its value will increase rapidly with increasing incident angle. The multiple scattering for random orientation was not large enough at 250 GeV/c beam momentum (and to a lesser extent at 100 GeV/c beam momentum) to account for the increase in the azimuthal component of the multiple scattering angle spread for increasing angle of incidence. There was therefore a large increase in the total multiple scattering angle spread, above the random orientation value (Fig. 8.1) for 250 GeV/c data (and, to a smaller degree, in 100 GeV/c data).

CHAPTER 9

ENERGY LOSS

When a charged particle passes through a medium, it loses energy through elastic and inelastic collisions with the electrons and the nuclei of the atoms in the medium. The nuclear collisions are very infrequent at very high energies of the beam particles. They are the source of the wide angle Rutherford scatterings and are responsible for depositing higher energies, in a single collision, in the medium. They contribute to the long tail on the higher energy side of the distribution of energy deposited in the medium (Landau distribution).

The bulk of the energy loss of the beam particles in the medium is due to the large number of small scattering angle collisions with the electrons. These collisions produce excitation and ionization of the electrons close to the path of the beam particle (close collisions). They also produce resonant excitation and ionization far from the particle path (distant collisions). At intermediate energies of the incident particles there is an equipartition of the energy loss between the close and the distant collisions. But at

higher energies the distant collisions are affected by the polarization of the medium, causing a decrease in the energy loss. This effect is more significant for dense materials and is therefore called the "density effect."

The energy loss of relativistic charged particles, incident on a crystal along a direction far away from any major crystal axes or planes (random direction), will be discussed first and then the axial and planar channeling energy loss results will be presented. In both cases, the density effect is important and will be included in the calculations.

9.1 LANDAU DISTRIBUTION (RANDOM ORİENTATION)

It is very difficult to orient a crystal such that the beam direction is not along any crystal axes or planar directions, i.e., a direction along which the crystal appears like an amorphous medium with atoms in random positions. For the purpose of this experiment a direction far away from any major low index axes and planar directions was considered as the random direction.

The excitations and ionizations by the incident particles of the electrons and the nuclei in the medium are statistical in nature. Consequently, the energy loss values for particles traversing a material of a given thickness follow a statistical distribution. The

sharp cutoff on the low energy side is due to a minimum path length that the particles will have for a finite thickness of the medium. The long tail on the high energy side is due to infrequent nuclear collisions (as mentioned in the previous section).

The energy loss distribution in an amorphous medium was obtained by Landau [La44] by solving the transport equation for energy loss of charged particles in thin targets. The Landau distribution depends on a single parameter, λ, and has the form:

$$\phi(\lambda) = \frac{1}{2\pi i} \int_{-i\infty}^{+i\infty} e^{u\ell n(u) + \lambda u} \, du \qquad .9.1$$

This integral has been evaluated by Borsch-Supan [Bor61] for a wide range of λ values. The parameter, λ, is defined as:

$$\lambda = \frac{\Delta E - \langle \Delta E \rangle}{\xi} - 1 - \beta^2 + \gamma - \ell n\left(\frac{\xi}{T_{max}}\right) \qquad 9.2$$

where $\xi = \frac{2\pi Z_1^2 e^4 N Z_2 t}{mc^2\beta^2}$, Z_1 and Z_2 are the atomic numbers of the incident particle and the target atom, respectively, N is the number density of atoms in the target material, e is the electron charge, $\beta = v/c$, m is the mass of electron, t is the thickness of the target, $\langle \Delta E \rangle$ is the mean energy loss, $\gamma = 0.577216$ (Eulers constant) and T_{max} is the maximum energy transferred

to the electron in a head-on collision, i.e.,

$$T_{max} = \frac{2mc^2\beta^2}{1-\beta^2}\left[1 + \frac{2m}{M_1\ 1-\beta^2} + \left(\frac{m}{m_1}\right)^2\right]^{-1} \qquad 9.3$$

where M_1 is the mass of the incident particle. If the medium has finite thickness, then there is a large probability for the electrons, undergoing head-on collision with relativistic particles, to come out of the medium without depositing all their energy in the medium (delta rays). For such a case, the logarithm term in the λ parameter has to be modified by replacing T_{max} with the value of the mean energy loss of the delta rays, T_o, (refer for further details to Sec. 9.2).

For the purpose of fitting the Landau distribution to the experimental data, the experimental most probable energy loss value, $E_{\text{most probable}}$, was matched with the peak of the Landau distribution which occurs for $\lambda = -0.225$. The experimental energy loss distribution for 250 GeV/c beam particles incident on the randomly oriented, 2 cm thick Germanium crystal is shown in Fig. 9.1 by the open circles. The fitted Landau curve is also drawn in the figure as a solid line. The experimental points fit the Landau distribution very well near the peak and the high energy tail region.

The low energy tail in the experimental distribu-

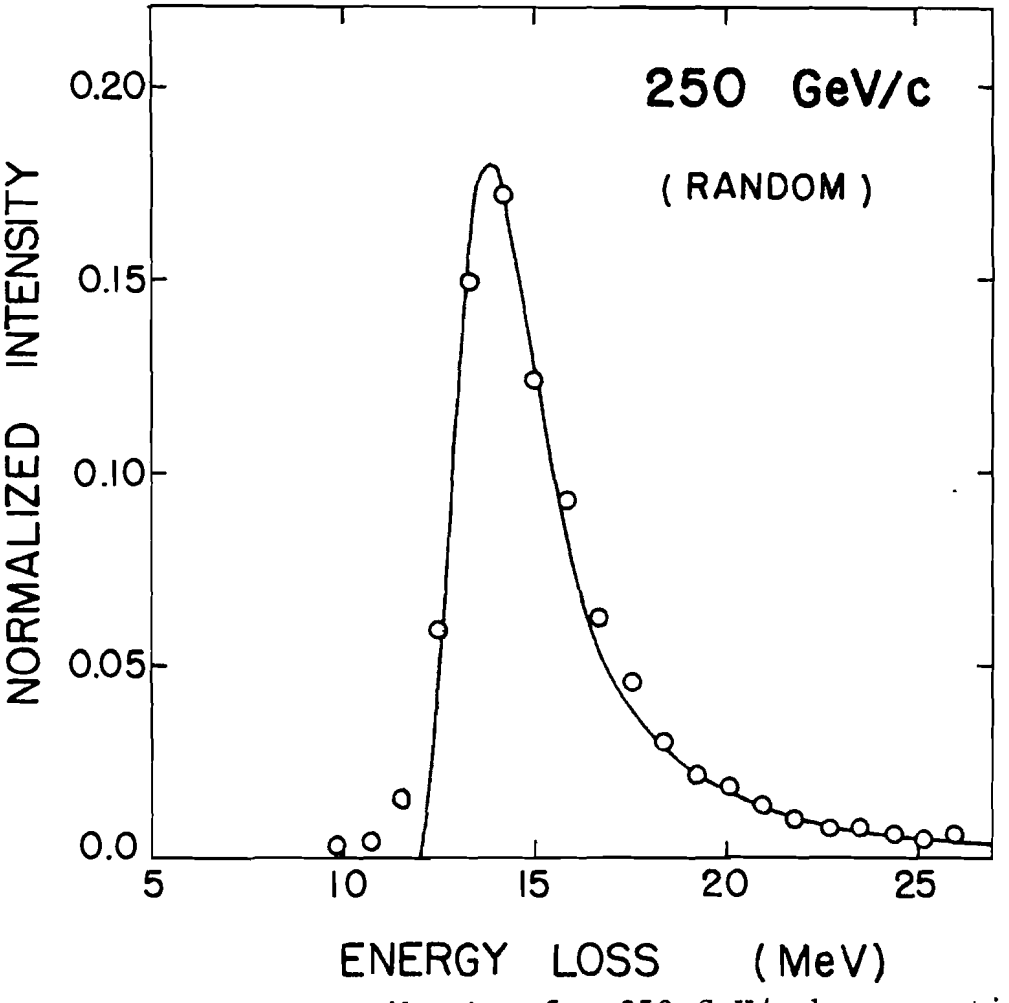

Fig. 9.1 Landau distribution for 250 GeV/c beam particles incident on 2 cm thick Germanium crystal in random orientation. The open circles represent the experimental points.

tion was probably because of a combination of the following reasons: There could be some high index axes and planes still present along the beam direction, i.e., the crystal was not aligned along a perfectly random direction. There could be two particles coming close in time and the amplifier remained dead for part of the time in the second particle's passage, thereby not collecting all the ions due to the second particle. It could be due to some particles grazing the surface of the crystal.

9.2 MEAN AND MOST PROBABLE STOPPING POWER (RANDOM ORIENTATION)

The mean dE/dx loss (stopping power) along a random direction in a dense medium has been given by Fano [Fa63] as

$$\left\langle \frac{dE}{dx} \right\rangle = \frac{2\pi Z_1^2 e^4 N Z_2}{mc^2\beta^2}\left\{ \ell n \frac{2mc^2\beta^2 T_{max}}{I^2(1-\beta^2)} - 2\beta^2 - \delta - \frac{2C}{Z_2}\right\} \qquad 9.4$$

where I is the mean excitation energy of the target atoms, δ is the density effect contribution and C is the shell correction. The other terms are the same as in Sec. 9.1. The shell correction for relativistic particles is small and was neglected for calculating <dE/dx> losses in this experiment.

As mentioned in the previous section, the knock-on

electrons (delta rays) do not deposit all their energy in the medium. Therefore the maximum energy transferred to the electron, T_{max}, has to be replaced in Eq. 9.4 by the mean energy lost by the delta ray, T_o. This yields the following formula for the restricted mean stopping power [Fa63], i.e.,

$$\left\langle \frac{dE}{dx} \right\rangle_{rest.} = \frac{2\pi Z_1^2 e^4 N Z_2}{mc^2\beta^2} \left\{ \ell n \frac{2mc^2\beta^2 T_o}{I^2(1-\beta^2)} - \beta^2 - \delta - \frac{2C}{Z_2} \right. \qquad 9.5$$

$$\left. - \frac{(1-\beta^2)T_o}{2mc^2} - \Delta C \right\}$$

where ΔC is a small correction factor of the order of 1 for gases and 0.01 for solids. This correction factor was also neglected in the calculation of the mean restricted stopping power (along with the shell correction). Sternheimer and Peierls [Ste71] give the most probable stopping power as

$$\left(\frac{dE}{dx} \right)_{\substack{most \\ prob.}} = \frac{2\pi Z_1^2 e^4 N Z_2}{mc^2\beta^2} \left\{ \ell n \frac{4\pi Z_1^2 e^4 N Z_2 t}{I^2(1-\beta^2)} - \beta^2 \right.$$

$$\left. - \delta + 0.198 \right\} \qquad 9.6$$

The mean energy loss of the delta rays is apparently accounted for by the constant factor, 0.198.

The density effect correction, δ, in the above three expressions for stopping power was obtained from

the following parametric equations [Ste66]:

$$(X) = 4.606X + C + a(X_1 - X)^m \quad (X_o < X < X_1)$$

$$(X) = 4.606X + C \quad (X > X_1)$$

and

$$X = \log_{10}\left(\frac{P}{M_1 c}\right) \qquad 9.7$$

where C, a, X_o, X_1, and m are parameters whose values for many common substances have been listed in Ref. [Ste66]. For Germanium the values of these parameters are:

C = -5.10 a = 0.1666 m = 3.136 X_o = 0.10 and X_1 = 3.0.

A rough estimate of the mean excitation energy is obtained from I = Z_2x10 eV, which for Germanium yields 320 eV. A more accurate value of I = 340 ± 10 eV, recommended by Ahlen [Ah80], was used in calculating the stopping powers. The mean energy deposited by the delta rays, T_o, in the 2 cm thick Germanium crystal was estimated in the following manner.

The energetic delta ray electrons were scattered mostly in the forward direction. It was therefore assumed that all the energetic knock-on electrons came out of the back end of the crystal. It was also assumed that the delta rays of energy T are produced with equal probability throughout the crystal. The production probability of the delta rays of energy T is given by

[Br78]:

$$\frac{dN}{dTdx} \simeq \frac{2\pi Z_1^2 e^4 N Z_2}{mc^2\beta^2} \frac{1}{T^2} \qquad 9.8$$

for $I << T \leq T_{max}$

The energy deposited by a delta ray of energy T produced at a distance, x, from the back end of the crystal was obtained by dividing the thickness, x, into strips of width 0.1 cm and calculating the energy deposited in successive strips from the tabulated stopping powers of electrons [Ber64]. Using the probability expression of Eq. 9.8 and the energy deposited by the delta rays, produced at different depths in the crystal, an average value of the energy loss was found. For a 2 cm thick Germanium crystal the average energy loss of the delta rays was T_o = 5.23 MeV for 35, 100, and 250 GeV/c beam particles. Although the method outlined above for estimating T_o is very crude, an error of 30% in T_o value would produce an error of only 1% in the mean restricted stopping power, i.e., the mean restricted stopping power is not sensitive to the exact value of T_o. However, the correction due to the mean energy deposited by the delta rays, T_o, is important because the T_{max} value it is supposed to replace in the stopping power formula is 2 to 4 orders of magnitude higher than the T_o value.

The most probable, the mean restricted, and the mean unrestricted stopping powers of the composite beam of protons, pions, and kaons incident on a 2 cm thick Germanium crystal, oriented in a random direction, were calculated for relativistic momenta in the range of 5 to 300 GeV/c. A weighted average of the stopping powers, using the percentage composition of the beam particles from Ref.[Ba78], was found for each beam momentum value. The maximum difference in the mean stopping power was 2% for 35 GeV/c pions and protons.

The above mentioned stopping powers are shown by solid curves in Fig. 9.2. The experimentally observed values of the mean restricted stopping power and the most probable stopping power are indicated by circles and triangles in the figure, respectively. The theoretical and the experimental values of the stopping powers are also listed below:

(MeV/cm)		35 GeV/c	100 GeV/c	250 GeV/c
$(dE/dx)_{rest}$	exp.	15.7±0.1	15.5±0.1	15.5±0.1
	theo.	15.61	15.63	15.65
$(dE/dx)_{most\ prob.}$	exp.	14.6±0.2	14.6±0.2	14.6±0.2
	theo.	14.33	14.35	14.36

There is very good agreement between the theoretically calculated values and the experimental data

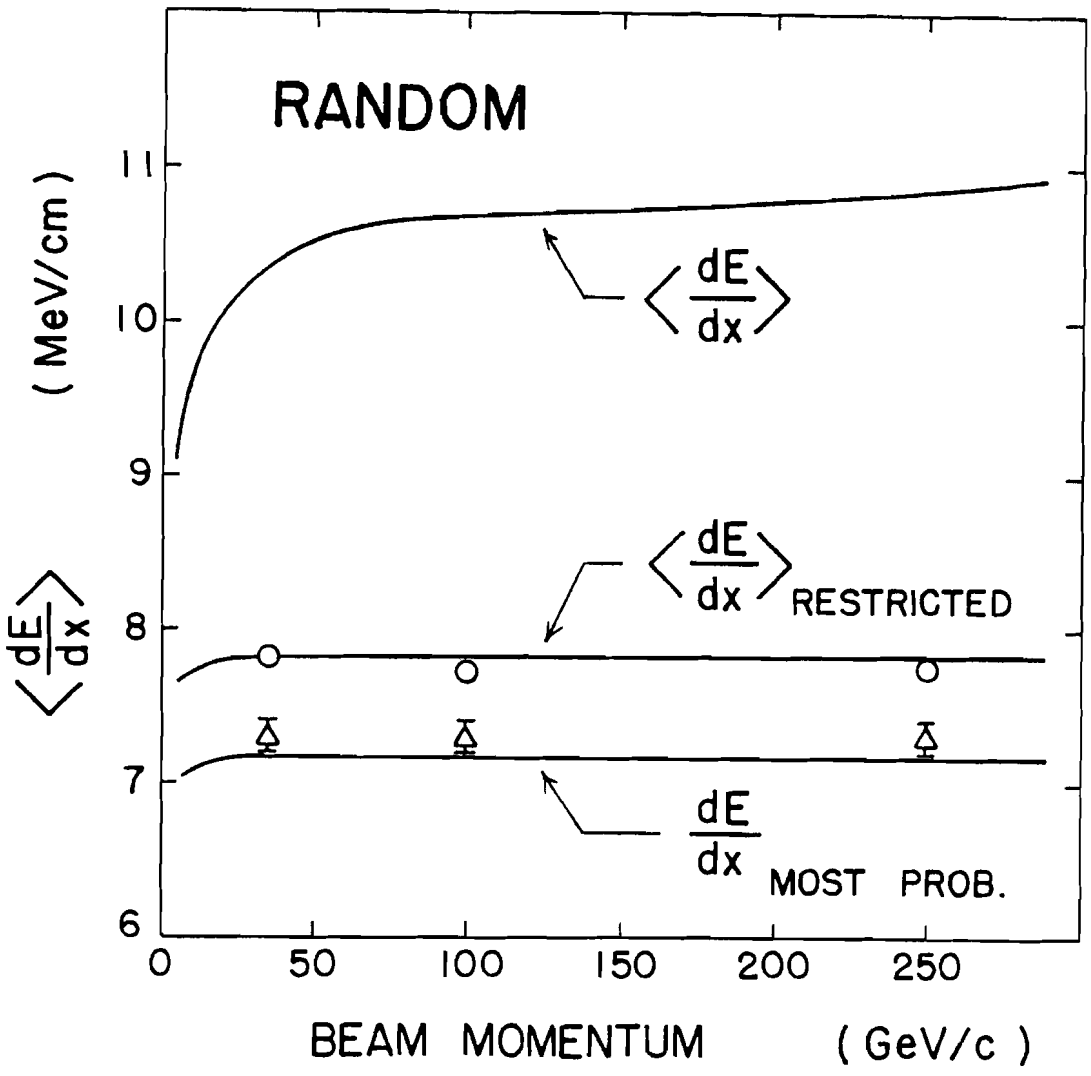

Fig. 9.2 Comparison of the theoretical and experimental values of the restricted mean and most probable energy loss in 2 cm thick randomly oriented Germanium crystal. The unrestricted mean energy loss curve is also drawn. The open circles and triangles are the experimental values of the restricted mean and most probable energy losses, respectively.

points. This also proves that the estimate of the mean energy loss of the delta rays, T_o, was reasonable.

The fact that the mean stopping power, $\langle dE/dx \rangle$, with no correction for the delta rays, is 40% higher than the restricted mean stopping power, $\langle dE/dx \rangle_{rest.}$, with delta ray corrections applied, indicates that the delta ray correction is very important for high energy beams penetrating a crystal of finite thickness.

9.3 ENERGY LOSS DISTRIBUTION (AXIAL CHANNELING)

The positively charged beam particles that enter the crystal at an angle less than the critical angle with respect to the axis direction, are steered away from the high density regions of the rows of atoms. These particles therefore spend more time in the low electron density regions. The close collision probability with the electrons is greatly reduced, but the resonant excitation and ionization probability of the distant electrons remain unchanged in comparison to the random orientation case. The density effect will therefore be the same for the axial as well as the random orientation of the crystal.

The nuclear collisions will be negligible for channeled particles that do not approach the string of atoms closer than the critical distance. This reduced electronic and nuclear collison probability for the

channeled particles will produce a reduction in the energy deposited in the crystal.

The energy loss distribution of the channeled particles at 35, 100, and 250 GeV/c beam momenta are shown in Figs. 9.3(a), (b) and (c). The open circles represent the distributions for channeled particles and were obtained by selecting particles that were within the critical angle in the incident and the exit projected angle plane with respect to the <110> axis direction. The dots represent distributions with no selection and are primarily the random energy loss distribution.

The small peak on the high energy side of the 35 GeV/c channeled particle energy loss distribution is at the same position as the most probable energy loss for random orientation. This suggests that the peak is perhaps due to the contamination of the random particles energy loss. The contamination is seen as a shoulder in the channeled particle energy loss distribution at 100 GeV/c beam momentum. It is practically absent in the 250 GeV/c data.

The decrease of error in the angle measurement with increasing energy of the beam (cf. Table 4.4), and the fact that the selections on the incident and exit angles were applied, is a strong indication that the random particle energy loss component may be due to the

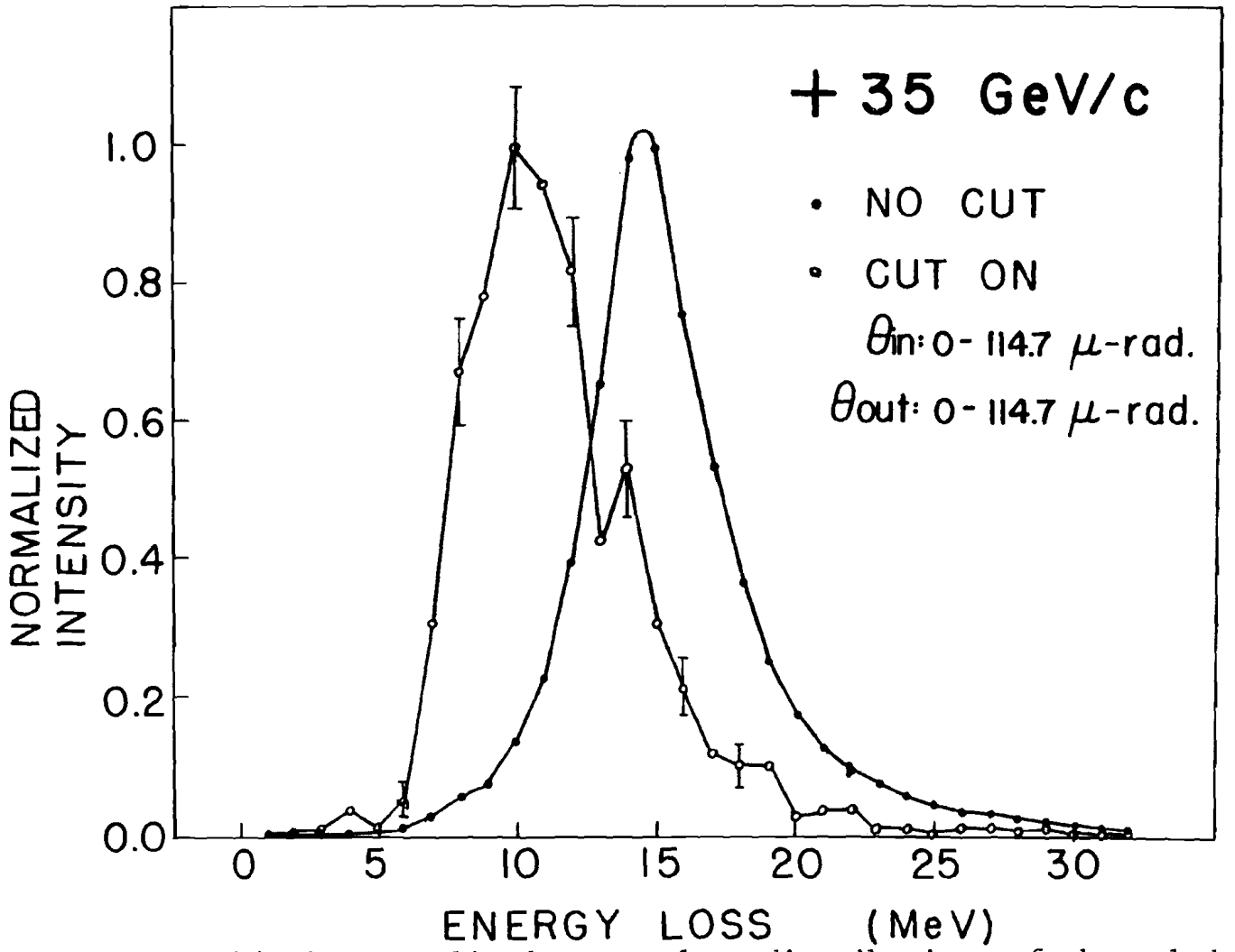

Fig. 9.3 (a) The normalized energy loss distributions of channeled (open circles) and random (solid circles) particles.

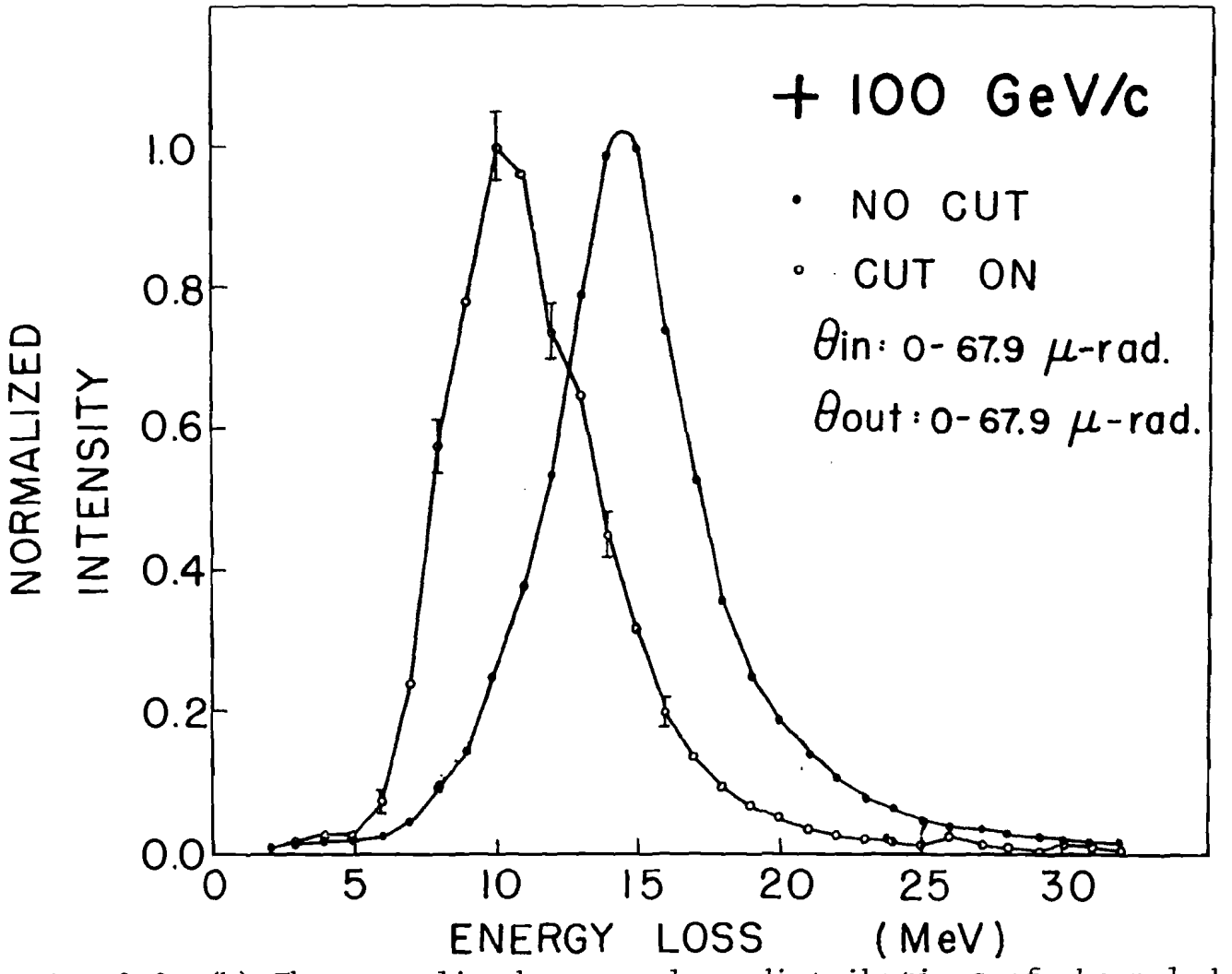

Fig. 9.3. (b) The normalized energy loss distributions of channeled (open circles) and random (solid circles) particles.

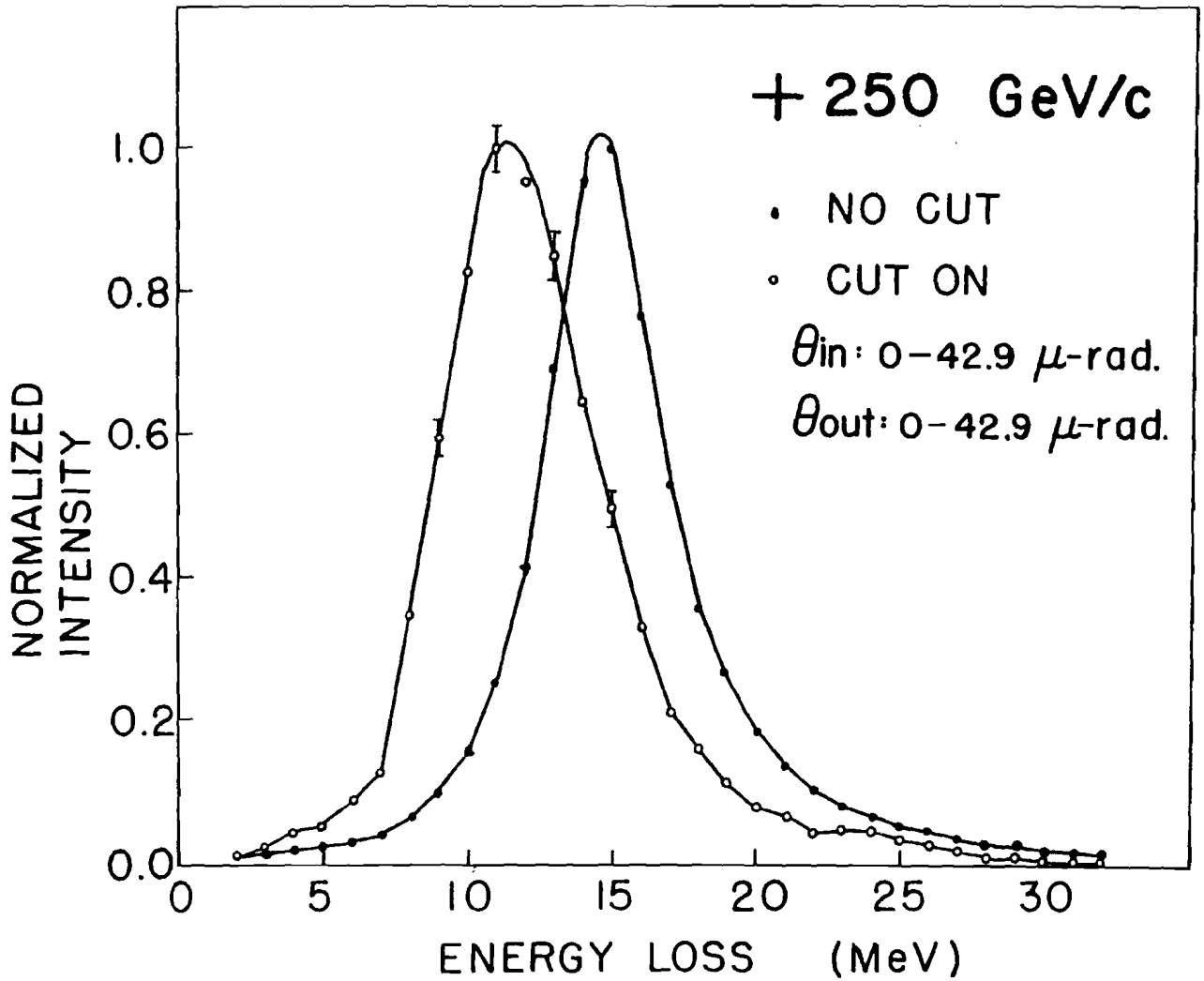

Fig. 9.3 (c) The normalized energy loss distributions of channeled (open circles) and random (solid circles) particles..

resolution in the incident and the exit angle measurement. Since the error in the angle measurement is largest at 35 GeV/c momentum, therefore the random component of the energy loss is also maximum at this momentum value.

9.4 ENERGY LOSS AND IMPACT PARAMETER (AXIAL ORIENTATION

Various authors [Bel78,De74,Es77] have proposed different mechanisms to calculate the stopping power of the channeled particles as a function of impact parameter, $\vec{b}$, in the transverse plane.

The results of this experiment agree well with Esbensen and Golovchenko's calculation [Es77]. They calculate the energy loss of the fast channeled particles on the basis of quantum perturbation methods. Their results, modified to include relativistic particles, is [Es78c]:

$$\left\langle \frac{dE}{dx}(\vec{b}) \right\rangle = \frac{2\pi Z_1^2 e^4 N}{mc^2\beta^2}\{[Z_2+Z(\vec{b})] \ln \frac{2mc^2\beta^2}{I^2(1-\beta^2)} - \beta^2 - Z_2\delta + C(\vec{b})\} \qquad 9.9$$

where $\vec{K}$ is the reciprocal lattice vector in the transverse space, $Z(\vec{b})$ is the average electron density at $\vec{b}$,

$$C(\vec{b}) = \sum_{\vec{K}\neq 0} e^{i\vec{K}\cdot\vec{b}} \ln\left(\frac{2mI}{\hbar^2 K^2}\right)\rho(\vec{K})$$

and

$$\rho(\vec{K}) = \langle 0|e^{-i\vec{K}\cdot\vec{r}}|0\rangle \qquad 9.10$$

The last term $\rho(\vec{K})$ is the fourier transform of the electronic charge density in the target atom in its ground state. It is also known as the atomic form factor.

Doyle and Turner [Do68] have given an eight parameter equation to calculate the atomic form factors of all the elements except hydrogen. The average electron density $Z(\vec{b})$ in the transverse space is obtained by taking the inverse fourier transform of the atomic form factor in the transverse reciprocal lattice space, i.e.,

$$Z(\vec{b}) = \sum_{\vec{K}} e^{i\vec{K}\cdot\vec{r}} \rho(K) \qquad 9.11$$

The comparison of the mean stopping power of Eq. 9.9 as a function of impact parameter with the experimental results was difficult to obtain for individual values of $\vec{b}$. This was because it was impossible to isolate, experimentally, the particles with a single impact parameter value.

A measure of the energy loss of best channeled

particles could nevertheless be obtained from the channeled particle energy loss distribution and compared with the theoretical prediction of Eq. 9.9. The best channeled particles were defined as the particles going through the center of the channel. For the <110> axis in the Germanium crystal, the center of the channel is equidistant from the six closest strings of atoms (Fig. 5.5) and the distance is b = 2.122 Å.

The distributions of the energy loss of 100 GeV/c beam particles along <110> axis in the Germanium crystal are shown in Fig. 9.4. The open triangles and the open circles represent the distributions with selections on incident angle of 0 to 45 micro-radians and 0 to 75 micro-radians, respectively. The two distributions have zero incident angle with respect to the <110> axis direction in common, and consequently they contain the best channeled particles.

The extrapolated intercepts on the low energy side of these two distributions lie at the same point (within experimental error). This type of behaviour is also observed in the 35 and 250 GeV/c data. This clearly indicates that the intercept of the channeled particles energy loss distribution is not too sensitive to the selections on the incident angle, as long as the best channeled particles are included in the selection.

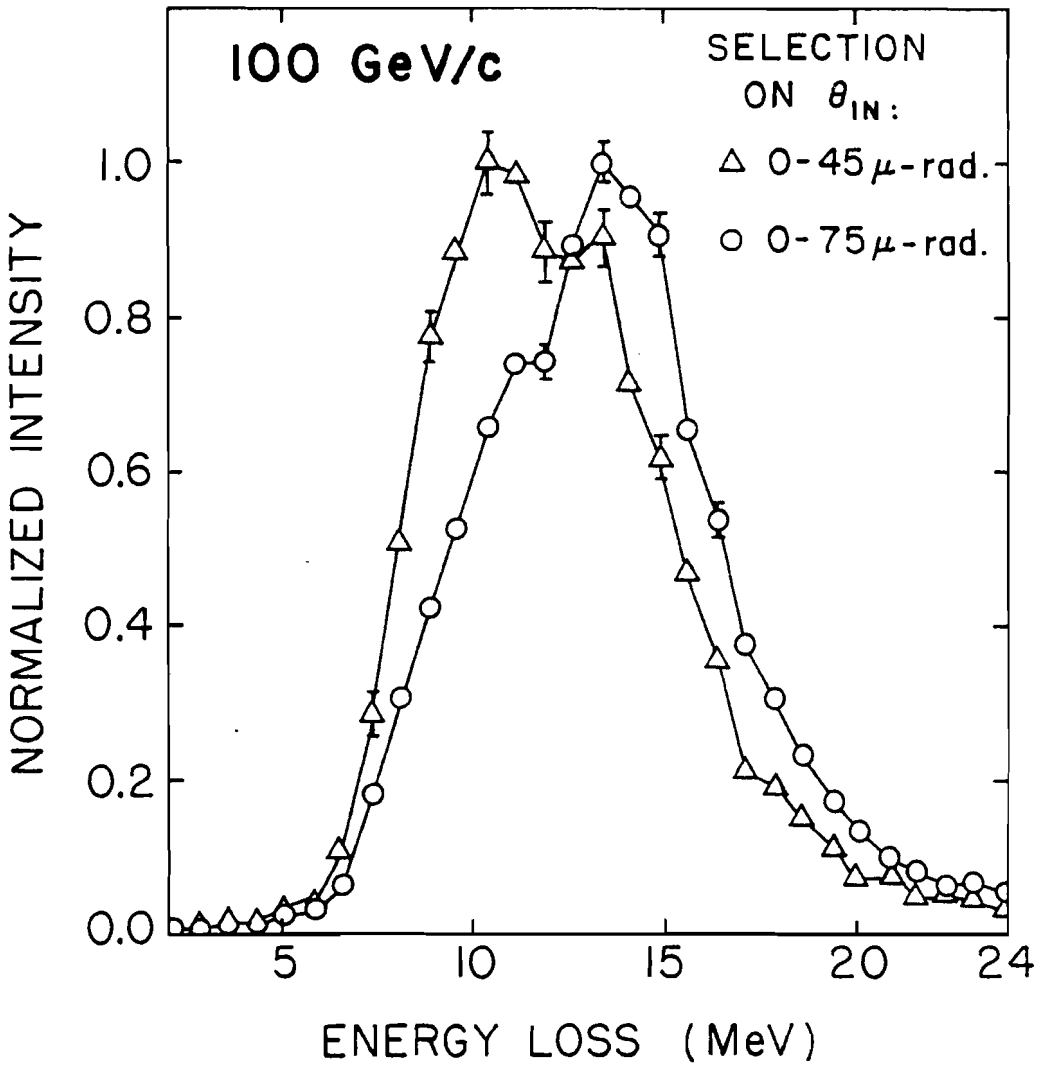

Fig. 9.4 Normalized energy loss distribution for two different selections on the incident angle.

Therefore, the intercept value on the low energy side of the channeled particles energy loss distribution was used for comparison with Esbensen and Golovchenko's calculation [Es77].

It was assumed that the energy loss of the best channeled particles follow the Landau distribution. The stopping power corresponding to the intercept value was then obtained from the mean stopping power of Eq. 9.9 by using the Landau distribution parameter, λ, defined in Eq. 9.2. The value of λ for the intercept on the low energy side of the Landau distribution is -2.5. With this value in Eq. 9.2 one obtains

$$\left(\frac{dE}{dx}(\vec{b})\right)_{Intercept} = \left\langle\frac{dE}{dx}(\vec{b})\right\rangle + \frac{\xi}{t}\{-1.077 + \ell n(\frac{\xi}{T_{max}})\} \qquad 9.12$$

where $\xi = \dfrac{2\, Z_1^2 e^4 N Z_2(\vec{b})}{mc^2\beta^2}$ and the other quantities have already been defined in previous sections. The intercept value of the stopping power, as calculated from Eq. 9.12, with the mean energy loss of the well channeled particles obtained from Ref. Es78a, is plotted as a solid line in Fig. 9.5. The experimental points are shown as open circles and they agree quite well with the predicted values. The experimental and the calculated values at the three beam momenta are listed below:

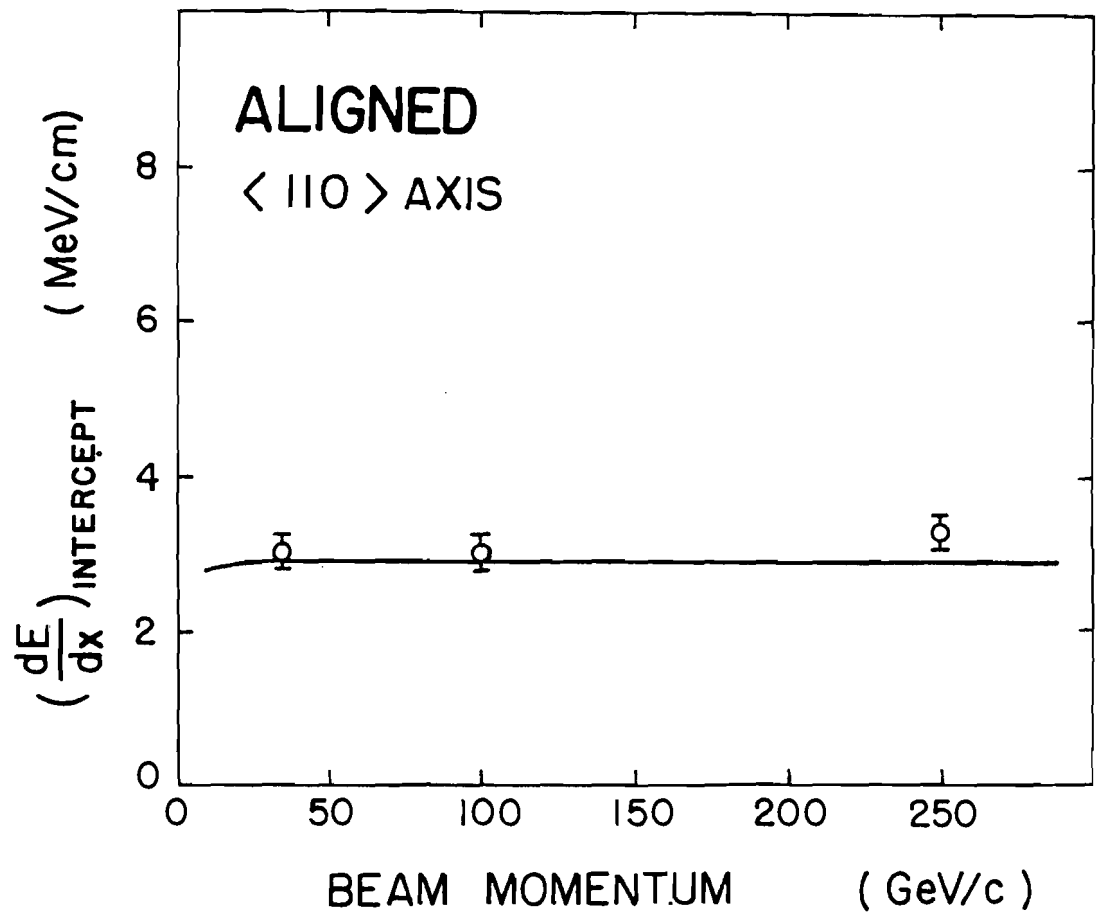

Fig. 9.5 The stopping power at the intercept value on the low energy side of the energy loss distribution for channeled particles. The solid line is the theoretical curve and the open circles are the experimental values.

$(dE/dx)_{intercept}$ (MeV/cm)	35 GeV/c	100 GeV/c	250 Gev/c
Experimental	3.06±0.20	3.05±0.20	3.32±0.20
Theoretical	2.90±0.02	2.91±0.02	2.91±0.02

It may be pointed out here that the authors of reference [Es78a] take the position of half the peak value on the low energy side of the channeled particle energy loss distribution as the reference point to compare their results with the theory. Since they had many more events in each configuration as compared to this experiment, they could apply stricter selections on the incident and exit angle and thereby eliminate almost completely the random component in the channeled particles energy loss distribution. Under those conditions they found that the position of half the peak value on the low energy side of the channeled particle energy loss distribution was not sensitive to selections on the incident and exit angles. They calculated the stopping power corresponding to half the peak value on the low energy side from Eqs. 9.9 and 9.2 with $\lambda = -1.6$.

9.5 ENERGY LOSS AND INCIDENT ANGLE (AXIAL CHANNELING)

Lindhard, in his famous 1965 paper on channeling [Li65] has derived expressions for the electronic and the nuclear stopping power as a function of the incident angle with respect to the crystal axis direction. He has

suggested that the nuclear stopping power will be very small compared to the electronic stopping power for particles with relativistic velocities. This difference will be even greater for channeled particles because of the absence of nuclear collisions for the best channeled particles. Therefore, the electronic stopping power for the channeled particles will be considered and the nuclear stopping power will be disregarded.

Lindhard gives the following form for the mean electronic stopping power as a function of the incident angle as

$$\left\langle \frac{dE}{dx}(\theta_{in}) \right\rangle_e = \left\langle \frac{dE}{dx} \right\rangle_e \{1 - \alpha e^{-2\theta_{in}^2/\psi_1^2}\} \qquad 9.13$$

where ψ_1 is the Lindhard critical angle defined in Sec. 2.1, $\langle dE/dx \rangle_e$ is the electronic stopping power for random orientation of the crystal and α is a constant whose value was suggested by Lindhard to be between 1/2 and 1.

Since the nuclear stopping power is neglected, the total mean stopping power has the same form as Eq. 9.13. The mean energy loss of the beam particles in a finite thickness of the crystal will then be given by

$$\langle \Delta E(\theta_{in}) \rangle = \langle \Delta E \rangle (1 - \alpha e^{-2\theta_{in}^2/\psi_1^2}) \qquad 9.14$$

A curve of the functional form of Eq. 9.14 was fitted to the experimental data of the mean energy loss versus the

incident angle (θ_{in}) at 35, 100, and 250 GeV/c beam momenta. These are shown in Figs. 9.6(a), (b), and (c). The values obtained for the parameters are:

	35 GeV/c	100 GeV/c	250 GeV/c
$\langle\Delta E\rangle$(MeV)	15.31±0.67	15.02±0.69	15.36±0.57
α	0.20	0.26	0.27
$\chi^2(n_D = 17)$	40.4	20.3	17.1

The curve fitting is best for 250 GeV/c data and worst for the 35 GeV/c data as can be seen from the χ^2 values. The worst fit for 35 GeV/c momentum was due to the bad resolution of the system for angle measurements at that momentum (see Table 4.4).

The mean energy loss, $\langle\Delta E\rangle$, agrees well with the values presented in Sec. 9.2 for random orientation.

The general behaviour of the energy loss as a function of the incident angle with respect to the axis direction follows Lindhard's prediction quite well to the highest momentum of the beam particles in this experiment and the parameter values are essentially unchanged with energy.

9.6 MEAN ENERGY LOSS OF WELL CHANNELED PARTICLES (PLANAR CHANNELING)

The energy loss distribution for 35 and 250 GeV/c beam particles are shown in Figs. 9.7(a) and (b),

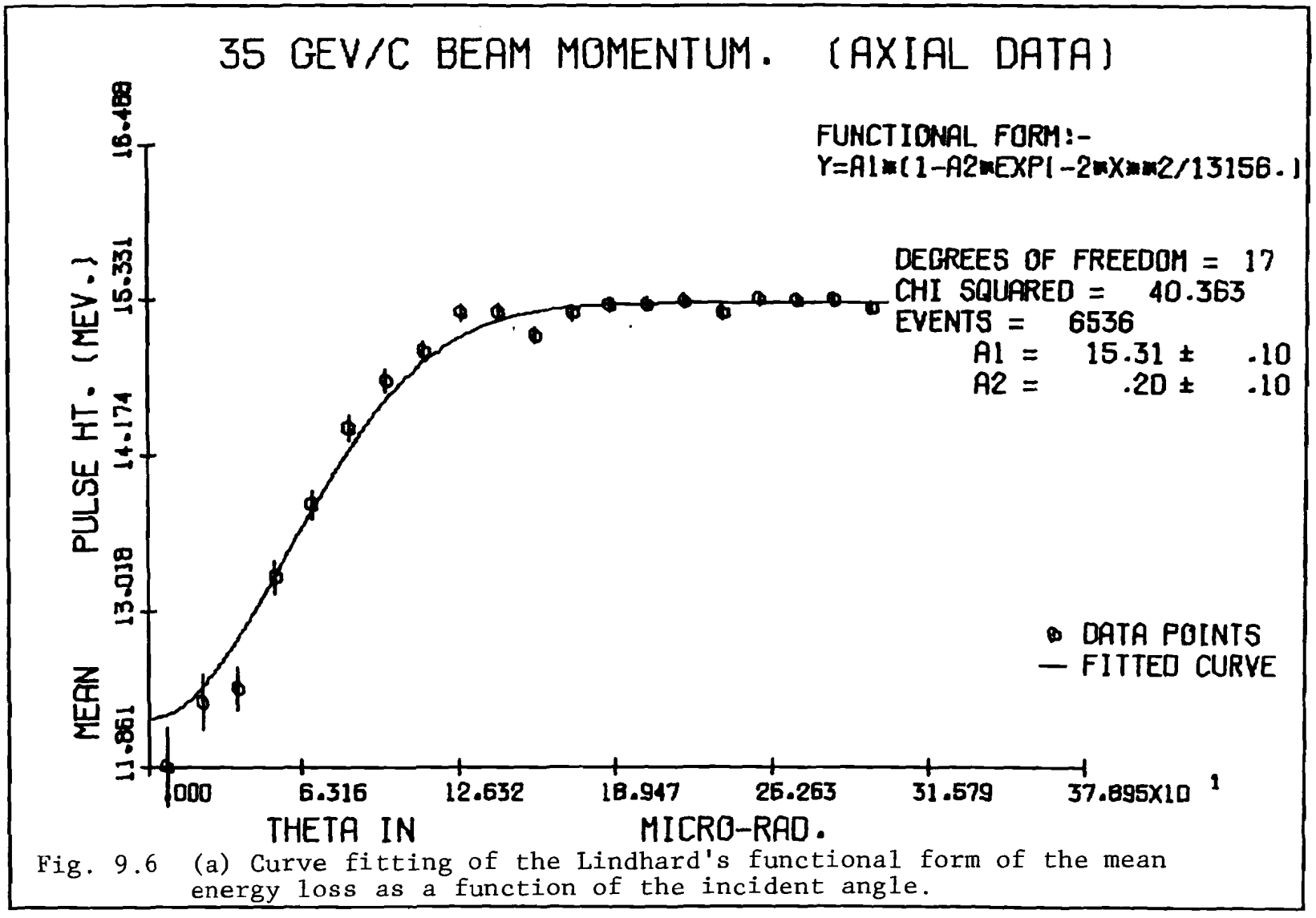

Fig. 9.6 (a) Curve fitting of the Lindhard's functional form of the mean energy loss as a function of the incident angle.

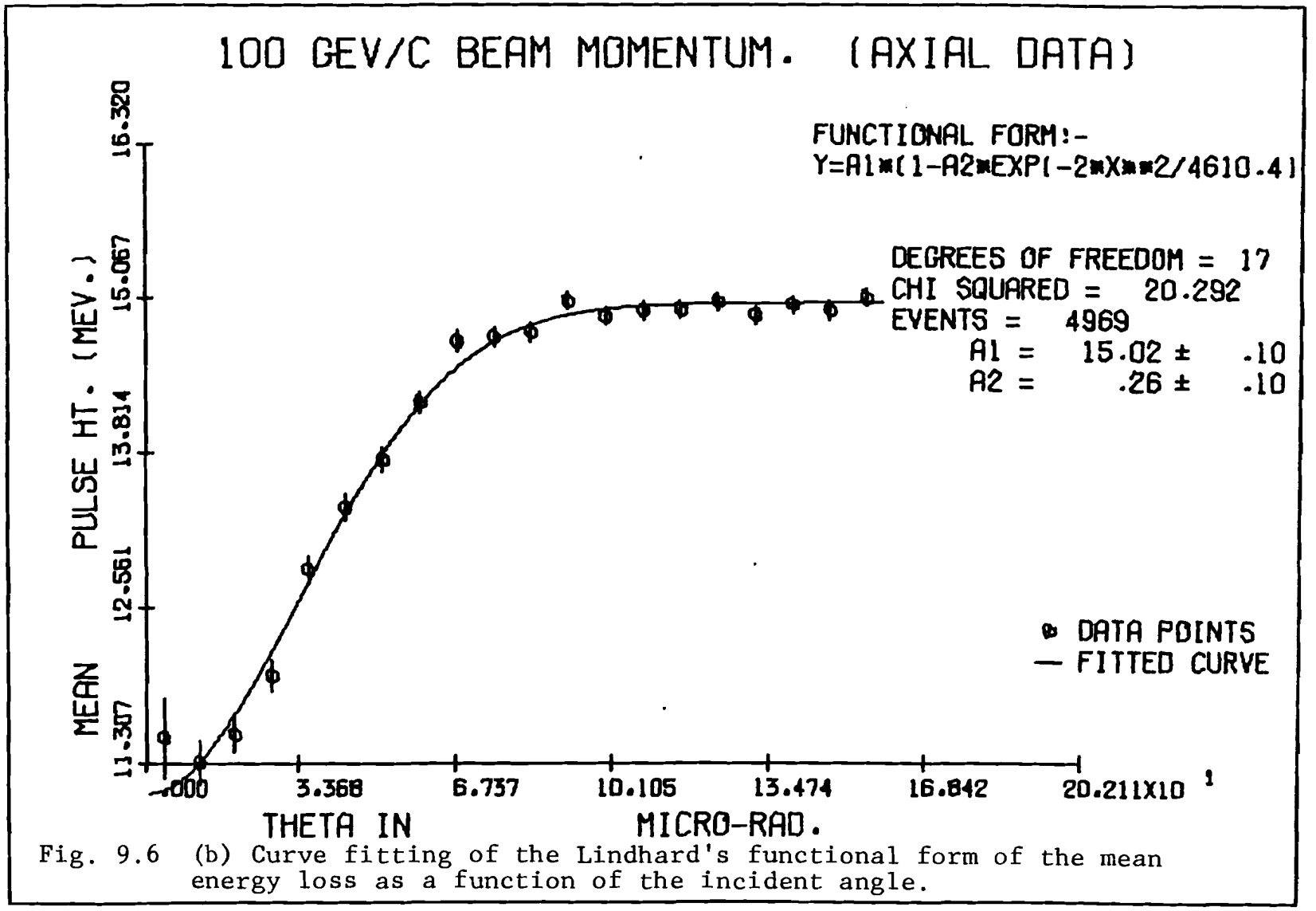

Fig. 9.6 (b) Curve fitting of the Lindhard's functional form of the mean energy loss as a function of the incident angle.

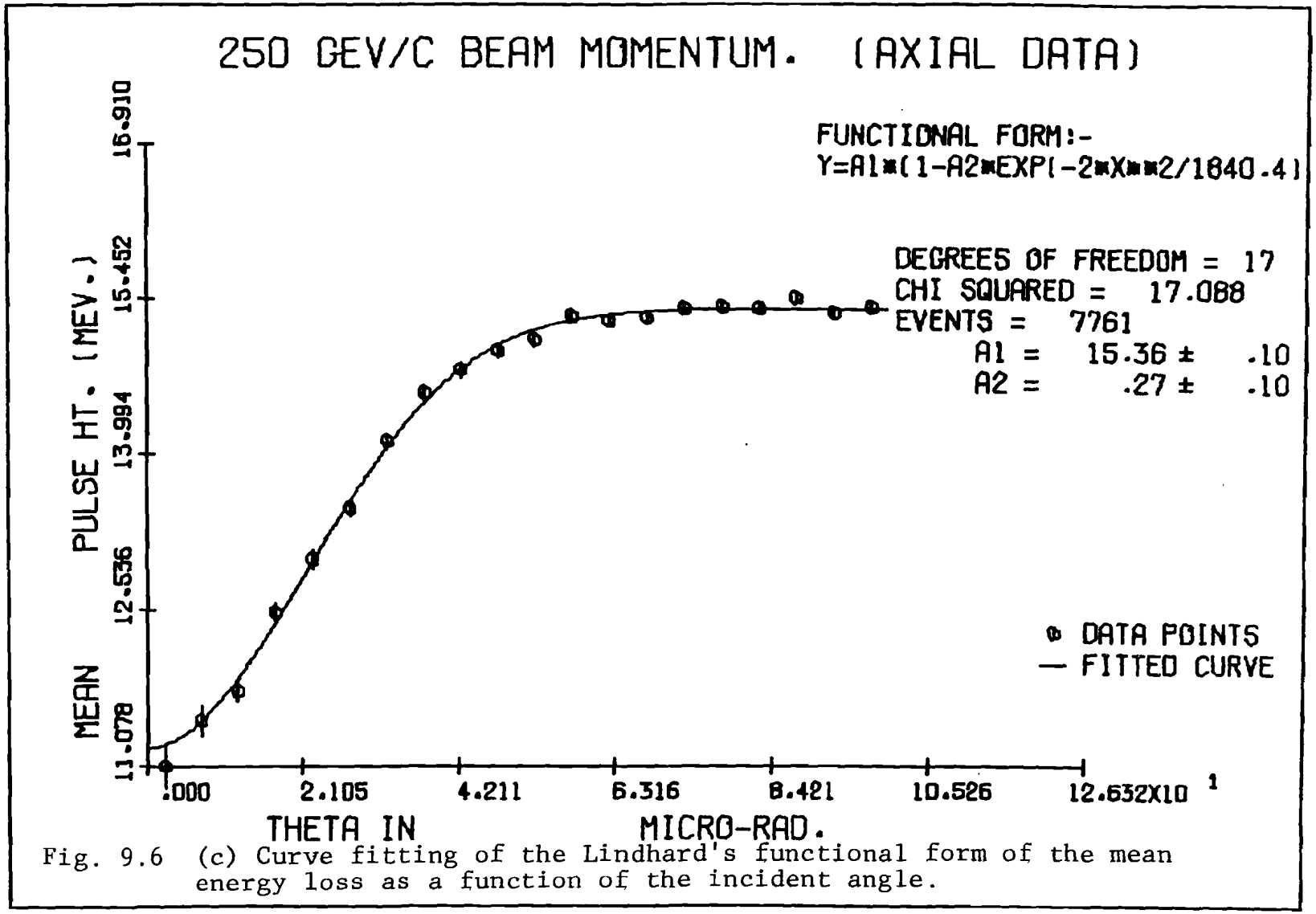

Fig. 9.6 (c) Curve fitting of the Lindhard's functional form of the mean energy loss as a function of the incident angle.

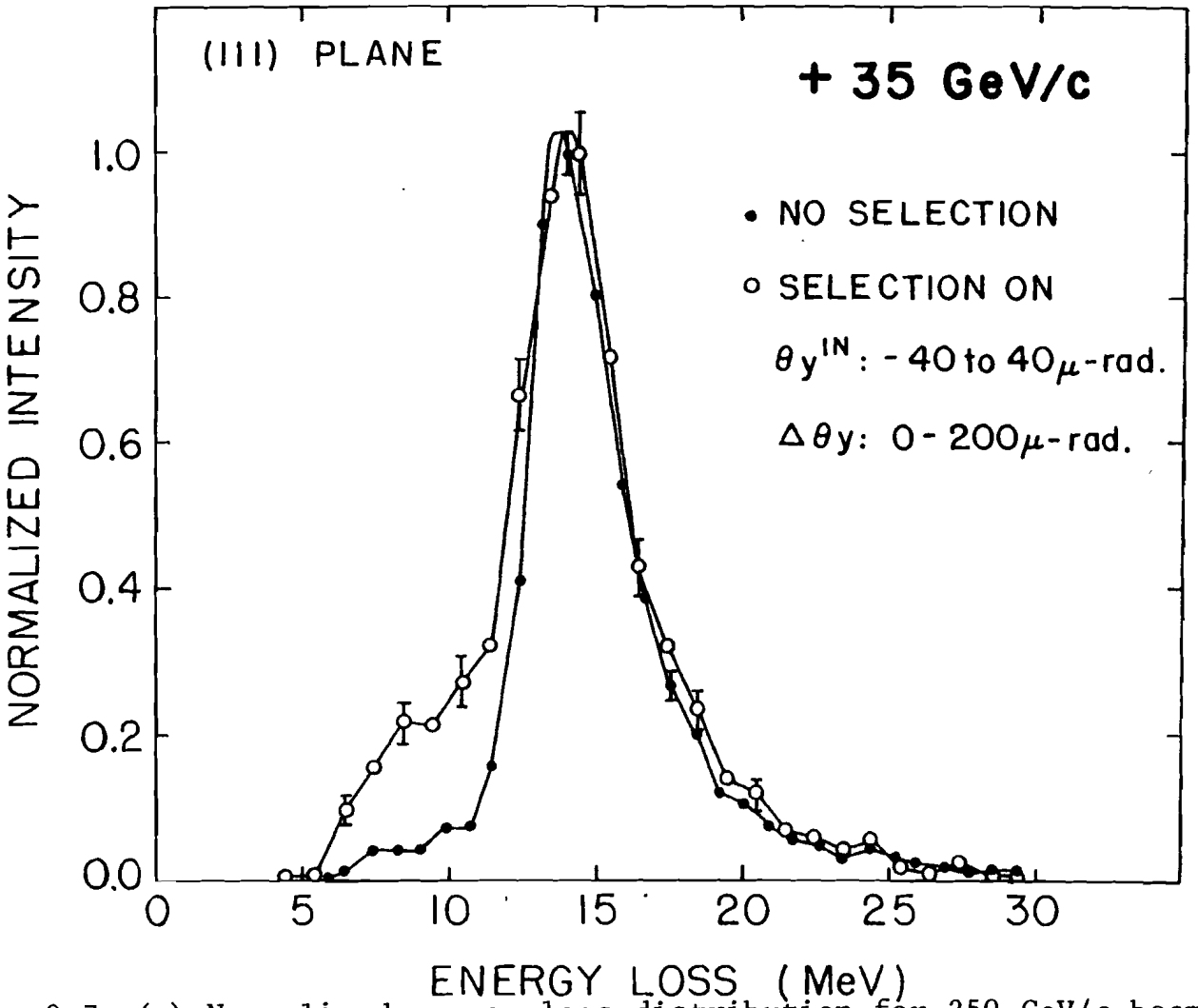

Fig. 9.7 (a) Normalized energy loss distribution for 250 GeV/c beam momentum. The selections are indicated in the figure.

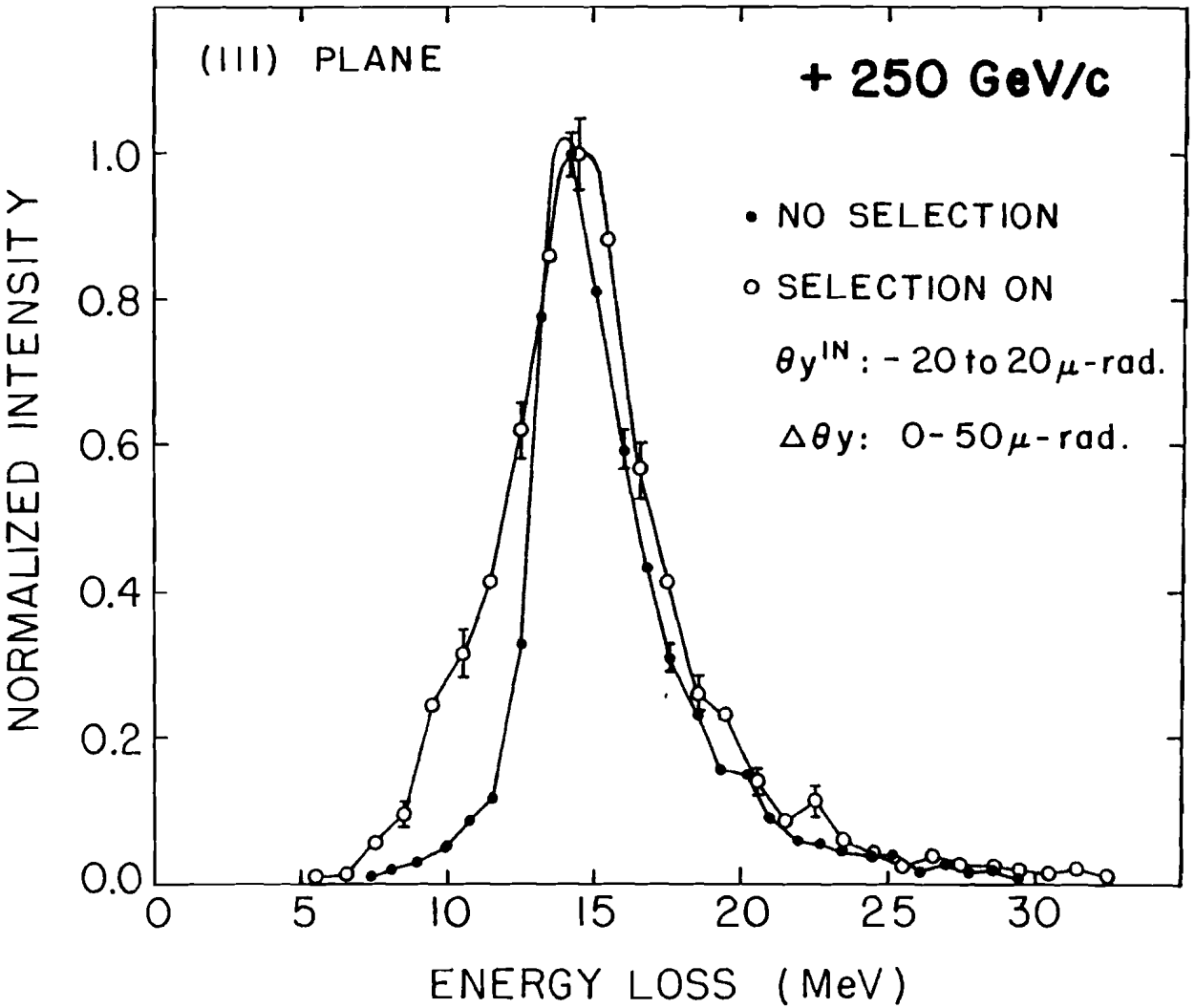

Fig. 9.7 (b) Normalized energy loss distribution for 35 GeV/c beam momentum. The selections are indicated in the figure.

respectively. The solid circles represent distribution with no selection on incident angle. The open circles represent distributions with a selection on the Y-component of the incident angle around the origin, which is along the (111) planar direction in the crystal. A selection on the Y-component of the scattering angle, $\Delta\theta_Y$, was also applied. The range of the selections for the two beam momenta values are indicated in the figures. These two selections were applied, in combination, to pick out as many well channeled particles as possible and at the same time have enough events to get statistically significant results.

Since the multiple scattering resolution of the system (see Table 4.4) is of the same order of magnitude as the planar channeling distribution half widths, $\psi_{\frac{1}{2}}$ (cf. Sec. 5.2), there was a large contamination of the random beam particle energy loss distribution.

It was explained in detail in Sec. 9.4 that the intercept value on the low energy side of the energy loss distribution of the channeled particles could be used for comparison with the theoretical predictions. These intercept values were obtained from the shoulders of the channeled particles energy loss distribution in Figs. 9.7(a) and (b). The stopping powers corresponding

to the intercept value of the energy loss were compared to the calculations of Esbensen and Golovchenko [Es78c] using the same technique as used for the energy loss of the axially channeled particles described in Sec. 9.4.

The calculated and the experimental values are listed below:

$(dE/dx)_{intercept}$	35 GeV/c	250 GeV/c
Experimental (MeV/cm)	2.7±0.3	3.1±0.3
Calculated (MeV/cm)	2.99±0.05	3.15±0.05

From these numbers one can see that there is good agreement between the Esbensen and Golovchenko calculations [Es78c] and the experimental results.

CHAPTER 10

NEGATIVE BEAM PARTICLES

The behaviour of the negatively charged beam particles is expected to be different from that of the positively charged particles, when they are interacting with rows of atoms along a channeling axis direction. Whereas the positive particles are steered away from the higher potential regions of the rows of atoms, the negatively charged particles are attracted towards them. This leads to an increase in physical processes involving small impact parameter collisions, such as large angle Rutherford scattering, nuclear reactions, multiple scattering, x-ray production, etc. This is in contrast to a decrease in such processes for positively charged particles.

The increase in large angle scattering processes will lead to a broad dip in the transmission yield of the negative particles in the exit angle plane around the axis direction. The particles that are incident at small angle to the <110> axis direction and have large angular momentum with respect to the axis direction will stay away from the high density regions of rows of atoms. This is due to the repulsive angular

momentum term because of which the particles spiral around one string of atoms, as they pass through the crystal. This will lead to a decrease in large angle scattering of the beam particles with such angular momentum and therefore a peak in the middle of the broad dip is expected to be observed in the exit angle plane. This type of behaviour has been observed for negative particles at lower energies [Es77]. The width of the dip was 3 to 4 times the critical angle.

The projected exit angle distribution with selection of 1 to 14 MeV on energy loss showed a broad dip around the <110> axis (Fig. 10.1). The low energy loss selected on particles that did not approach the string too closely. This broad dip indicates that most of the particles undergo small impact parameter collisions with the string when they are incident at small angles to the crystal axis direction. The peak in the center of the broad dip was not observed probably because of the bad statistics of the data.

The data for the negative particles were taken only at 35 GeV/c beam momentum. This was unfortunate because the multiple scattering resolution of the system was appreciably greater at this momentum than what it would be at the 100 and 250 GeV/c momenta.

Since there is no comprehensive theory of negative

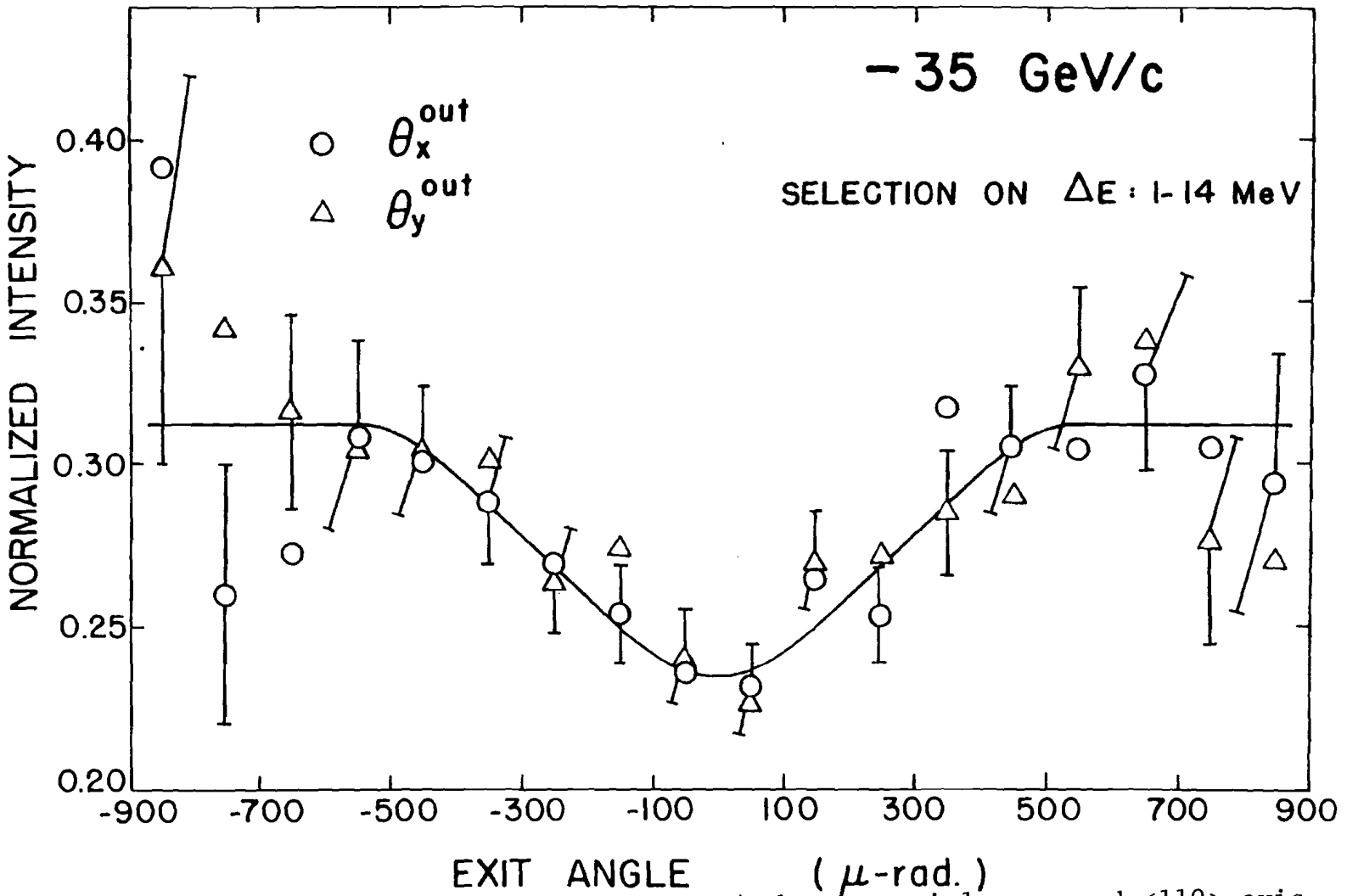

Fig. 10.1 Exit angle distribution of -35 GeV/c beam particles around <110> axis. The <110> axis is at the origin of the exit angle axis.

particle behaviour in the axial channeling region, as there is for positive particles (Lindhard's Theory, [Li65]), a qualitative comparison was made between the behaviour of the negative and the positive particles at 35 GeV/c beam momentum, and these are presented in the following sections.

10.1 AXIAL ORIENTATION

The negative particles that are incident at small angles to the <110> axis in the crystal are attracted towards the positively charged nuclei in the string of atoms along the axis direction. These particles spend more time in the high density regions near the center of the string in the transverse plane and therefore lose more than average energy in the crystal. The particles that go along the channeling axis direction may therefore be identified by their energy loss. A greater proportion of particles going along the channeling axis direction would be contained among particles which have higher than average energy loss. This is also seen in the energy loss spectrum of the negative particles in Sec. 10.5.

Negative particles with energy loss in the range of 17 to 32 MeV were selected and their normalized distribution in the exit angle is shown in Fig. 10.2. The distribution was normalized by dividing the data with a similar distribution with no selection applied.

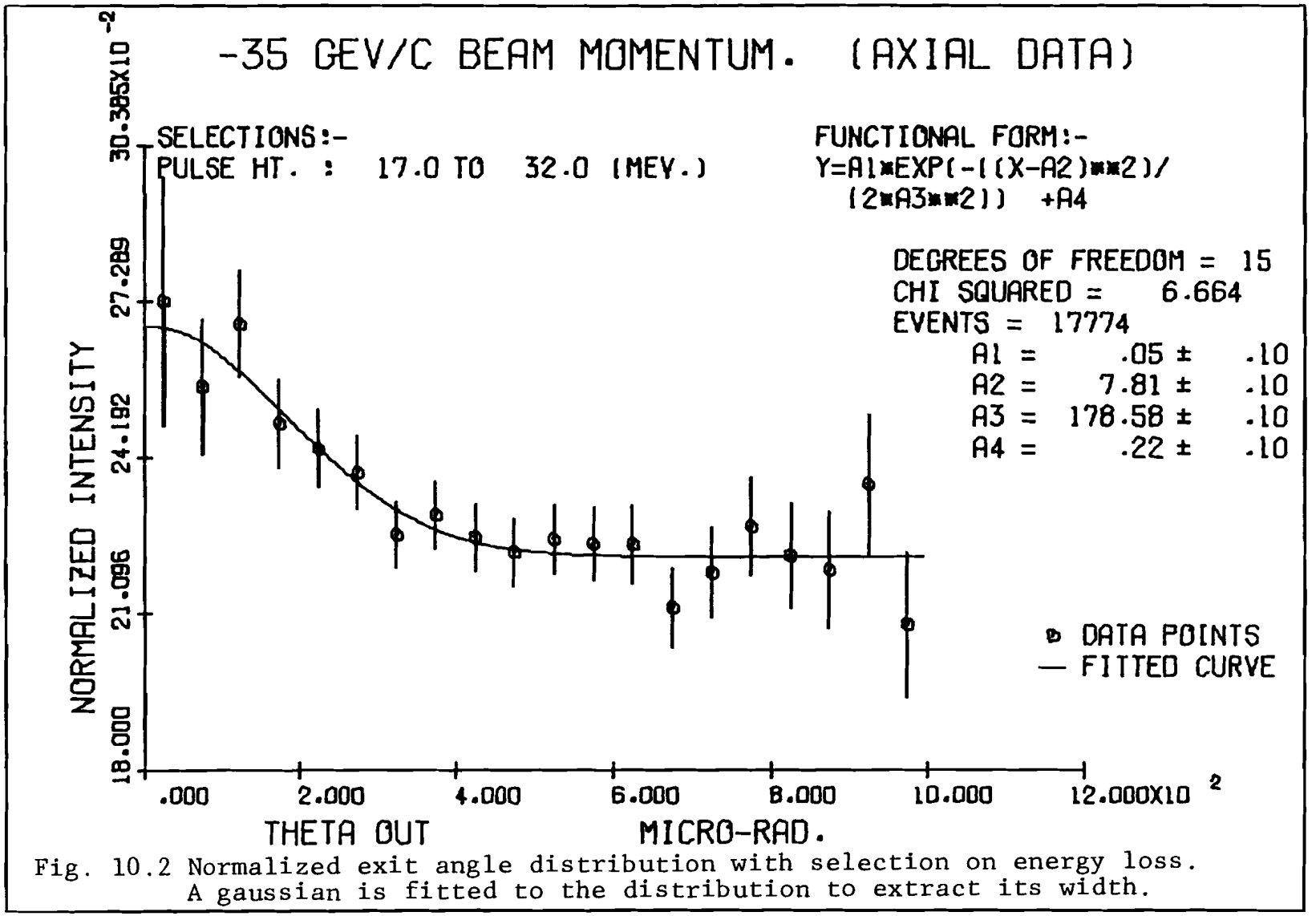

Fig. 10.2 Normalized exit angle distribution with selection on energy loss. A gaussian is fitted to the distribution to extract its width.

An enhancement in the intensity was observed near the channeling axis direction, which is at the origin of the exit angle axis. A gaussian curve was fitted to the distribution and the Half Width at Half the Maximum (HWHM) value, $\psi_{\frac{1}{2}}$<110>, was extracted from the fitted parameters. This value of $\psi_{\frac{1}{2}}$<110> for the negative particles and the positive particles value are listed below

	+35 GeV/c	-35 GeV/c
$\psi_{\frac{1}{2}}$<110> (micro-radians)	45.22±9.52	210.18±0.95

The $\psi_{\frac{1}{2}}$<110> value for the negative particles is ∿4.5 times that of the positive particles. This is consistent with the broad width observed for the negative particles distribution in other experiments.

10.2 AZIMUTHAL DIFFUSION

The rms distribution of the azimuthal scattering angle for -35 GeV/c (open circles) and +35 GeV/c data (solid triangles) is shown in Fig. 10.3. The theoretically predicted value of 1.813 (cf. Eq. 7.1) for statistical equilibrium in the azimuthal scattering angle distribution is also shown.

The data indicate that the positive and the negative particles attain statistical equilibrium in the azimuthal scattering angle distribution for incident

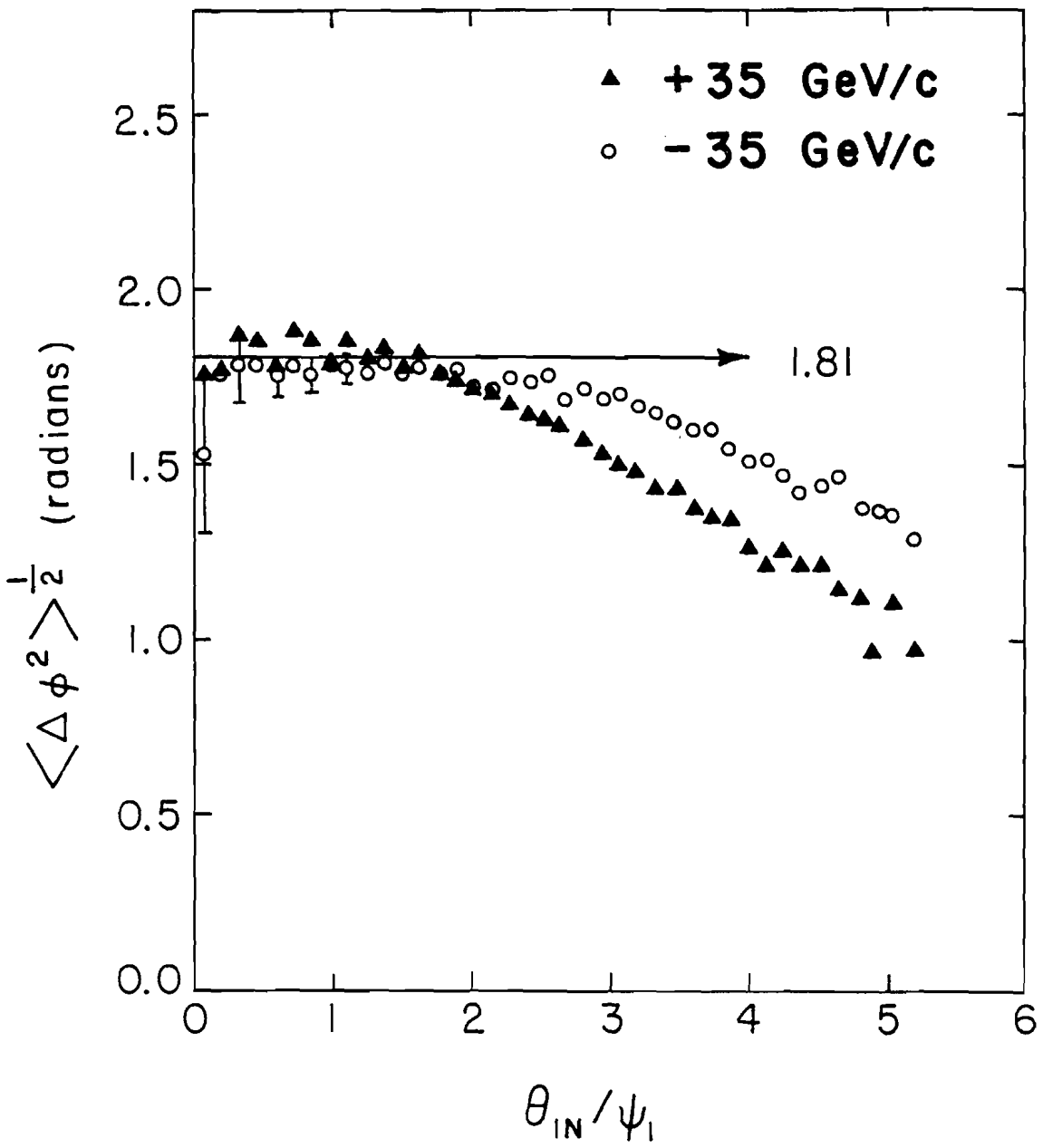

Fig. 10.3 The rms azimuthal scattering angle distribution for -35 GeV/c (open circles) and +35 GeV/c (solid triangles) data. The theoretically expected value of 1.81 for equilibrium in the azimuthal scattering angle is also indicated.

angle of zero to $2\psi_1$ with respect to the <110> crystal axis. For incident angle larger than $2\psi_1$, the rms spread of the azimuthal scattering angle decreases more slowly for negative particles than for positive particles.

The equilibrium in azimuthal scattering angle for negative particles is due to the spiraling of the beam particles around the string of atoms because of the particle angular momentum. This process is basically different from the azimuthal scattering of the positive particles (Sec. 7.2) but the net effect of the statistical equilibrium in the azimuthal diffusion process is same for both positive and negative particles.

10.3 RADIAL DIFFUSION

Figure 10.4 is a plot of the shift of mean value of the radial angle distribution for positive (solid triangles) and negative particles (open circles) passing through the crystal.

The beam shift in the radial direction is similar for the positive and the negative particles with incident angles greater than the critical angle, ψ_1. For incident angle values of less than the critical angle the change in the mean value of the radial angle distribution does not decrease for negative particles as compared to the positive particles. This type of

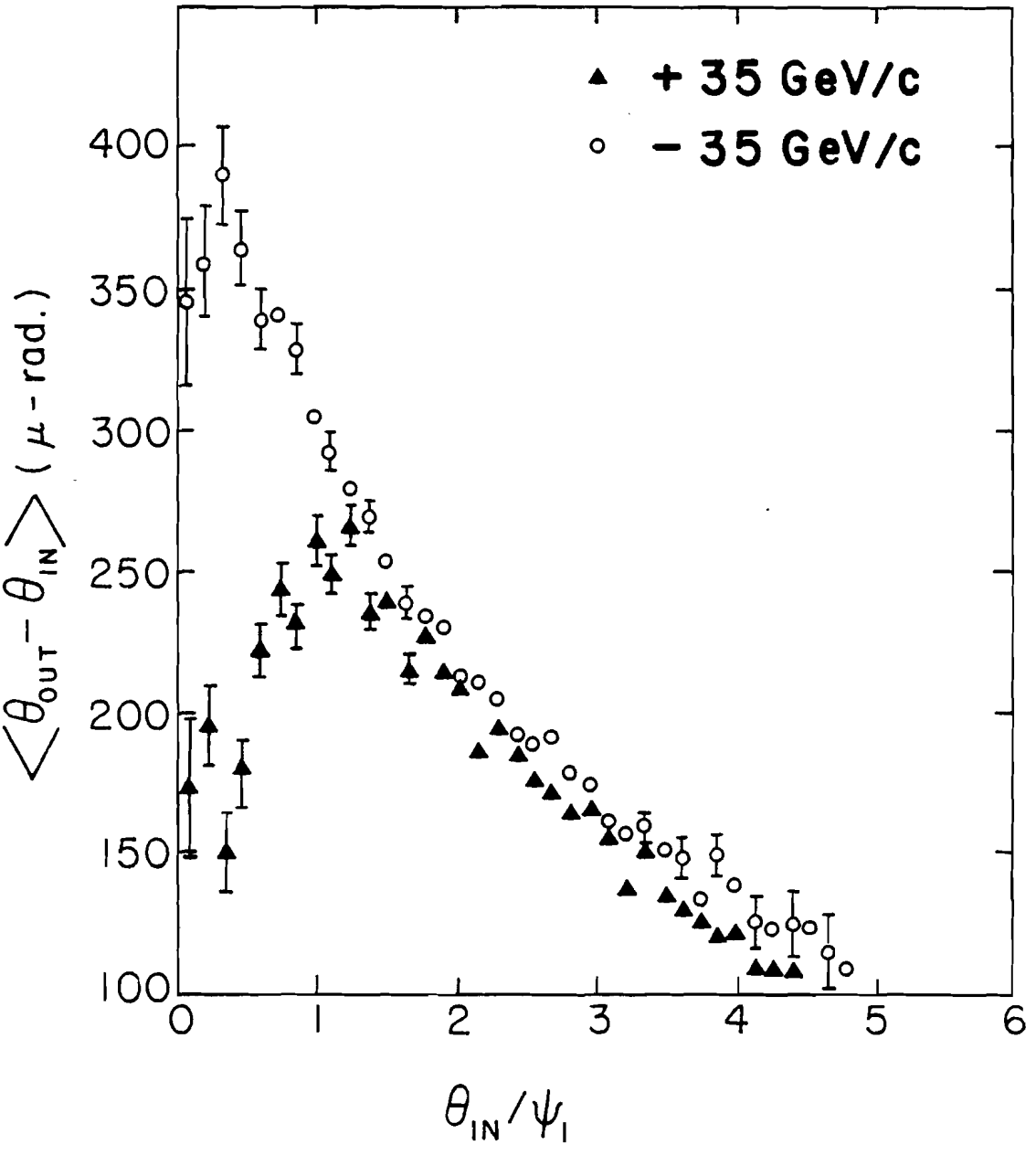

Fig. 10.4 The shift in the mean value of the angle with respect to the <110> channeling axis direction for positive (solid triangles) and negative (open circles) particles passing through the crystal.

behaviour is expected of the negative particles because, instead of being gently steered away from the string direction, as is the case with positive particles, they are attracted towards the string of atoms and undergo greater scattering than the positive particles.

The change in the mean transverse energy of the positive and the negative particles is shown in Fig. 10.5. The mean transverse energy shift is similar and constant for the positive and the negative beam particles incident at angles greater than the critical angle ψ_1. For angles of incidence less than the critical angle there is an increase in the change of the mean transverse energy for the negative particles in contrast to a decrease, relative to the random case, for the positive particles. This is again related to the greater radial scattering of the negative particles incident at small angles to the string of atoms.

10.4 MULTIPLE SCATTERING

The root mean square (rms) spread of the multiple scattering angle, $\langle\Delta\theta^2\rangle^{\frac{1}{2}}$ for the positive and negative particles are plotted in Fig. 10.6. The random orientation value for positive particles is also indicated in the figure.

The $\langle\Delta\theta^2\rangle^{\frac{1}{2}}$ value is similar for the positive and the negative particles with incident angle in the quasi-

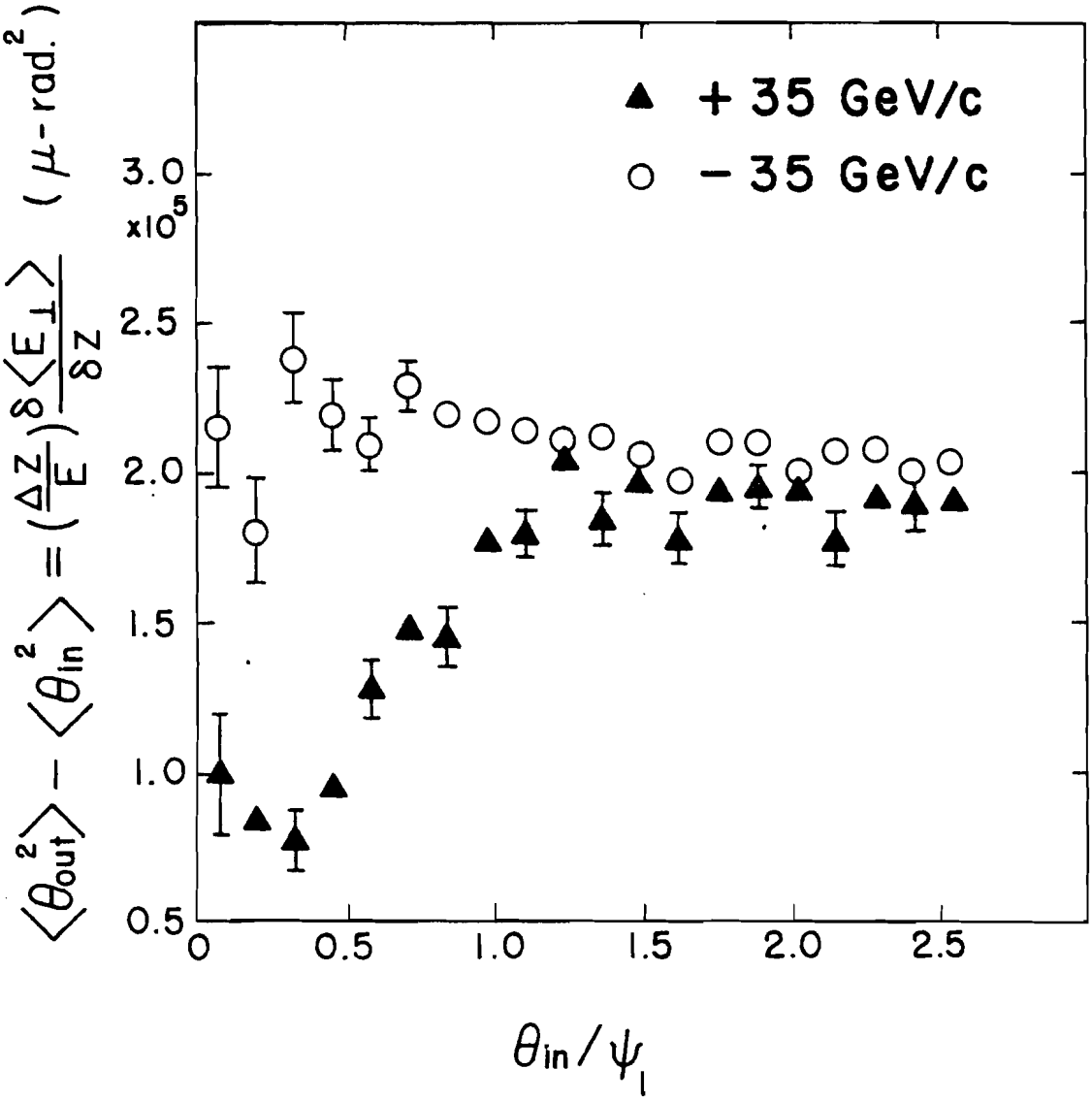

Fig. 10.5 The change in the mean transverse energy of the positive (solid triangles) and negative (open circles) beam particles are plotted as a function of the scaled incident angle.

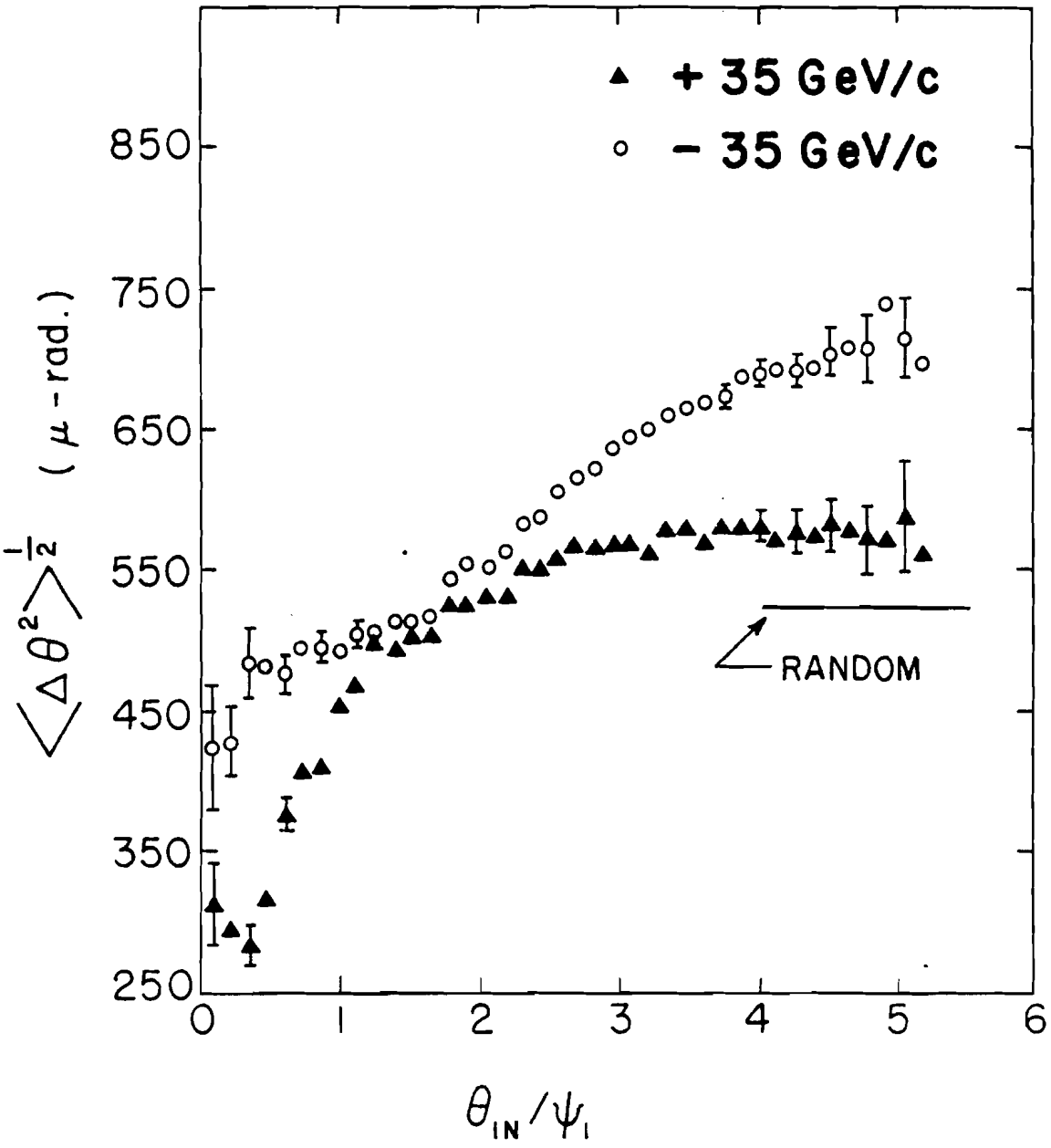

Fig. 10.6 The rms spread of the multiple scattering angle for positive (solid triangles) and negative (open circles) beam particles. The theoretically predicted value for random orientation is also indicated.

channeling region, i.e., ψ_1 to $2\psi_1$. For incident angle values smaller than the critical angle of channeling the multiple scattering for negative particles is larger than the positive particles. This is due to the greater interaction with the string of atoms along the <110> axis for negative particles because of the attractive nature of the string continuum potential.

For beam particles incident at greater than twice the critical angle of channeling, ψ_1, the multiple scattering angle spread is again larger for negative particles. In this case the azimuthal scattering angle distribution is responsible for the larger value of $\langle\Delta\theta^2\rangle^{\frac{1}{2}}$ (cf. Sec.10.2). The angular momentum of the negative particles with respect to the string of atoms would swing them around the string in the first few collisions with the string and thereafter the beam would behave as if the crystal were randomly oriented.

From the multiple scattering and the azimuthal scattering angle distributions one can see that the string affects the negative particles over a wider range of incident angles than positive particles. This is supported by the large HWHM, i.e., $\psi_{\frac{1}{2}}$<110> value for negative particles (see Sec. 10.1) as compared to the $\psi_{\frac{1}{2}}$<110> value for positive particles (cf. Sec. 5.1).

10.5 ENERGY LOSS

The energy loss distribution for the negative particles is shown in Fig. 10.7. The open circles represent data with no selection and the solid circles the distribution with selection on the incident angle of zero to 120.0 micro-radians.

The distribution with selection, which represents negative particles incident at small angles to the string direction, was shifted towards the higher energy loss side. This indicates an increase in the energy loss of the negative particles incident at small angles to the channeling axis direction. This is expected because of the attractive nature of the string potential for negative particles, which leads to an increase in the interaction of the particles with the nuclei and therefore an increase in the energy loss.

The mean energy loss of the positive and the negative particles as a function of the scaled incident angle is shown in Fig. 10.8. This clearly shows the marked difference in the behaviour of the positive and the negative channeled particles.

The mean energy loss actually increases for negative particles when the particles are incident within the critical angle region. In contrast, the positive particles show a significant decrease in the mean energy loss for particles incident close to the <110> axis direction.

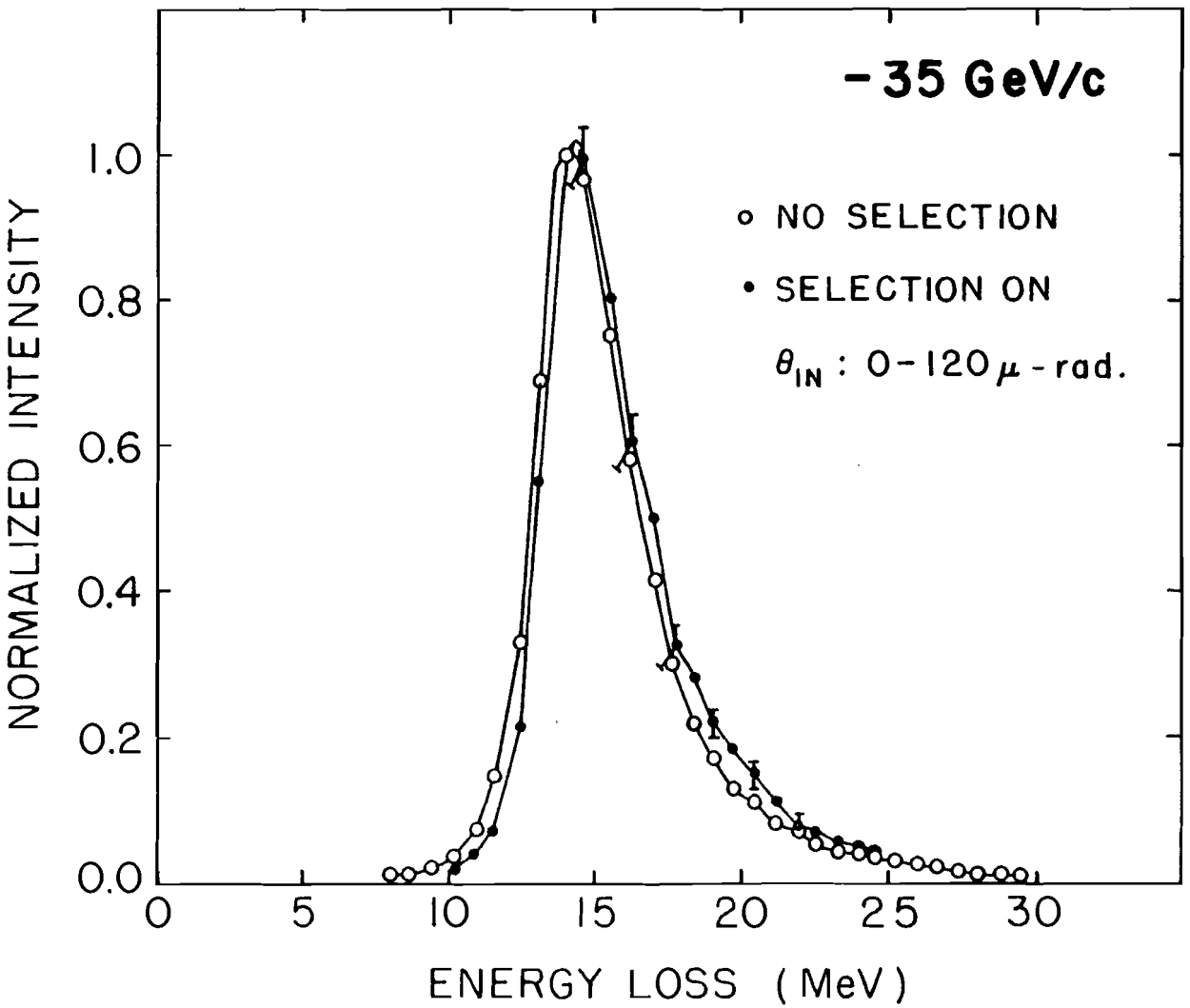

Fig. 10.7 Normalized energy loss distribution for -35 GeV/c particles. The selections are indicated in the figure.

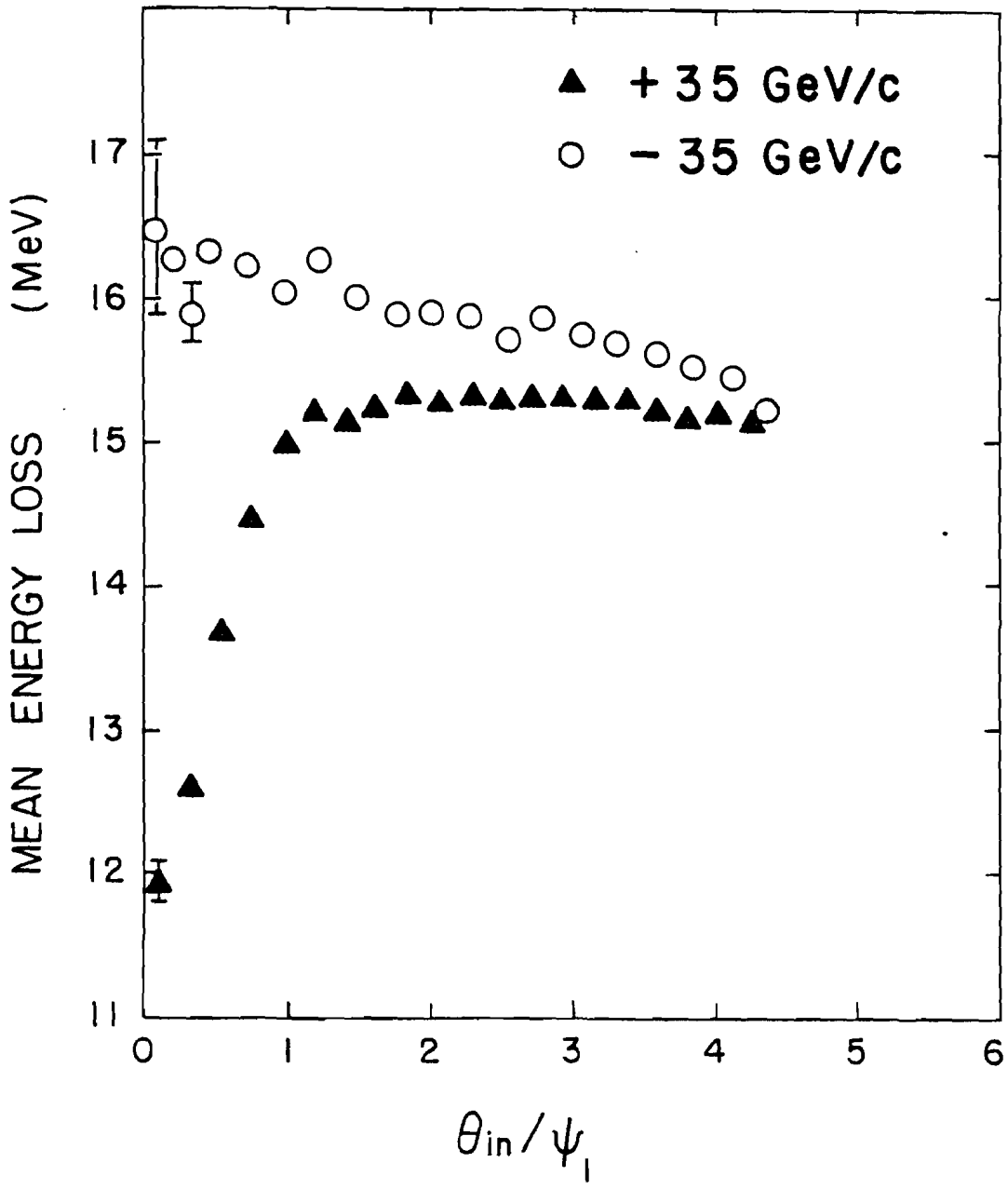

Fig. 10.8 The mean energy loss of 35 GeV/c positive (solid triangles) and negative (open circles) particles as a function of the scaled incident angle.

CHAPTER 11

CONCLUSIONS

11.1 SUMMARY OF THE RESULTS

This thesis describes an experiment on channeling of a mixed beam of pions, kaons, and protons through a 2 cm thick hyperpure Germanium single crystal, performed at 35, 100, and 250 GeV/c beam momentum values. The axial and the planar channeling data were taken for the <110> axis and (111) plane, respectively. Data with negative particles was taken only at 35 GeV/c momentum with crystal oriented along <110> axis. The results of the data analysis, summarized in the following paragraphs, pertain to the above beam and crystal configurations.

The axial and the planar channeled particle distribution widths were found to scale as $1/\sqrt{E}$, as predicted by Lindhard (Chapter 5).

Blocking dips were observed when beam particles with higher than average energy loss were selected. The widths of the blocking dips were found to be larger than the axial channeling widths and they scaled as $1/\sqrt{E}$. This is in accordance with Lindhard's theory

where blocking is defined as a complementary process to channeling (Chapter 6).

The transverse motion of the beam around the axis position was resolved into the radial and the azimuthal components.

For the 2 cm thick crystal, Lindhard's [Li65] rough estimate, as well as the Golovchenko's [Go76] more detailed calculation predicts statistical equilibrium in the azimuthal component of the transverse motion of channeled particles (cf. Sec. 2.4). This was actually observed for not only the channeled particles but also quasi-channeled particles (cf. Sec. 7.2). The scattering in the azimuthal direction, about the <110> axis, persisted (to a lesser extent) beyond the quasi-channeling region and was appreciable even for particles incident at four times the critical angle for channeling, ψ_1<110>, in the 250 GeV/c data (cf. Sec. 7.1). This implies that the influence of the string extends far beyond the critical angle of channeling.

The diffusion function for the radial motion rose sharply with increasing angle of incidence with respect to <110> axis direction. It peaked in the neighbourhood of the critical angle and then rose very slowly beyond the critical angle region (cf. Sec. 7.3.1).

The radial component of the transverse motion was

explained quite well by the diffusion equation for axial symmetry, for beam particles incident at angles of zero to the critical angle of channeling (cf. Sec. 7.3.2). For angle of incidence in the neighbourhood of the critical angle and the quasi-channeling region ($\theta_{in} \sim \psi_1$ to $2\psi_1$), the computer simulation results were in good qualitative agreement with the radial component of the transverse motion of the beam (cf. Sec. 7.5). The simulation was based on the impulse collision approximation of the beam particles with the continuum potential due to the string of atoms along the channeling axis direction (Sec. 2.1). This indicates that the Lindhard's continuum potential for the string of atoms is a good approximation for calculating the motion of the channeled as well as the quasi-channeled particles.

The decrease in the transverse energy of the 250 GeV/c beam particles for angle of incidence greater than $\sim 3.5\ \psi_1$ (cf. Sec. 7.3.2 suggested that the cooling of the transverse energy of the channeled particles could take place for higher beam momentum values. An upper limit of $\sim$3 TeV/c beam momentum was estimated for the <110> axis in the 2 cm thick Germanium single crystal.

The multiple scattering angle spread of the well channeled particles was found to scale as 1/E (Chapter

8). This is the functional form predicted by Bohr and Williams [Boh48,Wi29] for particles incident on a crystal in random orientation. Their prediction for the rms spread of the multiple scattering angle was in agreement with the experimental value at 250 GeV/c momentum for random orientation of the crystal (cf. Fig. 8.1).

The energy loss distribution of the 250 GeV/c particles incident on the randomly oriented crystal followed the Landau distribution (cf. Sec. 9.1).

The density effect and the restricted energy loss of the delta rays were important corrections in the calculation of the mean stopping power for beam particles incident on a randomly oriented crystal. The experimentally obtained mean stopping power agreed quite well with the calculated values (cf. Sec. 9.2).

The stopping power corresponding to the intercept on the low energy side of the energy loss distribution of the well channeled particles were compared with Esbensen and Golovchenko's [Es77]calculation. Reasonable agreement was found between the results of this experiment and their predictions.

The mean energy loss of the channeled particles, as a function of their incident angle, follows the functional form predicted by Lindhard [Li65]. The parameters of

the fit have the same value at 35, 100, and 250 GeV/c beam momenta.

The behaviour of the 35 GeV/c negative particles was quite different from the positively charged particles. The negative particles, going along the <110> axis direction, were observed to have larger than average energy loss (cf. Sec. 10.5), in marked contrast to the positive particle behaviour, where a significant decrease in the energy loss is observed. The low energy loss particles showed a broad dip ($\sim 3\psi_1$) around the axis position. This is consistent with broad dips observed for negative particles distribution in other experiments. The central peak in the neighbourhood of the axis direction (observed by other experimenters) was not seen probably because of the bad statistics of the data.

Selection on the high energy loss for the negative particles showed a broad peak along the <110> axis direction (cf. Sec. 10.1). The width of the peak was roughly 4 times that of the positive channeled particle distribution of same beam momentum.

The only similarity between the negative and the positive particles was in the azimuthal component of the transverse motion. Statistical equilibrium was observed in the azimuthal scattering angle distribution

for channeled as well as quasi-channeled particles (cf. Sec. 10.2).

The radial component of the scattering angle for the negative particles was larger than their positive counterpart when their incident angles were less than the critical angle of channeling, as expected (cf. Sec. 10.3).

11.2 SUGGESTIONS FOR FUTURE EXPERIMENTS

There were certain things that were learned in analysing this experiment. The following suggestions are based on these analysis hindsights and are directed to people who are interested in doing channeling in the multi-hundred GeV/c beam momentum range.

The critical angle of channeling in the multi-hundred GeV/c range is very small and therefore it was essential that the error in the angle measurement be minimized. The drift chamber accuracies were found adequate in measuring small angles. The errors due to the multiple scattering in the system were appreciably large at 35 GeV/c compared to their values at 100 and 250 GeV/c momenta. These could have been reduced by using thinner mylar windows on the vacuum pipes and the goniometer and decreasing the air gap between the drift chambers as much as possible. The main contribution of the system multiple scattering in this experiment was due to the air gaps.

The channeling critical angle, which is a measure of the extent of influence of the string of atoms in the crystal, decreases less rapidly ($\propto 1/\sqrt{E}$) than the multiple scattering angle spread ($\propto 1/E$) in the crystal. Therefore the multiple scattering in the thick crystal would produce a larger masking of the channeling effect at 35 GeV/c than at 250 GeV/c momentum.

Besides increasing the energy of the beam, the effect of multiple scattering in the crystal could be reduced by decreasing the length of the crystal. The 2 cms thick crystal was used in this experiment to make sure that there was statistical equilibrium in the azimuthal component of the transverse motion.

From Golovchenko's calculation (cf. Sec. 2.4 and Sec. 7.2) one can see that there would be statistical equilibrium in the azimuthal component of the transverse motion for 250 GeV/c channeled particles passing through a crystal as thin as 1 mm. This would reduce the multiple scattering by a factor of 4.5 and make the channeling effect that much more prominent. In future experiments one should take note of this fact while selecting the thickness of the crystal.

Since the multiple scattering is the largest at 35 GeV/c momentum in comparison to the multiple scattering at 100 and 250 GeV/c, it is unfortunate that the

negative particle channeling data was taken only at 35 GeV/c beam momentum in this experiment. It is suggested that in future experiments on channeling at higher energies, the negative particle data be taken at the highest possible beam momentum values. This would yield more accurate and better information about the influence of the string of atoms on the negative particles. There are very few negative particle results on channeling in the current literature.

The results on radial diffusion of the transverse motion of the beam at 250 GeV/c momentum suggests that the focusing or cooling of the channeled particles may be observed at 2-3 TeV/c beam momentum for 2 cm thick Germanium crystal along <110> axis direction (cf. Sec. 7.3.2). Such high energy beams are not available at present in the accelerator facilities around the world. But as a first step, it is suggested that the next series of experiments on channeling at high energy be done at 1 TeV/c beam momentum. These experiments could be done at FERMILAB where the installation of the ENERGY DOUBLER by 1983 will raise the beam momentum to 1 TeV/c.

The obvious choice of the crystal material is again Germanium or Silicon, which can be fabricated in a very pure and defect free single crystal state of large size. It is suggested that the thickness of the

crystal be kept same as in this experiment, i.e., 2 cms for easy comparison with the data at 35, 100 and 250 GeV/c beam momenta.

The critical angle of channeling for <110> axis in Germanium crystal is 21.5 micro-radians for 1 TeV/c beam particles. This is a very small angle. But this experiment has already proved that high precision drift chambers can be used to measure the very small angles needed in studying channeling at multi-hundred GeV/c momentum. The critical angle at 1 TeV/c is a factor of 2 smaller than the critical angle at 250 GeV/c and, therefore, by increasing the distance between the drift chambers to at least 50 meters, the uncertainty in the exit angle measurement due to the drift chambers would be reduced from 5.5 micro-radians (in this experiment) to 2.0 micro-radians. The fractional error would then be of the same order of magnitude at 1 TeV/c as it was at 250 GeV/c.

The other source of error in the angle measurement is the multiple scattering in the system. It was small at 250 GeV/c and would be reduced by a factor of 4 at 1 TeV/c beam momentum. It can be minimized further by using thin mylar windows on the vacuum pipes and goniometer and decreasing the air gap between the drift chambers as much as possible.

The rms multiple scattering angle spread for random orientation of the crystal at 1 TeV/c is 18.4 micro-radians. This is smaller than the critical angle of channeling at the same beam momentum value and therefore the channeling effect due to the string of atoms in this case would be more prominent in comparison to the 250 GeV/c data. It is also possible that one may see COOLING or FOCUSING of the channeled beam particles even at 1 TeV/c. This is because the estimate of 3 TeV/c beam momentum for which one expects cooling of the beam transverse energy of the channeled particles was an upper limit and the actual value should be smaller than that.

The deflection and bending of the beam due to the string of atoms would be another effect that would be interesting to look at 1 TeV/c beam momentum. This would have important applications in steering and bending of high energy external beams in accelerator facilities.

BIBLIOGRAPHY

Ah80 Ahlen, S. P., Revs. of Mod. Physics 52, 121 (1980).

Al76 Allen, D., D. Gockley, G. Lazo, W. Gibson, H. Wegner, and A. Kanofsky, Lettere Al Nuovo Cimento 15, 529-534 (1976).

An78 Anderson, S. K., H. Esbensen, O. Fich, J. A. Golovchenko, H. Nielsen, H. E. Schiott, E. Uggerhoj, C. Vraast-Thomsen, G. Cherpale, G. Petersen, F. Sauli, J. P. Ponpon, and R. Siefert, Nuclear Physics B144, 1 (1978).

Ba78 Baker, W. F., A. S. Carroll, I-H Chiang, D. P. Eartly, O. Fackler, G. Giacometti, A. M. Jonekheere, P. F. M. Koehler, T. F. Kycia, K. K. Li, M. O. Marx, P. O. Mazur, D. C. Rahm, and R. Rubinstein, FERMILAB INTERNAL REPORT, FERMILAB 78/79, Exp 7110-104.

Bel78 Beloshitsky, V. V., and M. A. Kumakov, Radiation Effects, 35, 209 (1978).

Ber64 Berger, M. J., and S. M. Seltzer, Studies in Penetration of Charged Particles in Matter, Nat. Acad. Sci (National Research Council) publ. 1133 (1964) 103.

Boh48 Bohr, N., Mat. Fys. Medd. Dan. Vidd. Selsk., 18, No. 8 (1948).

Bor61 Börsch-Supan, W., Journal of Research, NBS, 65B, 245 (1961).

Br74 Breskin, A., G. Charpak, B. Gabionel, F. Sauli, N. Trautner, W. Duinker, G. Schultz, Nucl. Instr. & Meth. 119, 9 (1974).

Br78 Bricman, C., C. Dionisi, R. J. Hemingway, M. Muzzucato, L. Montanet, N. Barash-Schmidt, R. L. Crawford, M. Roos, A. Barbaro-Galtieri, C. P. Horne, R. L. Kelly, M. J. Losty, A. Rittenberg, T. G. Trippe, G. P. Yost, and B. Armstrong, LAWRENCE-BERKELEY LABORATORY PUB.LBL-100, April 1978.

Ca75 Carrigan, R. A., Phys. Rev. Letts. 35, 206 (1975).

Da60 Davis, J. A., J. Friesen, and J. D. McIntyre, Can. J. Chem. 38, 1526 (1960).

De74 Dettmann, K., and M. T. Robinson, Phys. Rev. B. 10, 1 (1974).

Do68 Doyle, P. A., and P. S. Turner, Aeta Cryst. A24, 390 (1968).

Ed75 Edge, R. D., and Q. C. Murphree, Atomic Collisions in Solids, Vol. II, eds. S. Datz, B. R. Appleton, and C. D. Moak (New York: Plenum Press, 1975) p. 877.

El79 Elishev, A. F., Phys. Lett., 88B, 387 (1979).

Es77 Esbensen, H., O. Fich, J. A. Golovchenko, K. O. Nielsen, E. Uggerhoj, C. Vraast-Thomsen, A. Charpak, S. Majewski, F. Sauli, J. P. Ponpon, Nucl. Phys. B 127, 281 (1977).

Es78a Esbensen, H., et al., Phys. Rev. B18, 1039 (1978).

Es78b Esbensen, H., O. Fich, J. A. Golovchenko, S. Madsen, H. Nielsen, H. E. Schiott, E. Uggerhoj, C. Vraast-Thomsen, C. Charpak, S. Majewski, R. Odyniee, C. Petersen, F. Sauli, J. P. Ponpon, and P. Siffert, Phys. Letts. 72B, No. 3, 408 (1978).

Es78c Esbensen, H., and J. A. Golovchenko, Nucl Phys. A A298, 382 (1978).

Fa63 Fano, U., Ann. Rev. Nucl. Sci., 13, 67 (1963).

Fic75 Fich, O., J. A. Golovchenko, K. O. Nielsen, E. Uggerhoj, G. Charpak and F. Sauli, Phys. Letts. 57B, No. 1, 90 (1975).

Fic76 Fich, O, J. A. Golovchenko, K. O. Nielsen, E. Uggerhoj, C. Vraast-Thomsen, G. Charpak, S. Majewski, F. Sauli and J. P. Ponpon, Phys. Rev. Letts. 36, 1245 (1976).

Fi176 Filatova, N. A., T. S. Nigmanov, V. P. Pugachevich, V. D. Riabtsov, M. D. Shefranov, E. N. Tsyganov, D. V. Uralsky, A. S. Vodopianov, F. Sauli, and M. Atec, FERMILAB PUB 76/97 EXP 7500-456.

Ge74 Gemmell, D. S., Revs. of Mod. Phys. 46, 129 (1974).

Ge76 Golovchenko, J. A., Phys. Rev. B 13, 4672 (1976).

Hu77 Hurle, D. T. J., Ed. P. Hartman, North-Holland Series in Crystal Growth, Eds. W. Bardsley, D. T. J. Hurle and J. B. Mullin.

Ka76 Kanofsky, A., Lettere Al Nuovo Cimento 17, 191 (1976).

Ka77 Kanofsky, A., Rev. of Scientific Instr., 48, 34 (1977).

Ka78 Kanofsky, A., Proceedings of the 1978 Summer Workshop, July 1978, Brookhaven National Laboratory, Associated Universities, Inc., BNL 50885, (1978) pp. 406-410.

Ku76 Kumakhov, M. A., Phys. Lett. A57, 17 (1976).

La44 Landau, L., J. Exp. Phys. (USSR), 8, 201 (1944).

Li65 Lindhard, J., Matematisk-fysiske Meddelelser udgivet af Det Kongelige Danske Videnskabernes Selskab (Mat.Fys. Modd. Dan. Vid. Selsk) 34, No. 14, 1 (1965).

Mo "Optical Orientation Alignment," Monsanto 16-ME-003-1268.

Pa77 Pathak, A. P., Phys. Rev. B 15, 3309 (1977).

Po65 Powell, M. J. D., Computer Journal 8, 303 (1965).

Ro62 Robinson, M. T., Appl. Phys. Lett. 1, 49 (1962).

Ro63 Robinson, M. T., and O. S. Oen, Phys. Rev. 132, 2385 (1963).

Sta12 Stark, J., Phys. Z., 13, 973 (1912).

Ste66 Sternheimer, R. M., Phys. Rev. 145, 247 (1966).

Ste71 Sternheimer, R. M., Phys. Rev. B 3, 3681 (1971).

Te77 Terhune, R. W., and R. H. Pantell, Appl. Phys. Lett. 30, 265 (1977).

Wi29 Williams, E. J., Proc. Roy. Soc. London, A125, 420 (1929).

APPENDIX A

Fig. A.1 shows the six sets of drift planes in the three drift chamber modules. The circles represent the signal wires and the numbers below them are their identifier. The 56 signal wires indicated in the figure are the ones for which the TDC counts were recorded. The third drift chamber module, DC3, was twice as big as the first and the second but only 16 wires were active in DC3 and these are indicated in the figure. The signal wires 19, 20, 21, 22, 23, 24, 38, and 39 were dead for all the experimental runs.

The TDC conversion factors (a scale factor giving the number of nano-seconds corresponding to one count of the TDC) for each active signal wire are listed in Table A.1. The conversion factors are also called the least counts of the TDCs. The least counts were obtained by starting and then stopping all the TDCs with two standard signals separated by an accurately known time interval.

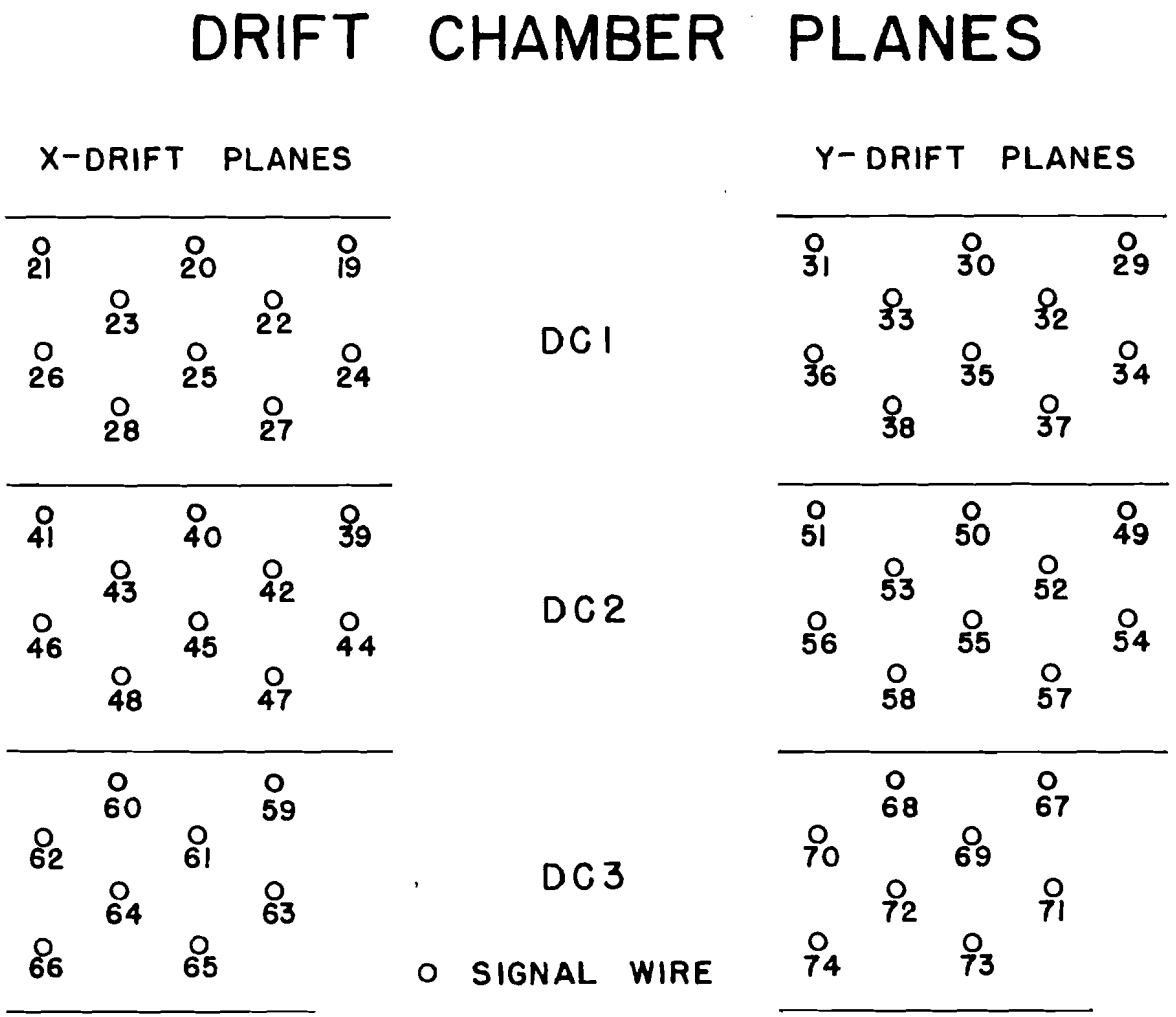

Fig. A.1 The six set of drift planes in the three drift chamber modules. The signal wires and their identifying numbers are indicated.

Table A.1 The TDC conversion factors for each signal wire. Conversion factors for the dead wires are not listed.

Wire Number	TDC Conversion Factor (n-sec)	Wire Number	TDC Conversion Factor (n-sec)
24	0.24413	51	0.25656
25	0.24018	52	0.25387
26	0.24363	53	0.24845
27	0.24675	54	0.25151
28	0.24695	55	0.24688
29	0.24622	56	0.25246
30	0.24485	57	0.25338
31	0.24494	58	0.24852
32	0.24458	59	0.23579
33	0.24494	60	0.23627
34	0.24512	61	0.23737
35	0.25210	62	0.23865
36	0.25011	63	0.23671
39	0.24952	64	0.23509
40	0.24903	65	0.24234
41	0.24971	66	0.23491
42	0.24933	67	0.24570
43	0.24856	68	0.24519
44	0.25181	69	0.24222
45	0.25292	70	0.24689
46	0.25303	71	0.24506
47	0.25453	72	0.24523
48	0.25319	73	0.24385
49	0.25070	74	0.24385
50	0.25536		

APPENDIX B

MEASUREMENT OF T_o

The raw TDC (Time-to-Digital Convertors) counts for each signal wire were converted to time in nano-seconds by multiplying them with their corresponding TDC conversion factors listed in Table A.1 in Appendix A.

Histograms of the time interval distribution for each wire was made in the range of 0 to 40 nano-seconds. Samples of data were taken from experimental runs spread throughout the whole experiment. Events were accumulated in 40 bins, each 1 nano-second wide. Figure B.1 shows the distributions of time intervals for two typical wires. The distributions are flat up to a certain point and then falls to zero sharply. The time interval at half the maximum height was taken as T_o. The maximum error in T_o was estimated as ±1 nano-seconds. The T_o values obtained by the method described above are listed in Table B.1. It contains values for those wires that were activated by the beam particles.

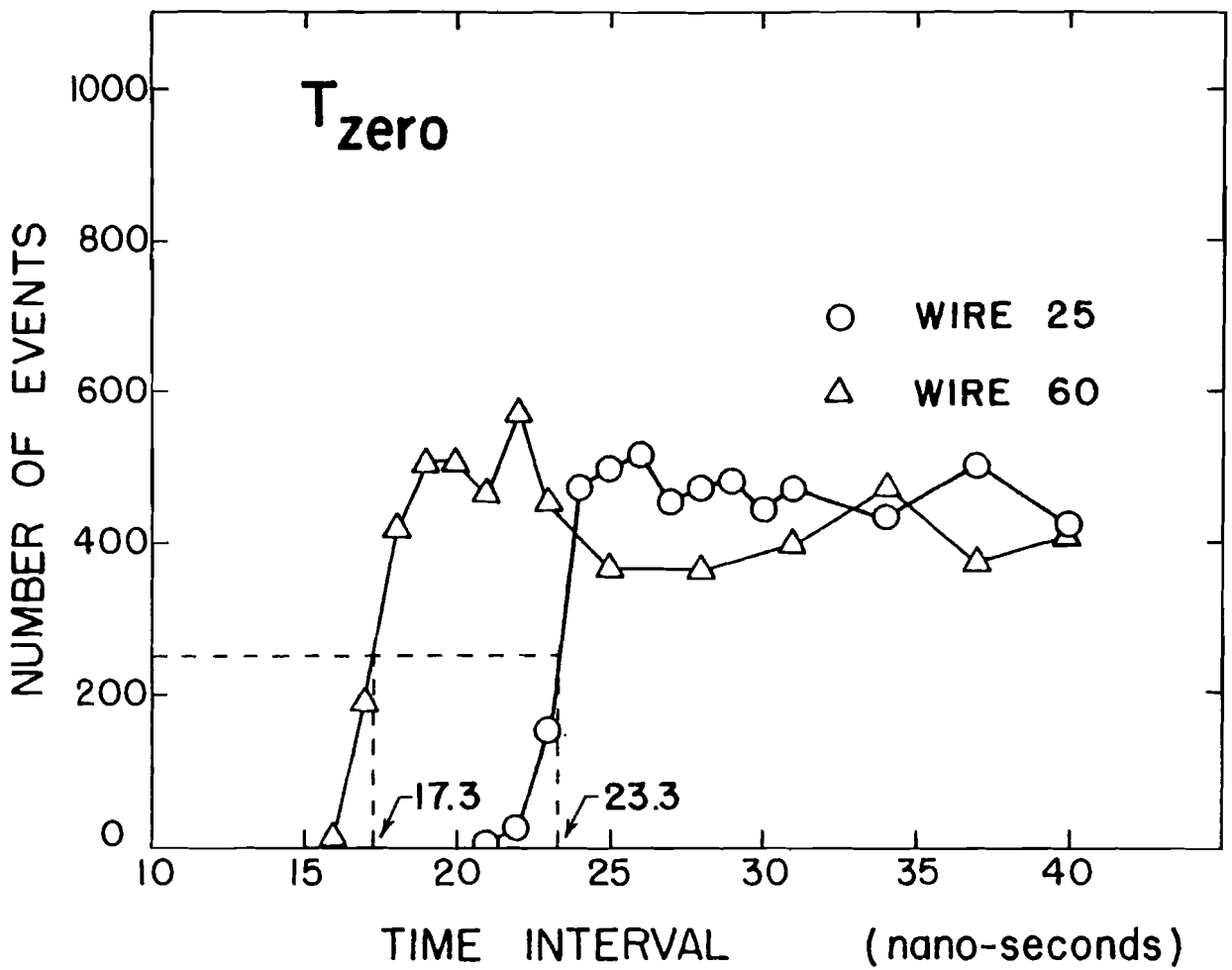

Fig. B.1 Time interval distributions for two typical drift chamber signal wires. The time interval at half the maximum height on the leading edge is the T_o value for that wire.

Table B.1 The T_o values for all the active wires in the three drift chamber modules, DC1, DC2, and DC3.

Wire Number	T_o (n-sec)	Wire Number	T_o (n-sec)
25	23.3	55	22.6
26	20.0	58	20.6
27	22.4	59	15.8
28	25.4	60	17.3
29	25.0	61	17.3
30	23.4	62	17.9
31	25.0	63	16.3
32	23.1	64	15.4
33	22.6	65	15.8
34	22.0	66	9.6
35	25.4	67	22.4
36	23.5	68	23.0
40	20.8	69	18.2
43	24.1	70	19.3
45	22.1	71	23.6
48	22.2	72	22.8
50	21.3	73	22.6
53	22.7	74	22.0

APPENDIX C

AXES AND PLANES IN GERMANIUM CRYSTAL

Fig. C.1(a) shows the unit cell in a Germanium crystal. The three transaltion vectors $\vec{a}$, $\vec{b}$, and $\vec{c}$ of the unit cell are also shown. The Germanium crystal is cubic and it has a diamond structure, in the language of crystallographers.

The planes in the crystal are defined in terms of the translation vectors $\vec{a}$, $\vec{b}$, and $\vec{c}$. The intercept of the plane on the $\vec{a}$, $\vec{b}$, and $\vec{c}$ axes are found as a fraction of the length of these vectors. The reciprocals of these intercepts are then reduced to three smallest integer values having the same ratios. These reciprocal integers, in parentheses, define the crystal plane, i.e., (h,k,l). The triplet of the smallest integers representing a plane are called the Miller Indices. The (111) plane for the unit cell shown in Fig. C.1(a) is indicated by the heavy triangular outline in Fig. C.1(b).

The axis or direction of rows of atoms in a crystal is defined by a set of the three smallest integers <uvw> representing the ratios of its vector components, referred to the three translational vectors of the unit cell. For the cubic crystal, as a special case, the axis may also be defined in terms of the plane perpendi-

UNIT CELL

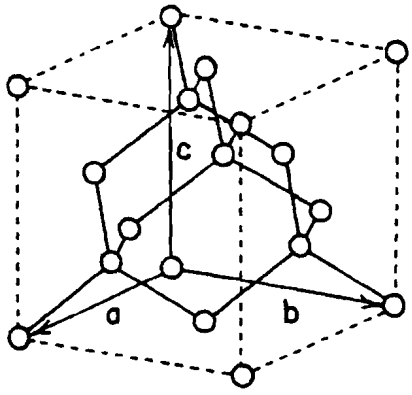

(a)

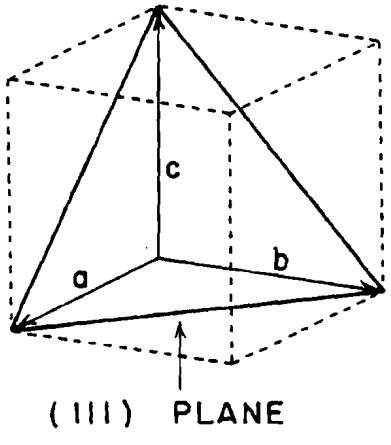

(b)

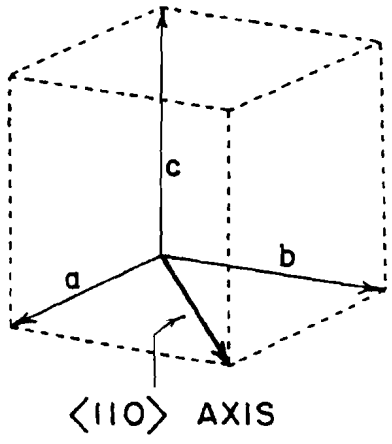

(c)

Fig. C.1 (a) Unit cell of Germanium crystal. $\vec{a}$, $\vec{b}$, and $\vec{c}$ are the three translation vectors. (b) The (111) plane indicated by the triangular outline. (c) The <110> axis direction in a unit cell.

cular to the axis direction. The Miller Indices of the perpendicular plane is enclosed in brackets to represent the axis. The <110> axis direction for the unit cell of the Germanium crystal is shown in Fig. C.1(c).

The major low index planes parallel to the <110> axis are shown in Fig. 5.5.

VITA

Muhammad Abul Hasan, second son of Dr. M. Hasan and Mrs. S. Hasan, was born in Dacca, Bangladesh, on March 9, 1950. After graduating from Govt. Senior Model School, Karachi, Pakistan, in 1965 he spent two years in D. J. Govt. Science College, Karachi. He entered the Physics Department of Karachi University in 1967 and received his B.Sc.(Hons.) and M.Sc. degrees in 1970 and 1971, respectively. He was awarded a Gold Medal for standing first in the M.Sc. examination.

He taught in the Physics Departments of Baluchistan University, Quetta, Pakistan, in 1972-73 and Karachi University in 1973-74.

He began his graduate work at Lehigh University, Bethlehem, Pennsylvania, USA, in the Fall of 1974 and received his Master of Science degree, in Physics, in May 1976. During his graduate work at Lehigh he has been a teaching and a research assistant and was awarded a Byllesby Fellowship for the 1978-79 academic year by the Graduate School.

In the course of the work for the Ph.D. degree at Lehigh he has been co-author of "Observation of Characteristic γ Radiation from the $(K^-, \pi^- \gamma)$ Reaction

on Light Nuclei," J. C. Herrera, et al., Phys. Rev. Lett. 40, 158 (1978), "Modulation of Nuclear Interactions Using Channeling at Multi-hundred GeV Energies," R. A. Carrigan, et al., Nucl. Phys. B163, 1-20 (1980), and many other contributed papers in International Topical Conferences on Meson-Nuclear Physics and APS meetings.

He is a member of the American Physical Society and Sigma Xi, the Scientific Research Society.